

INFORMATION TO USERS

This manuscript has been reproduced from the microfilm master. UMI films the text directly from the original or copy submitted. Thus, some thesis and dissertation copies are in typewriter face, while others may be from any type of computer printer.

The quality of this reproduction is dependent upon the quality of the copy submitted. Broken or indistinct print, colored or poor quality illustrations and photographs, print bleedthrough, substandard margins, and improper alignment can adversely affect reproduction.

In the unlikely event that the author did not send UMI a complete manuscript and there are missing pages, these will be noted. Also, if unauthorized copyright material had to be removed, a note will indicate the deletion.

Oversize materials (e.g., maps, drawings, charts) are reproduced by sectioning the original, beginning at the upper left-hand corner and continuing from left to right in equal sections with small overlaps. Each original is also photographed in one exposure and is included in reduced form at the back of the book.

Photographs included in the original manuscript have been reproduced xerographically in this copy. Higher quality 6" x 9" black and white photographic prints are available for any photographs or illustrations appearing in this copy for an additional charge. Contact UMI directly to order.

UMI

A Bell & Howell Information Company
300 North Zeeb Road, Ann Arbor MI 48106-1346 USA
313/761-4700 800/521-0600

Abstract

Title of Dissertation: LIE METHODS.
EXACT MAP COMPUTATION.
AND THE PROBLEM OF DISPERSION
IN SPACE CHARGE
DOMINATED BEAMS

Marco Venturini, Doctor of Philosophy, 1998

Dissertation directed by: Professor Alexander J. Dragt
Department of Physics
and Professor Martin P. Reiser
Department of Electrical Engineering

The concept and use of 'transfer maps' has become a fundamental ingredient in a modern description of single-particle beam dynamics. Lie methods, in particular, provide a useful framework for map computation. In the autonomous case calculation of a transfer map is equivalent to evaluating a Lie transformation. In general this is a nontrivial problem. The first part of the Dissertation contains a discussion of two possible ways to compute Lie transformations based on the theory of normal forms for Lie maps and the Scaling, Splitting, and Squaring algorithm. Implementation of the latter in the code MARYLIE5.0 is also discussed.

In the second part we study fringe field effects in magnets and develop suitable methods to describe these effects without idealization of field profiles. In particular, we introduce a method for the exact computation of transfer maps using a realistic description of magnetic fields. The magnetic field data can be obtained either from numerical computation with the aid of a 3D electromagnetic code or from measurements with spinning coils. The method is applied to study beam dynamics in the Large Hadron Collider. In other special situations one can investigate fringe-fields effects using a realistic analytical model. This is the case for the University of Maryland E-Ring, for which we present a thorough study of single particle dynamics. Using the analytical model we show how the third-order intrinsic aberrations, due to fringes, decrease with increasing magnet aperture.

In the third part of the Dissertation we shift our attention to space charge effects in small rings and analyze the interplay between space charge and dispersion. We work out a novel set of equations that can be used to obtain simultaneous matching of rms-envelopes and the dispersion function in space-charge dominated beams. Central to the derivation of the new equations is the existence of a new linear invariant that generalizes the rms emittance to the case where bending magnets and an energy spread are present.

**LIE METHODS,
EXACT MAP COMPUTATION,
AND THE PROBLEM OF DISPERSION
IN SPACE CHARGE
DOMINATED BEAMS**

by

Marco Venturini

Dissertation submitted to the Faculty of the Graduate School of the
University of Maryland, College Park in partial fulfillment
of the requirements for the degree of
Doctor of Philosophy
1998

Advisory Committee:

Professor Alexander J. Dragt, Chairman/Advisor
Professor Martin P. Reiser /Advisor
Professor Robert L. Gluckstern
Professor Jon Orloff
Professor Frederick N. Skiff

UMI Number: 9909022

**UMI Microform 9909022
Copyright 1998, by UMI Company. All rights reserved.**

**This microform edition is protected against unauthorized
copying under Title 17, United States Code.**

UMI
300 North Zeeb Road
Ann Arbor, MI 48103

Preface

In accelerator physics there exists a certain dichotomy between the subfields devoted to the study of 'single particle' and 'multi particle' effects. Such a dichotomy is reflected by a difference of methods, applications, goals and somehow a certain separation between the communities of scientists working in the two areas.

The challenge underlying part of the work that led to this Dissertation was to provide a bridge between the two communities, which at Maryland are well represented by the Dynamical System and Accelerator Theory (DSAT) and Charged Particle Beam Research Lab (CPBRL) groups. The motivation for the collaboration and one of the unifying themes for this Dissertation was the Electron Ring (E-Ring) project, currently under development at the University of Maryland

Although the construction of the E-Ring was proposed by the CPBRL group to study the physics of space charge dominated beams, methods originated in a single particle context turned out to be useful to assist in the design. Fringe field effects, for example, which are important for the E-Ring could be efficiently and exactly studied using a properly expanded version of MARYLIE, a code developed by the DSAT group. Working on the E-Ring project has eventually given me an opportunity to broaden my horizons and come across interesting and challenging problems involving space charge effects.

The composite content of the Dissertation reflects the variety of the experiences I have been exposed to while working in the two groups. The Dissertation can approximately be divided into three parts. The first is devoted to the development of Lie algebraic methods applied to map computation in the study of single particle dynamics. The second part covers various issues related to the problem of the exact map computation from magnetic field data and the role of magnet fringe fields in determining beam dynamics. Specific applications are reported for the E-Ring and the Large Hadron Collider to be built at CERN. Finally, in the third part we investigate the problem of dispersion in space charge dominated beams and present a novel theory for beam matching in the presence of dispersion and space charge.

Here is more in detail an outline for the single Chapters.

Chapter 1 serves as a general introduction to Lie methods applied to beam dynamics and a general source of reference for the rest of the Dissertation. It also contains a detailed introduction to the concept of normal form for a Lie map.

Chapter 2 is dedicated to the problem of how to evaluate Lie maps starting from autonomous Hamiltonians. We describe two techniques. The first is based on using the normal form for maps, the second on the Scaling, Splitting, Squaring (SSS) algorithm. Implementation of the latter in MARYLIE5.0 is also discussed. The last part of the Chapter contains a discussion of a method based on spectral decomposition to compute the transfer matrices in the linear case.

In Chapter 3 we face the problem of determining the exact transfer maps for magnet elements from magnetic field data. The data may originate from computation or direct measurement. The method we introduce makes possible a

very accurate description of the dynamic effects of fringe fields in magnets. The Chapter also contains a thorough discussion of the multipole representation of a magnetic field, scalar potential and vector potential.

The discussion on the multiple field representation of Chapter 4 is used in the following Chapter to address some issues of iron-free magnet design. The study was motivated by the need to assist in the design of the printed circuit magnet planned to be used in the Maryland E-Ring.

In Chapter 5 we report the single particle study of the Maryland E-Ring. The study is based on an exact analytical description of the magnet fields including the fringes.

The following Chapter reports the semianalytical study of how the third order aberrations due to the fringes scale with respect to the extension of the fringes. Contrary to some expectations the study shows that for a fixed value of the focal length and magnet length, the third order aberrations due to the fringes become smaller for a larger aperture of the magnets.

In Chapter 7 the method developed in Chapter 3 is applied to the analysis of the magnetic field data for the high gradient superconducting quadrupoles in the interaction regions of the Large Hadron Collider at CERN. The field data are then used to compute the transfer maps and carry out a study of the beam dynamics.

Chapter 8 introduces the problem of dispersion in the presence of significant space charge effects and outlines two possible approaches. One is based on the study of a simplified self-consistent model. Such an approach is explored in Chapter 9 where self-consistent solutions of the Vlasov-Poisson equation in the form of generalized KV beam distributions are investigated. The second

approach involves the equations for the second moments of the beam distribution and is discussed in Chapter 10. There we succeed in finding a generalization of the standard rms envelope equations to the more general case where bending magnets and a longitudinal momentum spread are present. The resulting new set of equations, the rms envelope-dispersion equations, can be used to work out the required matching conditions for the dispersion function for highly space charge dominated beams.

In conclusion, having to highlight what I think are the most important contributions contained in this Dissertation I would indicate: (i) the implementation of the SSS algorithm in MARYLIE. (ii) the development of a method for transfer map calculation from either computed or measured magnetic field data (iii) the definition a new generalized rms emittance, which is invariant when dispersion is present. (iv) the derivation of the new rms envelope-dispersion equations.

Dedication

To the Memory of Maria Teresa Ronca

...ΤΗΙ ΓΑΡ ΜΕ ΠΟΛΥΦΡΑΣΤΟΙ ΦΕΡΟΝ ΙΠΠΟΙ
ΑΡΜΑ ΤΙΤΑΙΝΟΥΣΑΙ ΚΟΥΠΑΙ ΔΕ ΟΔΟΝ ΗΓΕΜΟΝΕΥΟΝ.

...There I was carried; for the well-discerning horses
were straining the chariot and the maidens where leading the way.

...La' fui condotto: la' infatti mi portarono i saggi corsieri
che trascinano il carro, e le fanciulle mostraronon il cammino.

Parmenides. On Nature. Fragment 1.4-5.

Acknowledgements

First and foremost I would like to thank Alex Dragt and Martin Reiser, real ‘maestri’, for the privilege they gave me to work with them, their support and assistance. Sharing my time between the ‘Dynamical System and Accelerator Theory’ and ‘Charged Particle Beam Research Lab’ groups has been a fertile and fruitful experience.

I would also like to mention Tino Pusterla and Walter Scandale, who first introduced me to accelerator physics.

Special thanks to Dan Abell for his assistance in a number of problems, ranging from understanding Lie algebras and unveiling the mysteries of Latex to selecting the right place to have a romantic date. He also provided me with the phase space pictures of Chapter 7 obtained by his code CTRACK.

I have greatly benefitted from Bob Gluckstern’s deep knowledge of classical electromagnetism and beam physics.

With Peter Walstrom I had useful conversations on magnet modeling. He also allowed me to use his Bessel function and integration Fortran routines. Gianluca Sabbi provided the magnetic field data for the

LHC magnets used in Chapter 7. Rami Kishek carried out the PIC code calculations to test the theory discussed in Chapter 10.

Discussions with Santiago Bernal, Alexi Fedotov, Al Garren, Terry Godlove, J.G. Wang on various issues have also been fruitful.

I thank Janice Schoonover secretary of the CPBRL group for her kindness and help, and Rachel Needle secretary of the DSAT group as well.

Also, I am thankful to Jon Orloff and Frederick Skiff for accepting to serve in my Dissertation Committee.

Finally I would like to express my gratitude to the Italian 'Ministero della Ricerca Scientifica', and 'Fondazione A. Gini' in Padova for financing my first year at College Park, and the US Department of Energy for financing the remaining part of my stay.

Contents

Preface	ii
Dedication	vi
Acknowledgments	vii
List of Tables	xiv
List of Figures	xv
1 Lie Methods and Beam Dynamics	1
1.1 Why Maps?	2
1.2 Hamiltonian for Charged Particles	6
1.3 Hamiltonian Systems. Maps and Lie Methods	11
1.4 Computation of Lie Maps in the General Case	18
1.5 Normal Form Analysis	21
1.5.1 Semisimple case.	24
1.5.2 The general case.	26
2 Development of Lie Calculus	33
2.1 Lie Map Factorization Using Normal Forms.	33

2.2	Lie Map Factorization Using Splitting, Scaling, Squaring	37
2.3	Exponentiation of Hamiltonian Matrices	45
2.3.1	The Decomposition Method	47
2.3.2	Two Dimensions	49
2.3.3	Four Dimensions	49
2.3.4	Six Dimensions	50
2.3.5	Numerical Implementation	52
2.4	Evaluation of $iex(\mathbf{A})$	53
3	Map Computation from Magnetic Field Data	56
3.1	Introduction	56
3.2	Multipole Expansion for the Scalar Potential and Generalized Gradients	59
3.3	Multipole Expansion for the Vector Potential	61
3.4	Calculation of the Generalized Gradients from Numerical Field Data	65
3.4.1	B_ρ Known	66
3.4.2	B_z Known	68
3.4.3	B_ϕ Known	70
3.4.4	Scalar Potential Known	71
3.5	Calculation of the Generalized Gradients from Field Measurements	71
3.6	Insensitivity to Errors	77
3.7	Numerical Tests	78
4	Design of Current Sheet Magnets	84
4.1	Pure Multipole Magnets	85

4.2	2D Current Sheet Magnets with Arbitrary Cross Section	89
4.2.1	Circular aperture	92
4.2.2	Rectangular aperture	92
4.3	Further Discussion on Lambertson Magnets	93
4.3.1	The discrete model	97
4.4	Further Discussion on Panofsky Quadrupoles	97
5	Beam Dynamics Study for the Maryland Electron Ring	99
5.1	Introduction	99
5.2	Lattice Design Overview	103
5.3	Quadrupole Magnets	106
5.4	Dipole Magnets	117
5.5	Map Computation	120
5.6	Lattice Functions	123
5.7	Single Particle Dynamics Study: Main Results	127
5.8	Single Particle Dynamics Study: Other Results	132
5.8.1	Nonlinear (Nonresonant) Normal form Analysis	138
5.9	Summary	141
6	Dynamical Effects of Soft Fringes: an Analytical Model	142
6.1	The Quadrupole Magnet Model	145
6.2	Transfer Map Computation	148
6.3	Analytical Model	152
6.4	Summary	159
7	Magnetic Field Analysis for the LHC High Gradient Quadrupoles	159

7.1	Introduction	160
7.2	Magnetic Field Analysis	163
7.3	Dynamical Effect of the HG Quad Triplets	168
7.4	Summary	174
8	Dispersion and Space Charge	176
8.1	Introduction	176
8.2	Dispersion for Single Particles	178
8.3	A Multiparticle Perspective	180
8.3.1	The Matching Problem	183
8.4	Inclusion of Space Charge	186
9	Self-consistent Beam Distributions with Space Charge and Dispersion	189
9.1	The Vlasov-Poisson Equations	190
9.2	Monochromatic KV Beam	192
9.3	Generalized KV Beam	193
9.3.1	Emittance Calculation	195
9.4	The Algorithm	198
9.5	The Numerical Solutions	199
9.6	Discussion	203
9.7	'Time' Dependent Vlasov Equation	207
9.8	Summary	210
10	Envelope Equations in the Presence of Space Charge and Dispersion	212
10.1	Introduction.	212

10.2 Envelope Equations in the Absence of Dispersion	216
10.3 Generalization of the rms Emittance	219
10.4 Envelope Equations in the Presence of Dispersion	223
10.5 Transition from a Straight Beam Line to a Dispersive Channel . .	227
10.5.1 Limit of vanishing space charge	229
10.5.2 Space Charge Included	232
10.5.3 Numerical Solutions for the Stationary Case	234
10.6 Numerical Tests over a FODO Lattice	238
10.7 Summary	243
A Multipole expansion for the Vector Potential in the Coulomb Gauge	245
B Miscellanea of Mathematical Formulae	251
C Dispersion and Second Moments of a Beam Distribution	254
D Mathematica Notebook	257
Bibliography	261

List of Tables

3.1	Relative difference between the surface-data-based map and the exact map.	81
3.2	Relative error of the noisy surface-data-based map compared to the exact map.	82
5.1	Design Parameters for the E-Ring	103
5.2	Relative Integrated multipoles for a PC Quad at $\rho_o = .5R$ in units of 10^{-4}	113
5.3	Relative e.m.f for a rotating coil of radius $R_s = 2.54$ cm (units of 10^{-4}) in a PC Quad.	113
5.4	Relative Integrated multipoles for a PC Dipole at $\rho = .5R$ in units of 10^{-4}	118
5.5	Parameters for the PC Quad and PC Dip (ideal design)	119
5.6	Pseudo Hamiltonian Coefficients (ideal E-Ring lattice)	138
5.7	Pseudo Hamiltonian Coefficients	139
9.1	Parameters for the Maryland Electron Ring smooth model.	199
9.2	Current, perveance, tune depression and rms emittance for round KV beams of 10 keV electrons. Beam radius=1 cm.	204

List of Figures

2.1	Logarithm (\log_{10}) of the relative error vs. number of squarings for the Lie generator x^5 of a map as calculated using the SSS algorithm with a 5 th order Taylor and a 4 th symplectic integrator split formula. The error is computed against a calculation done with GENMAP.	44
2.2	CPU time vs. number of squarings in computing a map using the SSS algorithm. The 5 th order Taylor and the 4 th symplectic integrator splitting methods are compared.	44
3.1	The function $C_{2,s}^{[0]}$ as calculated numerically from the surface data (dots) and analytically (solid line).	80
3.2	The function $C_{2,s}^{[4]}$ as calculated numerically from the surface data (dots) and analytically (solid line).	81
4.1	Arbitrary cross section for a current sheet magnet. The integrated multipoles vanish within the area spanned by the circle.	90
4.2	Schematic outline of the current flow in a Lambertson quadrupole. $m = 2$	93

5.1	Generalized gradient $C_2(z)$ for a PC Quad (it is half of the on-axis gradient, $I = 1$ A. single layer).	107
5.2	Generalized gradient $C_6(z)$ for a PC Quad ($I = 1$ A. single layer).	107
5.3	The component B_x of the magnetic field (dots) as a function of y/R at $x = 0, z = 0$. is compared with the linear approximation (dashed line), and the approximation (solid line) obtained by retaining all the terms through 6 th order in the radius (see the expansion 5.13).	109
5.4	Component B_x of the magnetic field (in Tesla) as a function of y/R at $x = 0, z = l$	111
5.5	Spiral design for one quadrant of the PC quad ($0 \leq \phi < \pi/2$). The line with larger thickness corresponds to the conductor lying on the bottom layer, the thiner line corresponds to the conductor lying on the upper layer.	115
5.6	On-axis vertical magnetic field B_y in a PC dipole (it is equal to $C_1(z)$, $I = 1$ A. single layer).	116
5.7	Generalized gradient $C_3(z)$ in a PC dipole ($I = 1$ A. single layer).	116
5.8	Generalized gradient, $C_5(z)$ in a PC dipole ($I = 1$ A. single layer).	117
5.9	The component B_y (dots) as a function of the radial coordinate ρ/R normalized with respect to R . compared to its analytic approximation through 6 th order (solid line).	119
5.10	Betatron functions for the E-Ring.	123
5.11	Dispersion function for the E-Ring.	124
5.12	Horizontal (solid line) and vertical (dashed line) tunes as a function of the current in the quadrupole magnet windings.	125

5.13	Dynamic aperture for E-Ring (ideal lattice).	127
5.14	Dynamic aperture for E-Ring vs. relative multipole error strength (in units of 10^{-4} . The DA is expressed in units of the acceptance ellipse. See Fig. 5.13	129
5.15	Modified E-Ring lattice (dipoles replaced by drifts). Dynamic aperture obtained by circulating through \mathcal{M}_I , \mathcal{M}_{II} with $\mathcal{M}_{FODO} =$ $\mathcal{M}_I \circ \mathcal{M}_{II}$	132
5.16	Modified E-Ring lattice. Dynamic aperture obtained by iterating \mathcal{M}	132
5.17	Modified E-Ring lattice. Dynamic aperture obtained by using the Cremona simplified map \mathcal{M}_{FODO}	133
5.18	Dynamic aperture in the presence of random multipole errors on top of a linear lattice (dashed line) and the ideal lattice (solid line) with the nonlinear fringe effects included. Modified E-Ring model.	134
5.19	Dynamic aperture DA_x (gray points, bottom) and DA_y (black points, top) vs. phase advance per FODO Cell (which equals tune/36). Modified E-Ring model.	135
5.20	First order (solid line) and second order (dashed line) nonlinear detuning as a function of the physical amplitude of oscillations ($y = 0$).	138
6.1	Gradient profiles for different values of the aspect ratio γ . The in- tegral of the various curves are the same. (Quadrupole semilength $l = .022$ m, $I_1 = 20$ A).	146
6.2	First derivative of the gradient profiles for $\gamma = 1, .4, .2$	146

6.3	Approximation of the focusing function with a stepwise function..	151
6.4	Gradient $\mathcal{G}(z = 0, \gamma)$ evaluated at $z = 0$ as a function of the aperture ratio (defined as $1/\gamma$, the inverse of the aspect ratio γ). .	152
6.5	Lie generator $f_{x^4}^{dyn}$ as a function of the aperture ratio $1/\gamma$ for different values of I_1 . The hard edge limit is defined by $1/\gamma \rightarrow 0$. The solid lines correspond to the analytical calculation discussed in the paper, the dots to a numerical calculation using MARYLIE.	155
6.6	Lie generator $f_{x^3 p_x}^{dyn}$ as a function of the aperture ratio $1/\gamma$ for different values of I_1 . The hard edge limit corresponds to $1/\gamma \rightarrow 0$.	156
6.7	Lie generator f_{x^4} (including both the kinematic and dynamic term) as a function of the aspect ratio γ for different values of I_1	157
6.8	Lie generator $f_{x^3 p_x}$ (including both the kinematic and dynamic term) as a function of the aspect ratio γ for different values of I_1 . .	158
7.1	Harmonic $\mathcal{B}_2(R, z)$ for the Return end: R=3 cm.	162
7.2	Harmonic $\mathcal{B}_6(R, z)$ for the Return end: R=3 cm.	162
7.3	Harmonic $\mathcal{B}_2(R, z)$ for the Lead end: R=2 cm.	163
7.4	Harmonic $\mathcal{B}_6(R, z)$ for the Lead end: R=2 cm.	164
7.5	Generalized gradient $C_2(z)$ for the Return end.	164
7.6	Second derivative of the generalized gradient $C_2^{[2]}(z)$ for the Return end.	165
7.7	Fourth derivative for the generalized gradient $C_2^{[4]}(z)$ for the Return end.	165
7.8	Generalized gradient $C_6(z)$ for the Return end.	166

7.9	Projection of the Poincaré surface of section on the horizontal plane at the IP (normalized coordinates). Map calculated from the magnetic field data.	167
7.10	Projection of the Poincaré surface of section on the vertical plane at the IP (normalized coordinates). Map calculated from the magnetic field data.	167
7.11	Projection of the Poincaré surface of section on the horizontal plane at the IP (normalized coordinates). Map calculated from the magnetic field data with the duodecapoles turned off.	170
7.12	Hard edge model. The fringes are treated in the hard edge limit: the systematic duodecapoles in the kick approximation.	172
7.13	As in Fig. 7.12 but with the pseudo-octupoles turned off.	172
9.1	Scaled density profile $n(x,y)/n(0,0)$ for the generalized KV beam at $y = 0$. Ten density profiles are shown corresponding to values of δ_o ranging from .001 to .01. ($I = .105$ A, $\nu/\nu_o = 0.317$).	193
9.2	Density distribution $n(x,y)$ for $I = .105$ A, $\nu/\nu_o = 0.317$, $\delta_o = .01$. .	194
9.3	Scaled rms horizontal size of the beam. $x_{rms} = (\langle x^2 \rangle_{\delta_o} / \langle x^2 \rangle_o)^{\frac{1}{2}}$, as a function of δ_o . ($I = .105$ A, $\nu/\nu_o = 0.317$).	197
9.4	Scaled horizontal rms emittance $\epsilon_x / \epsilon_{ox}$, as a function of δ_o . ($I = .105$ A, $\nu/\nu_o = 0.317$).	198
9.5	Section of the density distributions $n(x,y)$ at $y = 0$ for various beam currents (see Table 9.2). The densities are in units of 10^7 particles/cm ³ . $\delta_o = .01$	198

9.6 Scaled horizontal rms size $x_{rms} = (\langle x^2 \rangle_{s_0} / \langle x^2 \rangle_o)^{1/2}$ as a function of the tune depression ν/ν_o , (dots). The dashed line represents Eq. (9.27).	202
9.7 Scaled horizontal rms emittance ϵ_x/ϵ_{ox} , as a function of the tune depression ν/ν_o .	203
9.8 Scaled density profile $n(x,0)/n(0,0)$ of the KV beam (simplified analytical model) after a matched injection (solid line) and profile corresponding to the stationary solution of the Vlasov-Poisson equation evaluated numerically (dashed line).	206
9.9 Evolution of a KV beam with gaussian longitudinal momentum spread injected into a smooth dispersive channel (simplified analytical model). Mismatched injection. The four beam density profiles correspond to $z = \lambda_b/16, \lambda_b/8, \lambda_b/4, \lambda_b/2$, where λ_b is the betatron oscillation wavelength.	206
10.1 Scaled horizontal rms beam size $x_{rms} = \sigma_x/\sigma_{rs}$, after injection into a small recirculator as a function of the tune depression ν/ν_o (solid lines). See the text for further comments.	231
10.2 Scaled horizontal rms beam size $x_{rms} = \sigma_x/\sigma_{rs}$, after injection into a small recirculator as a function of the tune depression ν/ν_o (solid lines) compared with the results (dots) obtained in the previous Chapter by studying self-consistent beam distributions in the recirculator satisfying the Vlasov-Poisson equation.	232

10.3 Dispersion function in the small recirculator as a function of the tune depression ν/ν_o (solid lines). The dashed line is the value of the dispersion function as calculated without taking into account the enlargement of the horizontal beam size in the recirculator due to dispersion.	233
10.4 Scaled emittance as a function of the tune depression ν/ν_o (solid line). The dots are from the self-consistent calculation of the previous chapter.	233
10.5 Effective emittances $4\epsilon_x$ (solid lines), $4\epsilon_y$ (dashed lines) as calculated by WARP as a function of z for two beams with different rms relative longitudinal momentum spreads σ_δ	236
10.6 Beam envelope σ_x as calculated by WARP (solid line) and from the rms envelope-dispersion equations ($\sigma_\delta = .015$).	237
10.7 The second moment $\langle x\delta \rangle$ as calculated by WARP (solid line) and $\langle \delta^2 \rangle D(z)$ as calculated from the rms envelope-dispersion equations ($\sigma_\delta = .015$).	238
10.8 As in Fig. 10.7 but with a smaller rms longitudinal momentum spread $\sigma_\delta = .005$	239

LIE METHODS.
EXACT MAP COMPUTATION,
AND THE PROBLEM OF DISPERSION
IN SPACE CHARGE
DOMINATED BEAMS

Marco Venturini

July 31, 1998

No Comment

This comment page is not part of the dissertation.

Typeset by L^AT_EX using the **dissertation** style by Pablo A. Straub, University of Maryland.

Chapter 1

Lie Methods and Beam Dynamics

The main purpose of this first Chapter is to provide a source of reference for the rest of the Dissertation. It is also meant to be an introduction to the basic concepts and use of Lie algebraic methods applied to the study of beam dynamics. For the most part it is a review of well established techniques that have been developed at Maryland over the last decade and a half. The emphasis is on conciseness rather than completeness: for a comprehensive treatment we refer to [19]. The outline of the Chapter is the following. After introducing in Sec. 1.1 the concept and use of maps for beam dynamics and the relevance of Lie methods in map computation and analysis, in Sec. 1.2 we discuss the form of the Hamiltonian that we will use through the next chapters. The following two sections are devoted to illustrate in more detail the use of Lie methods in map computation. Finally, normal form analysis for Lie maps is the topic of the last section. There the presentation is more general than and slightly different from what it is usually done in the context of beam dynamics, where the discussion is typically restricted to the case of stable linear motion (this represents the physical case for a one-turn map). The most general case in 6D is treated in

view of a possible application of normal form techniques to the computation of Lie maps in factored form, which will be discussed in the next Chapter. In the attempt to gain in clarity the style of the last section is more formal than in the rest of the Chapter.

1.1 Why Maps?

The concept and use of maps arise naturally in the description of charged particle motion in accelerators. A beam line typically consists of a sequence of beam optic elements of different kinds: for example, dipole magnets, quadrupole magnets, RF cavities, and so on. Each one performs a specific function in terms of beam dynamics: a dipole magnet bends the beam, a quadrupole focuses it, an RF cavity accelerates it. Moreover, if there is no field overlap the effect of each element is independent of the action of each other. As a consequence, a physical machine results from the collection of various functionally and dynamically independent elements. What is the most natural way to describe mathematically the motion of a particle through such a system?

From a dynamical viewpoint the action of a beamline element is to produce a change in the state of a particle as the particle travels through that element. Because the state of a classical dimensionless particle is determined by a point in a 6D phase space, the mathematical object that naturally describes the action of a beamline element is a function or ‘map’¹ from the 6D phase space into itself. To illustrate the way one can combine together a relatively small number of beam elements of different kinds to build machines serving various purposes.

¹The term ‘transfer map’ is also often used.

the ‘Lego blocks’ analogy has been suggested in [26]. The ‘Lego blocks’ logic is also reflected in a modern theoretical description of an accelerator based on maps. The peculiar characteristic of this approach is that it is ‘local’ in nature: when determining the dynamical action of an element, i.e. in calculating the map associated with a particular element, one can disregard the rest of the machine. The ‘global’ character of the beam dynamics is then recovered by combining the various local maps into the one-turn map. A properly computed one-turn map will contain all the information necessary to characterize the dynamical features of the machine. This approach stresses the fact that calculation of local maps and their concatenation on one side, and one-turn map analysis or ray tracing computation using maps on the other, are two conceptually and practically distinct steps in the study of a beam lattice. In addition to the conceptual clarity coming from a theoretical model close to the physical system, an approach based on maps has also a practical convenience. The most important advantage is that the various operations one needs to perform over maps, as computation, concatenation or iteration, are very easily and efficiently implemented on a computer.

Lie methods come into this picture because they provide a suitable and convenient set of mathematical tools that can be used for the purpose of both map computation and analysis. The convenience stems from the very nature of the transfer maps associated with Hamiltonian systems and has to do with the ‘symplecticity’ property. As we will see in some detail in the next sections, Lie-factorized forms provide the most efficient way to represent symplectic maps. In practice, this implies that one has to make the least numerical effort in terms of storage and computation time when treating symplectic maps in the Lie factorized form. In addition, Lie methods also provide a convenient representation

to carry out map analysis. Starting from the one-turn map, Normal form techniques can be applied to extract the global functions describing a machine such as the betatron and dispersion functions, chromaticities, tune and tuneshift, anharmonicities etc. In this chapter and the following the Reader will find an introduction to and a further development of these Lie techniques.

Although a viewpoint based on maps is quite natural, it did not reflect the way physicists would traditionally think about beam dynamics in accelerators. The traditional way of thinking can be found for example in the classical paper by Courant and Snyder [16]. There the effort is focused on describing the beam dynamics in terms of global functions e.g. the focusing function, or the radius of curvature. Those functions would then enter into the global Hamiltonian representing the machine and the resulting canonical equations. This method is powerful and elegant in the linear approximation (as in the Courant-Snyder paper), where the Hamiltonian and the resulting canonical equations can actually be used to write the one-turn linear map analytically. But it becomes increasingly complicated as one wishes to include nonlinear effects. And although it may still be useful for some kind of analysis, its convenience becomes questionable from a computational view point. Whether one is interested in calculating numerically some global quantities as the tunes or the chromaticities or carrying out the computation for the particle orbit in order to estimate the dynamic aperture, it is in general much more convenient to rely on a local map description of the machine.

Having said that, however, and having emphasized the importance of maps, one should not forget the virtues of an approach based on global Hamiltonians. For example, suppose one has to solve the problem of where to locate a thin

quadrupole so that the effect on the tune is the largest. Knowing how to compute maps would give little clue. Instead a familiarity with the integral formulas involving the betatron functions derived in the Courant-Snyder paper will give a quick answer (and a deeper insight into the beam dynamics as well). As it happens, wisdom is often somewhere in between the two extremes. And it is always in the ability to understand which tool is better suited for the problem at stake. Incidentally, the solution to the problem is that one should locate the quadrupole where the betatron function is the largest.

We would like to end this Introduction with a couple of remarks. First, we should mention that Lie methods are not the only framework suitable for map computations. Techniques based on Differential Algebras (DA), for example, are also being successfully used [9]. Although algorithms based on DA are intrinsically less efficient than those based on Lie methods (we will briefly comment on this in Sec. 1.3), they offer the advantage of a relatively straightforward implementation to arbitrary order. Finally, a remark on the generality of Lie methods. In this Dissertation we will limit ourselves only to Hamiltonian models of beam dynamics. However, it should be pointed out that even in the presence of non-Hamiltonian effects (like the damping due to the synchrotron radiation occurring in high energy electron rings) methods to compute transfer maps based on Lie algebraic techniques can be applied and may still be useful.

1.2 Hamiltonian for Charged Particles

In cartesian coordinates the relativistic Hamiltonian of a particle of mass m and charge q in an electromagnetic field is given by [38] (MKS units):

$$H_t(x, p_x, y, p_y, z, p_z; t) = \sqrt{m^2 c^4 + c^2(\mathbf{p} - q\mathbf{A})^2} - q\Phi. \quad (1.1)$$

with the electric potential $\Phi = \Phi(x, y, z, t)$ and vector potential $\mathbf{A} = \mathbf{A}(x, y, z, t)$ related to the electric and magnetic field by:

$$\mathbf{B} = \nabla \times \mathbf{A},$$

$$\mathbf{E} = \nabla\Phi - \partial_t \mathbf{A}.$$

The subscript t in the notation of the Hamiltonian (1.1) emphasizes that the time is the independent variable. In view of the observations made in the Introduction, we can expect that in describing the beam dynamics in a particle accelerator it would be most convenient to consider the longitudinal variable (not the time) as the independent variables (having oriented the cartesian frame in such a way that the longitudinal variable, let us say ' z ', is the one running parallel to the beam element). This is because we are interested in computing transfer maps. And a transfer map gives the state of a charged particle at the exit of the beamlne element as a function of the state the particle has at the entrance.

It turns out that under a mild assumption ($\frac{dz}{dt} \neq 0$, which is always naturally satisfied in an accelerator) one can transform the space variable z into the independent variable. In particular, it can be shown that the new Hamiltonian displaying z as the independent variable is

$$H_z(x, p_x, y, p_y, t, p_t; z) = -\sqrt{\frac{(p_t + q\Phi)^2}{c^2} - m^2 c^2 - (p_x - qA_x)^2 - (p_y - qA_y)^2 - qA_z} \quad (1.2)$$

In the process the time t has been demoted to the status of dynamical variable. Its canonical conjugate is p_t , which is related to the original Hamiltonian (1.1) by $p_t = -H_t$ (that is, p_t is minus the total energy of the particle).

The expression (1.2) is not quite yet what we need in order to compute transfer maps in the form we desire. What we are interested in, most often, is to determine particle dynamics relative to the so called ‘reference orbit’ or, for a circular machine, the ‘closed orbit’. The closed orbit can be defined as a periodic orbit having the same periodicity as the machine length. In practice, a closed orbit by design will lie as close as possible to the geometric center of the vacuum chamber. Its very existence is a prerequisite for the proper functioning of a machine. Therefore, we need the Hamiltonian in terms of variables that represent deviations from the reference orbit. More precisely, let us use the notation q_i, p_i with $i = 1, 2, 3$ to indicate respectively the canonical variables x, y, t and their canonical conjugates p_x, p_y, p_t . We define the deviation variables Q_i, P_i with ($i = 1, 2, 3$) as:

$$\begin{aligned} Q_i &= q_i - q_i^r, \\ P_i &= p_i - p_i^r. \end{aligned} \tag{1.3}$$

with q_i^r, p_i^r representing the reference orbit, [which by definition is a solution of the canonical equations associated with the Hamiltonian (1.2)]. The transformation (1.3) is canonical. Indeed, one can find the generating function for the transformation (1.3) and then derive the desired Hamiltonian [19]. Since it is always a nuisance to remember the right combination of the variables entering the generating functions an alternative calculation can be done as follows. First let us write the Legendre transformation linking the Lagrangian and the

Hamiltonian in the form:

$$Ldt = q_i dq_i - H(q_i, p_i) dt. \quad (1.4)$$

Here we used the convention that a summation is understood for $i=1,2,3$, whenever the indices are repeated. We can insert $q_i = Q_i + q_i^r$, and $p_i = P_i + p_i^r$ into (1.4) to find

$$\begin{aligned} Ldt &= (P_i + p_i^r)d(Q_i + q_i^r) - H(P_i + p_i^r, Q_i + q_i^r)dt \\ &= P_i dQ_i + p_i^r dQ_i + P_i dq_i^r + p_i^r dq_i^r - \left[H(P_i + p_i^r, Q_i + q_i^r) \right. \\ &\quad \left. + \frac{\partial H(q_i^r, p_i^r)}{\partial p_i^r} P_i - \frac{\partial H(q_i^r, p_i^r)}{\partial p_i^r} P_i + \frac{\partial H(q_i^r, p_i^r)}{\partial q_i^r} Q_i - \frac{\partial H(q_i^r, p_i^r)}{\partial q_i^r} Q_i \right] dt. \end{aligned} \quad (1.5)$$

What we have done in the last line of (1.5) is to just add and subtract the same quantities. Next observe that

$$P_i dq_i^r - \frac{\partial H}{\partial p_i^r} P_i dt = P_i \left[\dot{q}_i^r - \frac{\partial H(q_i^r, p_i^r)}{\partial p_i^r} \right] dt = 0, \quad (1.6)$$

because by definition, the reference orbit (q_i^r, p_i^r) is a solution of the canonical system associated with H . Also notice we can write

$$p_i^r dQ_i = d(p_i^r Q_i) - Q_i dp_i^r. \quad (1.7)$$

The first term on the RHS is an exact differential and can be neglected because Lagrangians are defined modulo exact differentials. The second term on the RHS of (1.7) cancels with $\frac{\partial H(q_i^r, p_i^r)}{\partial q_i^r} Q_i$, [as in (1.6) because (q_i^r, p_i^r) is solution of the canonical equations]. Finally the term $p_i^r dq_i^r$ does not depend on the dynamical variables and can be disregarded. After collecting the various pieces (1.5) becomes

$$Ldt = P_i dQ_i - \left[H(P_i + p_i^r, Q_i + q_i^r) - \frac{\partial H(q_i^r, p_i^r)}{\partial p_i^r} P_i - \frac{\partial H(q_i^r, p_i^r)}{\partial q_i^r} Q_i \right] dt.$$

which can be interpreted as the Legendre transformation defining the Hamiltonian $H^{dev} = H^{dev}(Q_i, P_i)$ in the deviation variables as:

$$H^{dev} = H(P_i + p^r, Q_i + q^r) - \frac{\partial H(q_i^r, p_i^r)}{\partial p_i^r} P_i - \frac{\partial H(q_i^r, p_i^r)}{\partial q_i^r} Q_i. \quad (1.8)$$

By applying formula (1.8) to the Hamiltonian (1.2) we finally get:

$$\begin{aligned} H^{dev} = & - \left[\frac{(P_t + p_t^r + q\Phi^{dev})^2}{c^2} - m^2 c^2 \right. \\ & \left. - (P_X + p_x^r - qA_x^{dev})^2 - (P_Y + p_y^r - qA_y^{dev})^2 \right]^{\frac{1}{2}} \\ & - qA_z^{dev} - \dot{x}^r P_X + \dot{p}_x^r X - \dot{y}^r P_Y + \dot{p}_y^r Y - \dot{T}^r P_T + \dot{p}_T^r T. \end{aligned} \quad (1.9)$$

In the expression above it is understood that the vector and scalar potentials are transformed accordingly:

$$\mathbf{A}^{dev}(X, Y, z) = \mathbf{A}(X + x^r, Y + y^r, z).$$

$$\Phi^{dev}(X, Y, z) = \Phi(X + x^r, Y + y^r, z).$$

Finally, it is convenient to introduce a scaling in order to obtain an Hamiltonian depending on the dimensionless variables:

$$\begin{aligned} x &= X/\ell, & p_x &= P_X/p^o, \\ y &= Y/\ell, & p_y &= P_Y/p^o, \\ \tau &= cT/\ell, & p_\tau &= P_T/(p^o c). \end{aligned} \quad (1.10)$$

Here we use (x, p_x, y, p_y) to denote the scaled variables giving the deviation with respect to the reference orbit. Of course they should not be confused with the variables appearing in (1.1) and (1.2). The Hamiltonian $H^{scl} = H^{dev}/(p^o c)$ in the scaled coordinates is:

$$H^{scl} = -\frac{1}{\ell} \left[\left(p_\tau + \bar{p}_t^r + \frac{q\Phi^{dev}}{p^o c} \right)^2 \right]$$

$$\begin{aligned}
& - \left[\left(\frac{mc}{p^o} \right)^2 - \left(p_x + \bar{p}_x^r - \frac{q}{p^o} A_x^{dev} \right)^2 - \left(p_y + \bar{p}_y^r - \frac{q}{p^o} A_y^{dev} \right)^2 \right]^{\frac{1}{2}} \\
& - \frac{q}{p^o} A_z^{dev} - \dot{x}^r p_x + \dot{\bar{p}}_x^r x - \dot{y}^r p_y + \dot{\bar{p}}_y^r y - \dot{\tau}^r p_\tau + \dot{\bar{p}}_\tau^r \tau. \quad (1.11)
\end{aligned}$$

[The bar over the coordinates for the reference orbit indicates that those coordinates have also been scaled according to (1.10)]. While ℓ can be arbitrary, a convenient choice for p^o is the design momentum (i.e. the mechanic momentum of a particle travelling along the design reference orbit). In this way the scaled momenta are similar to the non-canonical variables $x' = \frac{dx}{dz}$, $y' = \frac{dy}{dz}$ that are often used in modeling accelerators. In particular, the variable x' is directly related to the angle θ_x between the particle orbit and the reference orbit: $x' = \tan \theta_x$. In the absence of the transverse components of the vector potential and assuming the motion is in the horizontal plane, one can see that the scaled transverse canonical momentum is given by $p_x = \sin \theta_x$. That is x' and p_x are the same through second order in θ_x . The same is also true for y' and p_y .

The Hamiltonian (1.11) in cartesian variables is the one that will be mostly used throughout this Dissertation. However, we observe that, depending on the particular beam line, other choices for the coordinate frame may be more appropriate, like cylindrical variables or more general curvilinear coordinate systems. Sometimes curvilinear coordinate systems based on the reference orbit are employed. Although useful in theoretical analysis they may not provide the most convenient frame in which to carry out the computation of maps. In fact, in order to compute the reference orbit one needs to first have solved the canonical equations for the Hamiltonian (1.2), which is most easily done in a coordinate frame consistent with the geometry of the beam-line element.

1.3 Hamiltonian Systems, Maps and Lie Methods

Let us first introduce some notation. We will use z to indicate the independent ‘time-like’ variable. The superscripts i and f will refer to ‘initial’ and ‘final’ values. A point in the 6D phase space. (to which the following discussion is restricted for simplicity), will be denoted by either $\mathbf{z} = (z_1, z_2, z_3, z_4, z_5, z_6)$ or $(q_1, p_1, q_2, p_2, q_3, p_3)$.² Given a Hamiltonian system H one can write the associated canonical equations:

$$\begin{aligned}\dot{q}_k &= \frac{\partial H}{\partial p_k}, \\ \dot{p}_k &= -\frac{\partial H}{\partial q_k}.\end{aligned}\tag{1.12}$$

A more compact way to write the same equations is:

$$\dot{\mathbf{z}} = \mathbf{J} \nabla_{\mathbf{z}} H.\tag{1.13}$$

where \mathbf{J} is the 6×6 matrix

$$\mathbf{J} = \begin{pmatrix} 0 & 1 & 0 & 0 & 0 & 0 \\ -1 & 0 & 0 & 0 & 0 & 0 \\ 0 & 0 & 0 & 1 & 0 & 0 \\ 0 & 0 & -1 & 0 & 0 & 0 \\ 0 & 0 & 0 & 0 & 0 & 1 \\ 0 & 0 & 0 & 0 & -1 & 0 \end{pmatrix}.\tag{1.14}$$

The solutions of a canonical system define in a natural way a map as a function of the phase space into itself. Having specified an initial $z = z^i$ and

²The Reader notice the difference in notation between z , the independent variable, and \mathbf{z} , point is phase space.

final ‘time’ $z = z^f$, let $\mathbf{z}(z)$ be the solution of the canonical system (1.13) with the initial conditions $\mathbf{z}(z^i) = \mathbf{z}^i$. The map $\mathcal{M}^{z^i \rightarrow z^f}$ associated with the Hamiltonian flow is then defined as

$$\mathbf{z}^f = \mathcal{M}^{z^i \rightarrow z^f}(\mathbf{z}^i). \quad (1.15)$$

There are some conditions that need to be satisfied in order for the map $\mathcal{M}^{z^i \rightarrow z^f}$ to be well defined. For example, the canonical system needs to fulfill the conditions for the existence and uniqueness of the solution. Moreover, even if locally the solution exists and is unique, it may not be defined for an arbitrary time scale $z^i \rightarrow z^f$. This is the case for example when the solution exhibits a singularity in z . However, we will not get into the details and we will just assume, here as well later on, that the various mathematical objects we are dealing with are well defined.

A map that results from a Hamiltonian flow has a certain mathematical signature, i.e. its ‘symplecticity’. A general map defined as a function from the phase space into itself is said to be symplectic if the Jacobian matrix $\mathbf{M}(z^i)$ associated with the map \mathcal{M}

$$M_{jk}(\mathbf{z}^i) = \frac{\partial z_j^f(\mathbf{z}^i)}{\partial z_k^i}. \quad (1.16)$$

is a symplectic matrix. In turn, a matrix is defined to be symplectic if it satisfies the following equation:

$$\mathbf{M}^T(\mathbf{z}^i) \mathbf{J} \mathbf{M}(\mathbf{z}^i) = \mathbf{J} \quad \forall \mathbf{z}^i. \quad (1.17)$$

where the matrix \mathbf{J} is the same as in (1.14). Notice that equation (1.17) is very restrictive, since it is required to be satisfied for any \mathbf{z}^i . A more sophisticated but equivalent way to express the symplectic condition is to say that a symplectic

map preserves the differential two-form:

$$\omega_2 = \sum_{k=1}^3 dq_k \wedge dp_k. \quad (1.18)$$

Such a definition is somehow more insightful because it makes apparent the geometrical meaning of a symplectic transformation as the one that preserves the sum of the infinitesimal areas projected on the coordinate planes of the phase space. Moreover, notice that as a consequence of (1.17), the determinant of the Jacobian matrix of a symplectic transformation is unimodular. Therefore, symplectic transformations preserve volumes in phase space as well (a property, however, that is not characteristic of Hamiltonian systems only, but is shared with the so called ‘Liouvillian systems’).

The connection between the canonical formalism and the language of Lie operators is given by writing the canonical equations in terms of the Poisson brackets

$$\begin{aligned} \dot{q}_i &= -[H, q_i], \\ \dot{p}_i &= -[H, p_i]. \end{aligned} \quad (1.19)$$

We recall the Poisson bracket of two functions f and g is

$$[f, g] = \sum_{k=1}^3 \frac{\partial f}{\partial q_k} \frac{\partial g}{\partial p_k} - \frac{\partial f}{\partial p_k} \frac{\partial g}{\partial q_k}. \quad (1.20)$$

More generally, if one has an arbitrary (and differentiable) function f of the dynamical variables the equation for f can also be written in terms of Poisson brackets:

$$\dot{f} = -[H, f]. \quad (1.21)$$

Equation (1.21) suggests that one should think of the Poisson brackets involving the Hamiltonian as defining an operator on the space of the differentiable functions of the dynamical variables into itself. We call this a Lie operator. That is,

for a fixed Hamiltonian H the Lie operator associated with H is an operator \mathcal{L}_H defined over any differentiable function f by

$$\mathcal{L}_H f = [H, f]. \quad (1.22)$$

In the following, for the Lie operators we will use the ‘colon’ notation “ $: \ :$ ”, i.e. $\mathcal{L}_H =: H :$. The operators so defined owe their name to the fact that Poisson brackets have the structure of a Lie algebra. That is they satisfy the following three conditions (antisymmetry, linearity, and Jacobi identity respectively):

$$\begin{aligned} [f, g] &= -[g, f]; \\ [\lambda f, g + h] &= \lambda[f, g] + \lambda[f, h], \quad \lambda \in \mathbb{R}; \\ [f, [g, h]] + [g, [h, f]] + [h, [f, g]] &= 0. \end{aligned} \quad (1.23)$$

Why are Lie methods useful? A reason is because they offer an efficient way to compute maps. One can appreciate the power of the method by considering the case where the Hamiltonian is autonomous (i.e. does not explicitly depend on the independent variable z). Inspection of Eq. (1.21) suggests that a solution of this first order linear equation can be constructed as the exponential of the Lie operator $: H :$. Indeed one can verify that a solution of Eq. (1.21) is

$$f(\mathbf{z}^f; z^f) = \exp[(z^f - z^i) : -H :] f(\mathbf{z}^i; z^i). \quad (1.24)$$

that is:

$$\mathcal{M}^{z^i \rightarrow z^f} = \exp[(z^f - z^i) : -H :]. \quad (1.25)$$

The exponential of a Lie operator $: H :$.

$$\exp[t : H :] = \sum_{k=0}^{\infty} \frac{t^k}{k!} : H :^k. \quad (1.26)$$

is known in the literature as a Lie transformation. Powers of a Lie operator are defined in an obvious way. : $H^0 = \mathcal{I}$ and

$$: H^k = \underbrace{[H, [H, [\underbrace{H, \dots [H}_k \text{ times}, \cdot]]]. \quad (1.27)$$

Consider, for example, the simple but important case where the Hamiltonian $H = H_2$ is a quadratic function of the dynamical variables. Associated with H_2 is a symmetric matrix \mathbf{S} such that

$$H_2 = \frac{1}{2} \sum S_{jk} z_j z_k. \quad (1.28)$$

By applying the definition of a Lie operator one finds:

$$: -H_2 : z_k = (\mathbf{JS})_{kj} z_j. \quad (1.29)$$

or in vectorial notation : $-H_2 : \mathbf{z} = (\mathbf{JS})\mathbf{z}$. More generally for an arbitrary power m , one has : $-H_2 :^m \mathbf{z} = (\mathbf{JS})^m \mathbf{z}$. As a consequence, one can write the map as the exponential of the matrix \mathbf{JS} , ($t = z^f - z^i$):

$$\mathbf{z}^f = \mathcal{M} \mathbf{z}^i = \exp(t : -H_2 :) \mathbf{z}^i = \exp(t \mathbf{JS}) \mathbf{z}^i. \quad (1.30)$$

This example shows that the problem of computing the solutions of a set of differential equations has been solved by an algorithm that involves only algebraic operations (in this case the exponentiation of a matrix). The resulting map, calculated once forever, can be applied to various points in the phase space to compute the effect on the dynamics of the system. If the Hamiltonian is nonautonomous, in general one has to give up the advantage of not having to solve differential equations; however, Lie methods still provide a convenient way to compute maps. The details for the nonautonomous case are reported in Sec. 1.4.

The second reason that justifies the importance of Lie maps is that they permit a very general and efficient way to represent symplectic maps. A basic factorization theorem of the Lie calculus states that any analytic symplectic map \mathcal{M} can be represented as a product of a possibly infinite number of Lie transformations, each one generated by a homogeneous polynomials in the dynamical variables. More in detail:

$$\mathcal{M} = \exp(: f_1 :) \exp(: f_2^c :) \exp(: f_2^a :) \exp(: f_3 :) \exp(: f_4 :) \cdots \quad (1.31)$$

where each f_m is a homogeneous polynomial of degree m in the dynamical variables. Notice there are two polynomials of second degree f_2^c and f_2^a . They differ because of the properties of the symmetric matrix \mathbf{S} associated with them. In particular, having written

$$f_2 = -\frac{1}{2} \sum_{a,b} S_{ab} z_a z_b, \quad (1.32)$$

the matrix \mathbf{S}^c associated with f_2^c commutes with the matrix \mathbf{J} defined in (1.14), the the matrix \mathbf{S}^a associated with f_2^a anticommutes with \mathbf{J} . A remarkable property of the factored representation is that any truncation of the infinite sequence of Lie transformation generates a *symplectic* approximation of the original map.

The representation provided by (1.31) is optimal in the sense that it involves the smallest number of parameters that are necessary to fully characterize a symplectic map (the parameters are the coefficients of the monomials appearing in the homogeneous polynomials f_m). This property makes concatenating maps, a basic operation when one has to deal with beamline modeling, intrinsically faster than by using any other method.

In order to appreciate the advantage of representing a map in the Lie factorized form one should consider the alternative representation in terms of Taylor

series. An analytical map has a convergent Taylor expansion in the form:

$$z_a^f = K_a + \sum_b M_{ab} z_b^i + \sum_{bc} T_{abc} z_b^i z_c^i + \sum_{abcd} U_{abcd} z_b^i z_c^i z_d^i + \dots \quad (1.33)$$

In practical calculations one has to introduce a truncation at some order in the power expansion of (1.33). Let us say we retain all the terms through order D and call the truncated Taylor map \mathcal{T}_D . From the factorization theorem one can see that a map in the Lie form (1.31) truncated through $m = D + 1$, let us call it \mathcal{L}_{D+1} , will represent a map coinciding with \mathcal{T}_D through the order D . Next we compare the amount of information needed to represent \mathcal{T}_D vs. \mathcal{L}_{D+1} . In both cases the number of parameters we need to specify results from counting the number of monomials appearing in (1.33) and in all the generators f_m in (1.31). Suppose the dimension of the phase space is d . It is possible to show [19] that we need to specify the following numbers of parameters to specify a Lie and a Taylor map:

$$\frac{(D+d+1)!}{(D+1)!d!} - 1, \quad \text{Lie maps with generators through order } D+1: \quad (1.34)$$

and

$$\frac{d(D+d)!}{(D)!d!}. \quad \text{Taylor maps of order } D: \quad (1.35)$$

By taking the ratio between (1.34) and (1.35) one can see that the number of monomials required to specify the Taylor map is consistently larger than the number of monomials required in a correspondent Lie map. In particular, for the case $D = 5$ and for a 6D phase space ($d = 6$) the ratio is about 3.2 to 1. The reason is the redundancy of the coefficients appearing in the Taylor map due to the fact that the symplectic condition is not taken into account.

We end this Section by mentioning a useful relationship involving the Lie

transform that will be employed subsequently,

$$\exp(: f :)G(: g :) \exp(: -f :) = G[: \exp(: f :)g :]. \quad (1.36)$$

In particular, if G is the exponential function, we have:

$$\exp(: f :) \exp(: g :) \exp(: -f :) = \exp[: \exp(: f :)g :]. \quad (1.37)$$

There are a number of rules and relationships that are useful in map manipulation and computation that have not been reported here. We refer the interested Reader to [19] and the Ph.D. dissertations of former students in the DSAT Group at the University of Maryland.

1.4 Computation of Lie Maps in the General Case

As already mentioned, the computation of Lie maps for the general case of nonautonomous Hamiltonians still involves the solution of some (in general nonlinear) differential equations. It can be shown that in general the transfer map itself obeys the differential equations

$$\frac{d}{dz} \mathcal{M} = \mathcal{M} : -H :. \quad (1.38)$$

with the initial condition $\mathcal{M}(z = 0) = \mathcal{I}$. This equation can be translated into a system of differential equations involving the generators of the map in Lie form. Let us assume the Hamiltonian H is expanded into a series of homogeneous polynomials:

$$H = H_2 + H_3 + H_4 + H_5 + \dots = H_2 + H_{NL}. \quad (1.39)$$

For this calculation it is convenient to write the map in the reversed Lie factorized form,

$$\mathcal{M} = \cdots \exp(: f_5 :) \exp(: f_4 :) \exp(: f_3 :) \mathcal{R}. \quad (1.40)$$

The linear part of the map \mathcal{R} is associated to the matrix \mathbf{M} by

$$z_j^f = \mathcal{R}z_j^i = M_{jk}z_k^i. \quad (1.41)$$

The matrix $\mathbf{M} = \mathbf{M}(z)$ can be shown to obey the differential equation

$$\frac{d}{dz}\mathbf{M} = \mathbf{JS}\mathbf{M}. \quad (1.42)$$

where \mathbf{S} is the symmetric matrix associated with the quadratic form H_2 ,

$$H_2 = \frac{1}{2} \sum_{ab} S_{ab} z_a z_b. \quad (1.43)$$

The matrix \mathbf{JS} is sometimes called an ‘infinitesimal symplectic’ matrix or Hamiltonian matrix. In the case \mathbf{S} is z -independent the solution of equation (1.42) can be obtained by exponentiation $\mathbf{M} = \exp(z\mathbf{JS})$, as shown in (1.30). In the general case one can only solve Eq. (1.42) numerically. Having solved for the linear part of the map one can transform the H_{NL} part of the Hamiltonian into the ‘interaction picture’. The terminology is borrowed from quantum mechanics. More precisely we define H_m^{int} to be homogeneous polynomials of degree m obtained from the original H_m appearing in (1.39) as the result of acting with the linear transformation \mathbf{M} or \mathcal{R} ,

$$H_m^{int}(\mathbf{z}) = \mathcal{R}H_m(\mathbf{z}) = H_m(\mathcal{R}\mathbf{z}) = H_m(\mathbf{M}\mathbf{z}). \quad (1.44)$$

These quantities are useful in order to write the differential equations obeyed by the generators of the nonlinear part of the map. Below we list the equations for the Lie generators through order $m = 8$:

$$\dot{f}_3 = -H_3^{\text{int}}, \quad (1.45)$$

$$\dot{f}_4 = -H_4^{\text{int}} + \frac{1}{2} : f_3 : (-H_3^{\text{int}}). \quad (1.46)$$

$$\dot{f}_5 = -H_5^{\text{int}} + : f_3 : (-H_4^{\text{int}}) + \frac{1}{3} : f_3 :^2 (-H_3^{\text{int}}). \quad (1.47)$$

$$\begin{aligned} \dot{f}_6 = & - H_6^{\text{int}} + : f_3 : (-H_5^{\text{int}}) + \frac{1}{2} : f_4 : (-H_4^{\text{int}}) \\ & + \frac{1}{4} : f_4 :: f_3 : (-H_3^{\text{int}}) + \frac{1}{2} : f_3 :^2 (-H_4^{\text{int}}) \\ & + \frac{1}{8} : f_3 :^3 (-H_3^{\text{int}}). \end{aligned} \quad (1.48)$$

$$\begin{aligned} \dot{f}_7 = & - H_7^{\text{int}} + : f_3 : (-H_6^{\text{int}}) + : f_4 : (-H_5^{\text{int}}) + : f_4 :: f_3 : (-H_4^{\text{int}}) \\ & + \frac{1}{3} : f_4 :: f_3 :^2 (-H_3^{\text{int}}) + \frac{1}{2} : f_3 :^2 (-H_5^{\text{int}}) \\ & + \frac{1}{6} : f_3 :^3 (-H_4^{\text{int}}) + \frac{1}{30} : f_3 :^4 (-H_3^{\text{int}}), \end{aligned} \quad (1.49)$$

$$\begin{aligned} \dot{f}_8 = & - H_8^{\text{int}} + : f_3 : (-H_7^{\text{int}}) + : f_4 : (-H_6^{\text{int}}) + : f_4 :: f_3 : (-H_5^{\text{int}}) \\ & + \frac{1}{2} : f_4 :: f_3 :^2 (-H_4^{\text{int}}) + \frac{1}{8} : f_4 :: f_3 :^3 (-H_3^{\text{int}}) \\ & + \frac{1}{2} : f_5 : (-H_5^{\text{int}}) + \frac{1}{2} : f_5 :: f_3 : (-H_4^{\text{int}}) \\ & + \frac{1}{6} : f_5 :: f_3 :^2 (-H_3^{\text{int}}) + \frac{1}{2} : f_3 :^2 (-H_6^{\text{int}}) \\ & + \frac{1}{3} : f_4 :^2 (-H_4^{\text{int}}) + \frac{1}{6} : f_4 :^2 : f_3 : (-H_3^{\text{int}}) \\ & + \frac{1}{6} : f_3 :^3 (-H_5^{\text{int}}) + \frac{1}{24} : f_3 :^4 (-H_4^{\text{int}}) \\ & + \frac{1}{144} : f_3 :^5 (-H_3^{\text{int}}). \end{aligned} \quad (1.50)$$

The above equations have been obtained using the *Mathematica* [47] program reported in Appendix D.

1.5 Normal Form Analysis

Given a symplectic map \mathcal{M} , one can introduce a similarity transformation induced by (a symplectic) transformation \mathcal{A} , and write:

$$\mathcal{N} = \mathcal{A}\mathcal{M}\mathcal{A}^{-1}. \quad (1.51)$$

Because of group properties the transformation \mathcal{N} must also be symplectic. A precise definition of Normal form will be given below. The intuitive idea is that the transformation \mathcal{A} should be chosen in such a way that the resulting \mathcal{N} is as simple as possible. Normal forms were first introduced in accelerator physics as a useful tool to carry out an analysis of one-turn maps. They provide, for example a convenient way to compute important quantities like chromaticities (dependence of tunes on momentum), anharmonicities (dependence of tunes on the amplitude of the betatron oscillations), etc. In this Section the main goal is to establish a framework for a possible way to carry out the computation of maps in Lie form starting from an autonomous Hamiltonian. The method will be discussed in Section 2.1 of Chapter 2.

Let us first establish notation. The map $\mathcal{M} = \exp(: F :)$ is the Lie transformation generated by the analytic function $F = \sum_{k=2} f_k$, written as a series of homogeneous polynomials f_k of degree k in the dynamical variables $\mathbf{z} = (z_1, z_2, \dots, z_{2n})$. With \mathcal{P}_k we will indicate the vector space of homogeneous polynomials of degree k , i.e. $f_k \in \mathcal{P}_k$. Consider the quadratic polynomial f_2 . As already noticed, a quadratic form f_2 can be associated to a symmetric matrix \mathbf{S} so that $f_2(z) = \frac{1}{2}(z, \mathbf{S}z)$ where (\cdot, \cdot) is the ordinary inner product. The Lie operator $: f_2 :$ associated with f_2 has the property of mapping homogeneous polynomials of degree k into homogeneous polynomials of the same degree. We

denote the restriction of the operator $: f_2 :$ to \mathcal{P}_k by $: f_2 :_{(k)}$. We already pointed out that by using the definition (1.20), (1.22) one can verify that the Lie operator $: f_2 :$ can be associated to the infinitesimally symplectic matrix $\mathbf{A} = \mathbf{JS}$ so that

$$: f_2 :_{(k)} g_k(\mathbf{z}) = (\mathbf{Az}, \nabla_{\mathbf{z}} g_k(\mathbf{z})). \quad (1.52)$$

(in particular for $k = 1$, $: f_2 :_{(1)} z_i = \sum_{j=1}^{2n} A_{ij} z_j$).

In this Section we will limit the discussion to the case where the transformation \mathcal{A} appearing in (1.51) has the form $\mathcal{A} = \mathcal{T} = \exp(: T :)$ with $T = \sum_{k=3} t_k$. That is, the quadratic terms in \mathcal{T} are missing. As a consequence the transformation \mathcal{T} does not affect the linear part of the map \mathcal{M} . For the discussion contained here we do not need to assume that the linear part of the map be already in the normal form. If necessary reduction to a normal form for the linear part of the map can always be done by a suitable $\mathcal{A} = \mathcal{A}_2 = \exp(: a_2 :)$ using the well known methods of linear algebra. A listing of all the possible different normal forms for linear Hamiltonians will be reported below.

We are now in the position to state the main Theorem for normal forms. [3, 15, 17].

Theorem 1 *For any integer m it is possible to find m homogeneous polynomials $t_3 \in \mathcal{P}_3, \dots, t_m \in \mathcal{P}_m$, such that :*

$$(\exp \sum_{k=3}^m : t_k :)F = f_2 + \sum_{k=3}^m \tilde{f}_k + \mathcal{O}(m+1)$$

with $\tilde{f}_k \in \mathcal{C}_k$, where \mathcal{C}_k is a subspace of \mathcal{P}_k complementary to $\text{Range}\{ : f_2 :_{(k)} \}$:
i.e. $\mathcal{P}_k = \mathcal{C}_k \oplus \text{Range}\{ : f_2 :_{(k)} \}$.

$\mathcal{O}(m+1)$ indicates polynomials of degree $\geq m+1$

Proof.

By induction: suppose the theorem is true for $m - 1$. Then:

$$\begin{aligned}
 & (\exp : \sum_{k=3}^m : t_k :)F = \\
 &= (\exp : t_m :) \cdot (\exp \sum_{k=3}^{m-1} t_k) F + \mathcal{O}(m+1) \\
 &= (1 + : t_m : + \mathcal{O}(m+1)) \cdot (f_2 + \sum_{k=3}^{m-1} : \tilde{f}_k : + x_m + \mathcal{O}(m+1)) \\
 &= f_2 + \sum_{k=3}^{m-1} \tilde{f}_k + : t_m : f_2 + x_m + \mathcal{O}(m+1).
 \end{aligned}$$

In the previous expression x_m is a homogeneous polynomial $\in \mathcal{P}_m$ depending on t_k and f_k ³. Define $\tilde{f}_m = : t_m : f_2 + x_m$ and use the antisymmetric property of the Poisson brackets to write: $\tilde{f}_m = x_m - : f_2 : t_m$. Because of $\mathcal{P}_m = \mathcal{C}_m \oplus \text{Range}\{ : f_2 :_{(m)} \}$ we can decompose x_m as $x_m = (x_m)_{\text{Range}} + (x_m)_{\mathcal{C}_m}$ and therefore, if we choose t_m in such a way that

$$: f_2 : t_m = (x_m)_{\text{Range}}, \quad (1.53)$$

we get $\tilde{f}_m = (x_m)_{\mathcal{C}_m} \in \mathcal{C}_m$. \square

The polynomial $F = \sum_{k=2}^m \tilde{f}_k$ with $\tilde{f}_k \in \mathcal{C}_k$ for $k = 3, 4, \dots, m$ is said to be in the normal form up to the m th order.

Now we want to distinguish between the case when $: f_2 :_{(k)}$ is semisimple as a linear operator $\mathcal{P}_k \rightarrow \mathcal{P}_k$, and the case when it is not. The two cases are treated separately in the next two sections.

Definition 1 A linear operator acting on a finite dimension vector space is said to be semisimple if the set of its eigenvectors forms a basis for the space.

In other words a linear operator is said to be semisimple if the associated matrix is diagonalizable.

³More precisely one can verify that x_m has the structure: $x_m = f_m + X(t_{m-1}, \dots, t_3, f_m, f_{m-1}, \dots, f_2)$.

1.5.1 Semisimple case.

The following three propositions can be proved for the semisimple case.

Proposition 1 *The operator $:f_2:(1)$ acting on \mathbb{R}^{2n} is semisimple iff the corresponding matrix A is semisimple.*

Proposition 2 *The operator $:f_2:(m)$ acting on \mathcal{P}_k is semisimple if $:f_2:(1)$ is semisimple.*

Proof. Let e_i be an eigenvector of $:f_2:(1)$ with eigenvalue λ_i , $i = 1, 2, \dots, 2n$.

The e_i 's are linear combinations of z_1, \dots, z_{2n} . Then $e_{i_1, \dots, i_k} = e_{i_1}e_{i_2}\dots e_{i_k} \in \mathcal{P}_k$ is an eigenvector of $:f_2:(k)$ with eigenvalue $\lambda_{i_1, i_2, \dots, i_k} = \sum_{j=1}^k \lambda_{i_j}$, in fact:

$$\begin{aligned} :f_2:(k) e_{i_1, i_2, \dots, i_k} &= (:f_2:(k) e_{i_1})e_{i_2}\dots e_{i_k} + e_{i_1}(:f_2:(k) e_{i_2})\dots e_{i_k} + \dots = \\ &= (\sum_{j=1}^k \lambda_{i_j})e_{i_1}e_{i_2}\dots e_{i_k}. \end{aligned}$$

Since the number of these eigenvectors, $(k+2n-1)!/(2n)!k!$, equals the dimension of the space \mathcal{P}_k , the set of eigenvectors is complete. \square

Proposition 3 *If $:f_2:(k)$ is semisimple then*

$$\mathcal{P}_k = \text{Ker}\{|:f_2:(k)\} \oplus \text{Range}\{|:f_2:(k)\}.$$

The last proposition allows us to identify the \mathcal{C}_k of **Theorem 1** with $\text{Ker}\{|:f_2:(k)\}$. In other words, because of ⁴

$$\{|:f_2:\tilde{f}_k:\} = (:f_2:\tilde{f}_k) := 0. \quad (1.54)$$

we can choose the t_k 's defining the transformation \mathcal{T} in such a way that $:f_2:$ commutes with all $:\tilde{f}_k:$'s. We stress the fact that the identification of \mathcal{C}_k as $\text{Ker}\{|:f_2:(k)\}$ is peculiar to the semisimple case.

⁴ $\{\dots\}$ is the commutator.

The evaluation of the polynomials t_k is easily done: from (1.53) it suffices to express the x_m in terms of the eigenvectors e_{i_1, i_2, \dots, i_k} , that is $x_k = \sum_{i_1, \dots, i_k} X_{i_1, \dots, i_k} e_{i_1, \dots, i_k}$ and then take $t_k = \sum'_{i_1, \dots, i_k} (\frac{X_{i_1, \dots, i_k}}{\lambda_{i_1, \dots, i_k}}) e_{i_1, \dots, i_k}$, where the sum ' \sum' is understood to be carried out only over the eigenvectors of nonvanishing eigenvalues.

After this is done up to the desired order we can finally write the the normal form for \mathcal{M} :

$$\tilde{\mathcal{M}} = T \mathcal{M} T^{-1} = e^{f_2 + f_3 + f_4 + \dots} = e^{f_2} e^{f_3 + f_4 + \dots}. \quad (1.55)$$

Notice that because of (1.54) the term $:f_2:$ could be factorized in (1.55). This fact suggests the possibility of using normal form to compute Lie map in the factorized form. See Sec. 2.1. Here we used the notation $\tilde{\mathcal{M}}$ for the map in the normal form to stress that the linear part of the map itself may not be in normal form.

We end this section by giving the normal form to which any quadratic polynomial $f_2(z)$, whose associated Lie operator $:f_2:$ is semisimple, can be brought by means of a linear symplectic transformation [15],[4], [70].

First we characterize the matrix $A \in sp(2n, \mathbb{R})$ associated with $:f_2:$. The eigenvalues λ of A occur in couples or in quadruples of the type:

$$\begin{aligned} \lambda &= \pm\alpha; \quad \alpha \geq 0. \\ \lambda &= \pm i\beta; \quad \beta > 0. \\ \lambda &= \pm(\gamma \pm i\delta); \quad \gamma, \delta \geq 0. \end{aligned} \quad (1.56)$$

The most general semisimple matrix A (up to a symplectic transformation) is best expressed in terms of the representation in which the canonical variables

appear ordered in alternating couples: i.e. $x = (q_1, p_1, \dots, q_n, p_n)$ ⁵. In such a representation

$$\mathbf{A} = \underbrace{\mathbf{A}_I \oplus \mathbf{A}_I \oplus \dots \oplus \mathbf{A}_I}_{r \text{ terms}} \oplus \underbrace{\mathbf{A}_{II} \oplus \mathbf{A}_{II} \oplus \dots \oplus \mathbf{A}_{II}}_{s \text{ terms}} \oplus \underbrace{\mathbf{A}_{III} \oplus \mathbf{A}_{III} \oplus \dots \oplus \mathbf{A}_{III}}_{t \text{ terms}},$$

where $2r + 2s + 4t = 2n$ and the matrices \mathbf{A}_I , \mathbf{A}_{II} , and \mathbf{A}_{III} have dimensions 2×2 and 4×4 respectively and the form:

$$\mathbf{A}_I = \begin{pmatrix} \alpha & 0 \\ 0 & -\alpha \end{pmatrix}, \quad \mathbf{A}_{II} = \begin{pmatrix} 0 & \pm\beta \\ \mp\beta & 0 \end{pmatrix}, \quad \mathbf{A}_{III} = \begin{pmatrix} \gamma & 0 & \delta & 0 \\ 0 & -\gamma & 0 & \delta \\ -\delta & 0 & \gamma & 0 \\ 0 & -\delta & 0 & -\delta \end{pmatrix}.$$

The correspondent quadratic polynomial $f_2 = \frac{1}{2}(x, \mathbf{J}\mathbf{A}x)$ assumes the form:

$$\begin{aligned} f_2 = & \sum_{i=1}^r \alpha_i q_i p_i \pm \sum_{i=r+1}^{r+s} \frac{1}{2} \beta_i (q_i^2 + p_i^2) + \\ & + \sum_{i=r+s+1}^{2n} \gamma_i (q_i p_{i+1} + q_{i+1} p_i) + \delta_i (q_{i+1} p_i - q_i p_{i+1}). \end{aligned} \quad (1.57)$$

For $2n = 6$, in the particular case where all the eigenvalues lie on the unit circle ($\alpha = \delta = \gamma = 0$) and the linear part of the map is already in normal form. then the \tilde{f}_m are combinations of polynomials of the form $(q_1^2 + p_1^2)^l (q_2^2 + p_2^2)^p (q_3^2 + p_3^2)^q$, with $l + p + q = m$.

1.5.2 The general case.

In this section we relax the condition that the matrix \mathbf{A} , and therefore : f_2 :. (see the beginning of last section) is semisimple.

⁵in this representation the matrix J has the form $J = J_2 \oplus J_2 \oplus \dots \oplus J_2$ where $J_2 = \begin{pmatrix} 0 & 1 \\ -1 & 0 \end{pmatrix}$.

It is a known fact of linear algebra [45] that any linear operator \mathbf{A} , over a finite dimension vector space, has the unique decomposition $\mathbf{A} = \mathbf{D} + \mathbf{N}$, where \mathbf{D} is semisimple, \mathbf{N} is nilpotent, and $\mathbf{ND} = \mathbf{DN}$. If we introduce such a decomposition for the matrix \mathbf{A} in (1.52), as a result we also get a decomposition of the Lie operator $: f_2 :.$, that is, $: f_2 : = : s_2 : + : n_2 :.$, where the two quadratic polynomials s_2 and n_2 are connected to the matrices \mathbf{D} and \mathbf{N} by $s_2 = \frac{1}{2}(z, -\mathbf{JD}z)$ and $n_2 = \frac{1}{2}(z, -\mathbf{JN}z)$. Not surprisingly, it turns out that

Proposition 4 $: f_2 : = : s_2 : + : n_2 :$ with s_2 and n_2 defined as above, is the semisimple-nilpotent ($S - N$) decomposition for $: f_2 :.$

Proof. See [15]. \square

What is different here, with respect to the semisimple case, is that in our attempt to find the normal form of F , it is no longer possible in general to choose $\text{Ker}\{ : f_2 :_{(k)} \}$ as the complementary space C_k of $\text{Range}\{ : f_2 : \}$.

In the general case a choice for C_k can be given in terms of $\text{Ker}\{ : f_2 :_{(k)}^\dagger \}$ ⁶ where $: f_2 :_{(k)}^\dagger$ is the adjoint of $: f_2 :_{(k)}$. This, of course, requires the introduction of an inner product. Indeed such an inner product can be defined (an explicit definition can be found in [15, 19, 1]).

The following facts will be useful (V is a vector space):

Proposition 5 *If \mathbf{D} , a linear operator on V , is semisimple, then $V = \text{Range}\{\mathbf{D}\} \oplus \text{Ker}\{\mathbf{D}\}$. (This is a restatement of Proposition 3).*

Proposition 6 *If the linear operator \mathbf{A} acting on V has the $S - N$ decomposition $\mathbf{A} = \mathbf{D} + \mathbf{N}$, then $\text{Ker}\{\mathbf{A}\} = \text{Ker}\{\mathbf{D}\} \cap \text{Ker}\{\mathbf{N}\}$.*

⁶It is a basic fact of linear algebra that if $\mathbf{A} : V \rightarrow V$, then $V = \text{Range}\{\mathbf{A}\} \oplus \text{Ker}\{\mathbf{A}^\dagger\}$.

Proof.

$\text{Ker}\{\mathbf{A}\} \supseteq \text{Ker}\{\mathbf{D}\} \cap \text{Ker}\{\mathbf{N}\}$ is obvious. For the converse: suppose $v \in V$ is in $\text{Ker}\{\mathbf{A}\}$. Then $\mathbf{D}v = -\mathbf{N}v$. Let l be the index of nilpotency for \mathbf{N} , that is $\mathbf{N}^l = 0$, therefore $\mathbf{N}^{l-1}\mathbf{D}v = -\mathbf{N}^{l-1}\mathbf{N}v = 0$. On the other hand, it is also true that $\mathbf{D}^k v = (-1)^k \mathbf{N}^k v$. Therefore, $0 = \mathbf{N}^{l-1}\mathbf{D}v = (-1)^{(l-1)} \mathbf{D}^{l-1}\mathbf{D}v$. Because of **Proposition 5** the operator \mathbf{D} , and its powers, are invertible in $\text{Range}\{\mathbf{D}\} \ni \mathbf{D}^{l-1}v$, and therefore, $\mathbf{D}v = 0 = \mathbf{N}v$. That is, v belongs also to the kernels of both \mathbf{D} and \mathbf{N} . \square

Proposition 7 *If \mathbf{D} is semisimple then $\text{Ker}\{\mathbf{D}\} = \text{Ker}\{\mathbf{D}^\dagger\}$.*

Proof. Consider \mathbf{D} in the basis of its eigenfunctions. \square

From **Proposition 6** it follows that $\mathbf{A}^\dagger = \mathbf{D}^\dagger + \mathbf{N}^\dagger$. Therefore, the subspace \mathcal{C}_k of **Theorem 1** can be chosen to be ⁷:

$$\mathcal{C}_k = \text{Ker}\{ : f_2 :^\dagger \} = \text{Ker}\{ : s_2 :^\dagger \} \cap \text{Ker}\{ : n_2 :^\dagger \} = \text{Ker}\{ : s_2 : \} \cap \text{Ker}\{ : n_2 :^\dagger \}. \quad (1.58)$$

This ends the characterization of the normal form of the polynomial F for the case when the Lie operator associated with its quadratic part is not semisimple. In view of the application we have in mind, however, we do not need really all what we can achieve. That is, instead of $\mathcal{C}_k = \text{Ker}\{ : s_2 : \} \cap \text{Ker}\{ n_2^\dagger \}$, for our purposes it is enough to require:

$$\mathcal{C}_k = \text{Ker}\{ : s_2 : \}. \quad (1.59)$$

⁷For simplicity we drop the ' k ' in the notation for $: f_2 :_{(k)}$ and $: s_2 :_{(k)}$.

Of course .**Theorem 1** and 1.58 allow us this choice.

We can now move on to indicate a possible way to evaluate explicitly the transformation \mathcal{T} so that (1.59) is true. The polynomials t_k which enter the transformation \mathcal{T} are defined by the requirement $(x_k - :f_2:t_k) \in \text{Ker}\{ :s_2 :\}$, or equivalently

$$:s_2:(x_k - :f_2:t_k) = 0. \quad (1.60)$$

A way to solve for t_k is to expand it in terms of the eigenvectors of $:s_2:$ in \mathcal{P}_k and work with the matrix representation of the operators $:s_2:$ and $:f_2:$ in \mathcal{P}_k with respect to the same basis. Let us denote with a $\tilde{\cdot}$ the various quantities in such a representation. The relation (1.60) then becomes

$$:\widetilde{s_2}:(\widetilde{x_k} - :\widetilde{f_2}:\widetilde{t_k}) = 0. \quad (1.61)$$

Let $:\widetilde{f_2}:\tilde{\cdot}$, $\widetilde{x_k}\tilde{\cdot}$, etc. denote the restriction (or the projection). of the various quantities on $\text{Range}\{ :\widetilde{s_2}:\}$. Since $:\widetilde{s_2}:$ is semisimple (and therefore **Proposition 5** holds), we can rewrite 1.61 as:

$$(\widetilde{x_k}\tilde{\cdot} - :\widetilde{f_2}:\widetilde{t_k}\tilde{\cdot}) = 0. \quad (1.62)$$

Since $\det[:\widetilde{f_2}:\tilde{\cdot}] \neq 0$ ⁸ then $:\widetilde{f_2}:\tilde{\cdot}$ is invertible and therefore⁹

$$\widetilde{t_k}\tilde{\cdot} = [:\widetilde{f_2}:\tilde{\cdot}]^{-1}\widetilde{x_k}\tilde{\cdot} \quad (1.63)$$

The other entries of $\widetilde{t_k}$ can be set to 0.

The trouble with this method is that the dimension of the representation depends factorially on k , the degree of the polynomials and on $2n$, the dimension

⁸ $:\widetilde{f_2}:\tilde{\cdot}$ and $:\widetilde{s_2}:\tilde{\cdot}$ have the same eigenvalues.

⁹ in the following expression $[:\widetilde{f_2}:\tilde{\cdot}]^{-1}$ could be reexpressed using the relation $(1 - N)^{-1} = 1 + N^2 + N^3 + \dots N^{m-1}$, which is true for a nilpotent operator N with index of nilpotency m .

of the phase space. We recall that the dimension of \mathcal{P}_k is $(k + 2n - 1)! / [(2n)!k!]$. The difficulty of dealing with very large matrices, as long as k and $2n$ assume values not too small, is partially tempered by the fact that most of the entries of $\widetilde{\mathcal{M}}$ actually are zero. Finally we can write the normal form:

$$\mathcal{M} = T^{-1}\mathcal{M}T = e^{is_2}e^{in_2+\tilde{f}_3+\tilde{f}_4+\dots}. \quad (1.64)$$

The factorization of e^{is_2} is possible because $\tilde{f}_k \in \text{Ker}\{s_2\}$.

We conclude this section with the list of all the different forms to which any quadratic polynomial f_2 , whose associated Lie operator $:f_2:$ is not semisimple (and indecomposable), can be brought by means of a linear symplectic transformation [15]. For simplicity only the dimensions $2n = 2, 4, 6$ will be considered. We distinguish between different cases according to the spectrum $(\pm\lambda_1, \pm\lambda_2, \pm\lambda_3)$ 1.56 of the matrix \mathbf{A} .

1 dim.=2n=2 spectrum= $\{\lambda_1 = 0\}$:

$$\mathbf{A} = \pm \mathbf{N}_2 \text{ where } \mathbf{N}_2 = \begin{pmatrix} 0 & 0 \\ 1 & 0 \end{pmatrix}.$$

$$f_2 = n_2 = \mp \frac{1}{2}q^2.$$

2 dim.=2n=4: spectrum = $\{\lambda_1 = \lambda_2 = 0\}$:

$$2.1 \quad \mathbf{A} = \begin{pmatrix} \mathbf{N}_2 & 0 \\ 0 & -\mathbf{N}_2^T \end{pmatrix}$$

$$f_2 = n_2 = q_1 p_2.$$

$$2.2 \quad \mathbf{A} = \begin{pmatrix} \mathbf{N}_2 & 0 \\ \pm \mathbf{M}_2 & -\mathbf{N}_2^T \end{pmatrix} \text{ where } \mathbf{M}_2 = \begin{pmatrix} 0 & 0 \\ 0 & 1 \end{pmatrix}.$$

$$f_2 = n_2 = q_1 p_2 \mp \frac{1}{2}q_2^2.$$

2.3 spectrum = $\{\lambda_1 = \lambda_2 = \alpha > 0\}$:

$$\mathbf{A} = \begin{pmatrix} \mathbf{A}_2 + \mathbf{N}_2 & 0 \\ 0 & -\mathbf{A}_2 - \mathbf{N}^T \end{pmatrix} \text{ where } \mathbf{A}_2 = \begin{pmatrix} \alpha & 0 \\ 0 & \alpha \end{pmatrix}.$$

$$f_2 = s_2 + n_2 = \alpha(q_1 p_1 + q_2 p_2) + q_1 p_2.$$

3 dim.=2n=6 spectrum= $\{\lambda_1 = \lambda_2 = \lambda_3 = 0\}$:

3.1

$$\mathbf{A} = \begin{pmatrix} \mathbf{N}_3 & 0 \\ 0 & -\mathbf{N}_3^T \end{pmatrix} \text{ where } \mathbf{N}_3 = \begin{pmatrix} 0 & 0 & 0 \\ 1 & 0 & 0 \\ 0 & 1 & 0 \end{pmatrix}.$$

$$f_2 = n_2 = q_1 p_2 + q_2 p_3.$$

3.2

$$\mathbf{A} = \begin{pmatrix} \mathbf{N}_3 & 0 \\ \mathbf{M}_3 & -\mathbf{N}_3^T \end{pmatrix} \text{ where } \mathbf{M}_3 = \begin{pmatrix} 0 & 0 & 0 \\ 0 & 0 & 0 \\ 0 & 0 & 1 \end{pmatrix}.$$

$$f_2 = n_2 = q_1 p_2 + q_2 p_3 \mp \frac{1}{2}q_3^2.$$

3.3 spectrum= $\{\lambda_1 = \lambda_2 = \lambda_3 = \alpha > 0\}$

$$\mathbf{A} = \begin{pmatrix} \mathbf{A}_3 + \mathbf{N}_3 & 0 \\ 0 & -\mathbf{A}_3^T - \mathbf{N}_3^T \end{pmatrix} \text{ where } \mathbf{A} = \begin{pmatrix} \alpha & 0 & 0 \\ 0 & \alpha & 0 \\ 0 & 0 & \alpha \end{pmatrix}.$$

$$f_2 = s_2 + n_2 = (\alpha \sum_{i=1}^3 q_i p_i) + (q_1 p_2 + q_2 p_3).$$

3.4 spectrum = $\lambda_1 = \lambda_2 = \lambda_3 = i\beta$.

$$\mathbf{A} = \begin{pmatrix} \mathbf{N}_3 & B_3 \\ -B_3 & -\mathbf{N}_3^T \end{pmatrix} \quad \text{where} \quad B = \begin{pmatrix} 0 & 0 & -\beta \\ 0 & \beta & 0 \\ -\beta & 0 & 0 \end{pmatrix}.$$

$$f_2 = s_2 + n_2 = [(-\beta q_1 q_3 + p_1 p_3) + \frac{1}{2}\beta(q_2^2 + p_2^2)] + [q_1 p_2 + q_2 p_3].$$

Chapter 2

Development of Lie Calculus

2.1 Lie Map Factorization Using Normal Forms.

In Sec. 1.2 we wrote a general Hamiltonian governing the beam dynamics through a beam line element in an accelerator. In many situations to good approximation the fields entering the Hamiltonian are z -independent. In these cases computing the transfer map through the desired order requires evaluation of the Lie transformation (1.25). As already noticed Lie transformations reduce the problem of integrating the Hamiltonian flow for autonomous systems into an algebraic calculation. Although in many regards this simplifies the problem, the evaluation of a Lie transformation in general is not trivial. By evaluation of a Lie transformation we mean either computation of the map in the form of a Taylor series (as in (1.33)) or reduction to the Lie factored form (1.31) through a certain order. For a fixed order the two representations are formally equivalent and computationally it is relatively easy to convert one into the other.

The problem with Lie transformations is that in general it is not possible to compute each coefficient of the resulting Taylor series using the exponential

series (1.26) in a finite number of operations. The source of the difficulty is the Lie operator associated with the quadratic part of the Hamiltonian, i.e. : H_2 :. This is related to the fact, already pointed out in Sec. 1.5, that the operator : H : transforms any homogeneous polynomial of order k into a homogeneous polynomial of the same order. Clearly this is also true for the action of arbitrary powers : H : m . Let us see for a simple example how this turns into a problem. Suppose we want to evaluate $q^f = \mathcal{M}q^i$ with $\mathcal{M} = \exp(: H_2 + H_3 :)$. By applying the formula for the exponential we have:

$$q^f = \sum_{k=0} : (H_2 + H_3) :^k \frac{q^i}{k!} = q^i + : (H_2 + H_3) : q^i + \frac{: (H_2 + H_3) :^2}{2} q^i + \dots \quad (2.1)$$

In order to express results in Taylor series one has to first collect the terms with the same power on the RHS of (2.1). An infinite numbers of terms contributes to each power. The linear terms in (2.1) are:

$$q^i + : H_2 : q^i + \frac{1}{2} : H_2 :^2 q^i + \dots \quad (2.2)$$

and can be summed as $\exp(: H_2 :)q^i$. The second order term is made of pieces like : H_2 : n : H_3 :: H_2 : m q^i , and so on. In general there are no analytical formulas to carry out these summations (there exist some formulas that give partial summations, but they are useful only for lower order calculations). This Chapter is mainly devoted to discuss two possible ways to cope with the problem. In this section in particular we show how the problem could in principle be solved using normal form techniques. In the following section we discuss the Splitting, Scaling, and Squaring (SSS) algorithm and its implementation in the code MARYLIE. In both cases the problem is stated in terms of obtaining a Lie map in the factored form. That is, given the Hamiltonian $H = H_2 + H_3 + H_4 + H_5 + \dots$, we want to determine the generators g_m , (homogeneous polynomial of

degree m) so that the following is true:

$$\begin{aligned}\exp(: H :) &= \exp(: H_2 + H_3 + H_4 + H_5 + \dots :) \\ &= \exp(: g_2 :) \exp(: g_3 :) \exp(: g_4 :) \exp(: g_5 :) \dots. \quad (2.3)\end{aligned}$$

The use of normal forms to carry out the computation (2.3) is based on the following observation. The factorization (2.3) would be possible if the Lie operator $: H_2 :$ happened to commute with all the Lie operators associated with $: H_k :$. This follows from the basic property of the exponential

$$\exp(A + B) = \exp(A) \exp(B), \quad (2.4)$$

which holds if A and B commute. Alternatively, the calculation of the Lie transformation would still be obtainable in a finite number of operations if the Lie operator $: H_2 :$, [or its projections $: H_2 :_k$ on \mathcal{P}_k (see Sec. 1.5)] happened to be nilpotent. In this case there would exist an index of nilpotency m_k such that $: H_2 :_k^{m_k} = 0$. As a consequence the number of terms contributing to each power of the Taylor series would be finite. These two cases are rather special. However we can use the discussion on normal forms outlined at the end of Chapter 1 to show that one can always introduce a transformation or a change of coordinates so that a generic Lie transformation can exhibit either one of the properties above.

Following the discussion of Sec. 1.5 one has to distinguish between the two cases where the Lie operator $: H_2 :$ is semisimple and the more general case where it can decomposed into the sum of a semisimple and a nilpotent term.

Consider first the semisimple case. The map $\mathcal{M} = \exp(: H :)$ can be written in terms of the transformation function T and its normal form $\tilde{\mathcal{M}}$ evaluated in

(1.55) as :

$$\mathcal{M} = \mathcal{T}^{-1} \tilde{\mathcal{M}} \mathcal{T} = e^{-:t_3+t_4+...:} e^{:H_2:} e^{:\tilde{H}_3:+\tilde{H}_4:+...} e^{:t_3+t_4+...:}. \quad (2.5)$$

The functions $\tilde{H}_3, \tilde{H}_4, \dots$ are known and determined according to Theorem 1 of Sec. 1.5. Notice that because $: H_2 :$ commutes with each $: \tilde{H}_k :$ the isolation of the factor $\exp(: H_2 :)$ in (2.5) could be done immediately. Next we insert the identity in front of the RHS of (2.5):

$$\mathcal{M} = \overbrace{e^{:H_2:} e^{-:H_2:}}^{\mathbf{I}} e^{-:t_3+t_4+...:} e^{:H_2:} e^{:\tilde{H}_3:+\tilde{H}_4:+...} e^{:t_3+t_4+...:}. \quad (2.6)$$

and make use of the relation (1.37) to write:

$$e^{-:H_2:} e^{-:t_3+t_4+...:} e^{:H_2:} = e^{-:\tilde{t}_3+\tilde{t}_4+...} \quad (2.7)$$

where $\tilde{t}_k(\mathbf{z}) = e^{-:H_2:} t_k(\mathbf{z}) = t_k(e^{-:H_2:} \mathbf{z})$. After inserting (2.7) into (2.6) we finally get:

$$\mathcal{M} = e^{:H_2:} \underbrace{\tilde{\mathcal{T}}^{-1} e^{:\tilde{H}_3:+\tilde{H}_4:+...} \mathcal{T}}_{\mathcal{O}(3)}. \quad (2.8)$$

The last expression shows that the quadratic term has been fully isolated. This is because the transformation \mathcal{T} is in the form of a Lie transformation not depending on generators of degree 2. At this point there is no problem in principle to write the Taylor expansion corresponding to (2.8) through any desired order by simple and straightforward evaluation of the exponentials.

A similar procedure applies in the more general case where $: H_2 :$ has the $S - N$ decomposition $: H_2 :_{(k)} =: s_2 :_{(k)} +: n_2 :_{(k)}$ where $: s_2 :_{(k)}$ is semisimple and $: n_2 :_{(k)}$ is nilpotent. For a generic map \mathcal{M} (having used the fact that $: s_2 :$ commutes with $: n_2 :$ and each $: \tilde{H}_k :$) we have the result:

$$\mathcal{M} = \mathcal{T}^{-1} \tilde{\mathcal{M}} \mathcal{T} = e^{-:t_3+t_4+...:} e^{:s_2:} e^{:n_2+:\tilde{H}_3:+\tilde{H}_4:+...} e^{:t_3+t_4+...:} \quad (2.9)$$

with the $\check{H}_3, \check{H}_4, \dots$ calculated according to Theorem 1 and (1.62). And finally after some manipulations similar to those made in the semisimple case we have:

$$\mathcal{M} = e^{s_2} e^{-\check{i}_3 + \check{i}_4 + \dots} e^{n_2 + \check{j}_3 + \check{j}_4 + \dots} e^{t_3 + t_4 + \dots}. \quad (2.10)$$

The semisimple part of : H_2 : in (2.10) is already isolated, while the evaluation of the Lie transformation involving : n_2 : can now be carried out in a finite number of steps by exploiting the nilpotency of : n_2 :.

The effort required to compute the normal form in the more general case may be considerable as it involves manipulation of very large matrices (see Sec. 1.5.2). However, apart from its possible use in analytical calculations, the method presented here may be worth considering in some particular but common cases (for example when : H_2 : is nilpotent).

At this stage using normal forms to compute maps remains only a theoretical possibility. The algorithm which instead has been implemented in MARYLIE will be discussed below.

2.2 Lie Map Factorization Using Splitting, Scaling, Squaring

In this section we discuss the theory and implementation in MARYLIE5.0 of a different method to carry out the Lie map factorization. The method, Splitting, Scaling, Squaring (SSS) was proposed in [20]. SSS is an algorithm that can be applied in general to the evaluation of exponential functions. It applies for example to the exponential of a real number or matrix as well to the exponential of a Lie operator. In fact, the best way to see how it works is to apply it to the

evaluation of the exponential of a number. Suppose we want to calculate e^x with $x \in \mathbb{R}$. One way would be to use the representation of e^x as a power series:

$$\exp(x) = \sum_{k=0}^{\infty} \frac{x^k}{k!}. \quad (2.11)$$

This method is adequate if $x \ll 1$. However, it becomes increasingly less efficient as x becomes larger since more and more terms in the series have to be retained in order to achieve the desired accuracy. One can then use the property of the exponential function to write

$$\exp(x) = \left[\exp\left(\frac{x}{m}\right) \right]^m \quad (2.12)$$

where we chose m to be an integer. The RHS of (2.12) is the product of m exponentials $\exp(\frac{x}{m})$. If the integer m is large enough so that (x/m) is small we can efficiently calculate the exp function using only few terms in the power series representation (2.11). Let us say we retain the first $N + 1$ terms in the series. When we are done we take the m power of the result to get an approximated value for $\exp(x)$. One can see that the error in the final evaluation is of the order of $|x|(|x|/m)^N/(N+1)!$. For any given value of x the error can be made arbitrarily small by setting m and N appropriately.

A convenient choice for m is $m = 2^n$. In this way one can cut the number of operations necessary to evaluate the RHS of (2.12). Clearly in this case only n operations [squarings of $\exp(\frac{x}{m})$] are necessary to evaluate $\exp(x)$ from $\exp(\frac{x}{m})$.

As we look back to the steps we have gone through in the calculation we identify a ‘scaling’, consisting in dividing the exponent x by the integer $m = 2^n$, a summation over a few terms in the Taylor expansion, and a sequence of n ‘squarings’. We call this the Scaling and Squaring (SS) method for computing the exponential of a number or a matrix.

One can go through similar steps in the evaluation of a Lie transformation in the factored form. In particular the ‘scaling’ and the ‘squaring’ are formally the same ($t = z^f - z^i$):

$$\begin{aligned}\mathcal{M} &= \exp(t : -H :) = \{\exp[(t/2^n) : -H :]\}^{2^n} \\ &= \{\cdots \{\{\exp[(t/2^n) : -H :]\}^2\}^2 \cdots\}^2 \quad (n \text{ squarings}).\end{aligned}\quad (2.13)$$

The only difference is in the stage of evaluating $\exp[(t/2^n) : -H :]$. We call this the ‘splitting’ step. As in the case of the exponential of a number discussed above we exploit the small size of $\tau = (t/2^n)$. This can be done in at least two different ways.

The first way involves solutions, in the form of power series in τ , of the equation of motion for the map presented in Sec. 1.4. In practice, this way requires the calculation of the Taylor series in τ for each of the Lie generators g_n . The second way makes use of symplectic integrator formulas. Each method has its virtues and defects as we will soon see.

Let us consider the Taylor method first. Inspection of equations (1.42) through (1.50) shows that in the autonomous case one can in principle write a solution as a power series in z , the independent variable, to arbitrary order. The only difficulty is that the resulting expression becomes ‘exponentially’ complicated with the order of the solution. Use of a symbolic manipulator is therefore necessary for this kind of computation. Here we will report explicitly formulas through 5th order in τ and through 8th order in the Lie generators.

Specifically we will explicitly determine the factorization

$$\exp(\tau : -H :) = \mathcal{R}(\tau) \exp[: g_3(\tau) :] \exp[: g_4(\tau) :] \exp[: g_5(\tau) :] + \mathcal{O}(\tau^6). \quad (2.14)$$

Notice that in this section we prefer to work with the ‘direct’ Lie factorized map

(the order of the generator increases when reading the factorization from left to right). This contrasts with the ‘reversed’ form which was used in Sec. 1.4. In the reversed factorization the expression (2.14) would have the form:

$$\exp(\tau : -H :) = \exp[: f_5(\tau) :] \exp[: f_4(\tau) :] \exp[: f_3(\tau) :] \mathcal{R}'(\tau) + \mathcal{O}(\tau^6). \quad (2.15)$$

It turns out that the generators appearing in the two cases are related by simple formulas:

$$\begin{aligned} \mathcal{R}'(\tau) &= \mathcal{R}(\tau), \\ g_m(\tau) &= -f_m(-\tau). \end{aligned} \quad (2.16)$$

Let us look back again at equations (1.42) through (1.50). The equation for the linear part can be readily integrated

$$\mathcal{R} = \exp(\tau : -H_2 :). \quad (2.17)$$

The corresponding matrix can be obtained by exponentiation using the SS or other methods (see Sec. 2.3).

The RHS of the equations (1.45) through (1.50) for the higher order generators can be divided into two parts. The first, the ‘direct term’, involves the polynomials H_m^{int} of the Hamiltonian in the interaction picture having the same degree as the generator f_m . The second term includes all the rest (‘feed up’ term). The same structure is maintained by the g_m ’s:

$$g_m(\tau) = g_m^d(\tau) + g_m^{fu}(\tau). \quad (2.18)$$

In particular for the direct terms we have, (remember the definition (1.44)) :

$$g_m^d(\tau) = - \int_0^\tau d\tau' H_m^{int}(\mathbf{z}) = - \int_0^\tau d\tau' \mathcal{R} H_m(\mathbf{z}) = - \sum_{k=1}^{\infty} \frac{\tau^k}{k!} : -H_2 :^{k-1} H_m. \quad (2.19)$$

The feed-up term $g_n^{fu}(\tau)$, on the other hand receives contributions from all the terms in H having a degree $s \leq m$. We report here the expressions for the feed-up terms, through 5th order in τ that have been produced using the Mathematica program reported in Appendix D.

$$g_3^{fu} = 0.$$

$$\begin{aligned} g_4^{fu} = & \quad (1/12)\tau^3[:H_2:H_3,H_3] + (1/24)\tau^4[:H_2:{}^2H_3,H_3] \\ & + \tau^5\{(1/80)[:H_2:{}^3H_3,H_3] + (1/120)[:H_2:{}^2H_3,:H_2:H_3]\} + \mathcal{O}(\tau^6) \end{aligned}$$

$$\begin{aligned} g_5^{fu} = & \quad -(1/2)\tau^2[H_3,H_4] - \tau^3\{(1/3)[H_3,:H_2:H_4] + (1/6)[:H_2:H_3,H_4]\} \\ & - \tau^4\{(-1/24)[H_3,[:H_2:H_3,H_3]] + (1/8)[H_3,:H_2:{}^2H_4] \\ & + (1/8)[:H_2:H_3,:H_2:H_4] + (1/24)[:H_2:{}^2H_3,H_4]\} \\ & + \tau^5\{(1/45)[H_3,[:H_2:{}^2H_3,H_3]] - (1/30)[H_3,:H_2:{}^3H_4] \\ & + (1/60)[:H_2:H_3,[:H_2:H_3,H_3]] - (1/20)[:H_2:H_3,:H_2:{}^2H_4] \\ & - (1/30)[:H_2:{}^2H_3,:H_2,H_4:] - (1/120)[:H_2:{}^3H_3,H_4]\} + \mathcal{O}(\tau^6). \end{aligned}$$

$$\begin{aligned} g_6^{fu} = & \quad -(1/2)\tau^2[H_3,H_5] \\ & + \tau^3\{(-1/6)[H_3,[H_3,H_4]] - (1/3)[H_3,:H_2:H_5] \\ & - (1/3)[H_3,:H_2:H_5] - (1/6)[:H_2:H_3,H_5] \\ & + (1/12)[:H_2:H_4,H_4]\} \\ & - \tau^4\{(1/8)[H_3,[H_3,:H_2:H_4]] + (1/6)[H_3,[:H_2:H_3,H_4]] \\ & + (1/8)[H_3:H_2:{}^2H_5] - (1/48)[H_4,[:H_2:H_3,H_3]] \\ & + (1/16)[:H_2:H_3,[H_3,H_4]] + (1/8)[:H_2:H_3,:H_2:H_5] \\ & + (1/24)[:H_2:{}^2H_3,H_5] - (1/24)[:H_2:{}^2H_4,H_4]\} \end{aligned}$$

$$\begin{aligned}
& + \tau^5 \{ (1/80)[H_3, [H_3, [: H_2 : H_3, H_3]]] - (1/20)[H_3, [H_3, : H_2 :^2 H_4]] \\
& - (1/20)[H_3, [: H_2 : H_3, : H_2 : H_4]] - (1/60)[H_3, [: H_2 :^2 H_3, H_4]] \\
& - (1/30)[H_3, : H_2 :^3 H_5] + (1/80)[H_4, [: H_2 :^2 H_3, H_3]] \\
& - (1/20)[[: H_2 : H_3, [H_3, : H_2 : H_4]]] - (1/40)[[: H_2 : H_3, [: H_2 : H_3, H_4]]] \\
& - (1/20)[[: H_2 : H_3, : H_2 :^2 H_5]] + (1/240)[[: H_2 : H_4, [: H_2 : H_3, H_3]]] \\
& - (1/60)[[: H_2 :^2 H_3, [H_3, H_4]]] - (1/30)[[: H_2 :^2 H_3, : H_2 : H_5]] \\
& + (1/20)[[: H_2 :^2 H_4, : H_2 : H_4]] - (1/120)[[: H_2 :^3 H_3, H_5]] \\
& + (1/180)[[: H_2 :^3 H_4, H_4]] \} + \mathcal{O}(\tau^6).
\end{aligned}$$

From a practical view point one would like to retain as many powers of τ as possible to improve accuracy. Clearly, the more accurate the splitting formula is the smaller is the number of squarings that one needs to carry out in order to obtain the desired result. The dividing line is set by a compromise between programming effort and speed of execution.

The second way to evaluate the splitting terms makes use of symplectic integrators. As before one has the choice of setting the order in τ . However the choice here is mostly motivated by a compromise between accuracy and speed, since the implementation of symplectic integrators is relatively straightforward. As the order of the integrator increases so does the accuracy but also the number of operations necessary to produce the splitting.

The idea of a symplectic integrator is to write a Lie transformation as an approximated product of more elementary Lie transformations. The order of the symplectic integrator refers to the error introduced by such a factorization. A second order symplectic integrator (i.e. producing error of the order of τ^3) is

given by:

$$\exp[\tau(: A + B :)] = \exp(\tau : A : /2) \exp(\tau : B :) \exp(\tau : A : /2) + \mathcal{O}(\tau^3). \quad (2.20)$$

The way one can verify (2.20) is by expanding the exponential on both sides according to their series representation. A fourth order integrator is given by

$$\begin{aligned} S_4(\tau) = & \exp(w_1\tau : A :) \exp(w_2\tau : B :) \exp(w_3\tau : A :) \exp(w_4\tau : B :) \times \\ & \exp(w_5\tau : A :) \exp(w_6\tau : B :) \exp(w_7\tau : A :) + \mathcal{O}(\tau^5) \end{aligned} \quad (2.21)$$

with the weights w_i having the values

$$\begin{aligned} w_1 = w_7 &= -1/[2(2 - 2^{1/3})], \quad w_3 = w_5 = (1 - 2^{1/3})w_1, \\ w_2 = w_6 &= 2w_1, \quad w_4 = -2^{1/3}w_2. \end{aligned} \quad (2.22)$$

Higher order integrators are also known and could be used. How can we apply symplectic integrators formulas for our purpose? The natural choice is to identify $A = H_2$ and $B = H_3 + H_4 + H_5 + \dots$. In this way we see that a symplectic integrator provides us with a factorization of the quadratic part of the Lie generator valid through the order of the symplectic integrator.

A convenient way to rewrite the symplectic integrator with the aid of (1.37) is the following:

$$\begin{aligned} S_4(\tau) = & \exp(w_1\tau : H_2 :) \exp(w_2\tau : B :) \exp(w_3\tau : H_2 :) \exp(w_4\tau : B :) \times \\ & \exp[(w_5 + w_7)\tau : H_2 :] e^{\exp(-w_7\tau : H_2 :) B w_6} + \mathcal{O}(\tau^5). \end{aligned} \quad (2.23)$$

In this way the symplectic integrator formula is expressed as the product of three maps each one exhibiting explicitly the factorization of the quadratic term. The two ways presented in this section have been implemented in MARYLIE5.0 and

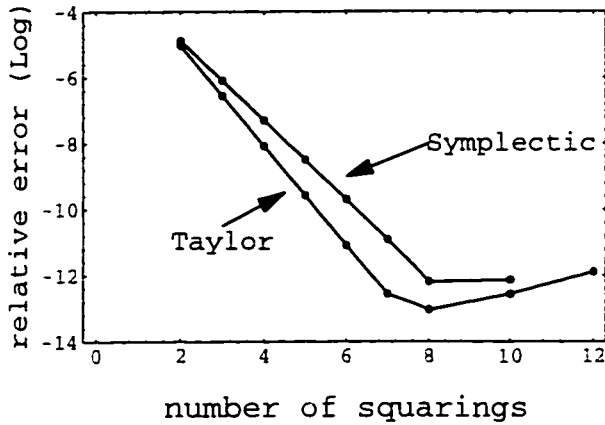


Figure 2.1: Logarithm (\log_{10}) of the relative error vs. number of squarings for the Lie generator x^5 of a map as calculated using the SSS algorithm with a 5th order Taylor and a 4th symplectic integrator split formula. The error is computed against a calculation done with GENMAP.

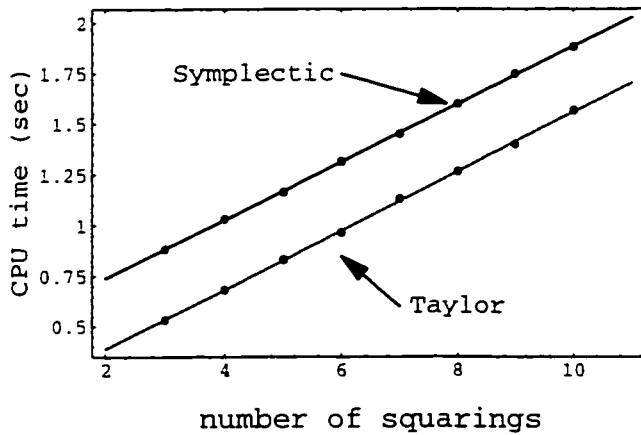


Figure 2.2: CPU time vs. number of squarings in computing a map using the SSS algorithm. The 5th order Taylor and the 4th symplectic integrator splitting methods are compared.

tested against each other and against the existing routine GENMAP that solves exactly the equation of motion for the map (1.38) in the general case with the z dependence.¹

The two figures reported here give an idea about how the SSS algorithm implemented with 5th order Taylor split formula compare to the one that uses a 4th order symplectic integrator. One can see that a 5th order Taylor splitting formula is more accurate (see Fig. 2.1) and more efficient (see Fig. 2.2) than the corresponding 4th order symplectic integrator. Also notice (Fig. 2.1) that there is an optimal number of splitting/squaring. Beyond that number the accuracy worsens because of round-off errors.

2.3 Exponentiation of Hamiltonian Matrices

The SS algorithm outlined in the previous section could also be used to carry out the calculation for the the linear part of the map. In fact, this is at present the algorithm implemented in MARYLIE. However, other methods can also be applied. See [49] for a comprehensive review of methods suitable for exponentiating matrices. Here we will explore in some detail a method based on the spectral decomposition theory (see [45] and references there contained) which can be conveniently applied to the exponentiation of low dimension Hamiltonian matrices. The method is based on the calculation of the matrix eigenvalues. For Hamiltonian matrices of dimension 6D (the highest dimension we are interested in) the eigenvalue problem requires the solution of a characteristic equation of

¹In principle one could use GENMAP routinely to compute maps also in the autonomous case. However this would be very inefficient.

third order, which can be solved analytically. The formulas we derive may be useful for analysis as well for computation. The only delicate aspect from a computational viewpoint is given by those situations where the eigenvalues are close to coalescing. In order to preserve the desired accuracy these cases require some additional care and numerical effort which may slow down the computation. An advantage of this method, however, is that it can be easily extended to compute other functions of matrices like the ‘iex’ function (see Sec. 2.4) to which the SS algorithm could not be applied.

Let us restate the problem. Given a quadratic Hamiltonian

$$H_2 = \frac{1}{2} \sum_{jk} S_{jk} z_j z_k,$$

we want to calculate the exponential of the Hamiltonian matrix $\mathbf{A} = \mathbf{JS}$ associated with S , i.e. $\exp(t\mathbf{JS})$. In this Section we present analytic formulas of the form

$$\epsilon^{t\mathbf{JS}} = \sum_{k=0}^{2n-1} a_k(t)(\mathbf{JS})^k. \quad (2.24)$$

for dimensions 2–6.

The decomposition method requires us to find all the eigenvalues of \mathbf{JS} . It is not difficult to show that the characteristic polynomial $P(\lambda)$ of \mathbf{JS} is an even function:

$$\begin{aligned} P(\lambda) &\equiv \det(\mathbf{JS} - \lambda\mathbf{I}) = \det(\mathbf{S} + \lambda\mathbf{J}) \\ &= \det(\check{\mathbf{S}} + \lambda\check{\mathbf{J}}) = \det(\mathbf{S} - \lambda\mathbf{J}) \\ &= P(-\lambda). \end{aligned}$$

Thus $P(\lambda)$ is a polynomial of λ^2 of degree n , and for $n \leq 4$ we can solve the characteristic equation analytically.

The coefficients of the characteristic polynomial $P(\lambda)$ of matrix \mathbf{A} can be

calculated by taking traces of \mathbf{A}^k , $k = 1, 2, \dots, 2n$. Expanding $P(\lambda)$ we find

$$P(\lambda) = \lambda^{2n} - \sigma_1 \lambda^{2n-1} + \sigma_2 \lambda^{2n-2} + \dots - \sigma_{2n-1} \lambda + \sigma_{2n},$$

where σ_k are the standard symmetric polynomials of the eigenvalues $\lambda_1, \dots, \lambda_{2n}$.

On the other hand, the trace of \mathbf{A}^k is just the k th power sum of the eigenvalues.

$$\text{trace}(\mathbf{A}^k) = \lambda_1^k + \dots + \lambda_{2n}^k \equiv s_k,$$

which are also symmetric polynomials of the eigenvalues. Given s_k it is very easy to calculate σ_k by Newton's identity

$$\sigma_1 = s_1,$$

$$\sigma_k = \frac{(-1)^{k-1}}{k} [s_k - \sigma_1 s_{k-1} + \sigma_2 s_{k-2} + \dots + (-1)^{k-1} \sigma_{k-1} s_1].$$

Therefore as long as we have calculated the powers of \mathbf{A} , it is very simple to obtain the coefficients of the characteristic polynomial, and in turn the eigenvalues.

2.3.1 The Decomposition Method

It is well known, and in Sec. 1.5 we have already made used of the fact that any matrix can be written as a sum of a diagonalizable part and a nilpotent part: $\mathbf{A} = \mathbf{D} + \mathbf{N}$ with $\mathbf{D}\mathbf{N} = \mathbf{N}\mathbf{D}$. Moreover, such decomposition is unique. The general procedure can be found in e.g. [45]. For our purpose in this study we will confine ourselves to the case when all eigenvalues of \mathbf{A} are distinct, meaning that \mathbf{A} is diagonalizable. The degenerate cases can be recovered from the nondegenerate result in the limit when eigenvalues coalesce.

Suppose the characteristic polynomial is

$$P(\lambda) = \prod_{j=1}^N (\lambda - \lambda_j).$$

Define

$$P_i(\lambda) = \prod_{j \neq i} (\lambda - \lambda_j) = \frac{P(\lambda)}{\lambda - \lambda_i}.$$

Obviously we have

$$\sum_{i=1}^N \frac{P_i(\lambda)}{P_i(\lambda_i)} = 1. \quad (2.25)$$

(See any text on Lagrange's interpolation formula.) Then the matrices.

$$\mathbf{E}_i \equiv \frac{P_i(\mathbf{A})}{P_i(\lambda_i)}$$

have the following properties:

(a) $\sum_i \mathbf{E}_i = \mathbf{I}$;

(b) $\mathbf{E}_i \mathbf{E}_j = 0$ if $i \neq j$:

(c) $\mathbf{E}_i^2 = \mathbf{E}_i$;

(d) $\mathbf{A} = \sum_i \lambda_i \mathbf{E}_i$.

The property (a) follows directly from Eq. 2.25. The property (b) follows from the fact that $\mathbf{E}_i \mathbf{E}_j$ is divisible by $P(\mathbf{A})$, which vanishes by the Cayley-Hamilton theorem. Property (c) is a trivial consequence of properties (a) and (b). To prove (d) we have

$$\begin{aligned} \mathbf{A} - \sum_i \lambda_i \mathbf{E}_i &= \mathbf{A} \sum_i \mathbf{E}_i - \sum_i \lambda_i \mathbf{E}_i \\ &= \sum_i (\mathbf{A} - \lambda_i \mathbf{I}) \mathbf{E}_i \\ &= \sum_i P(\mathbf{A}) / P_i(\lambda_i) = 0. \end{aligned}$$

Hence the matrices \mathbf{E}_i represent orthogonal projections into various subspaces.

Using these properties we can expand $e^{t\mathbf{A}}$ into a Taylor series

$$\exp(t\mathbf{A}) = \exp\left(t \sum_i \lambda_i \mathbf{E}_i\right) = \prod_i \exp(t\lambda_i \mathbf{E}_i)$$

$$\begin{aligned}
&= \prod_i \left[\mathbf{I} + (e^{t\lambda_i} - 1) \mathbf{E}_i \right] \\
&= \mathbf{I} + \sum_i (e^{t\lambda_i} - 1) \mathbf{E}_i \\
&= \sum_i e^{t\lambda_i} \mathbf{E}_i.
\end{aligned} \tag{2.26}$$

Therefore we have obtained the following formula for exponentiating a matrix with distinct eigenvalues:

$$\exp(t\mathbf{A}) = \sum_{i=1}^N e^{t\lambda_i} \frac{P_i(\mathbf{A})}{P_i(\lambda_i)}. \tag{2.27}$$

Notice how similar this is to Lagrange's interpolation formula. Formula (2.27) is a particular instance of a more general relationship valid for any analytic function f :

$$f(t\mathbf{A}) = \sum_{i=1}^N f(t\lambda_i) \frac{P_i(\mathbf{A})}{P_i(\lambda_i)}.$$

Next we apply (2.27) to problems of dimension 2–6, and work out all the degenerate cases by taking limits.

2.3.2 Two Dimensions

In two dimension, the two eigenvalues are $\pm\lambda_1$, and the characteristic polynomial reads $P(\lambda) = \lambda^2 - \lambda_1^2$. Eq. 2.27 then gives

$$\exp t\mathbf{A} = \cosh(t\lambda_1)\mathbf{I} + \frac{\sinh(t\lambda_1)}{\lambda_1}\mathbf{A}.$$

In the limit $\lambda_1 \rightarrow 0$ we have

$$\exp t\mathbf{A} = \mathbf{I} + t\mathbf{A}.$$

2.3.3 Four Dimensions

In four dimension the characteristic polynomial reads $P(\lambda) = \lambda^4 - \sigma_1\lambda^2 + \sigma_2 = (\lambda^2 - \lambda_1^2)(\lambda^2 - \lambda_2^2)$ where

$$\begin{aligned}\sigma_1 &= -\frac{1}{2}tr(A^2), \\ \sigma_2 &= \frac{1}{8}tr(A^2)^2 - \frac{1}{4}tr(A^4).\end{aligned}$$

Therefore,

$$\exp(tA) = \sum_{k=0}^3 a_k A^k.$$

with

$$\begin{aligned}a_0 &= (\lambda_1^2 \cosh(t\lambda_2) - \lambda_2^2 \cosh(t\lambda_1)) / (\lambda_1^2 - \lambda_2^2), \\ a_1 &= (\frac{\lambda_1^2}{\lambda_2} \sinh(t\lambda_2) - \frac{\lambda_2^2}{\lambda_1} \sinh(t\lambda_1)) / (\lambda_1^2 - \lambda_2^2), \\ a_2 &= (\cosh(t\lambda_1) - \cosh(t\lambda_2)) / (\lambda_1^2 - \lambda_2^2), \\ a_3 &= (\frac{1}{\lambda_1} \sinh(t\lambda_1) - \frac{1}{\lambda_2} \sinh(t\lambda_2)) / (\lambda_1^2 - \lambda_2^2).\end{aligned}$$

The cases with degeneracy in the eigenvalues can be obtained by taking the appropriate limits. In particular for $\lambda_2 = \lambda_1 \neq 0$ we have

$$\begin{aligned}a_0 &= (\cosh(t\lambda_1) - \frac{t\lambda_1}{2} \sinh(t\lambda_1)), \\ a_1 &= (3 \sinh(t\lambda_2) - t\lambda_1 \cosh(t\lambda_1)) / (2\lambda_1), \\ a_2 &= (t \sinh(t\lambda_1)) / (2\lambda_1), \\ a_3 &= (t\lambda_1 \cosh(t\lambda_2) - \sinh(t\lambda_1)) / (2\lambda_1^3).\end{aligned}$$

Finally for $\lambda_2 = \lambda_1 = 0$

$$\exp tA = \mathbf{I} + tA + \frac{t^2}{2}A^2 + \frac{t^3}{6}A^3.$$

2.3.4 Six Dimensions

In six dimension the characteristic polynomial reads $P(\lambda) = \lambda^6 - \sigma_1\lambda^4 - \sigma_2\lambda^2 + \sigma_3 = (\lambda^2 - \lambda_1^2)(\lambda^2 - \lambda_2^2)(\lambda^2 - \lambda_3^2)$ where

$$\begin{aligned}\sigma_1 &= -\frac{1}{2}tr(A^2), \\ \sigma_2 &= -\frac{1}{4}[(tr(A^2))^2 - \frac{1}{2}tr(A^4)], \\ \sigma_3 &= -\frac{1}{6}[tr(A^6) + \sigma_1tr(A^4) + \sigma_2tr(A^2)].\end{aligned}$$

Using the definitions

$$L_{1,2} = (\lambda_3^2 - \lambda_1^2)(\lambda_3^2 - \lambda_2^2),$$

$$L_{1,3} = (\lambda_2^2 - \lambda_1^2)(\lambda_2^2 - \lambda_3^2),$$

$$L_{2,3} = (\lambda_1^2 - \lambda_2^2)(\lambda_1^2 - \lambda_3^2).$$

the coefficients in

$$\exp tA = \sum_{k=0}^5 a_k A^k$$

have the form

$$\begin{aligned}a_0 &= \frac{\lambda_2^2 \lambda_3^2}{L_{2,3}} \cosh(t\lambda_1) + \frac{\lambda_1^2 \lambda_3^2}{L_{1,3}} \cosh(t\lambda_2) + \frac{\lambda_1^2 \lambda_2^2}{L_{1,2}} \cosh(t\lambda_3), \\ a_1 &= \frac{\lambda_2^2 \lambda_3^2}{\lambda_1 L_{2,3}} \sinh(t\lambda_1) + \frac{\lambda_1^2 \lambda_3^2}{\lambda_2 L_{1,3}} \sinh(t\lambda_2) + \frac{\lambda_1^2 \lambda_2^2}{\lambda_3 L_{1,2}} \sinh(t\lambda_3), \\ a_2 &= -\frac{\lambda_2^2 + \lambda_3^2}{L_{2,3}} \cosh(t\lambda_1) - \frac{\lambda_1^2 + \lambda_3^2}{L_{1,3}} \cosh(t\lambda_2) - \frac{\lambda_1^2 + \lambda_2^2}{L_{1,2}} \cosh(t\lambda_3), \\ a_3 &= -\frac{\lambda_2^2 + \lambda_3^2}{\lambda_1 L_{2,3}} \sinh(t\lambda_1) - \frac{\lambda_1^2 + \lambda_3^2}{\lambda_2 L_{1,3}} \sinh(t\lambda_2) - \frac{\lambda_1^2 + \lambda_2^2}{\lambda_3 L_{1,2}} \sinh(t\lambda_3), \\ a_4 &= \frac{1}{L_{2,3}} \cosh(t\lambda_1) + \frac{1}{L_{1,3}} \cosh(t\lambda_2) + \frac{1}{L_{1,2}} \cosh(t\lambda_3), \\ a_5 &= \frac{1}{\lambda_1 L_{2,3}} \sinh(t\lambda_1) + \frac{1}{\lambda_2 L_{1,3}} \sinh(t\lambda_2) + \frac{1}{\lambda_3 L_{1,2}} \sinh(t\lambda_3).\end{aligned} \tag{2.28}$$

Again, the cases with degeneracy can be obtained by taking the appropriate limits. In particular, for the case $\lambda_1 = \lambda_2 = \lambda_3 \neq 0$, we have

$$\begin{aligned}
a_0 &= \cosh(t\lambda_1) \left(1 + \frac{t^2\lambda_1^2}{8} \right) - \frac{5}{8}t\lambda_1 \sinh(t\lambda_1), \\
a_1 &= \frac{1}{8\lambda_1} \sinh(t\lambda_1)(t^2\lambda_1^2 + 15) - \frac{7}{8}t \cosh(t\lambda_1), \\
a_2 &= \frac{3}{4\lambda_1}t \sinh(t\lambda_3) - \frac{1}{4}t^2 \cosh(t\lambda_1), \\
a_3 &= -\frac{1}{4\lambda_1^3} \sinh(t\lambda_1)(t^2\lambda_1^2 + 5) + \frac{5}{4\lambda_1^2}t \cosh(t\lambda_1), \\
a_4 &= -\frac{1}{8\lambda_1^3}t \sinh(t\lambda_3) + \frac{1}{8}t^2 \cosh(t\lambda_1^2), \\
a_5 &= \frac{1}{8\lambda_1^5} \sinh(t\lambda_1)(t^2\lambda_1^2 + 3) - \frac{3}{8\lambda_1^4}t \cosh(t\lambda_1).
\end{aligned}$$

For $\lambda_1 = \lambda_2 \neq \lambda_3$, we have

$$\begin{aligned}
a_0 &= [-4\lambda_2^2\lambda_3^2 \cosh(\lambda_2 t) + 2\lambda_3^4 \cosh(\lambda_2 t) + 2\lambda_2^4 \cosh(\lambda_3 t) \\
&\quad + \lambda_2^3\lambda_3^2 t \sinh(\lambda_2 t) - \lambda_2\lambda_3^4 t \sinh(\lambda_2 t)]/[2(\lambda_2^2 - \lambda_3^2)^2], \\
a_1 &= [\lambda_2^3\lambda_3^3 t \cosh(\lambda_2 t) - \lambda_2\lambda_3^5 t \cosh(\lambda_2 t) - 5\lambda_2^2\lambda_3^3 \sinh(\lambda_2 t) \\
&\quad + 3\lambda_3^5 \sinh(\lambda_2 t) + 2\lambda_2^5 \sinh(\lambda_3 t)]/[2\lambda_2\lambda_3(\lambda_2^2 - \lambda_3^2)^2], \\
a_2 &= [4\lambda_2^3 \cosh(\lambda_2 t) - 4\lambda_2^3 \cosh(\lambda_3 t) - \lambda_2^4 t \sinh(\lambda_2 t) + \lambda_3^4 t \sinh(\lambda_2 t)] \\
&\quad / [2\lambda_2(\lambda_2^2 - \lambda_3^2)^2], \\
a_3 &= [-(\lambda_2^5\lambda_3 t \cosh(\lambda_2 t)) + \lambda_2\lambda_3^5 t \cosh(\lambda_2 t) + 5\lambda_2^4\lambda_3 \sinh(\lambda_2 t) \\
&\quad - \lambda_3^5 \sinh(\lambda_2 t) - 4\lambda_2^5 \sinh(\lambda_3 t)]/[2\lambda_2^3\lambda_3(\lambda_2^2 - \lambda_3^2)^2], \\
a_4 &= [-2\lambda_2 \cosh(\lambda_2 t) + 2\lambda_2 \cosh(\lambda_3 t) + \lambda_2^2 t \sinh(\lambda_2 t) - \lambda_3^2 t \sinh(\lambda_2 t)] \\
&\quad / [2\lambda_2(\lambda_2^2 - \lambda_3^2)^2], \\
a_5 &= [\lambda_2^3\lambda_3 t \cosh(\lambda_2 t) - \lambda_2\lambda_3^3 t \cosh(\lambda_2 t) - 3\lambda_2^2\lambda_3 \sinh(\lambda_2 t) \\
&\quad + \lambda_3^3 \sinh(\lambda_2 t) + 2\lambda_2^3 \sinh(\lambda_3 t)]/[2\lambda_2^3\lambda_3(\lambda_2^2 - \lambda_3^2)^2].
\end{aligned} \tag{2.29}$$

2.3.5 Numerical Implementation

From a computational point of view the main difficulty in implementing the formulas outlined in the previous chapter arises from the loss of accuracy that one would experience when the eigenvalues are close to each other. A way to overcome the problem is to rewrite the expressions of the coefficients a_k in (2.24) as Taylor series in the differences between the eigenvalues.

Let write $\lambda_2 = \lambda_1 + \epsilon$ and suppose λ_1 and λ_2 are identical through the first 7 digits. That is $\frac{\epsilon}{\lambda_1} \sim 10^{-8}$. If the machine precision is 15 digits in calculating $\lambda_1 - \lambda_2$ we are left with a result that is accurate through the first 8 digits with an accuracy loss of 7 digits.

We can write.

$$a_k(\epsilon) = a_{k0} + \frac{\partial a_k}{\partial \epsilon} \epsilon + \dots . \quad (2.30)$$

With a relative difference between the eigenvalues of the order 10^{-8} , as in the example above, the formula (2.30) gives a result with a relative error of the order 10^{-16} . The coefficients of the Taylor expansion in ϵ for the coefficients a_k can be easily carried out using a code for symbolic manipulations.

2.4 Evaluation of $iex(\mathbf{A})$

The decomposition theory discussed in the previous section to evaluate the exponential of a Hamiltonian matrix can easily be extended to carry out some operations that occur in the Lie calculus. In particular, suppose we want to perform the factorization:

$$e^{h_1+h_2} = e^{f_2} e^{f_1}.$$

where h_1 and h_2 are two given homogeneous polynomial of degree 1 and 2, and the task is to evaluate f_1 and f_2 . One can show [19] that $f_2 = h_2$ and

$$f_1 = iex(- : h_2 :)h_1, \quad (2.31)$$

where 'iex' is the integrated exponential:

$$iex(A) = \sum_{n=0}^{\infty} \frac{A^n}{(n+1)!}. \quad (2.32)$$

We already showed in (1.30) that if we write the quadratic polynomial h_2 in the form:

$$h_2 = -\frac{1}{2} \sum_{i,j} \mathbf{S}_{ij} z_i z_j,$$

where \mathbf{S} is a symmetric matrix, the map

$$z'_i = e^{h_2} z_i,$$

can be written in the matrix form:

$$z'_i = [e^{\mathbf{JS}}]_{ij} z_j.$$

By the same reasoning, one can easily convince oneself that the map

$$z'_i = iex(- : h_2 :) z_i,$$

can be written in the matrix form:

$$z'_i = [iex(-JS)]_{ij} z_j.$$

This formula can then be used to evaluate the function f_1 in (2.31).

$$iex(- : h_2 :)h_1 = \sum b_i iex(- : h_2 :) z_i = \sum b_i z'_i \quad (2.33)$$

$$= \sum b_i [iex(-JS)]_{ij} z_j = \sum_j c_j z_j, \quad (2.34)$$

where we have defined $c_j = \sum_i b_i [iex(-\mathbf{JS})]_{ij}$.

The calculation of $iex(\mathbf{A})$ can be carried out using the same technique we used to calculate $\exp(\mathbf{A})$. In fact, the formulas worked out in Sec. 2.3 for $D = 2, 4, 6$ can be adapted to our case simply by the replacements:

$$\exp \rightarrow iexp.$$

$$\cosh \rightarrow icosh.$$

$$\sinh \rightarrow isinh.$$

where $icosh$ and $isinh$ represent the even and the odd part of the Taylor expansion (2.32) of the function iex . This is a consequence of the fact that if a matrix \mathbf{A} has the decomposition $\mathbf{A} = \sum_i \lambda_i \mathbf{E}_i$, then

$$f(\mathbf{A}) = \sum_i f(\lambda_i) \mathbf{E}_i.$$

Chapter 3

Map Computation from Magnetic Field Data

3.1 Introduction

With the notable exception of some types of iron free magnets like the Lambertson current sheet magnets¹ or the Halbach permanent magnets, we cannot rely in general on a very accurate analytical modelling of the magnetic fields. In many cases the most accurate information about the fields comes either from direct measurement or from a numerical computation done with a 3D electromagnetic code.

The problem we face in this chapter is to relate the information obtained through measurement or computation to the vector potential that is needed to carry out a map calculation in a canonical framework. Eventually we want to be able to determine explicitly the coefficients of the Taylor expansion of the vector potential in the transverse variables. In the general case these coefficients will

¹Details on the design of this kind of magnets can be found in Chapter 4 and 5

be functions of z , the longitudinal variable.

The technique illustrated in this chapter will allow one to carry out a very accurate computation of the fringe effects in magnets, which are usually poorly modeled in most tracking studies.

We begin the chapter by reviewing the well known multipole expansion for the magnetic field in terms of the scalar potential which applies in a current-free regions. The multipole expansion involves certain z dependent functions which can be interpreted as generalized gradients for the field. Each multipole is associated with one generalized gradient and its derivatives. Specification of the generalized gradients is equivalent to knowing the magnetic field in the region of space where the multipole series is convergent.

For some specific non-Coulombian choices of the gauge one can easily relate the multipole expansion for the scalar potential to the vector potential. This is also a well known procedure. In the case of a Coulomb gauge one can derive the multipole expansion by working directly on the vector Laplace equation which is satisfied by the vector potential in current free region. The resulting expansion in its most general form does not seem to be widely known in the accelerator physics community and therefore we present it in some detail. In particular two different derivations are reported: the first is based on the theory of the general solution for the vector Laplace equation, the second (contained in Appendix A) builds up the solution starting from a general power series representation.

Once the multipole representation for the vector potential has been found it is only a matter of switching from cylindrical to cartesian variables to get the required Taylor expansion in the transverse variables.

In Section 3.4 we derive some integral formulas that give the generalized gra-

dients in terms of one component of the magnetic field in cylindrical variables on a cylindrical surface. The formulas have the appearance of Fourier-like integrals. An interesting feature of these integrals is the presence of a kernel with a natural cut-off that filters out the high frequencies. Because of this feature, those integral formulas are particularly suitable for use on numerical data, for which the presence of some kind of noise is unavoidable. In this case the cylindrical surface should lay parallel to the magnet axis and be contained within the magnet aperture. Similar formulas are shown to hold when one specifies the scalar potential on the same cylindrical surface (some electromagnetic codes do actually compute the scalar potential directly).

In Section 3.5 similar formulas are derived for the kind of data that can be obtained experimentally by making measurements with a spinning coil. One can recover the generalized gradients by moving the spinning coil by short steps along the magnet axis and Fourier-transforming the data.

The method described in Section 3.4 has been implemented in MARYLIE as a user defined routine and tested on a particular case where one has an analytical knowledge of the generalized gradient. The outcome of the test is summarized in Section 3.7. The routine can be used to carry out map computations upon specification of the radial component of the magnetic field on the surface of a cylinder.

For an application see Chapter 7 where we report a study of fringe effects in the high gradient low beta insertion quadrupoles in the LHC.

3.2 Multipole Expansion for the Scalar Potential and Generalized Gradients

Although we are ultimately interested in the expression for the vector potential, the description of the magnetic field in a current-free region is most conveniently carried out in terms of a *scalar* potential ψ , with $\mathbf{B} = \nabla\psi$.² obeying the Laplace equation:

$$\nabla^2\psi = 0. \quad (3.1)$$

In cylindrical coordinates the most general solution of (3.1) regular at the origin $\rho = 0$, can be expanded in terms of the eigenfunctions of the operator $\frac{\partial^2}{\partial\phi^2}$ as

$$\psi = \sum_{m=0}^{\infty} \psi_{m,s}(\rho, z) \sin m\phi + \psi_{m,c}(\rho, z) \cos m\phi. \quad (3.2)$$

where

$$\psi_{m,s}(\rho, z) = \frac{1}{\sqrt{2\pi}} \int_{-\infty}^{\infty} dk \exp(ikz) I_m(k\rho) b_m(k), \quad (3.3)$$

$$\psi_{m,c}(\rho, z) = \frac{1}{\sqrt{2\pi}} \int_{-\infty}^{\infty} dk \exp(ikz) I_m(k\rho) a_m(k), \quad (3.4)$$

and I_m is the modified Bessel function of order m . Equation (3.2) is usually referred to in accelerator physics literature as the ‘multipole expansion’ for the field. The integer m is the order of the multipole: for example, $m = 0$ corresponds to a pure solenoid, $m = 1$ to a dipole, $m = 2$ to a quadrupole, etc. . Notice that the solenoidal field is described by $\psi_{m=0,c}$; it is understood that $\psi_{m=0,s} = 0$. The ‘sin-like’ and ‘cos-like’ terms in the multipole expansion (3.2) correspond to the ‘normal’ and ‘skew’ components of the fields. The multipole expansion can be easily converted into a power series in the radial variable ρ by using the Taylor

²Notice our convention about the + sign in the definition of the scalar potential.

expansion for $I_m(x)$:

$$I_m(x) = \sum_{\ell=0}^{\infty} \frac{1}{\ell!(\ell+m)!} \left(\frac{x}{2}\right)^{2\ell+m}. \quad (3.5)$$

Moreover, we can isolate the integration over k to get the multipole expansion in the form that is usually found in the literature ($\alpha = c, s$)

$$\psi_{m,\alpha}(\rho, z) = \sum_{\ell=0}^{\infty} (-1)^\ell \frac{m!}{2^{2\ell} \ell! (\ell+m)!} C_{m,\alpha}^{[2\ell]}(z) \rho^{2\ell+m}. \quad (3.6)$$

where the functions $C_{m,\alpha}^{[2\ell]}(z)$ are defined by (for $m \neq 0$):

$$C_{m,c}^{[2\ell]}(z) = \frac{(-1)^\ell}{\sqrt{2\pi}} \frac{1}{2^m m!} \int_{-\infty}^{\infty} k^{2\ell+m} e^{ikz} a_m(k) dk, \quad (3.7)$$

$$C_{m,s}^{[2\ell]}(z) = \frac{(-1)^\ell}{\sqrt{2\pi}} \frac{1}{2^m m!} \int_{-\infty}^{\infty} k^{2\ell+m} e^{ikz} b_m(k) dk. \quad (3.8)$$

and (for $m = 0$, corresponding to a purely solenoidal field)

$$C_{m=0,c}^{[2\ell]}(z) = C_{sol}^{[2\ell]}(z) = \frac{(-1)^\ell}{\sqrt{2\pi}} \int_{-\infty}^{\infty} k^{2\ell} e^{ikz} a_0(k) dk. \quad (3.9)$$

Observe that $C_{m,\alpha}^{[2\ell+2]}(z) = \frac{d^2}{dz^2} C_{m,\alpha}^{[2\ell]}(z)$. Therefore, we conclude that for each m the coefficients of the series (3.6) can be obtained by successive differentiation of the functions $C_{m,\alpha}(z) = C_{m,\alpha}^{[0]}(z)$. We will refer to the functions $C_{m,\alpha}(z)$ as ‘generalized gradients’.

The corresponding expressions for the magnetic field in cylindrical coordinates are ($m \neq 0$):

$$\begin{aligned} B_\rho &= \sum_{m=1}^{\infty} \sum_{\ell=0}^{\infty} (-1)^\ell \frac{m!(2\ell+m)}{2^{2\ell} \ell! (\ell+m)!} C_{m,\alpha}^{[2\ell]}(z) \rho^{2\ell+m-1} \begin{Bmatrix} \sin m\phi \\ \cos m\phi \end{Bmatrix}, \\ B_\phi &= \sum_{m=1}^{\infty} \sum_{\ell=0}^{\infty} (-1)^\ell \frac{m!}{2^{2\ell} \ell! (\ell+m)!} m C_{m,\alpha}^{[2\ell]}(z) \rho^{2\ell+m-1} \begin{Bmatrix} \cos m\phi \\ -\sin m\phi \end{Bmatrix}, \\ B_z &= \sum_{m=1}^{\infty} \sum_{\ell=0}^{\infty} (-1)^\ell \frac{m!}{2^{2\ell} \ell! (\ell+m)!} C_{m,\alpha}^{[2\ell+1]}(z) \rho^{2\ell+m} \begin{Bmatrix} \sin m\phi \\ \cos m\phi \end{Bmatrix}. \end{aligned} \quad (3.10)$$

The upper choice of the trigonometric function corresponds to a normal field, the lower choice to a skew field. For the case of a purely solenoidal field ($m = 0$), we have $B_\phi = 0$ and

$$\begin{aligned} B_\rho &= \sum_{\ell=1}^{\infty} (-1)^\ell \frac{2}{2^{2\ell}\ell!(\ell-1)!} C_{sol}^{[2\ell]}(z)\rho^{2\ell-1}. \\ B_z &= \sum_{\ell=0}^{\infty} (-1)^\ell \frac{1}{2^{2\ell}(\ell!)^2} C_{sol}^{[2\ell+1]}(z)\rho^{2\ell}. \end{aligned} \quad (3.11)$$

For specific examples of multipole expansion for physical magnets, see Section 5.3.

3.3 Multipole Expansion for the Vector Potential

Having characterized the magnetic field in terms of the multipole expansion of the scalar potential, we want to use the generalized gradients to determine the vector potential. Two different strategies are possible. One way is to make an ansatz for the vector potential of the form

$$\begin{aligned} A_\rho(\rho, \phi, z) &= \sum_m A_{\rho,c}^{(m)}(\rho, z) \cos m\phi + A_{\rho,s}^{(m)}(\rho, z) \sin m\phi. \\ A_\phi(\rho, \phi, z) &= \sum_m A_{\phi,c}^{(m)}(\rho, z) \cos m\phi + A_{\phi,s}^{(m)}(\rho, z) \sin m\phi. \\ A_z(\rho, \phi, z) &= \sum_m A_{z,c}^{(m)}(\rho, z) \cos m\phi + A_{z,s}^{(m)}(\rho, z) \sin m\phi. \end{aligned} \quad (3.12)$$

and use directly the multipole expansion found for the scalar potential and the equation $\nabla \psi = \nabla \times \mathbf{A}$. Using this method it is straightforward to write the vector potential in the following three cases corresponding to three distinct choices of the gauge. The first gauge, $A_\phi = 0$, is suitable if $m \neq 0$. We have:

$$A_{z,s}^{(m)} = \frac{\rho}{m} \frac{\partial}{\partial \rho} \psi_{m,c}, \quad A_{z,c}^{(m)} = -\frac{\rho}{m} \frac{\partial}{\partial \rho} \psi_{m,s}. \quad (3.13)$$

$$A_{\rho,s}^{(m)} = -\frac{\rho}{m} \frac{\partial}{\partial z} \psi_{m,c}, \quad A_{\rho,c}^{(m)} = \frac{\rho}{m} \frac{\partial}{\partial z} \psi_{m,s}. \quad (3.14)$$

On the other hand, in the gauge $A_\rho = 0$,

$$A_{z,s}^{(m)} = m \int \psi_{m,c} d\rho, \quad A_{z,c}^{(m)} = -m \int \psi_{m,s} d\rho. \quad (3.15)$$

$$A_{\phi,s}^{(m)} = \frac{1}{\rho} \int \rho \frac{\partial}{\partial z} \psi_{m,s} d\rho, \quad A_{\phi,c}^{(m)} = \frac{1}{\rho} \int \rho \frac{\partial}{\partial z} \psi_{m,c} d\rho. \quad (3.16)$$

Notice that if $m = 0$, as in the case of a pure solenoidal field only the A_ϕ component is nonvanishing; this gauge is the natural choice for describing solenoidal fields.

Finally, in the gauge $A_z = 0$, we have

$$A_{\rho,s}^{(m)} = -m \int \psi_{m,c} dz, \quad A_{\rho,c}^{(m)} = m \int \psi_{m,s} dz. \quad (3.17)$$

$$A_{\phi,s}^{(m)} = - \int \frac{\partial}{\partial \rho} \psi_{m,s} dz, \quad A_{\phi,c}^{(m)} = - \int \frac{\partial}{\partial \rho} \psi_{m,c} dz. \quad (3.18)$$

The second method consists of trying to solve directly the equation satisfied by the vector potential

$$\nabla \times \nabla \cdot \mathbf{A} = \nabla(\nabla \cdot \mathbf{A}) - \nabla^2 \mathbf{A} = 0. \quad (3.19)$$

In the particular case where we are interested in finding solutions satisfying the Coulomb gauge, $\nabla \cdot \mathbf{A} = 0$, the equation above becomes the vector Laplace equation $\nabla^2 \mathbf{A} = 0$. One way to proceed is to first write down the general solution to the vector Laplace equation and then carry out the Taylor expansion in the radial variable ρ . The most general solution regular at $\rho = 0$ can be obtained by superposition of the following linearly independent solutions [48]

$$\mathbf{M}_{\alpha,m} = \frac{1}{k} \nabla \times \left(\mathbf{e}_z \begin{Bmatrix} \cos m\phi \\ \sin m\phi \end{Bmatrix} e^{ikz} I_m(k\rho) \right). \quad (3.20)$$

$$\mathbf{N}_{\alpha,m} = \frac{1}{k} \nabla \left(\begin{Bmatrix} \cos m\phi \\ \sin m\phi \end{Bmatrix} e^{ikz} I_m(k\rho) \right). \quad (3.21)$$

$$\mathbf{G}_{\alpha,m} = 2\mathbf{e}_z \begin{Bmatrix} \cos m\phi \\ \sin m\phi \end{Bmatrix} e^{ikz} I_m(k\rho). \quad (3.22)$$

These functions are analogous to the function (3.2 for the scalar Laplace equation. The index $\alpha = c$ corresponds to the upper choice of the trigonometric function; $\alpha = s$ to the lower choice. Since only $\mathbf{M}_{\alpha,m}$ and $\mathbf{N}_{\alpha,m}$ are divergenceless, we can disregard $\mathbf{G}_{s,m}$ as a possible candidate.

Two suitable combinations for the vector potential producing the normal and skew components are given by

$$\mathbf{A}^{nor} = \sum_{m=0}^{\infty} \int_{-\infty}^{\infty} dk \{ [2\epsilon_{m,c}(k) - \gamma_{m,c}(k)] \mathbf{M}_{s,m} + \gamma_{m,c}(k) \mathbf{N}_{c,m} \}. \quad (3.23)$$

$$\mathbf{A}^{skew} = \sum_{m=0}^{\infty} \int_{-\infty}^{\infty} dk \{ [-2\epsilon_{m,s}(k) + \gamma_{m,s}(k)] \mathbf{M}_{c,m} + \gamma_{m,s}(k) \mathbf{N}_{s,m} \}. \quad (3.24)$$

Specifically, for the ‘normal field’ the three components of the vector potential read

$$A_{\rho}^{nor} = \sum_{m=1}^{\infty} \sin m\phi \int dk e^{ikz} \left\{ 2\epsilon_{m,s} \frac{m}{k\rho} I_m(k\rho) + \gamma_{m,s} \left[I'_m(k\rho) - \frac{m}{k\rho} I_m(k\rho) \right] \right\}.$$

$$A_{\phi}^{nor} = \sum_{m=0}^{\infty} \cos m\phi \int dk e^{ikz} \left\{ -2\epsilon_{m,s} I'_m(k\rho) + \gamma_{m,s} \left[I'_m(k\rho) - \frac{m}{k\rho} I_m(k\rho) \right] \right\}.$$

$$A_z^{nor} = \sum_{m=1}^{\infty} \sin m\phi \int dk e^{ikz} \gamma_{m,s} I_m(k\rho);$$

and for the ‘skew’ field

$$A_{\rho}^{skew} = \sum_{m=1}^{\infty} \sin m\phi \int dk e^{ikz} \left\{ 2\epsilon_{m,s} \frac{m}{k\rho} I_m(k\rho) + \gamma_{m,s} \left[I'_m(k\rho) - \frac{m}{k\rho} I_m(k\rho) \right] \right\}.$$

$$A_{\phi}^{skew} = \sum_{m=1}^{\infty} \cos m\phi \int dk e^{ikz} \left\{ 2\epsilon_{m,s} I'_m(k\rho) - \gamma_{m,s} \left[I'_m(k\rho) - \frac{m}{k\rho} I_m(k\rho) \right] \right\}.$$

$$A_z^{skew} = \sum_{m=1}^{\infty} \sin m\phi \int dk e^{ikz} \gamma_{m,s} I_m(k\rho).$$

After using repeatedly the Taylor expansion (3.5) for the Bessel function I_m and having defined the functions:

$$E_{m,\alpha}(z) = \frac{1}{2^m m!} \int_{-\infty}^{\infty} \epsilon_{m+1,\alpha}(k) e^{ikz} k^m dk. \quad (3.25)$$

$$\Gamma_{m,\alpha}(z) = \frac{1}{2^m m!} \int_{-\infty}^{\infty} \gamma_{m,\alpha}(k) e^{ikz} k^m dk. \quad (3.26)$$

one finds the following results. For the normal components we have

$$\begin{aligned} A_{\rho,c}^{(m)}(\rho, z) &= \sum_{\ell=0}^{\infty} \frac{(-1)^\ell m!}{2^{2\ell} (\ell+m)! \ell!} [E_{m-1,c}^{[2\ell]}(z) + 2\ell \Gamma_{m,c}^{[2\ell-1]}(z)] \rho^{m+2\ell-1}. \\ A_{\phi,s}^{(m)}(\rho, z) &= \sum_{\ell=0}^{\infty} \frac{(-1)^\ell m!}{2^{2\ell} (\ell+m)! \ell!} \left[-\frac{(m+2\ell)}{m} E_{m-1,c}^{[2\ell]}(z) + 2\ell \Gamma_{m,c}^{[2\ell-1]}(z) \right] \rho^{m+2\ell-1}. \\ A_{z,c}^{(m)}(\rho, z) &= \sum_{l=0}^{\infty} (-1)^l \frac{m!}{2^{2l} l! (l+m)!} \Gamma_{m,c}^{[2l]}(z) \rho^{2l+m}. \end{aligned} \quad (3.27)$$

For the case of 'skew' multipoles.

$$\begin{aligned} A_{\rho,s}^{(m)} &= \sum_{\ell=0}^{\infty} \frac{(-1)^\ell m!}{2^{2\ell} \ell! (\ell+m)!} [2\ell \Gamma_{m,s}^{[2\ell-1]}(z) + E_{m-1,s}^{[2\ell]}] \rho^{2\ell+m-1}. \\ A_{\phi,c}^{(m)} &= \sum_{\ell=0}^{\infty} \frac{(-1)^\ell m!}{2^{2\ell} \ell! (\ell+m)!} [-2\ell \Gamma_{m,s}^{[2\ell-1]}(z) + \frac{2\ell+m}{m} E_{m-1,s}^{[2\ell]}] \rho^{2\ell+m-1} \\ A_{z,s}^{(m)} &= \sum_{\ell=0}^{\infty} \frac{(-1)^\ell m!}{2^{2\ell} \ell! (\ell+m)!} \Gamma_{m,s}^{[2\ell]}(z) \rho^{2\ell+m}. \end{aligned} \quad (3.28)$$

Equations (3.28) and (3.27) show that the most general multipole expansion for the vector potential can be written in terms of two functionally independent functions $E_{m-1,\alpha}$ and $\Gamma_{m-1,\alpha}$ and their derivatives. In particular the functions $E_{m-1,\alpha}$ alone generate the restricted Coulomb gauge satisfying the additional constraint $A_z = 0$.

From (3.27) and (3.28) we can derive the following useful relations:

$$\begin{aligned} \Gamma_{m,\alpha} &= \lim_{\rho \rightarrow 0} \frac{A_{z,\alpha}^{(m)}}{\rho^m}, \\ E_{m-1,\alpha} &= \lim_{\rho \rightarrow 0} \frac{A_{\rho,\alpha}^{(m)}}{\rho^{m-1}} = \lim_{\rho \rightarrow 0} \frac{A_{\phi,\alpha}^{(m)}}{\rho^{m-1}}. \end{aligned} \quad (3.29)$$

Finally we can calculate the magnetic field from $\mathbf{B} = \nabla \times \mathbf{A}$

$$\begin{aligned} B_\rho &= \sum_{m=1}^{\infty} \sum_{\ell=0}^{\infty} (-1)^\ell \frac{m!(2\ell+m)}{2^{2\ell}\ell!(\ell+m)!} \left[\Gamma_{m,\alpha}^{[2\ell]}(z) - \frac{E_{m-1}^{[2\ell+1]}}{m} \right] \rho^{2\ell+m-1} \begin{Bmatrix} -\sin m\phi \\ \cos m\phi \end{Bmatrix} \\ B_\phi &= -\sum_{m=1}^{\infty} \sum_{\ell=0}^{\infty} \frac{(-1)^\ell m!}{2^{2\ell}\ell!(\ell+m)!} \left[\Gamma_{m,\alpha}^{[2\ell]}(z) - \frac{E_{m-1}^{[2\ell+1]}}{m} \right] \rho^{2\ell+m-1} \begin{Bmatrix} \cos m\phi \\ -\sin m\phi \end{Bmatrix}. \\ B_z &= \sum_{m=1}^{\infty} \sum_{\ell=0}^{\infty} \frac{(-1)^\ell m!}{2^{2\ell}\ell!(\ell+m)!} \left[\Gamma_{m,\alpha}^{[2\ell+1]}(z) - \frac{E_{m-1}^{[2\ell+2]}}{m} \right] \rho^{2\ell+m} \begin{Bmatrix} -\sin m\phi \\ \cos m\phi \end{Bmatrix}. \end{aligned}$$

Comparison with Eq.'s (3.10) shows that the relationships between the generalized gradients and the functions $\Gamma_{m,\alpha}$ and $E_{m-1,\alpha}$ are given by

$$\begin{aligned} C_{m,s}(z) &= \Gamma_{m,s}(z) + \frac{1}{m} E'_{m-1,s}(z), \\ C_{m,c}(z) &= -\left[\Gamma_{m,c}(z) + \frac{1}{m} E'_{m-1,c}(z) \right]. \end{aligned} \quad (3.30)$$

Another way to obtain the same result is to start with an ansatz for the vector potential already in the form of a power series in ρ . This calculation is outlined in Appendix A.

3.4 Calculation of Generalized Gradients from Numerical Field Data

Given a current free bounded region in space, what is the minimum knowledge required to determine uniquely the magnetic field within that region? Consider the specific example of an infinitely long cylinder of radius R , which will be the case of interest in the following. We know the magnetic field can be expressed in terms of a scalar potential obeying the Laplace equation. The solutions of

Laplace equation are uniquely determined by either the boundary value of the potential itself (Dirichlet condition) or its derivative along the normal to the boundary (Neuman condition). In cylindrical variables one of the components of the magnetic field evaluated on the cylindrical surface suffices to determine the full magnetic field within the cylinder. We can easily convince ourselves that this is the case: the radial component already represents the normal derivative of the potential. On the other hand, the two equations

$$\frac{\partial}{\partial z}\psi = B_z(\rho = R, \phi, z), \quad \frac{\partial}{\partial \phi}\psi = B_\phi(\rho = R, \phi, z). \quad (3.31)$$

can be readily integrated to get the potential on the boundary from B_z and B_ϕ respectively.

Assume one of the components of the magnetic field is known on the surface of the cylinder

$$B_i(\rho = R, \phi, z) = \sum_{m=0}^{\infty} B_m(R, z) \sin(m\phi) + A_m(R, z) \cos(m\phi) \quad (3.32)$$

where the subscript i can be one of ρ, ϕ, z , and let us consider separately the three cases. In practical applications the choice of the most suitable component to use will depend on the dominant multipole term in the field.

3.4.1 B_ρ Known

Suppose the radial component B_ρ is known on a cylindrical surface of radius R . First we calculate $B_\rho = \frac{\partial}{\partial \rho}\psi$ from (3.2), (3.3), (3.4) and then we compare the resulting expression with (3.32) to get

$$a_m(k) = \frac{1}{\sqrt{2\pi}} \int_{-\infty}^{\infty} e^{-ikz} \frac{A_m(R, z)}{k I'_m(kR)} dz. \quad (3.33)$$

$$b_m(k) = \frac{1}{\sqrt{2\pi}} \int_{-\infty}^{\infty} e^{-ikz} \frac{\mathcal{B}_m(R, z)}{k I'_m(kR)} dz. \quad (3.34)$$

The two expressions for $a_m(k)$ and $b_m(k)$ can then be inserted into the integrals defining the generalized gradients (3.7), (3.8). The final expressions involve two integrations, one in z and the other in k . It is a matter of choice which one is to be carried out first. If the integration over z is carried out first we get:

$$C_{m,s}(z) = \frac{1}{2^m m!} \frac{1}{\sqrt{2\pi}} \int_{-\infty}^{\infty} dk e^{ikz} \frac{k^{m-1}}{I'_m(kR)} \tilde{\mathcal{B}}_m(R, k). \quad (3.35)$$

$$C_{m,c}(z) = \frac{1}{2^m m!} \frac{1}{\sqrt{2\pi}} \int_{-\infty}^{\infty} dk e^{ikz} \frac{k^{m-1}}{I'_m(kR)} \tilde{\mathcal{A}}_m(R, k). \quad (3.36)$$

Here $\tilde{\mathcal{B}}_m(R, k)$ and $\tilde{\mathcal{A}}_m(R, k)$ are the Fourier transforms of $\mathcal{B}_m(R, k)$ and $\mathcal{A}_m(R, k)$

$$\tilde{\mathcal{B}}_m(R, k) = \frac{1}{\sqrt{2\pi}} \int_{-\infty}^{\infty} dz e^{-ikz} \mathcal{B}_m(R, z). \quad (3.37)$$

$$\tilde{\mathcal{A}}_m(R, k) = \frac{1}{\sqrt{2\pi}} \int_{-\infty}^{\infty} dz e^{-ikz} \mathcal{A}_m(R, z). \quad (3.38)$$

In the case where the magnetic field is produced by an iron dominated magnet, and is therefore localized in space, the integrals (3.37), (3.38) can be considered to have, in practice, finite limits of integration. With some care, an effective cut-off can also be found even if the fields extend to infinity since they fall off sufficiently rapidly at infinity. Also, since the generalized Bessel function $I'_m(x)$ increases exponentially for large $|x|$, there is also, in effect, a cut-off in k for the integrals (3.35), (3.36) defining the generalized gradients.

Alternatively, if in the integral expression for the generalized gradients the integration over k is carried out before the integration over z , we can write,

$$C_{m,c}(z) = \frac{1}{2^m m!} \int_{-\infty}^{\infty} dz' \mathcal{A}_m(R, z') G(R, z - z'). \quad (3.39)$$

$$C_{m,s}(z) = \frac{1}{2^m m!} \int_{-\infty}^{\infty} dz' \mathcal{B}_m(R, z) G(R, z - z'), \quad (3.40)$$

where the function $G(R, z - z')$ is defined by

$$G(R, z - z') = \frac{1}{2\pi} \int_{-\infty}^{\infty} dk \frac{k^{m-1}}{I'_m(kR)} e^{ik(z-z')}.$$
 \quad (3.41)

For $\zeta = z - z' \neq 0$ the function above can be converted into a series involving the zeros $q_{m,n}$ of the derivative of the Bessel function $J'_m(x)$ using the calculus of residues.

$$G_m(R, \zeta) = \frac{(-1)^{m+1}}{R^m} \sum_{n=1} \frac{q_{m,n}^{m-1}}{J''_m(q_{m,n})} e^{-q_{m,n}|\zeta|/R}.$$
 \quad (3.42)

3.4.2 B_z Known

The calculation when B_z is known on the surface of a cylinder of radius R , can be carried out along the same lines as above. After calculating $B_z = \frac{\partial}{\partial z} \psi$ from (3.2) and comparing with (3.32), we get:

$$a_m(k) = \frac{-i}{\sqrt{2\pi}} \int_{-\infty}^{\infty} e^{-ikz} \frac{\mathcal{A}_m(R, z)}{k I_m(kR)} dz,$$
 \quad (3.43)

$$b_m(k) = \frac{-i}{\sqrt{2\pi}} \int_{-\infty}^{\infty} e^{-ikz} \frac{\mathcal{B}_m(R, z)}{k I_m(kR)} dz,$$
 \quad (3.44)

and therefore:

$$C_{m,s}(z) = \frac{-i}{2^m m!} \frac{1}{\sqrt{2\pi}} \int_{-\infty}^{\infty} dk e^{ikz} \frac{k^{m-1}}{I_m(kR)} \tilde{\mathcal{B}}_m(R, k).$$
 \quad (3.45)

$$C_{m,c}(z) = \frac{-i}{2^m m!} \frac{1}{\sqrt{2\pi}} \int_{-\infty}^{\infty} dk e^{ikz} \frac{k^{m-1}}{I_m(kR)} \tilde{\mathcal{A}}_m(R, k).$$
 \quad (3.46)

Here $\tilde{\mathcal{B}}_m(R, k)$ and $\tilde{\mathcal{A}}_m(R, k)$ are the Fourier transforms of $\mathcal{B}_m(R, k)$ and $\mathcal{A}_m(R, k)$.

Notice that the kernel $\frac{k^{m-1}}{I_m(kR)}$ in the integrals above has the unpleasant feature of being singular at $k = 0$, since for small k , $I_m(kR) \simeq (kR)^m$. Although this

may not compromise the convergence of the integrals it can pose some difficulties if we attempt to perform the integrals numerically. For this reason using the field data of B_ρ may be preferable to those of B_z . However, in the case of a solenoidal field, $m = 0$, the B_z would be the natural choice since it is the dominant component. In this case there is a way to go around the singularity.

First of all we have to recall that for the purpose of map computation only the expression for the vector potential matters. If we are interested only in a solenoid field, as pointed out earlier in this chapter the natural choice for the gauge is $A_\rho = 0$ [see (3.15),(3.16)]; in which case only the A_ϕ component is nonvanishing. Then notice A_ϕ does not depend directly on the generalized gradients but only on their derivatives with respect to z . Finally we observe that when the derivative with respect to z of the generalized gradients $C_{m,s}(z)$ is taken in Eqs. (3.46) the integrand gets an extra power in k that cancels the singularity.

Alternatively we can write

$$C_{m,c}(z) = \frac{-i}{2^m(m+1)!} \int_{-\infty}^{\infty} dz' \mathcal{A}_m(R, z) G(R, z - z'). \quad (3.47)$$

$$C_{m,s}(z) = \frac{-i}{2^m(m+1)!} \int_{-\infty}^{\infty} dz' \mathcal{B}_m(R, z) G(R, z - z'). \quad (3.48)$$

where

$$G(R, z - z') = \frac{1}{2\pi} \int_{-\infty}^{\infty} dk \frac{k^{m-1}}{I_m(kR)} e^{ik(z-z')}. \quad (3.49)$$

Notice that the function $G(R, z - z')$ is purely imaginary and odd in the argument $\zeta = z - z'$. For $\zeta > 0$ it can be cast into the following form using the residue calculus:

$$G_m(R, \zeta) = i \frac{2^{m-1} m!}{R^m} + i \sum_{n=1} (-1)^{m+1} \frac{p_{m,n}^{m-1}}{R^m J'_m(p_{m,n})} e^{-p_{m,n}\zeta/R}. \quad (3.50)$$

where $p_{m,n}$ are the zeros of $J_m(x)$.

3.4.3 B_ϕ Known

After calculating $B_\phi = \frac{\partial}{\partial \phi} \psi$ from (3.2) and comparing with (3.32) we get

$$a_m(k) = -\frac{R}{\sqrt{2\pi}} \int_{-\infty}^{\infty} e^{-ikz} \frac{\mathcal{B}_m(R, z)}{m I_m(kR)} dz. \quad (3.51)$$

$$b_m(k) = \frac{R}{\sqrt{2\pi}} \int_{-\infty}^{\infty} e^{-ikz} \frac{\mathcal{A}_m(R, z)}{m I_m(kR)} dz, \quad (3.52)$$

and therefore

$$C_{m,s}(z) = \frac{-1}{2^m(m+1)!} \frac{1}{\sqrt{2\pi}} \int_{-\infty}^{\infty} dk e^{ikz} \frac{k^m}{I_m(kR)} \tilde{\mathcal{A}}_m(R, k). \quad (3.53)$$

$$C_{m,c}(z) = \frac{1}{2^m(m+1)!} \frac{1}{\sqrt{2\pi}} \int_{-\infty}^{\infty} dk e^{ikz} \frac{k^m}{I_m(kR)} \tilde{\mathcal{B}}_m(R, k). \quad (3.54)$$

Here $\tilde{\mathcal{B}}_m(R, k)$ and $\tilde{\mathcal{A}}_m(R, k)$ are the Fourier transforms of $\mathcal{B}_m(R, k)$ and $\mathcal{A}_m(R, k)$ as defined in (3.37) and (3.38).

The asymptotic behavior of the kernel is similar to the one that appears in the case of B_ρ . However, because of the presence of an extra power of k , the approach to the asymptotic behavior is slower. For this reason it may be preferable to deal with B_ρ data rather than to use B_ϕ data.

Alternatively we can write

$$C_{m,c}(z) = \frac{-1}{2^m m!} \int_{-\infty}^{\infty} dz' \mathcal{A}_m G(R, z - z'). \quad (3.55)$$

$$C_{m,s}(z) = \frac{1}{2^m m!} \int_{-\infty}^{\infty} dz' \mathcal{B}_m G(R, z - z'). \quad (3.56)$$

where

$$G(R, z - z') = \frac{1}{2\pi} \int_{-\infty}^{\infty} dk \frac{k^m}{m I_m(kR)} e^{ik(z-z')}. \quad (3.57)$$

3.4.4 Scalar Potential Known

Some electromagnetic codes calculate the scalar scalar potential directly. Suppose the scalar potential is known on the surface of a cylinder of radius R in terms of the Fourier series

$$\psi(\rho = R, \phi, z) = \sum_{m=0}^{\infty} \Psi_{m,s}(R, z) \sin(m\phi) + \Psi_{m,c}(R, z) \cos(m\phi). \quad (3.58)$$

In this case the expressions for the generalized gradients read

$$C_{m,s}(z) = \frac{1}{2^m m!} \frac{1}{\sqrt{2\pi}} \int_{-\infty}^{\infty} dk e^{ikz} \frac{k^m}{I_m(kR)} \tilde{\Psi}_{m,s}(R, k), \quad (3.59)$$

$$C_{m,c}(z) = \frac{1}{2^m m!} \frac{1}{\sqrt{2\pi}} \int_{-\infty}^{\infty} dk e^{ikz} \frac{k^m}{I_m(kR)} \tilde{\Psi}_{m,c}(R, k). \quad (3.60)$$

Here $\tilde{\Psi}_{m,\alpha}(R, k)$ is the Fourier transform of the coefficients in the Fourier series ($\alpha = c, s$):

$$\tilde{\Psi}_{m,\alpha}(R, k) = \frac{1}{\sqrt{2\pi}} \int_{-\infty}^{\infty} dz e^{-ikz} \Psi_{m,\alpha}(R, z). \quad (3.61)$$

3.5 Calculation of Generalized Gradients from Field Measurements

The most widely used and accurate method to measure the magnetic field in magnets for beam optics relies on spinning coils [18]. Here, we will indicate a possible use of the spinning coils suitable for determining generalized gradients.

In most cases spinning coils are used to measure the integrated field harmonics or multipoles, which is customary to assume as a figure of merit for the magnetic field quality. To this end and in an ideal situation, the length of a spinning coil should be longer than the magnet length so that the measurement captures the total z -integrated harmonics.

Shorter length spinning coils can be used to measure the integrated harmonics originating from the magnet ends. In this case care is usually taken in order for the coil length to be long enough so that the two ends of the coil are in regions where the fields are no longer z -dependent (i.e. one end is in the body and the other is well out of the magnet where the fields are negligible).

By using the spinning coil in this way (which we can refer to as ‘single location’ spinning coil measurement) the information about the details of the z -dependence of the field in the fringe region gets lost since only the integrated harmonics contribute to the measurement. In order to access the information related to the z -dependence of the field harmonics one has to resort to non-rectangular spinning coils. Lee-Whiting [44, 18], for example, proposed the use of triangular shaped coils to measure directly some form factors that enter in the expression for the transfer matrix. This method, however, does not allow one to calculate all the nonlinear aberrations.

A way to recover the z -dependence of the field harmonics is to make repeated measurement by moving the spinning coil by small steps (let us say, of length Δ_z) along the magnet axis. We can call this procedure a ‘multiple location’ spinning coil measurement. In the way this kind of measurement is usually done, one extremity of the coil spans the z -varying field region while the other extremity should lie far enough from the magnet end region where the fields are z -independent (it could be either in the body or outside the magnet). Again, this sets a constraint on the minimum length of the spinning coil to be used. One can get the desired information about the z -dependence of the field harmonics by differencing the e.m.f signals from the spinning coil positioned at the various locations. Conceptually, the method is equivalent to using a tiny spinning coil

of length equal to the step Δ_z .

As far as we know, it has never been realized that the same information can be obtained also by using a relatively small size spinning coil, i.e. one with a length somewhere between the length of the varying field region and Δ_z . Use of smaller coils may in certain cases be preferable for the purpose of noise reduction in the measurements.

Also, and most important, it does not seem to have been realized that the information we get in this way, whether by employing a long or a relatively short spinning coil, can be used to recover the *entire* field expansion, including multipoles and pseudo-multipoles.

This section is devoted to deriving the formulas one can use to determine the generalized gradients appearing in the expansion for the magnetic field (scalar potential or vector potential) from measurement done with a spinning coil of arbitrary length.

Consider the case of a rectangular coil rotating in such a way that one side of the coil is always positioned along the magnet axis. As we mentioned, the idea is to make repeated measurements of the field harmonics (integrated over the coil length) by moving the coil along the magnet axis by small steps. The Fourier transforms of the experimental data for each harmonic are then calculated, multiplied by a suitable kernel, and then Fourier transformed back to obtain the desired generalized gradients. Not surprisingly, the kernel acts again as a high frequency filter, displaying the same features as the kernels we have encountered in the previous section, when we dealt with field data on the surface of a cylinder.

For the kind of coil we consider in this section the only relevant component of the magnetic field is B_ϕ because it is the only one generating a flux linked

to the coil. It should be mentioned that tangential coils are also used, in which case the relevant component of the magnetic field is B_ρ . The treatment of that case would follow the same lines as that given for the kind of coils considered here.

The e.m.f. produced by a rectangular spinning coil with barycenter positioned at z is given by

$$\mathcal{E}(z, t) = - \int_{z-l_c}^{z+l_c} dz' \int_0^{R_c} \frac{dB_\phi}{dt} d\rho, \quad (3.62)$$

where $2l_c$ is the length of the coil and R_c is its radius (in a realistic setup if one has a set of n_c identical concentric coils one needs to multiply the quantity below by n_c). The e.m.f. can be written in terms of a Fourier series in time:

$$\mathcal{E}(z, t) = \sum_{m=0} \mathcal{E}_{m,s}(z) \sin(m\omega t) + \mathcal{E}_{m,c}(z) \cos(m\omega t). \quad (3.63)$$

where we assume $\mathcal{E}_{m,s}(z)$ and $\mathcal{E}_{m,c}(z)$ can be experimentally determined over a sufficient number of locations in z in the fringe regions where the field varies with z . The frequency of the spinning coil is ω .

By using (3.2) we can write B_ϕ as

$$B_\phi = \frac{1}{\rho} \frac{\partial \psi}{\partial \phi} = \sum_{m=1}^{\infty} \int_{-\infty}^{\infty} dk e^{ikz} m \frac{I_m(k\rho)}{\rho} [b_m(k) \cos m\phi - a_m(k) \sin m\phi]. \quad (3.64)$$

By substituting (3.64) into (3.62) with $\phi = \omega t$ we get

$$\mathcal{E}(z) = \frac{\omega}{\sqrt{2\pi}} \sum_{m=1}^{\infty} \int_{-\infty}^{\infty} dk e^{ikz} \frac{2m^2 \sin kl_c}{k} [b_m(k) \sin m\omega t + a_m(k) \cos m\omega t]. \quad (3.65)$$

Then, by comparison between (3.65) and (3.63) we find

$$\mathcal{E}_{m,c}(z) = \frac{m^2 \omega}{\sqrt{2\pi}} \int_{-\infty}^{\infty} dk e^{ikz} \mathcal{I}_m(kR_c) \frac{2 \sin kl_c}{k} b_m(k), \quad (3.66)$$

$$\mathcal{E}_{m,s}(z) = \frac{m^2 \omega}{\sqrt{2\pi}} \int_{-\infty}^{\infty} dk e^{ikz} \mathcal{I}_m(kR_c) \frac{2 \sin kl_c}{k} a_m(k). \quad (3.67)$$

Here we have defined the new function

$$\mathcal{I}_m(kR_c) = \int_0^{R_c} \frac{I_m(k\rho)}{\rho} d\rho = \int_0^{kR_c} \frac{I_m(x)}{x} dx. \quad (3.68)$$

We shall come back to commenting on $\mathcal{I}_m(kR_c)$ in a moment.

Finally use of Eq.'s (3.7) and (3.8) allows us to write the expression for the generalized gradients.

$$C_{m,\alpha}(z) = \frac{1}{2^{m+1} m! m^2 \omega} \frac{1}{\sqrt{2\pi}} \int_{-\infty}^{\infty} dk e^{ikz} \frac{k^{m+1} \tilde{\mathcal{E}}_{m,\alpha}(k)}{\mathcal{I}_m(kR_c) \sin kl_c}. \quad (3.69)$$

where $\alpha = s, c$ as usual, and the $\tilde{\mathcal{E}}_{m,\alpha}(k)$ are the Fourier transforms of the experimental data,

$$\tilde{\mathcal{E}}_{m,\alpha}(k) = \frac{1}{\sqrt{2\pi}} \int_{-\infty}^{\infty} dz e^{-ikz} \mathcal{E}_{m,\alpha}(z). \quad (3.70)$$

Notice that because of the asymptotic form of the Bessel function I_m , as $k \rightarrow \infty$ the function $\mathcal{I}_m(kR_c)$ diverges exponentially, $\mathcal{I}_m(kR_c) \sim e^{kR_c}/\sqrt{k}$. Because the function $\mathcal{I}_m(kR_c)$ is in the denominator of the integrand in (3.70), for practical computation the integral in (3.70) can actually be carried out over a finite interval $[-k_{max}, k_{max}]$. In most cases $k_{max} R_c \simeq 20$ should be adequate.

The integral on the RHS of (3.68) for a general m cannot be carried out analytically but can be easily reduced to an infinite series either in the Bessel functions or, most conveniently, directly in kR_c :

$$\mathcal{I}_m(kR_c) = \frac{1}{kR_c} \frac{2}{m} \sum_{n=0}^{\infty} (-1)^n (m+2n+1) I_{m+2n+1}(kR_c) \quad (3.71)$$

$$= \sum_{\ell=0}^{\infty} \frac{1}{(2\ell+m)\ell!(\ell+m)!} \left(\frac{kR_c}{2}\right)^{m+2\ell}. \quad (3.72)$$

In the particular case $m = 2$ we have:

$$\mathcal{I}_2(kR_c) = \frac{I_1(kR_c)}{kR_c} - \frac{1}{2}. \quad (3.73)$$

For numerical purposes use of (3.72) may be perfectly adequate (in particular if speed is not an issue). For $kR_c < 20$, one can obtain values for the function $\mathcal{I}_m(kR_c)$ accurate through 15 digits by retaining the first 30 terms in the series.

We close this section by remarking that the formulas derived above apply also to the case in which the measured e.m.f. \mathcal{E} , is obtained as a difference between the signals obtained by using a long spinning coil moved along the z-axis by the step Δ_z .

Suppose the spinning coil first lies between $z = z_1$ and $z = z_2$. Let us say z_2 lies in the magnet-end region and z_1 lies in the magnet body or outside the magnet. Assume that the measured e.m.f. is \mathcal{E}_I . Then we move the coil by a small step Δ_z so that the spinning coil now lies in $[z_1 + \Delta_z, z_2 + \Delta_z]$, giving a signal \mathcal{E}_{II} . The two quantities can be written as the sum of two contributions:

$$\mathcal{E}_I = \mathcal{E}^{[z_1, z_1 + \Delta_z]} + \mathcal{E}^{[z_1 + \Delta_z, z_2]}, \quad (3.74)$$

$$\mathcal{E}_{II} = \mathcal{E}^{[z_1 + \Delta_z, z_2]} + \mathcal{E}^{[z_2, z_2 + \Delta_z]}. \quad (3.75)$$

where $\mathcal{E}^{[z_1, z_1 + \Delta_z]}$ is the contribution coming from the section of the spinning coil contained in $[z_1, z_1 + \Delta_z]$ and so on. Clearly

$$\mathcal{E}^{[z_2, z_2 + \Delta_z]} = \mathcal{E}_{II} - \mathcal{E}_I + \mathcal{E}^{[z_1, z_1 + \Delta_z]}. \quad (3.76)$$

If the side of the spinning coil at $z = z_1$ is in a vanishing field region then $\mathcal{E}^{[z_1, z_1 + \Delta_z]} = 0$ and we have simply $\mathcal{E}^{[z_2, z_2 + \Delta_z]} = \mathcal{E}_{II} - \mathcal{E}_I$. Otherwise, if $z = z_1$ is in the body of the magnet we have to evaluate $\mathcal{E}^{[z_1, z_1 + \Delta_z]}$. This is easily done if in the body of the magnet the fields can assumed to be z-independent. Under this assumption the magnetic field is simply

$$B_\phi = \sum_{m=1} m\rho^{m-1} (C_{m,s} \cos m\phi - C_{m,c} \sin m\phi), \quad (3.77)$$

and therefore, see (3.62),

$$\mathcal{E}_{m,\alpha}^{[z_1, z_1 + \Delta_z]} = \omega m \Delta_z C_{m,\alpha} R_c^m. \quad (3.78)$$

Here the generalized gradient $C_{m,\alpha}$, which is constant, can be obtained by a separate spinning coil measurement carried out in the body of the magnet.

The quantity $\mathcal{E}_{m,\alpha}(z) = \mathcal{E}_{m,\alpha}^{[z_2, z_2 + \Delta_z]}$, with $z = z_2 + \Delta_z/2$, obtained by measurement for various z_2 can then be Fourier transformed and used in equation (3.69) to get the z -dependent generalized gradients (with $l_c = \Delta_z/2$).

3.6 Insensitivity to Errors

In practical situations the magnetic field data, whether they come from measurements or from numerical computations, are unavoidably affected by errors. What effect do these errors have on the determination of the generalized on-axis gradients and their derivatives? We will see that the effect is relatively mild. This relative insensitivity to errors arises from a basic property of solutions to Laplace's equation: the value of ψ at some interior point is an appropriately weighted average of its values over any surrounding boundary. Consequently, ψ is smoother in the interior of a region than it may be on a boundary of this region. Correspondingly, errors in boundary values are averaged.

For example, suppose $\mathcal{B}_m(R, z)$ and $\mathcal{A}_m(R, z)$ in (3.32) are absolutely integrable.

$$\int_{-\infty}^{\infty} dz |\mathcal{B}_m(R, z)| < \infty, \text{ etc.} \quad (3.79)$$

This will certainly be the case if $\mathcal{B}_m(R, z)$ and $\mathcal{A}_m(R, z)$ are localized in z space.

It follows that the Fourier transforms $\check{\mathcal{B}}_m(R, k)$, $\check{\mathcal{A}}_m(R, k)$ are then bounded.

$$|\check{\mathcal{B}}_m(R, k)| < \int_{-\infty}^{\infty} dz |\mathcal{B}_m(R, z)| < \infty, \text{ etc.} \quad (3.80)$$

Now, for example, look at the integral representations (3.35) and (3.36) for the generalized gradients. We see that, due to the bounds (4.2) and the fall off in k at infinity produced by the $I'_m(kR)$ denominators, the integrals (3.2) and (3.3) are absolutely convergent in the domain

$$\operatorname{Re}(z) \in (-\infty, \infty), \operatorname{Im}(z) \in (-R, R). \quad (3.81)$$

Thus, under very mild assumptions about the surface data $B_\rho(\rho = R, \phi, z)$, including the possibility of errors, we conclude that the generalized gradients are *analytic* in the strip (3.81).

3.7 Numerical Tests

The method described in this Chapter has been implemented in the code MARYLIE 5.0 [23] as a user-defined routine. The routine reads from an external file the harmonics for the radial component of the magnetic field $\mathcal{A}_m(R, z)$ and $\mathcal{B}_m(R, z)$ see (3.32) or the scalar potential $\Psi_{m,s}(R, z)$ and $\Psi_{m,c}(R, z)$ see (3.58), evaluated on a discrete set of points z_i . It then generates the corresponding transfer map by using the built-in routine GENMAP to integrate the map equations. Since MARYLIE 5.0 is a 5th order code, only the multipoles through $m = 6$ need be considered.

The Fourier transforms (3.37) and (3.38) are calculated from the read-in values of $\mathcal{A}_m(R, z)$ and $\mathcal{B}_m(R, z)$ using Filon's method [5, 67] for various values of k in the interval $[-k_{max}, k_{max}]$ where k_{max} is a suitable k cut-off for the integrals

(3.36) and (3.35). For the cases described below, we have used the value $Rk_{max} = 20$. Filon's method requires interpolation of the functions $\mathcal{A}_m(R, z)$ and $\mathcal{B}_m(R, z)$ (or $\Psi_{m,s}(R, z)$ and $\Psi_{m,c}(R, z)$); and for this purpose we use local parabolic fits.

The integration algorithm of GENMAP is based on a 11th order multistep (Adams) method. Because the algorithm uses a fixed step size, one needs to provide values of the generalized gradients and their derivatives only at the predetermined locations in z required by GENMAP. The integrals (3.36) and (3.35) that provide the generalized on-axis gradients and their derivations are evaluated at the values of z needed by GENMAP, again using Filon's method. We emphasize that no interpolation of the generalized gradients is required by GENMAP.

We have tested the routine by treating the case of a Lambertson quadrupole as discussed in Chapter 4. For this case only $\mathcal{B}_2(R, z)$ and $\mathcal{B}_6(R, z)$ are nonzero. Correspondingly only the functions $C_{2,s}^{[0]}$, $C_{2,s}^{[1]}$, $C_{2,s}^{[2]}$, $C_{2,s}^{[3]}$, $C_{2,s}^{[4]}$, and $C_{6,s}^{[0]}$ are required. The use of this case as an example has the virtue that the various C functions can be found exactly.

Also, the surface data $B_\rho(\rho = R, \phi, z)$ can be found directly using the Biot-Savart law, and this data can be integrated over ϕ to yield $\mathcal{B}_2(R, z)$ and $\mathcal{B}_6(R, z)$. In our test we evaluated $B_\rho(\rho = R, \phi, z)$ for 279 equally spaced z values within the interval

$$z \in [z_{min}, z_{max}] = [-7r, 7r] \quad (3.82)$$

according to the rule

$$z_i = z_{min} + \Delta(i - 1) \text{ for } i = 1, 2, \dots, 279. \quad (3.83)$$

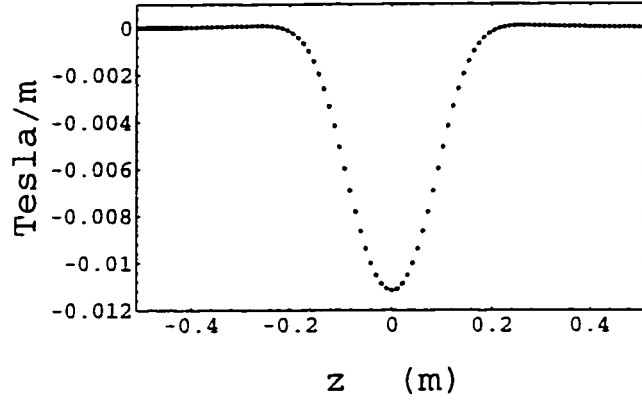


Figure 3.1: The function $C_{2,s}^{[0]}$ as calculated numerically from the surface data (dots) and analytically (solid line).

The cylinder on which we evaluated B_ρ had the radius

$$R = .75r. \quad (3.84)$$

Here $r = .128$ m is the radius of the quadrupole itself, and the length of the quadrupole is $2r$. Corresponding, $\Delta = 14r/278 = 6.44$ mm. The relatively large values of z_{min} and z_{max} were necessary because the large radius-to-length ratio of the quadrupole makes the fringe fields very extended.

For each z value the quantity $B_\rho(\rho = R, \phi, z)$ was evaluated for 256 equally spaced angles over the interval $[0, 2\pi]$, and these B_ρ values were used to compute the integrals

$$\mathcal{A}_m(R, z) = \frac{1}{\pi} \int_0^{2\pi} d\phi \cos(m\phi) B_\rho(\rho = R, \phi, z). \quad (3.85)$$

$$\mathcal{B}_m(R, z) = \frac{1}{\pi} \int_0^{2\pi} d\phi \sin(m\phi) B_\rho(\rho = R, \phi, z). \quad (3.86)$$

Because of the symmetries of a (normal) quadrupole only the functions b_2 and b_6 are non vanishing for $m \leq 6$. The net results of the steps just described are the values of these functions at the points (3.83).

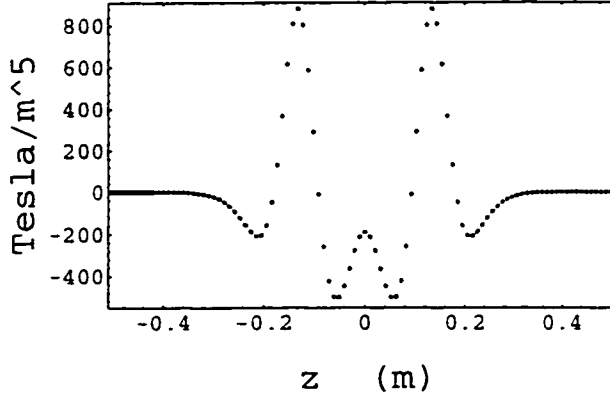


Figure 3.2: The function $C_{2,s}^{[4]}$ as calculated numerically from the surface data (dots) and analytically (solid line).

Figure Fig. 3.1 and Fig. 3.2 show a comparison between the functions $C_{2,s}^{[0]}$ and $C_{2,s}^{[4]}$ respectively, as computed analytically (solid lines) and using the numerical procedure we have outlined. One can see the agreement is very good.

Finally we compared the transfer maps for our Lambertson quadrupole obtained using either the analytically known on-axis gradients or on-axis gradients computed numerically from surface data. Table 3.1 shows that the (relative) difference in the surface-data-based map, as compared to the exact map, is very small. Of course, apart from numerical roundoff problems, we expect this difference will vanish as the number of sampling points in z and ϕ is made arbitrarily large.

Table 3.1: Relative difference between the surface-data-based map and the exact map.

map generators	relative difference
\mathcal{R}_2	$< 10^{-6}$
f_3, f_4	$< 10^{-5}$
f_5, f_6	$< 10^{-4}$

After verifying that the method works, we studied the sensitivity of transfer map calculations to the presence of random errors (noise) in the surface data. As a simple model, consider the perturbed functions

$$\mathcal{B}_2^{rnd}(R, z_i) = \mathcal{B}_2(R, z_i)[1 + \epsilon_2(z_i)], \quad (3.87)$$

$$\mathcal{B}_6^{rnd}(R, z_i) = \mathcal{B}_6(R, z_i)[1 + \epsilon_6(z_i)], \quad (3.88)$$

where the $\epsilon_2(z_i), \epsilon_6(z_i)$ are random variables uniformly distributed in the interval $[-\epsilon/2, \epsilon/2]$, and $\mathcal{B}_2(R, z_i), \mathcal{B}_6(R, z_i)$ are the same as before. What effect do these errors have on the on-axis gradients computed from the (noisy) surface data? If we set $\epsilon = 10^{-2}$, in the computationally worst case. that of $C_{2,s}^{[4]}$, comparison between the analytic results and results computed numerically from the noisy surface data shows deviations on the order of 1% or less. (which is comparable with $\epsilon = 10^{-2}$).

We obtain similar deviations for the map generators. Table 3.2 shows that the (relative) error in the noisy surface data based map (as compared to the exact map) is, at worst, on the order of the noise.

Table 3.2: Relative error of the noisy surface-data-based map compared to the exact map.

map generators	seed #1	seed#2	seed#3
\mathcal{R}_2	$< 3 \times 10^{-4}$	$< 8 \times 10^{-4}$	$< 5 \times 10^{-4}$
f_3, f_4	$< 10^{-3}$	$< 1.6 \times 10^{-3}$	$< 1.6 \times 10^{-3}$
f_5, f_6	$< 10^{-2}$	$< 1.5 \times 10^{-2}$	$< 1.3 \times 10^{-2}$

Chapter 4

Design of Current Sheet Magnets

In certain applications one is interested in iron-free current sheet magnets. Magnets of this kind built using printed circuits, for example, are planned to be used in the Maryland Electron Ring (see Chapter 5). The main advantage of this kind of low field magnets is the cost, which is far less than for iron dominated magnets. They are also interesting from a theoretical view point because they allow an accurate modeling of the magnetic field.

The purpose of this Chapter is to present some general considerations for the design of such magnets. We will start by mentioning in the first Section the possibility of designing magnets with a current configuration that realizes pure multipoles. Such a possibility has been recently pointed out by various authors [25, 68, 69, 8].

In the next Section we will show how it is possible to design magnets with arbitrary cross section that result in pure multipoles in an integrated sense. The derivation generalizes the magnet design first introduced by Lambertson [6] for magnets with cylindrical cross section. We then briefly review Lambertson's design for cylindrical cross section magnets since such a design has been adopted

for the Maryland E-Ring magnets (see Chapter 5). And finally we will consider the design of current sheet magnets with rectangular aperture which are also planned to be used in the Maryland Electron Ring at the intersection with the injection and extraction lines.

4.1 Pure Multipole Magnets

An interesting problem is to find a current configuration that produces a pure multipole magnetic field. In a steady state situation the current density must be divergenceless $\nabla \cdot \mathbf{J} = 0$. Such a condition is automatically satisfied if we express the current density in terms of a pseudo-magnetization \mathbf{M} with $\mathbf{J} = \nabla \times \mathbf{M}$. If we write the pseudo-magnetization as

$$M_\rho = \Psi_\rho(\rho, z) \begin{Bmatrix} \sin m\phi \\ \cos m\phi \end{Bmatrix}, \quad (4.1)$$

$$M_\phi = \Psi_\phi(\rho, z) \begin{Bmatrix} \cos m\phi \\ \sin m\phi \end{Bmatrix}, \quad (4.2)$$

$$M_z = \Psi_z(\rho, z) \begin{Bmatrix} \sin m\phi \\ \cos m\phi \end{Bmatrix}. \quad (4.3)$$

where the Ψ_ρ , Ψ_ϕ , Ψ_z are arbitrary differentiable functions, it is evident that the corresponding current distribution produces a pure multipole field. (The upper choice for the trigonometric function in (4.3) will generate a normal field, the lower choice a skew field). This can be shown by using the integral formula ¹ for

¹Use of these formulas automatically casts the vector potential into the Coulomb gauge.

the vector potential in *cylindrical variables* :

$$A_z = \frac{1}{c} \int \frac{J_z}{|\mathbf{x} - \mathbf{x}'|} d^3 \mathbf{x}', \quad (4.4)$$

$$A_\rho = \frac{1}{c} \int \frac{J_\rho \cos(\phi - \phi') + J_\phi \sin(\phi - \phi')}{|\mathbf{x} - \mathbf{x}'|} d^3 \mathbf{x}'. \quad (4.5)$$

$$A_\phi = \frac{1}{c} \int \frac{-J_\rho \sin(\phi - \phi') + J_\phi \cos(\phi - \phi')}{|\mathbf{x} - \mathbf{x}'|} d^3 \mathbf{x}'. \quad (4.6)$$

(The formulas above are in CGS; to convert them in MKS one has to make the change $1/c \rightarrow \mu_0/(4\pi)$). We first use the magnetization \mathbf{M} to derive the following current density

$$\begin{aligned} J_\rho &= \frac{m}{\rho} \Psi_z \begin{Bmatrix} \cos m\phi \\ -\sin m\phi \end{Bmatrix} - \frac{\partial \Psi_\phi}{\partial z} \begin{Bmatrix} \cos m\phi \\ \sin m\phi \end{Bmatrix}, \\ J_\phi &= \left(\frac{\partial \Psi_\rho}{\partial z} - \frac{\partial \Psi_z}{\partial \rho} \right) \begin{Bmatrix} \sin m\phi \\ \cos m\phi \end{Bmatrix}, \\ J_z &= \frac{1}{\rho} \frac{\partial}{\partial \rho} (\rho \Psi_\phi) \begin{Bmatrix} \cos m\phi \\ \sin m\phi \end{Bmatrix} - \frac{m \Psi_\rho}{\rho} \begin{Bmatrix} \cos m\phi \\ -\sin m\phi \end{Bmatrix}. \end{aligned} \quad (4.7)$$

Next we insert the above expressions for the current density into (4.4) through (4.6). In carrying out the integrals we use the expansion of $1/|\mathbf{x} - \mathbf{x}'|$ reported (B.1) and we isolate the integration over the angle to find a result that is consistent with the expression for a multipole of order m shown in Chapter 3.

In the remaining part of this section we will carry out in some detail the calculation for the particular case where $\Psi_\phi(\rho, z) = \Psi_z(\rho, z) = 0$ and

$$\Psi_\rho(\rho, z) = \Psi(z) \delta(\rho - a). \quad (4.8)$$

Equation (4.8) describes a cylindrical sheet current of radius a and was first used for the purpose of fringe field modeling by [68, 69]. Such a current distribution

can also be used to build physical magnets: in this case the function $\Psi(z)$ will be nonvanishing only over an interval of length $2l$, equal to the magnet length. The function $\Psi(z)$ can be viewed as a stream function. For the case of normal multipoles the current lines on the surface of the cylinder are solutions of the equation:

$$\Psi(z) \cos m\phi = \text{const.} \quad (4.9)$$

[Skew multipoles are obtained by rotating the current configuration by $\pi/(2m)$].

The corresponding current distribution is given by $J_\rho = 0$ and

$$\begin{aligned} J_\phi &= -\frac{m}{\rho} \Psi(z) \begin{Bmatrix} \sin m\phi \\ \cos m\phi \end{Bmatrix} \delta(\rho - a), \\ J_z &= \frac{\partial \Psi(z)}{\partial z} \begin{Bmatrix} \cos m\phi \\ -\sin m\phi \end{Bmatrix} \delta(\rho - a). \end{aligned} \quad (4.10)$$

As we noticed in Chapter 3 a multipole of order m is determined by a knowledge of the generalized gradients or, in the Coulomb gauge vector potential framework, by a knowledge of the functions Γ_m and E_{m-1} and their derivatives appearing in the expansions (3.27), (3.28). In the following we show how we can quickly recover the functions Γ_m and E_{m-1} , or the generalized gradients, using the integral expressions (4.4), (4.5). What we have to do is to insert the expressions for the currents into (4.4), (4.5) and use the expansion (B.1) to obtain:

$$\begin{aligned} A_z &= \frac{1}{c} 4m \begin{Bmatrix} \cos m\phi \\ -\sin m\phi \end{Bmatrix} \int_{-\infty}^{\infty} dz' \Psi(z') \int_0^{\infty} \cos[k(z - z')] I_m(k\rho) K_m(ka) dk, \\ A_\rho &= \frac{1}{c} 2a \begin{Bmatrix} \cos m\phi \\ -\sin m\phi \end{Bmatrix} \int_{-\infty}^{\infty} dz' \frac{\partial \Psi(z')}{\partial z'} \times \end{aligned}$$

$$\times \int_0^\infty \cos[k(z - z')][I_{m-1}(k\rho)K_{m-1}(ka) - I_{m+1}(k\rho)K_{m+1}(ka)]dk.$$

Next we use the definitions (3.29) together with the limiting form for the Bessel function

$$\lim_{x \rightarrow 0} I_m(x) = \frac{1}{m!} \left(\frac{x}{2}\right)^m. \quad (4.11)$$

to obtain:

$$\begin{aligned} \Gamma_m &= -\frac{1}{c} \frac{1}{2^{m-2}(m-1)!} \int_{-\infty}^\infty dz' \Psi(z') \int_0^\infty dk \cos[k(z - z')] k^m K_m(ka) \\ &= -\frac{1}{c} \frac{\pi a^m (2m-1)!!}{2^{m-1}(m-1)!} \int_{-\infty}^\infty dz' \frac{\Psi(z')}{[a^2 + (z - z')^2]^{m+\frac{1}{2}}}. \end{aligned} \quad (4.12)$$

and

$$\begin{aligned} E_{m-1} &= \frac{1}{c} \frac{a}{2^{m-2}(m-1)!} \int_{-\infty}^\infty dz' \frac{\partial \Psi(z')}{\partial z'} \int_0^\infty dk \cos[k(z - z')] k^{m-1} K_{m-1}(ka) \\ &= \frac{1}{c} \frac{\pi a^m (2m-3)!!}{2^{m-1}(m-1)!} \int_{-\infty}^\infty dz' \frac{\partial \Psi(z')}{\partial z'} \frac{1}{[a^2 + (z - z')^2]^{m-\frac{1}{2}}}. \end{aligned} \quad (4.13)$$

The formulas used in carrying out the integrals involving the Bessel functions are reported in Appendix B. The generalized gradient can then be obtained from (3.30).

$$C_m = \frac{1}{c} \frac{\pi a^m (2m-1)!!}{2^{m-1}(m-1)!} \int_{-\infty}^\infty dz' \Psi(z') \frac{m(z - z')^2 - (m+1)a^2}{[a^2 + (z - z')^2]^{m+\frac{3}{2}}}. \quad (4.14)$$

The particular case where $\Psi(z)$ is a constant and nonvanishing over a certain interval (i.e. $\Psi(z) = \Psi_o[\mathbf{H}(z - l) - \mathbf{H}(z + l)]$, with \mathbf{H} being the Heaviside step function) is interesting because the above integrals can be expressed in a closed form. In this case

$$\Gamma_m = \frac{\Psi_o}{c} \pi \frac{a^{m-2} (2m-3)!!}{2^{m-1}(m-1)!} g_m(z), \quad (4.15)$$

$$E_{m-1} = \frac{\Psi_o}{c} \pi \frac{a^m (2m-3)!!}{2^{m-1}(m-1)!} f_{m-1}(z), \quad (4.16)$$

where

$$f_{m-1}(z) = F_{m-1}(z + l) - F_{m-1}(z - l). \quad (4.17)$$

$$g_m(z) = G_m(z + l) - G_m(z - l). \quad (4.18)$$

with (see Appendix B)

$$G_m(t) = \frac{t}{(t^2 + a^2)^{\frac{2m-1}{2}}} \left[1 + \sum_{k=1}^{m-1} \frac{2^k(m-1)(m-2)\dots(m-k)}{(2m-3)(2m-5)\dots(2m-2k-1)} \frac{(t^2 + a^2)^k}{a^{2k}} \right]. \quad (4.19)$$

and

$$F(t) = \left(\frac{1}{t^2 + a^2} \right)^{\frac{2m-1}{2}}. \quad (4.20)$$

4.2 2D Current Sheet Magnets with Arbitrary Cross Section

In certain applications one is interested in current sheet distributions that deviate from a circular cross section. In these cases it is not possible in general to achieve a current configuration that results in a pure multipole field. However, one can see that current distributions exist that result in pure multipoles in the *integrated sense*.

It can be easily shown that if we assume $\lim_{z \rightarrow \pm\infty} A_\phi = \lim_{z \rightarrow \pm\infty} A_\rho = 0$. (i.e. the magnetic field sources are localized in space), the z -integrated transverse magnetic field components can be generated by using only the z -integrated A_z component of the vector potential,

$$A_z^{int}(\rho, \phi) = \int_{-\infty}^{\infty} A_z(\rho, \phi, z) dz. \quad (4.21)$$

That is,

$$B_\rho^{int}(\rho, \phi) = \int_{-\infty}^{\infty} B_\rho(\rho, \phi, z) dz = \int_{-\infty}^{\infty} \left(\frac{1}{\rho} \frac{\partial A_z}{\partial \phi} - \frac{A_\phi}{\partial z} \right) dz = \frac{1}{\rho} \frac{\partial A_z^{int}}{\partial \phi}. \quad (4.22)$$

$$B_\phi^{int}(\rho, \phi) = \int_{-\infty}^{\infty} B_\phi(\rho, \phi, z) dz = \int_{-\infty}^{\infty} \left(\frac{\partial A_\rho}{\partial z} - \frac{A_z}{\partial \rho} \right) dz = - \frac{\partial A_z^{int}}{\partial \rho}. \quad (4.23)$$

This is equivalent to saying that only currents pointing in the z -direction provide a net nonvanishing contribution to the integrated transverse magnetic field. Moreover, if no solenoidal component of the magnetic field is present, the component B_z integrates to zero as can be seen by inspecting the last of Eqs. (3.10). Clearly the most general $A_z^{int}(\rho, \phi)$ has the multipole expansion

$$A_z^{int}(\rho, \phi) = \sum_{m=1} [C_{m,c}^{int} \cos(m\phi) + C_{m,s}^{int} \sin(m\phi)] \rho^m. \quad (4.24)$$

We assume that in the x-y plane the current density J_z is non-vanishing only on a 1D closed contour corresponding to a current sheet with arbitrary cross section described in polar variables by the equation (see Fig. 4.1)

$$\rho'(\phi', z') = g(\phi'), \quad (4.25)$$

where g is an arbitrary continuous function, which is differentiable everywhere except on a finite set of points. Then we write $j_z(\phi', z') = J_z(\rho' = g(\phi'), \phi', z')$.

Therefore, the z -integrated A_z component of the vector potential is

$$A_z^{int}(\rho, \phi) = \frac{1}{c} \int_{-\infty}^{\infty} dz \int_0^{2\pi} d\phi' \sqrt{\left(\frac{dg}{d\phi'} \right)^2 + g^2} \int_{-\infty}^{\infty} dz' \frac{j_z(\phi', z')}{|\mathbf{x} - \mathbf{x}'|}. \quad (4.26)$$

The quantity $j_z(\phi', z')$ has the meaning of a current per unit length. In carrying out the integral (4.26) we make use of the expansion (B.1) and we also use $\int dz \cos[k(z - z')] = 2\pi\delta(k)$ to write (for $\rho < \rho'_{min}$, where ρ'_{min} is the minimum distance between the current sheet and the magnet axis),

$$A_z^{int} = \frac{1}{c} \sum_{m=1} \frac{\rho^m}{2m} \int_0^{2\pi} d\phi' \cos[m(\phi - \phi')] \frac{j_z^{int}(\phi')}{g(\phi')^m} \sqrt{\left(\frac{dg}{d\phi'} \right)^2 + g^2}. \quad (4.27)$$

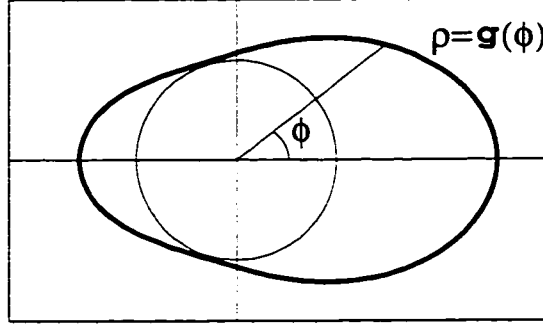


Figure 4.1: Arbitrary cross section for a current sheet magnet. The integrated multipoles vanish within the area spanned by the circle.

where

$$j_z^{int}(\phi') = \int j_z(\phi', z') dz'. \quad (4.28)$$

Consider for simplicity the case where $g(\phi')$ is symmetric with respect to the x axis and let us consider normal multipoles only. If we write the integrated current density $j_z^{int}(\phi')$ as a Fourier series,²

$$j_z^{int}(\phi') = \sum_{n=0} A_n \cos(n\phi'). \quad (4.29)$$

we can write Eq. (4.27) in the form

$$A_z^{int}(\rho, \phi) = \sum_{m=1} \rho^m \cos m\phi \sum_{n=0} M_{m,n} A_n, \quad (4.30)$$

with

$$M_{m,n} = \frac{1}{c} \frac{2}{m} \int_0^{2\pi} d\phi' \cos[m\phi'] \frac{\cos(n\phi')}{g(\phi')^m} \sqrt{\left(\frac{dg}{d\phi'}\right)^2 + g^2}. \quad (4.31)$$

One gets a pure multipole of order \bar{m} in the integrated sense if

$$\sum_{n=0} M_{m,n} A_n = P_{\bar{m}} \delta_{m,\bar{m}} \quad (4.32)$$

²We did not include the $\sin(n\phi)$ terms in the Fourier series, which would lead to skew components of the field.

with $P_{\bar{m}}$ being the strength of the desired integrated multipole of order \bar{m} . In practical calculations one can only make the integrated multipoles vanish through a certain max order $m = m_{max}$. To this end at least $n_{max} = m_{max}$ terms A_n in the Fourier expansion (4.29) are necessary in order to solve the linear problem (4.32)

We remark that the integrated multipoles of order $m \neq \bar{m}$ are guaranteed to vanish only within a circle of radius ρ'_{min} given by the minimum distance between the current sheet and the magnet axis.

In the following we will consider two specific cases: circular and rectangular cross section. (The analysis applies to the normal field case only, but extension to the most general case is straightforward.)

4.2.1 Circular aperture

For a circular cross section of radius a we have $g(\phi) = a$ and

$$M_{m,n} = \delta_{m,n} \frac{1}{c} \frac{2\pi}{m} \frac{1}{a^{m-1}}, \quad (4.33)$$

and, therefore, an integrated current of the form

$$j_z^{int}(\phi) = A_{\bar{m}} \cos \bar{m}\phi \quad (4.34)$$

will produce a pure integrated multipole with strength $P_{\bar{m}} = \frac{1}{c} \frac{2\pi}{m} \frac{A_m}{a^{m-1}}$.

4.2.2 Rectangular aperture

Next we consider the case of a current sheet with a rectangular cross section with sides of length $2a$ and $2b$. For the sake of concreteness, let $a > b$ and let the longer sides lay parallel to the x -axis.

The function describing the rectangular cross section for $-\phi_1 \leq \phi' \leq \phi_1$ and $\pi - \phi_1 \leq \phi' \leq \pi + \phi_1$ with $\phi_1 = \tan(b/a)$ (shorter sides) is

$$\rho = g(\phi') = \frac{a}{\cos \phi'}, \quad (4.35)$$

and for $\phi_1 \leq \phi' \leq \pi - \phi_1$ and $\pi + \phi_1 \leq \phi' \leq 2\pi - \phi_1$ (longer sides) the function is

$$\rho = g(\phi') = \frac{b}{\sin \phi'}. \quad (4.36)$$

As a result for $m = even$

$$\begin{aligned} M_{m,n} &= \frac{2}{a^{m-1}} \int_{-\phi_1}^{\phi_1} d\phi' \cos m\phi' \cos n\phi' \cos^{m-2} \phi' \\ &+ \frac{2}{b^{m-1}} \int_{\pi-\phi_1}^{\phi_1} d\phi' \cos m\phi' \cos n\phi' \sin^{m-2} \phi' \end{aligned} \quad (4.37)$$

while for $m = odd$, $M_{m,n} = 0$.

4.3 Further Discussion on Lambertson Magnets

In this section we discuss in detail how to design a Lambertson magnet made of a current distribution lying on a cylindrical surface consistent with Eq. (4.34), i.e. producing pure multipoles in the integrated sense. This is a generalization of the discussion contained in [6].

We consider a current flow (schematically outlined in Fig. 4.2 for the case of a quadrupole magnet) consisting of m sets of concentric rectangular loops equally spaced in the $z - \phi$ plane, where m is the order of the multipole component we want to produce (therefore, $m = 1$ for a dipole magnet, $m = 2$ for a quadrupole magnet and so on).

We shall call a magnet that realizes this current distribution an ‘ideal’ Lambertson magnet (the ideal case is to be distinguished from designs where the

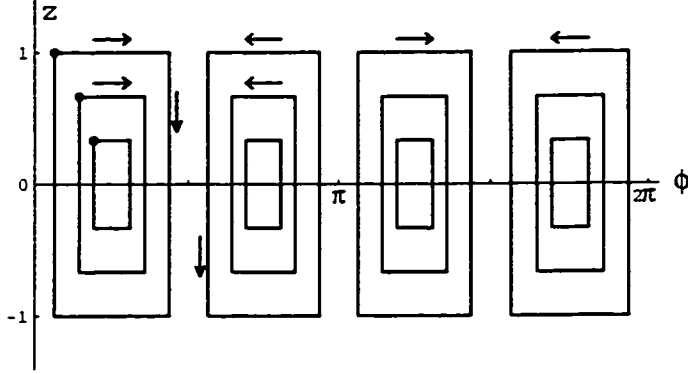


Figure 4.2: Schematic outline of the current flow in a Lambertson quadrupole. $m = 2$.

current distribution for practical convenience may deviate from the rectangular loop scheme. This is the case, for example, for the magnets employed in the Maryland E-Ring where the current flow is actually a rectangular spiral. See Sec. 5.3.).

In the following we will refer to the pieces of the loop parallel to \hat{z} as ‘active conductors’ and to the ones parallel to $\hat{\phi}$ as ‘return conductors’. In an ideal design the conductors are also assumed to have vanishing thickness.

We will first discuss the continuous limit (infinite number of loops for each of the m sets) of the current distribution of an ideal Lambertson magnet and we will then consider some possible discrete realization (finite number of loops for each of the m sets).

Let $z = lf(\phi)$ be the function that gives the semilength of the active conductors at any angle $0 \leq \phi \leq \pi/(2m)$ with l being the semilength of the magnet. For $\phi > \pi/(4m)$, the length of the active conductors can be recovered by using the m -fold symmetry of the magnet. For consistency, $f(\phi = 0) = 1$.

Let $\tilde{J}_z(\phi)$ and $\tilde{J}_\phi(z)$ be the current density on the surface of the cylinder

relative to the active and return conductors respectively, so that $\tilde{J}_z(\phi)ad\phi$ and $\tilde{J}_\phi(z)dz$ is the infinitesimal current dI flowing through the cylinder slice of width $ad\phi$ and dz .

The condition (4.34) can be written as:

$$\int_{-\infty}^{\infty} J_z(\rho, \phi, z) dz = 2lf(\phi)\tilde{J}_z(\phi)\delta(\rho - a) \equiv A_m\delta(\rho - a) \cos m\phi$$

The above equation translates into

$$f(\phi)\tilde{J}_z(\phi) = \frac{A_m}{2l} \cos m\phi. \quad (4.38)$$

Current conservation gives us a second equation, which relates the two components of the current density to $f(\phi)$,

$$\tilde{J}_z(\phi)a|d\phi| = \tilde{J}_\phi(z)|dz|. \quad (4.39)$$

Since, by definition $\frac{dz}{d\phi} = l\frac{df(\phi)}{d\phi}$, equation (4.39) can be written as

$$\frac{df}{d\phi} = -\frac{a}{l} \frac{\tilde{J}_z(\phi)}{\tilde{J}_\phi(z)} \quad (4.40)$$

(The minus sign appears because we require that the function $f(\phi)$ be decreasing). In the design of a quad we have the freedom of choosing separately one of the two components of current density, $J_z(\phi)$ and $J_\phi(z)$ or, alternatively, fixing the function $f(\phi)$.

In the following we will consider two cases: one where the component of the current density along $\hat{\phi}$ is a constant, and one where the component along \hat{z} is a constant.

Let $\tilde{J}_\phi(z) = \tilde{J}_{\phi o}$ be a constant . From (4.40) we have:

$$\tilde{J}_z(\phi) = -\frac{l}{a} \frac{df(\phi)}{d\phi} \tilde{J}_{\phi o}.$$

Now insert $\tilde{J}_z(\phi)$ in (4.38) to get

$$f(\phi) \frac{df(\phi)}{d\phi} = -k \cos m\phi. \quad (4.41)$$

with the constant k being defined as

$$k = \frac{a A_m}{2l^2 \tilde{J}_{\phi o}}. \quad (4.42)$$

The differential equation (4.41) can be easily integrated with the condition $\tilde{f}(0) = 1$ (for $0 \leq \phi \leq \pi/(2m)$)

$$f(\phi) = \left(1 - 2k \frac{\sin m\phi}{m} \right)^{\frac{1}{2}}. \quad (4.43)$$

For fixed values of $a, l, \tilde{J}_{\phi o}$, one is interested in maximizing A_m , which is proportional to the integrated multipole. Clearly this is equivalent to maximizing k . On the other hand, k cannot be greater than $m/2$, because otherwise the function $f(\phi)$ [see (4.43)] would become imaginary for some values of ϕ and the model would break down. Therefore, by imposing $k = m/2$ we determine A_m :

$$A_m = \tilde{J}_{\phi o} \frac{l^2 m}{a} = \frac{lm}{a} I. \quad (4.44)$$

In the last term in (4.44) $I = l\tilde{J}_{\phi o}$ is the total current flowing on the magnet surface.

If, on the other hand, we assume that $\tilde{J}_z(\phi) = \tilde{J}_{zo}$ is a constant, from (4.38) we have directly

$$f(\phi) = \lambda \cos m\phi \quad (4.45)$$

where the constant λ is defined as:

$$\lambda = \frac{A_m}{2l\tilde{J}_{zo}}.$$

From (4.45) and from the condition $f(0) = 1$, it follows $\lambda = 1$; that is

$$A_m = 2l\tilde{J}_{zo} = \frac{4lm}{a\pi} I, \quad (4.46)$$

where, again, $I = \tilde{J}_{zo}a\pi m/(2m)$ is the total current flowing on the magnet surface. Comparison between (4.44) and (4.46) shows that for equal currents I , the configuration with J_z constant is slightly more efficient.

4.3.1 The discrete model

In moving from the continuous model as described above to the discrete model the following approximate relations must be assumed:

$$\tilde{J}_\phi(z)\Delta z_i \sim dI, \quad (4.47)$$

$$\tilde{J}_z(\phi)a\Delta\phi_i \sim dI, \quad (4.48)$$

where dI is the current flowing in each rectangular loop, and Δz_i , $a\Delta\phi_i$ are the distances between two successive (return and active) conductors. Suppose we have n loops in each of the m sets. Let us distinguish again between two cases where $\Delta z_i = \Delta z = l/n$ is constant (corresponding to the case $J_\phi = J_{\phi o} = \text{const}$ in the continuous limit) and $\Delta\phi_i = \Delta\phi = \pi/(2m)/n$ is constant (corresponding to the case $J_z = \text{const}$ in the continuous limit). In the first case $\tilde{J}_{\phi o} = dI/\Delta z$, while in the second $J_z(z) = J_{zo} = dI/(a\Delta\phi)$.

4.4 Further Discussion of Panofsky

Quadrupoles

The expressions for a continuous current distribution derived earlier in this chapter may not be helpful in the design of a magnet if one is interested in using a

limited number of conductors to reproduce the current distribution. This is the case for the Panofsky quadrupoles that are planned to be used in the Maryland Electron Ring.

In this case a better strategy is to evaluate the integrated multipoles as a function of the location of the conductors and use these expressions to optimize the design.

The integrated current density representing a single conductor pointing in the z direction carrying the current I_i and located at $\phi = \phi_i$ is given by

$$j_z^{int}(\phi') = I_i \frac{\delta(\phi - \phi_i)}{\sqrt{g'^2 + g^2}}. \quad (4.49)$$

After inserting (4.49) into (4.27) one finds the following integrated multipole expansion due to the conductor distribution ϕ_i .

$$A_z^{int}(\rho, \phi) = \sum_{m=1} P_m \rho^m \cos m\phi. \quad (4.50)$$

with

$$P_m = \frac{1}{c} \frac{4}{m} 2l \left[\frac{1}{a^m} \sum_{i, \text{short sides}} \cos m\phi_i \cos^m \phi_i + \frac{1}{b^m} \sum_{i, \text{long sides}} \cos m\phi_i \sin^m \phi_i \right]. \quad (4.51)$$

Here we assumed that all conductors have the same length $2l$. In choosing the locations ϕ_i for the conductors one can try either to make the lower order multipoles $m > 2$ vanish or to minimize a certain function of merit obtained by adding up a certain number of multipoles with suitable weights. The latter choice is the strategy followed in the design of the Panofsky quads in the Maryland Electron Ring. See [31] for the details.

Chapter 5

Beam Dynamics Study for the Maryland Electron Ring

5.1 Introduction

The growing interest in applications of high current beams is the original motivation for the University of Maryland E-Ring, which is currently under construction at the Institute for Plasma Research. In particular, one field where achieving a sufficiently high beam current is crucial for success is inertial fusion. The idea is to use accelerator technology to achieve nuclear fusion as an alternative to magnetic confinement techniques. By hitting small metal pellets containing nuclear fuel with an ion beam sufficiently intense one can in principle achieve the required ignition temperature. Inertial fusion may have a number of advantages over magnetic confinement. The most important is probably the possibility of a more efficient control over the nuclear process (arresting the beam would immediately stop the nuclear reaction). Also radioactivation of the plant is likely to be less severe.

The main challenge for inertial fusion is the production of ion beams with the

required high current. There are two schemes that are presently being explored for the fusion driver: one is based on linear and the other on circular accelerators. The first approach is more conservative and is mainly motivated by the proven capability of linacs to handle high current beams. From a beam dynamics viewpoint one advantage of using linear machines, which are essentially single-pass systems is that those machines are immune to the resonance driven instabilities that affect the beam in circular machines. Moreover, linear machines do not present the additional complication that results from the linear coupling between the betatron motion and the longitudinal momentum that takes places in bends and the consequent finite value of the dispersion function.¹ On the other hand use of circular machines, or ‘recirculators’, is appealing for the size and cost cut they would introduce. We live in times where the cheap cost of crude oil is the toughest competitor to any research in alternative sources of energy. And therefore any innovation that had the chance to help keep the overall budget of the project low would be very welcome. Because very high current recirculators are basically ‘terra incognita’ they are also very appealing to the accelerator physicist. A number of beam physics issues and problems need to be investigated and solved in order for an operating recirculator to be built.

It was realized that many of these issues could be investigated in scaled-down versions of realistic recirculators [52]. Moreover, since many aspects of the physics of space-charge dominated beams, in some regimes, are basically independent of the species of particle employed one could conceivable envision the use low-energy electrons as a test bed. This observation underlies the motivation

¹We note that this particular problem is the topic of the last part of the Dissertation. Chapters 8 through 10.

of building a small size, low-energy electron beam at the University of Maryland where an expertise on high current beam physics has been already built up in the last decade by working on solenoidal transport lines. The E-Ring, which is presently under construction, will have a circumference of about 11 m and will carry 10 KeV and 100 mA electron beam. From a physical view point the low energy of the beam is required in order to have significant space-charge force effects even at relatively small values of the current. This is related to a basic relativistic effect governing space charge forces: as the beam energy increases the magnetic forces generated by the beam balance the repulsion due to electrostatic forces. Therefore, from the viewpoint of space charge, a low current, low energy electron beam is equivalent to a relatively high energy, high current ion beam.

A low value of the beam energy has the advantage of containing the cost of the project with consequent benefits in terms of construction time and flexibility. The kinetic energy will be only 10 KeV, comparable to the electron beam energy used in ordinary TV sets or computer monitors. Low energy means modest fields required to handle the beam (bending and focusing). Bending magnetic fields of the order of 10 gauss and magnetic field gradients of the order of a few gauss/cm will be sufficient. In the E-Ring design the choice was to use iron-free printed circuit magnets. Besides their low cost this kind of magnets offers the additional advantage of very accurate modelling of the fields.

The need to keep the Ring compact has forced the choice of relatively short magnets, with an aperture roughly equal to their length. When the design of the E-Ring was originally conceived this was a source of concern because of the nonlinearities associated with fringe fields. That concern motivated the study presented in this Chapter, which specifically addresses the possible limitation

coming from the nonlinearities associated with fringe fields.

Although in the typical working regime space-charge is important in determining the beam dynamics (partly because of tune depression, partly because of additional nonlinearities), the effect due to the magnet fringe fields is best investigated in a single particle regime. For this purpose one can fully exploit the possibility of an analytical description of the fields and the tools that we have developed in the previous Chapters. The conclusion of our study is that the nonlinearities associated with the fringe fields although significant, are not sufficient to reduce the dynamic aperture below acceptable limits. The same result has later been confirmed by independent calculations that also included space-charge effects [39].

The outline of the Chapter is as follows. After introducing a general outline of the Ring lattice we describe in detail the dipole and quadrupole magnets. We derive the analytical formulas for the fields in the ideal design displaying the exact dependence of the fields in the longitudinal variable. We also derive the expression for the integrated fields that one can measure using spinning coils. Moreover an estimate of possible multipole errors coming from some type of machining imperfections is also presented. The analytical formulas for the fields have been implemented in MARYLIE5.0 and used to calculate lattice functions and to study the particle dynamics with particular regard to determining the dynamic aperture. In order to locate the possible sources of instabilities we have also considered a version of the lattice where the dipoles are removed and replaced by drifts. Moreover, an analysis of the effect of random and systematic errors superimposed on the ideal lattice with extended fringes has also been

performed.²

We anticipate that Chapter 6 is closely related to this one. The purpose there is to present a semianalytical model to study how the aberrations due to the quadrupole fringes (the leading nonlinearities as we will see) scale with the magnet size and to provide an understanding for some of the facts obtained by numerical simulations. There the reader will find further evidence for the (to some extent surprising) fact mentioned in this chapter that a larger magnet aperture is better for minimizing fringe nonlinearities.

5.2 Lattice Design Overview

The E-Ring lattice consists of 36 identical FODO cells. Each cell is made of a pair of quadrupoles (focusing and defocusing) and a dipole. The length of each FODO cell is 32 cm, giving the Ring a circumference of 11.52 m. The quadrupoles along the Ring are equally distributed with a distance (center to center) of 8 cm. The 36-fold symmetry is broken at the two points where the beam is injected and extracted. At those points special large aperture quadrupoles (Panofsky quadrupoles) replace the standard quadrupoles used in the rest of the machines. All the magnets employed in the Ring are iron-free and all, with the exception of the two Panofsky quads at injection and extraction, are printed circuit magnets. Two layers of printed circuit, laid down to minimize the undesired currents needed for the connections, sit on the surface of a cylinder of radius 2.872 cm and 2.79 cm respectively for dipoles and quadrupoles. The magnet length is 4.4

²A preliminary study of single particle dynamics for the ring through 3rd was presented in [60].

Table 5.1: Design Parameters for the E-Ring

Ring circumference	11.5 m
FODO cell length L_{FODO}	32 cm
Beam Energy	10 KeV
Rigidity	3.389×10^{-4}
Beam Current	100 mA
Perveance	0.0015
Mean beam radius	1.04 cm
(Undepressed) tune	7.6
Lap time	197 ns

cm. In the following we will refer to this 36-fold perfectly symmetric lattice as the ‘ideal lattice’. It is understood that in this ideal lattice the fields of each magnet are realistically described with the correct longitudinal dependence and extension of the fringes, in accordance to the model discussed in Section 5.3.

The presence of diagnostic chambers, pumping ports, and induction gaps distributed along the Ring also breaks the lattice 36-fold symmetry. However, for the purpose of this study all the possible perturbations to the beam dynamics coming from these sources have been neglected.

A summary of the most important E-Ring and beam parameters is presented in Table 5.1. The design tune in a single particle regime has tentatively been set at 7.6 in both planes. The beam energy is fixed at 10 KeV, corresponding to the energy of the electron gun. No beam acceleration is envisioned in the first phase of the machine operation.

We should also mention that in our study we ignore the effect of the earth’s

magnetic field. This is justified here because our focus is to study the effect of the nonlinearities due to the magnet fringes. The perturbation due to magnetic field, however, is going to be a significant factor in determining the beam dynamics in the E-Ring. A homogeneous field of the strength of 0.3 Gauss, comparable to the average vertical component of the earth magnetic field, would cause a 10 keV electron to circulate on an orbit of about 11 m in radius, which is only about three times the radius of the E-Ring. In practice the E-Ring will be equipped with external Helmholtz coils for external magnetic field compensation. The residual reference orbit deviations will then be corrected locally by proper tuning of the 36 dipoles (for the motion on the horizontal plane) and possibly short steering coils for the motion in the vertical plane.

Finally we should mention a possible positive side effect of the natural bending caused by the earth's magnetic field is that it can relieve the load on the dipoles, provided that the direction of the bending is chosen in the proper way. As a consequence the nonlinearities associated with the dipoles fringes should also be smaller. At the end however, this will not turn out to be a significant advantage because, as we will show, the dominant nonlinearities in the ideal E-Ring come from the third order aberrations (pseudo-octupoles) associated with the quadrupole magnet fringes.

5.3 Quadrupole Magnets

In this and the following section we will illustrate in some detail the calculation of the vector potential \mathbf{A} for the quadrupole and dipole Lambertson magnets used in the E-Ring. It is a remarkable and fortunate feature of ideal Lambertson

magnets that the calculation of the fields can be carried out analytically.³ We are motivated to calculate the vector potential because eventually we want to study the beam dynamics for the Ring in a canonical framework. However, we point out that even if one were interested only in knowing the magnetic field, in this case the calculation would still be best carried out by first determining the vector potential.

An ideal Lambertson magnet, which we introduced in (4.3), carries a current distribution consisting of \bar{m} sets of concentric rectangular loops distributed on a cylindrical surface of radius R so as to create a \bar{m} -fold azimuthal symmetry. We have $\bar{m} = 1$ for a dipole magnet, $\bar{m} = 2$ for a quad magnet, etc. The outline of the current flow is shown in Fig. 4.2 for a quadrupole magnet. Because of the \bar{m} -fold symmetry, a current configuration so defined is uniquely determined by the locations of the ‘corners’ of the first set of loops contained in $[0, \phi = \pi/(2\bar{m})]$. See the dots in Fig. 4.2. Each ‘corner’ is determined by a pair of numbers (ϕ_i, l_i) , for $i = 1, 2, \dots, n$, with n being the number of loops in each of the \bar{m} sets, and l_i being the semilengths of the conductors lying parallel to the magnet axis. (We called these ‘active conductors’ as opposed to the ‘inactive’ or ‘return conductors’ lying perpendicularly to the magnet axis; see Section 4.3). The current I is the same in each loop. Such a current distribution is a good approximation of the real current flow in the physical magnets used in the Electron Ring. We will comment more on this point at the end of this Section.

In carrying out the calculation of the fields we work in a cylindrical coordinate system where the z axis is coincident with the magnet axis and the center of

³In the calculation we neglect any possible perturbation generated by magnetic material in the surrounding of the magnets.

the first set of loops is located at $\phi = \pi/(2\bar{m})$. (here, again, $\bar{m} = 1$ for a dipole magnet, $\bar{m} = 2$ for a quad magnet, etc). In this frame only the ‘normal’ components of the field are nonvanishing. Pure skew components can be obtained by rotating the magnet (or the frame) by an angle $\phi = \pi/(2\bar{m})$.

Having defined the current distribution we can calculate the associated vector potential by using the integral formulas (4.6), which automatically cast \mathbf{A} in the Coulomb gauge. In the Coulomb gauge the multipole expansion for the normal components have the form

$$A_z(\rho, \phi, z) = \sum_{m=1} A_z^{(m)}(\rho, z) \cos m\phi. \quad (5.1)$$

$$A_\rho(\rho, \phi, z) = \sum_{m=1} A_\rho^{(m)}(\rho, z) \cos m\phi, \quad (5.2)$$

$$A_\phi(\rho, \phi, z) = \sum_{m=1} A_\phi^{(m)}(\rho, z) \sin m\phi. \quad (5.3)$$

with the *nonvanishing* multipoles having the expressions (for brevity we omit the expression for A_ϕ)

$$A_z^{(m)} = \frac{1}{c} I 16 \mathcal{P}_{\bar{m}} \frac{1}{\pi} \sum_{i=1}^n \cos m\phi_i \int_{-l_i}^{l_i} dz' \int_0^\infty \cos[k(z - z')] I_m(k\rho) K_m(kR) dk. \quad (5.4)$$

and

$$\begin{aligned} A_\rho^{(m)}(\rho, z) &= \frac{1}{c} \frac{4}{\pi} \sum_{i=1}^n \int_0^\infty dk \{ \cos[(k(z + l)] - \cos[k(z + l)] \} I_m(k\rho) K_m(kR) \\ &\quad \times \int_{\Sigma_i} d\phi' \cos[m(\phi - \phi')] \sin(\phi - \phi'). \end{aligned} \quad (5.5)$$

Here I_m and K_m are the generalized Bessel functions. The coefficient $\mathcal{P}_{\bar{m}}$ depends on the particular kind of magnet, for a quadrupole magnet $\mathcal{P}_{\bar{m}} = 2$, for a dipole magnet $\mathcal{P}_{\bar{m}} = 1$.

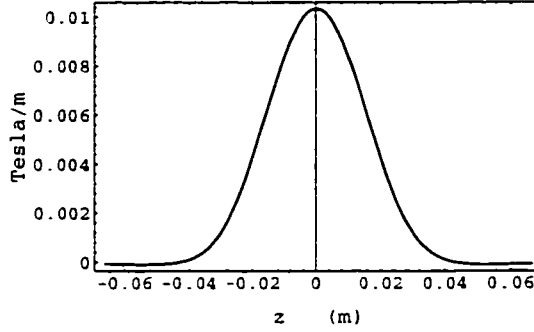


Figure 5.1: Generalized gradient $C_2(z)$ for a PC Quad (it is half of the on-axis gradient, $I = 1 \text{ A}$, single layer).

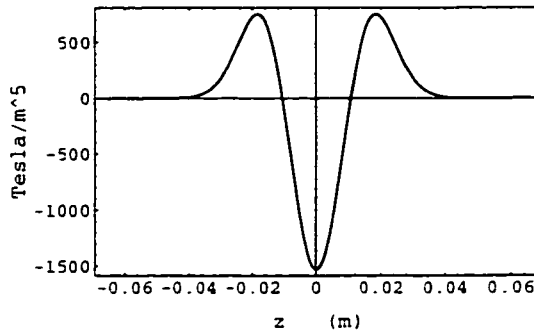


Figure 5.2: Generalized gradient $C_6(z)$ for a PC Quad ($I = 1 \text{ A}$, single layer).

The set Σ_i appearing in (5.5) as the domain of integration over the angle is, for a quadrupole $\Sigma_i = [\phi_i, \pi/2 - \phi_i] \cup [\pi/2 + \phi_i, \pi - \phi_i] \cup [\pi + \phi_i, 3\pi/2 + \phi_i] \cup [3\pi/2 - \phi_i, 2\pi - \phi_i]$, while for a dipole $\Sigma_i = [\phi_i, \pi - \phi_i] \cup [\pi + \phi_i, 2\pi - \phi_i]$.

Moreover, we have

$$\begin{aligned} & \int_{\Sigma_i} d\phi' \cos[m(\phi - \phi')] \sin(\phi - \phi') = \\ & - 4P_m \left[\frac{\cos[(m+1)\phi] \cos[(m+1)\phi_i]}{m+1} - \frac{\cos[(m-1)\phi] \cos[(m-1)\phi_i]}{m-1} \right] \end{aligned} \quad (5.6)$$

Next, by using (3.29), the limiting form (4.11) of the Bessel function $I_m(k\rho)$ as $\rho \rightarrow 0$, and the formula (B.3) reported in Appendix B to carry out the integrals in k , we can recover the functions Γ_m and E_{m-1} that appear in the radial power

series expansion (3.27), (3.28) for the vector potential in the Coulomb gauge,

$$\Gamma_m = \frac{1}{c} I 8 \mathcal{P}_{\bar{m}} \frac{(2m-1)!!}{m! 2^m} R^m \sum_{i=1}^n \cos m\phi_i \int_{-l_i}^{l_i} \frac{dz'}{[R^2 + (z - z')^2]^{m+\frac{1}{2}}}. \quad (5.7)$$

and

$$\begin{aligned} E_{m-1} &= \frac{1}{c} I 8 \mathcal{P}_{\bar{m}} \frac{(2m-3)!!}{m! 2^m} R^m \\ &\times \sum_{i=1}^n \cos m\phi_i \left[\frac{1}{[R^2 + (z + l)^2]^{m-\frac{1}{2}}} - \frac{1}{[R^2 + (z - l)^2]^{m-\frac{1}{2}}} \right]. \end{aligned} \quad (5.8)$$

Then we can combine the two functions Γ_m and E_{m-1} together, $C_m = \Gamma_m + (1/m)E_{m-1}$ (see 3.30), to get the expression for the generalized gradient $C_m(z)$ that appears in the multipole expansion for the magnetic field (5.13). We have

$$C_m(z) = \frac{1}{c} I 16 \mathcal{P}_{\bar{m}} \frac{(2m-1)!!}{(m-1)! 2^{2m}} R^m \sum_{i=1}^n \cos m\phi_i [G_m(z + l_i) - G_m(z - l_i)]. \quad (5.9)$$

where the function $G_m(t)$ is defined by:

$$G_m(t) = \frac{1}{m} \frac{t}{(R^2 + t^2)^{m+\frac{1}{2}}} + \int_0^t \frac{d\tau}{(R^2 + \tau^2)^{m+\frac{1}{2}}}. \quad (5.10)$$

The two terms on the RHS of the above equation describe the contribution from the active conductor and return conductors respectively. The integral can be carried out analytically (see Appendix B).

In the case of the quadrupole magnet the function $C_2(z)$, which is half of the on-axis gradient reads:

$$C_2(z) = \frac{1}{c} R^2 \sum_{i=1}^n \cos 2\phi_i [G_2(z + l_i) - G_2(z - l_i)], \quad (5.11)$$

with

$$G_2(t) = \frac{1}{2} \frac{t}{(R^2 + t^2)^{\frac{5}{2}}} + \frac{1}{3} \frac{t(3R^2 + 2t^2)}{R^4(R^2 + t^2)^{\frac{3}{2}}}. \quad (5.12)$$

A plot of the function $C_2(z)$ for the design implemented in the PC quadrupoles of the Electron Ring [32] is shown in Fig.5.1 for $I = 1A$ (One should multiply

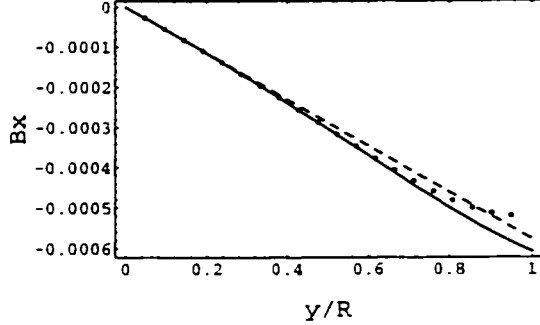


Figure 5.3: The component B_x of the magnetic field (dots) as a function of y/R at $x = 0, z = 0$, is compared with the linear approximation (dashed line), and the approximation (solid line) obtained by retaining all the terms through 6th order in the radius (see the expansion 5.13).

the values in the picture by a factor of 2 to get the field resulting from a double layer design).

In an ideal Lambertson quadrupole, because of the four-fold symmetry of the current distribution only the generalized gradients C_2, C_6, C_{10}, \dots with multipole $m = 2\ell$, with $\ell = 1, 3, 5, 7, \dots$ are non vanishing. In general, for the case of a \bar{m} -pole magnet displaying an \bar{m} -fold symmetry the only nonvanishing multipoles are $m = \bar{m}\ell/2$, $\ell = 1, 3, 5, 7, \dots$.

A plot of the next nonvanishing generalized gradient, $C_6(z)$, which is associated with the duodecapole component of the field is shown in Fig. 5.2.

It is convenient at this point to write the multipole expansion for the magnetic field as power series in the radial coordinates. The expansion depends only on the generalized gradients $C_m(z)$ defined in (5.9) and their derivatives. Through 6th order we have

$$\begin{aligned} B_\rho &= \left(2C_2\rho - \frac{1}{3}C_2''\rho^3 + \frac{1}{64}C_2^{iv}\rho^5\right) \sin 2\phi + 6C_6\rho^5 \sin 6\phi. \\ B_\phi &= \left(2C_2\rho - \frac{1}{6}C_2''\rho^3 + \frac{1}{192}C_2^{iv}\rho^5\right) \cos 2\phi + 6C_6\rho^5 \cos 6\phi. \end{aligned}$$

$$B_z = \left(C'_2 \rho^2 - \frac{1}{12} C'''_2 \rho^4 + \frac{1}{384} C''_2 \rho^6 \right) \sin 2\phi + C'_6 \rho^6 \sin 6\phi. \quad (5.13)$$

Let us take a closer look at the expansion (5.13). The term linear in ρ in the expansion of B_ρ and B_ϕ is the desired component of the field. In addition we have some nonlinear corrections that come from both the quadrupole term (with a 2ϕ azimuthal symmetry) and the duodecapole term (6ϕ azimuthal symmetry). Contributions from multipoles of higher order do not appear in the expansion (5.13) because they carry powers of ρ higher than 6.

Here we want to emphasize the different nature of the two nonlinear contributions. The nonlinear corrections coming with the quadrupole azimuthal symmetry, which are proportional to the derivatives of $C_2(z)$, are unavoidable in any physical quadrupole magnet, i.e. the derivatives of $C_2(z)$ must be there to allow the field to satisfy the Maxwell equations. This is true of course also for long magnets, although in this case the nonlinearities with quadrupole symmetry will be non vanishing only at the ends.

On the other hand there are no physical constraints (except those coming from mechanical limitations) to having the higher order multipoles vanish. Indeed, as we have shown in Chapter 4, it is possible to find current distributions that realize pure multipoles. In the case of Lambertson magnets the design aims at making the higher order multipoles vanish in the integrated sense.

Finally, we should mention that the first nonlinear correction [e.g. the term proportional to $\rho^3 \cos(2\phi)$] in the expansion for B_ρ , is often called in the literature ‘pseudo-octupole’ because it comes with the azimuthal symmetry of a quadrupole and the radial dependence of an octupole (at the lowest order). In the same way one can refer to the next nonlinear correction as ‘pseudo-duodecapole’.

In Fig. 5.3 and 5.4, as a way to represent the deviation of the real field from

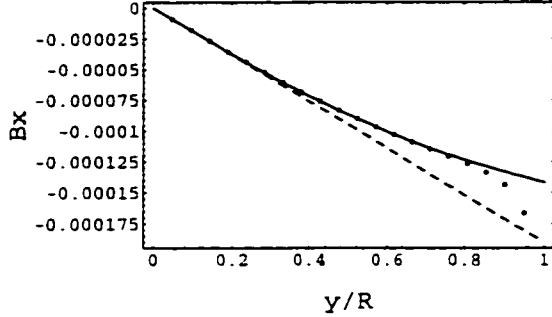


Figure 5.4: Component B_x of the magnetic field (in Tesla) as a function of y/R at $x = 0, z = l$.

its linear approximation, we show the B_x component of the magnetic field at $x = 0$ and $z = l$ as a function of the distance y from the magnet axis. [B_x at $\phi = 0$ is the same as $-B_\phi$, see Eq. (5.13)]. The field (dots) in the picture is plotted against its linear approximation and the approximation through ρ^6 , see Eq. (5.13). From the pictures one can conclude that a 6th order approximation seems to be adequate to describe the field within about 80% of the magnet aperture.

In characterizing the field quality of a magnet one often refers to the integrated multipoles, that is the functions $C_m(z)$ integrated in z from $-\infty$ to $+\infty$. In our case we can easily calculate those quantities (for $m = 2, 6, 10, \dots$):

$$P_m = \int_{-\infty}^{\infty} C_m(z) dz = \frac{1}{c} 16I \frac{\mathcal{P}_{\bar{m}}}{mR^m} \sum_{i=1}^n l_i \cos m\phi_i. \quad (5.14)$$

The coefficients P_m appear in the multipole expansion for the z-component of the integrated vector potential

$$A_z^{int}(\rho, \phi) = \int_{-\infty}^{\infty} dz A_z(\rho, \phi, z) = \sum_{m=1} \rho^m P_m \cos m\phi, \quad (5.15)$$

(the other components of \mathbf{A} vanish after integration over z). It is customary to

represent the integrated transverse components of the magnetic field in the form

$$B_y^{int} + iB_x^{int} = \sum_{m=1} (B_m + iA_m)(x + iy)^{m-1}. \quad (5.16)$$

or equivalently

$$B_\rho^{int} = \sum_{m=1} \rho^{m-1} (B_m \sin m\phi + A_m \cos m\phi), \quad (5.17)$$

$$B_\phi^{int} = \sum_{m=1} \rho^{m-1} (B_m \cos m\phi - A_m \sin m\phi). \quad (5.18)$$

with the connection between the harmonics B_m and the integrated gradient P_m given by

$$B_m = mP_m. \quad (5.19)$$

More often an expansion relative to the main field component at a specified radius is used. Suppose the main multipole component is $B_{\bar{m}}$ (for a quadrupole magnet $\bar{m} = 2$). If we introduce the relative integrated multipoles at a fixed radius $\rho = \rho_o$

$$b_m = \frac{\rho_o^{m-1} B_m}{\rho_o^{\bar{m}-1} B_{\bar{m}}}, \quad (5.20)$$

$$a_m = \frac{\rho_o^{m-1} A_m}{\rho_o^{\bar{m}-1} B_{\bar{m}}}. \quad (5.21)$$

we can then write, for example, the expansions (5.17) as

$$B_\rho^{int} = \rho_o^{\bar{m}-1} B_{\bar{m}} \sum \left(\frac{\rho}{\rho_o} \right)^{m-1} (b_m \sin m\phi + a_m \cos m\phi). \quad (5.22)$$

The relative integrated multipole for the PC Quads used in the Electron Ring [32] are reported in the first column of Table 5.2.

In a measurement using spinning coils one can directly determine the relative integrated multipoles. The e.m.f measured using an azimuthal rectangular spinning coil of radius R_s rotating with frequency ω is given by the relation

$$\mathcal{E} = - \int_{-\infty}^{\infty} dz \int_0^{R_s} \frac{dB_\phi}{dt} d\rho = \sum_{m=1} \mathcal{E}_m^{nor} \sin m\omega t + \mathcal{E}_m^{skew} \cos m\omega t. \quad (5.23)$$

Table 5.2: Relative Integrated multipoles for a PC Quad at $\rho_o = .5R$ in units of 10^{-4} .

	loops	spirals	A	B
b_2	10^4	9984.87	9972.6	10^4
a_2				-27.37
b_4		-7.55	-5.412	.0002
a_4				-5.4
b_6	1.422	0.48	.0801	1.422
a_6				-1.342
b_8		.004	-.333	
a_8				-.333
b_{10}	.0671	.009	-.0179	.0671
a_{10}				-.0851
b_{12}		-.029	-.0210	
a_{12}				-.0211
b_{14}	.0060	.002	-.0005	.0060
a_{14}				-.0054

Table 5.3: Relative e.m.f for a rotating coil of radius $R_s = 2.54$ cm (units of 10^{-4}) in a PC Quad.

	e_2	e_4	e_6	e_8	e_{10}	e_{12}	e_{14}
rectangular loops	1	0	15.6	0	8.1	0	8.0
spiral	1	25.0	5.3	.14	1.2	11.6	3.3

If the spinning coil is long enough to integrate all the field along the z -axis. we have up to a multiplicative constant the relations

$$\mathcal{E}_m^{norm} \propto \omega R_s^m B_m \quad \mathcal{E}_m^{skew} \propto \omega R_s^m A_m. \quad (5.24)$$

For a quadrupole ($\bar{m} = 2$) the relative e.m.f. multipoles are therefore

$$\epsilon_m = \frac{\mathcal{E}_m^{norm}}{\mathcal{E}_2^{norm}} = \frac{R_s^m B_m}{R_s^2 B_2} = \left(\frac{R_s}{\rho_o} \right)^{m-2} b_m, \quad (5.25)$$

and a similar expression holds for the skew components.

So far we have considered a design (the concentric rectangular loop model). which is actually an idealization of the real current configuration in the PC magnets used in the Electron Ring. Let us consider the particular the case of a quadrupole magnet. The current in each quadrant is confined to two superimposed layers. On each layer the current flow follows a rectangular spiral as shown in Fig. 5.5 . It turns out that such a configuration can be regarded as the superposition of a set of rectangular concentric loops of an ideal design (one on the top of the other) and a sequence of tiny rectangular loops placed along the upper right diagonal of the rectangular loops of the ideal design (see Fig. 5.5). The contribution of these tiny loops to the integrated multipoles can be easily calculated. In the calculation only the portions of the loops parallel to the magnet axis need to be retained. For a quadrupole magnet ($m=2,4,6,8,10,\dots$):

$$P_m^{corr} = \frac{1}{c} I \frac{16}{m R^m} \Delta l \sum_{i=1}^n (\cos m\phi_i - \cos m\phi_{i+1}) = \frac{1}{c} I \frac{16}{m R^m} \Delta l (\cos m\phi_1 - \cos m\phi_{21}) \quad (5.26)$$

where $\phi_{21} = \pi/2$ and Δl is the (constant) spacing between the return conductors. Notice that because of cancellations only two terms survive in the summation. Also, notice that the presence of the tiny loops breaks the four fold symmetry

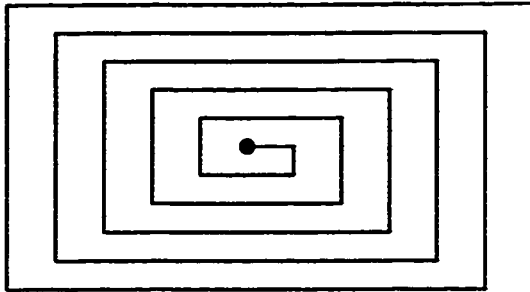


Figure 5.5: Spiral design for one quadrant of the PC quad ($0 \leq \phi < \pi/2$). The line with larger thickness corresponds to the conductor lying on the bottom layer, the thinner line corresponds to the conductor lying on the upper layer.

of the ideal design. As a consequence one has also integrated multipoles of order 4,8,12.... in addition to those of order 2,6,10... . Therefore, the expected integrated gradients for the design as implemented can be evaluated by

$$P_m^{spiral} = 2P_m - P_m^{corr}. \quad (5.27)$$

The relative integrated multipoles corresponding to the realistic spiral design are reported in the second column Table 5.2. Notice that the relative correction to the integrated gradient is of the order of 10^{-3} .

In the remaining columns of Table 5.2 we report the relative integrated multipoles in cases where we allow some kinds of mechanical error in the placement of the conductors. We consider two particular kind of deformations in which the conductors are maintained parallel to the magnet axis so that the integrated multipoles can be easily calculated using analytical formulas of the type (5.14). The two deformations mimic two possible types of mechanical errors that can actually occur when assembling the physical quadrupoles used in the Ring. In both cases the magnet is broken in two halves (top and bottom) each one having the cross section of a semicircumference. In the first case (column A) the half

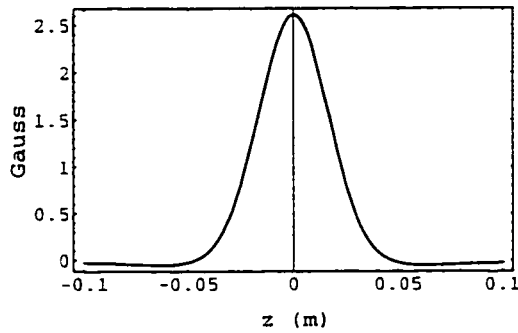


Figure 5.6: On-axis vertical magnetic field B_y in a PC dipole (it is equal to $C_1(z)$, $I = 1$ A, single layer).

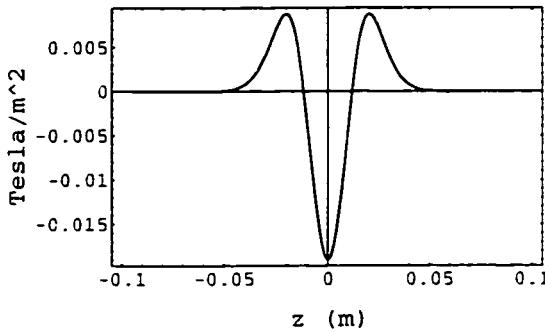


Figure 5.7: Generalized gradient $C_3(z)$ in a PC dipole ($I = 1$ A, single layer).

on the top is moved up in the vertical direction by .05 mm, and the half on the bottom is moved down by the same amount. In the second case (column B) the two halves are drifted in the opposite direction in the horizontal plane by -0.05 mm and $+0.05$ mm respectively.

Finally Table 5.3 reports the coefficients in Eq. (5.25) to be expected from spinning coil measurements in the case of an ideal design.

5.4 Dipole Magnets

The calculation of the fields in a Lambertson dipole can be carried out using the general formulas presented in the previous Section. In this case the symmetry

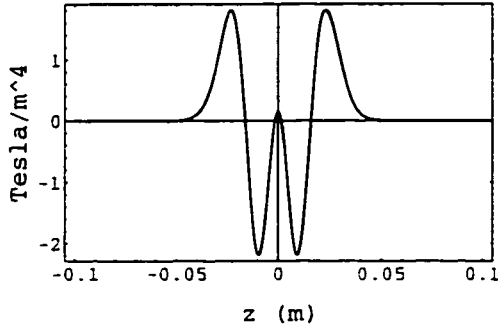


Figure 5.8: Generalized gradient, $C_5(z)$ in a PC dipole ($I = 1$ A. single layer).

of an ideal design rules out all the even multipoles. The multipole expansion for the magnetic field through 5th order in the radial coordinate is:

$$\begin{aligned}
 B_\rho &= \left(C_1 - \frac{3}{8} C_1'' \rho^2 + \frac{5}{192} C_1^{iv} \rho^4 \right) \sin \phi + \left(3C_3 \rho^2 - \frac{5}{16} C_3'' \rho^4 \right) \sin 3\phi \\
 &\quad + 5C_5 \rho^4 \sin 5\phi, \\
 B_\phi &= \left(C_1 - \frac{1}{8} C_1'' \rho^2 + \frac{1}{192} C_1^{iv} \rho^4 \right) \cos \phi + \left(3C_3 \rho^2 - \frac{3}{16} C_3'' \rho^4 \right) \cos 3\phi \\
 &\quad + 5C_5 \rho^4 \cos 5\phi, \\
 B_z &= \left(C_1' \rho - \frac{1}{8} C_1''' \rho^3 + \frac{1}{192} C_1^v \rho^5 \right) \sin \phi + \left(C_3' \rho^3 - \frac{1}{16} C_3'' \rho^5 \right) \sin 3\phi \\
 &\quad + C_5' \rho^5 \sin 5\phi.
 \end{aligned} \tag{5.28}$$

As in the case of a quadrupole, the correction (terms dependent on ρ) to the desired component of the field come from both the main field component, the dipole, as well from multipoles or higher order. [In particular notice the presence of the sextupole (proportional to $\sin 3\phi$, $\cos 3\phi$) and decapole (proportional to $\sin 5\phi$, $\cos 5\phi$) components in this fifth order expansion]. Notice that in B_ρ the term proportional to $C_1'' \rho^2 \sin \phi$ has the appearance of a ‘pseudo-sextupole’ and the ones proportional to $C_3'' \rho^4 \sin 3\phi$ and $C_3^{iv} \rho^4 \sin \phi$ have the appearance of

Table 5.4: Relative Integrated multipoles for a PC Dipole at $\rho = .5R$ in units of 10^{-4} .

relative multipole	
b_1	10^4
b_3	2.37
b_5	.366

'pseudo-decapoles'.

The generalized gradients are given by the formula (5.9) with $\mathcal{P}_{\bar{m}} = 1$. In particular the function $C_1(z)$ corresponding to the on-axis B_y component of the magnetic field is given by

$$C_1(z) = B_y(x = 0, y = 0, z) = \frac{1}{c} I \frac{1}{R^2} \sum_{i=1}^n \cos \phi_i [G_1(z + l_i) - G_1(z - l_i)] \quad (5.29)$$

with

$$G_1(t) = t \frac{2R^2 + t^2}{(R^2 + t^2)^{\frac{3}{2}}} \quad (5.30)$$

The plots of the functions $C_1(z)$, $C_3(z)$, $C_5(z)$ are shown in Fig. 5.6, 5.7, 5.8. The plot correspond to the design reported in [33].

In Fig. 5.9 some radial cuts of the B_y component (dots) of the magnetic field are shown and compared to the analytical approximation given by retaining the terms shown in the expansion (5.28) (5th order in ρ). In particular, the upper and lower lines in the picture refer to a section in the vertical plane ($x = 0$) at two different locations in z , corresponding to the middle ($z = 0$) and the edge of the magnet ($z = 2.1$ cm). The third line represents a section of B_y in the horizontal plane ($y = 0$) at $z = 0$.

Finally in Table 5.4 we report the expected integrated relative multipole

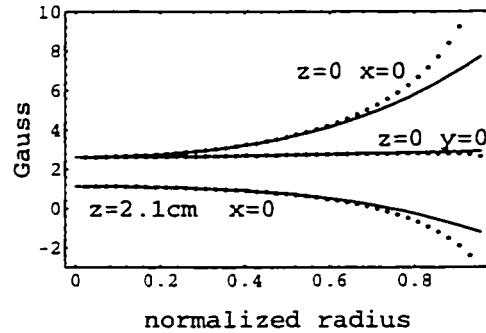


Figure 5.9: The component B_y (dots) as a function of the radial coordinate ρ/R normalized with respect to R , compared to its analytic approximation through 6th order (solid line).

Table 5.5: Parameters for the PC Quad and PC Dip (ideal design)

	PC Quad	PC Dip
semilength l	4.428 cm	4.226 cm
radius R	2.790 cm	2.872 cm
integrated gradient ($I=1$ A)	7.514 Gauss	
gradient peak value ($I=1$ A)	2.068 Gauss/cm	
integrated on-axis B_y ($I=1$ A)		9.717 Gauss cm
B_y peak value ($I=1$ A)		2.611 Gauss

components of the fields for the PC dipole and in Table 5.5 a summary of all the relevant parameters for both the PC quadrupole and dipole magnets.

5.5 Map Computation

The representation for the dipole and quadrupole fields derived in the last Section can be used in combination with the GENMAP routine in MARYLIE5.0 to compute the corresponding transfer maps. GENMAP integrates equation (1.38) for any Hamiltonian specified in the form of a Taylor series through 6th order. Physically, truncation through 6th order means inclusion in dynamics modelling of all fields multipole components through the duodecapole term.

The first thing one has to do is to recover the Taylor expansion for the three cartesian components of the vector potential from the expression of the generalized gradients (5.9). In determining the vector potential one has a certain degree of freedom because of the gauge invariance. One choice is the Coulomb gauge. See Eq. (3.27), (3.28) and Appendix A. From a computational viewpoint a more convenient choice is the gauge $A_\phi = 0$, see Eqs. (3.13), (3.14) because it minimizes the number of terms in the Taylor expansion of the Hamiltonian. The Taylor expansion of the Hamiltonian through 6rd order has been carried out using Mathematica [47].

A possible problem in calculating the map for the basic FODO cell of the E-Ring is the overlapping of the fields between adjacent magnets, in particular between the dipole and the two adjacent quadrupoles (see the FODO cell outline at the bottom of Fig. 5.10). However, since the overlapping is relatively small a way to proceed is to evaluate the transfer maps for the individual magnets by

ignoring the presence of the other magnets. In this way one can carry out the integration for the transfer map including the full extension of the fringes. The map for the overall FODO cell is then recovered by combining these maps with the maps for the inverse of appropriate drifts. We explain in a moment the detail of the calculation.

The computation of the map for the FODO results from the combination of the following four maps obtained using GENMAP: \mathcal{M}_Q^{QD-QF} , \mathcal{M}_Q^{QF-Dip} , $\mathcal{M}_{Dip}^{(Dip-10cm) \rightarrow (Dip+10cm)}$, \mathcal{M}_Q^{Dip-QD} . The superscripts refer to the domain of integration: *QF*, *QD*, *Dip* mean the middle of the focusing and defocusing quadrupole magnet, and dipole magnet. The subscript *Dip* or *Q* indicates the magnets whose fields are included in the computation. For example, the map $\mathcal{M}_{Dip}^{(Dip-10cm) \rightarrow (Dip+10cm)}$ is the transfer map from a $z = z^i$ located 10 cm before the center of the dipole magnet to a $z = z^f$ located 10 cm past the dipole magnet. The calculation does not include the fields arising from the adjacent quadrupole magnets. Similarly \mathcal{M}_Q^{QD-QF} is a transfer map from the center of a defocusing quad to the center of the next focusing quad. In this case the overlapping of the two adjacent quadrupole fields is taken into account, but not the overlapping with the dipole field.

Let us define \mathcal{D}_L as the transfer map associated with a drift of length L . The total transfer map for the FODO Cell is then given by the composition of the following Lie maps:

$$\mathcal{M}_{FODO} = \mathcal{M}_1 \circ \mathcal{M}_2 \circ \mathcal{M}_3 \circ \mathcal{M}_4 \quad (5.31)$$

where

$$\mathcal{M}_1 = \mathcal{M}_Q^{QD-QF},$$

$$\begin{aligned}
\mathcal{M}_2 &= \mathcal{M}_Q^{QF-Dip} \circ \mathcal{D}_{L_{DQ}}^{-1}, \\
\mathcal{M}_3 &= \mathcal{D}_{L_1}^{-1} \circ \mathcal{M}_{Prot1} \circ \mathcal{M}_{Dip}^{(Dip-10cm)-(Dip+10cm)} \circ \mathcal{M}_{Prot2} \circ \mathcal{D}_{L_1}^{-1}. \\
\mathcal{M}_4 &= \mathcal{D}_{L_{DQ}}^{-1} \circ \mathcal{M}_Q^{Dip-QD}.
\end{aligned} \tag{5.32}$$

In the expression above L_{QD} is the distance between the center of the dipole and the middle between the dipole and one of the two adjacent quadrupoles (center to center) and $L_1 = 10\text{cm} - L_{QD}$. The maps \mathcal{M}_{Prot1} and \mathcal{M}_{Prot2} provide the correct transformation that takes into account the rotation of 10° between the dipole and the quadrupole frames. In the calculations presented here \mathcal{M}_{Prot} was calculated using a specifically written user-routine that calls GENMAP with the appropriate generating Hamiltonian.⁴

The choice to compute maps starting or ending at the center of the quadrupoles is motivated by the fact that at those points the transverse mechanical and canonical momenta coincide. ($A_x = A_y = 0$ because of the field symmetries). This will make it easier to insert at this point multipole kicks when we model the effect or random errors (see Sec. 5.7).

5.6 Lattice Functions

The linear part of the map \mathcal{M}_{FODO} computed as outlined in the previous Section can be used to determine the betatron functions, the tunes and the dispersion function. We briefly recall the definitions. There are two independent ways one can define those quantities. One is based on writing the linear differential equations describing the linear motion in the transverse plane. The other is based on the transformation that brings the linear part of the map into a normal form.

⁴The standard command prot in MARYLIE5.0 is not available yet.

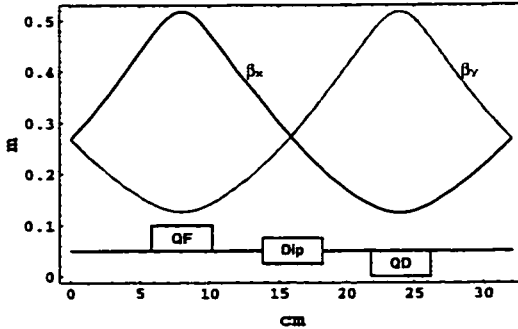


Figure 5.10: Betatron functions for the E-Ring.

Although the latter is the one that has actually been used in the computations the definition is probably most concisely done according to the first way, which goes back to Courant-Snyder paper [16].

The linearized canonical equations for motion in the transverse plane around the reference orbit are (in the linear approximation $x' = p_x, y' = p_y$):

$$x'' + k_x(z)x = \delta/\rho(z). \quad (5.33)$$

$$y'' + k_y(z)y = 0. \quad (5.34)$$

The functions $k_x(z)$ and $k_y(z)$ are the focusing functions. In straight elements (as in the quadrupoles) they are related to the gradient of the magnetic field. The quantity $\rho(z)$ is the local radius of the curvature for the design orbit. In our model all the three functions defined above have the periodicity of the basic FODO cell. Finally $\delta = (p - p_o)/p_o$ is the relative deviation from the design momentum p_o .

Because of linearity one can write the solution to (5.33) as the superposition of a particular solution denoted by $\delta D(z)$, having the same periodicity as the lattice functions, and a general solution of the associated homogeneous equation. The function $D(z)$ is called the dispersion function and describes the closed orbit for a particle ‘off-momentum’. More on the concept of the dispersion function

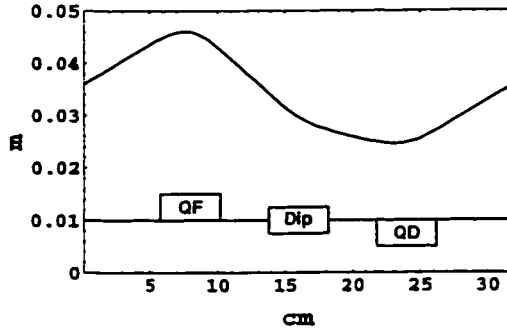


Figure 5.11: Dispersion function for the E-Ring.

can be found in Chapter 8. The solutions of the homogeneous part of (5.33) and (5.34) can be written in terms of the auxiliary functions $\beta_x(z)$ and $\beta_y(z)$, having the same periodicity as the lattice, known in the literature as betatron functions

$$x = \sqrt{\epsilon_x \beta_x} \sin[\psi_x(z) + \psi_{xo}],$$

$$y = \sqrt{\epsilon_y \beta_y} \sin[\psi_y(z) + \psi_{yo}]. \quad (5.35)$$

The phase function $\psi_x(z)$ is related to β_x by $\psi_x(z) = \int_0^z 1/\beta_x(s)ds$, and similarly for $\psi_y(z)$. The quantities ϵ_x, ϵ_y (the emittances), and ψ_{xo}, ψ_{yo} are constants of the motion.

The tunes in the vertical and horizontal plane are defined as $\nu_x = \psi_x(L)/(2\pi)$ and $\nu_y = \psi_y(L)/(2\pi)$ with L being the length of the machine. (The quantities $\psi_x(L_{FODO})$ and $\psi_y(L_{FODO})$ are the phase advance for the FODO cell). The tunes represent the number of oscillations in each direction of the transverse plane that a particle undergoes for each turn around the machine.

The the betatron and the dispersion functions for the E-Ring for a working point of $\nu_x = 7.80$ and $\nu_y = 7.67$ are shown in Fig. 5.10 and Fig. 5.11 respectively. We emphasize that in the calculation the fringe effects are fully taken into account. Finally in Fig. 5.12 we report the machine tunes as functions of the current circulating in the quadrupole windings (which is proportional to the

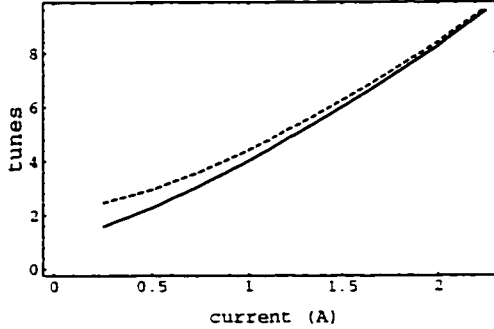


Figure 5.12: Horizontal (solid line) and vertical (dashed line) tunes as a function of the current in the quadrupole magnet windings.

quadrupole gradient). The absolute value of the gradient is the same for the focusing and the defocusing quadrupoles. In the absence of the dipole magnets the tunes ν_x and ν_y in each direction would be the same. Instead, as one can observe from Fig. 5.12 the symmetry between the two planes is broken. This is due to the extra focusing provided by the dipoles. The nature of this extra focusing is twofold: it is partly geometric and partly due to the extended fringes (see e.g. [66] for a discussion).

5.7 Single Particle Dynamics Study: Main Results

Once the transfer map for the FODO cell has been computed one can use it to calculate and study particle orbits by successive iteration (ray tracing or ‘tracking’). Different choices are possible. One can choose to compute the one turn map and use this for tracking. Or one can compute the map corresponding to the largest period of the lattice, i.e. in our case the map for the FODO cell. Alternatively, one can decide to apply all the maps corresponding to portions

of the FODO cell. In general the shorter the interval in z spanned by a map the more accurate the computation of the orbit is. More accuracy, however, is achieved at the expense of increased computing time.

Moreover, one has the freedom to choose among symplectic integrators. A map in Taylor form in general is not suitable for tracking because the symplectic condition is usually significantly violated by truncation. There are different schemes that one can apply to produce maps that are exactly symplectic (to round-off error precision) and accurate through the same order as the original map. The scheme implemented in MARYLIE is based on the use of generating functions for canonical transformations. The approximating symplectic map is implicitly defined by a system of nonlinear algebraic equations that have to be solved numerically at each iteration.

More recently the Cremona symplectification algorithm [1] has been proposed. Cremona maps are *polynomial* symplectic maps. For any given symplectic Taylor map truncated through a certain order the idea of Cremona symplectification is to write a polynomial symplectic map that agrees with the original map through the same order. The additional higher order terms that need to be added to the truncated Taylor map to restore the symplectic condition are chosen in an optimal fashion so that they are, in some sense, as small as possible.

In this study we mostly used the MARYLIE ray tracing routine. However, for the purpose of a cross checking in some cases we have also used the program CTRACK [2], that implements the idea of Cremona symplectification. We will comment on this comparison later on.

The purpose of ray tracing is to determine the domain of stability for beam particles in phase space, or as it is often called in the literature the 'dynamic

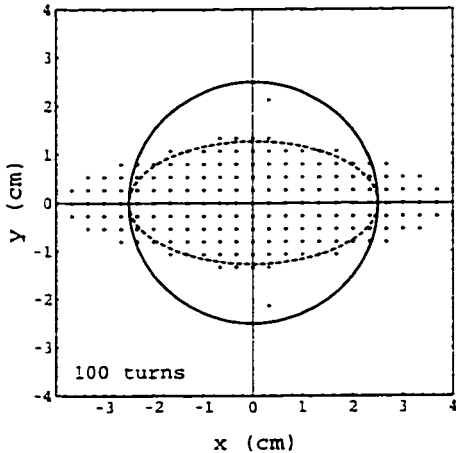


Figure 5.13: Dynamic aperture for E-Ring (ideal lattice).

aperture' (DA). Let us define the dynamic aperture operatively. First of all one fixes an 'observation point' along the Ring which we take to be $z = z_o$. Next consider the phase space defined at $z = z_o$. Each point of the phase space specifies a different orbit under the action of the one turn (or FODO cell) map. The orbit can be stable, that is after a certain number of map iterations the orbit still remains in the vicinity of the initial conditions, or unstable. The set of initial conditions in phase space leading to stable orbits defines the domain of stability for the map or dynamic aperture. Sampling the all 6D phase space, however, would be too-time consuming. And most often one considers plane sections of the phase space. A possible choice, which we will make is to consider the surface of section given by the $x - y$ plane (i.e. the initial conditions for the transverse momenta are set to be zero).

There is a certain arbitrariness in defining operatively if an orbit is stable. In practice one sets a maximum value for the amplitude of the betatron oscillations. If the amplitude of a particle oscillations exceeds that maximum value the orbit is considered unstable. In many cases, and in this study in particular, it turns

out that the resulting DA is not strongly affected by the exact setting of the threshold amplitude.

The choice of how long to follow a particle along its orbit is also somewhat arbitrary. One is often limited by computation time and can simulate the particle dynamics only over a small fraction of the number turns that the beam is expected to circulate. For the case of the E-Ring the situation is different. The goal is to get the full-current beam to go through a dozen turns. Therefore, only a modest number of iterations needs to be considered. In this study we set the standard choice for the number of iteration to be 100 turns with occasional excursions to larger numbers. We set $z = z_o$, the ‘observation point’ for the beam dynamics along the Ring, to be in the center of a focusing quadrupole.

The main result contained in this Chapter is summarized in Fig. 5.13. The dots in the picture represent the dynamic aperture for the E-Ring defined over 100 turns of the Ring at a working point $\nu_x = 7.711$, $\nu_y = 7.877$. This working point corresponds to the following choice of the currents in the magnets windings:

$$I_{DQ_{quad}} = I_{FQ_{quad}} = 1.8854 \text{ A} \text{ and } I_{dip} = 2.9404 \text{ A}$$

This result has been obtained by using the MARYLIE symplectic ray tracing routine. By using the MARYLIE symplectic raytracing routine it can happen that the algorithm that solves for the implicitly defined symplectified map does not converge within the required accuracy. This is usually the case when the nonlinearities associated with the map are strong. Failure in the converge of the algorithm is interpreted as a loss of the particle. In the calculation tracking has been carried out according to the splitting (5.31) and (5.32). The physical boundary of the pipe wall has not been taken into account. As a consequence the dynamic aperture is allowed to be larger than the pipe cross section (cir-

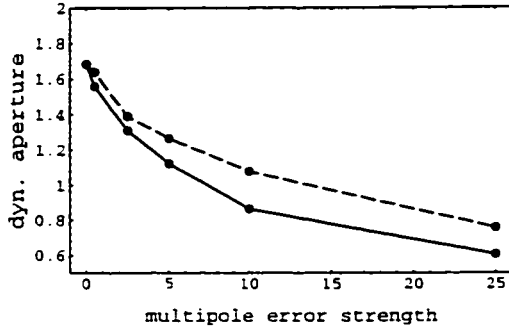


Figure 5.14: Dynamic aperture for E-Ring vs. relative multipole error strength (in units of 10^{-4} . The DA is expressed in units of the acceptance ellipse. See Fig. 5.13 .

cumference in the picture). The dashed ellipse in Fig. 5.13 defines the linear acceptance. The dots contained within the dashed ellipse designate orbits that in the linear approximation will not hit the wall of the vacuum pipe. The acceptance ellipse has its major axis in the horizontal (x) plane because the betatron function $\beta_x(z)$ has its maximum and $\beta_y(z)$ has its minimum at $z = z_o$. As one can observe the dynamic aperture is limited, but it exceeds the machine acceptance. This is good news for the E-Ring project. Also notice that the profile of the DA is elongated in the x direction. This is consistent with the observation regarding the values of the betatron functions at $z = z_o$. If we had taken the ‘observation point’ z_o in the middle of a defocusing quadrupole the DA would appear elongated in y .

The second most important result is related to a study of the sensitivity of the dynamic aperture to possible random error distributions. A study of this dependence is important because deviations from the ideal values of the fields are unavoidable in any real machine. Magnet mispowering, misplacement, and imperfect manufacture are all possible sources of undesired errors. A realistic modeling for all these errors would be very difficult if not impossible. A crude

but widely used model is to represent the errors as multipole kicks to add on top of the main fields. In the present study the error kicks are placed in the middle of the focusing and defocusing quadrupoles magnets. Only kicks of order higher than the first (dipole kicks) have been considered. That is we do not take into account errors that can affects the reference orbit. One reason is that here we are mostly interested in studying the dependence of the DA on nonlinear effects. The second reason is that errors in the reference orbit would require the enormous computational effort of calculating the transfer map 'individually' for each segment of the 36 FODO cells. A study of the effect of reference orbit distortions is best carried out in a simplified model where the magnet fringes are not extended.

In the modeling of errors we assume a random distribution over the spectrum of all multipoles through 6th order. The relative multipoles are defined according to (5.20) and (5.21) at the reference radius $\rho_o = .5R_{Quad} = 1.395$ cm. The relative strength of each multipole is

$$|b_i| \leq s_i, \quad (5.36)$$

$$|a_i| \leq s_i. \quad (5.37)$$

Each multipole distribution is uniform between $-s_i$ and $+s_i$ and is uncorrelated to the distributions of the other multipoles. Various values of the strength s_i and various realization of the random distribution have been considered. Fig. 5.14 shows a possible way to represent the results. For a fixed realization of the random distribution of errors we have varied the multipole strength s_i and computed the area of the DA and expressed it in units of the area of the acceptance ellipse (dashed ellipse in Fig. 5.13). The dashed line corresponds to the case where higher (> 2) order skew components are set to zero (i.e $a_3 = a_4 = a_5 = a_6 = 0$);

the solid line corresponds to the case of Eq. (5.37) with the maximum strength s being the same as for the multipole components ($s_i = s$, $i = 2, 3, 4, 5, 6$). The two curves clearly set an upper bound to the tolerable strength of the errors of the order of $s_{max} \simeq 5 \times 10^{-4}$, to have a DA exceeding the linear acceptance. It turns out that the DA in the presence of random errors does not seem to depend significantly (at least through 100 turns) on the particular realization of the error distributions.

5.8 Single Particle Dynamics Study: Other Results

In this Section we present some additional results found in connection with simulations for the E-Ring. First of all, as a way to locate the main source of the nonlinearities determining the DA, we studied a modified version of the E-Ring lattice where the dipoles are replaced by drifts (of the same length). Fig. 5.15 shows the DA for this case. The ray tracing has been carried out by circulating through the maps \mathcal{M}_I , \mathcal{M}_{II} with $\mathcal{M}_{FODO} = \mathcal{M}_I \circ \mathcal{M}_{II}$. The map \mathcal{M}_I , is calculated from a focusing quadrupole to the next defocusing quadrupole (center to center). In turn, the map \mathcal{M}_{II} , is calculated from a defocusing quadrupole to next focusing quadrupole. The strength of the quadrupole gradients is as in the case discussed in the previous section (see Fig. 5.13). Therefore, also the strength of the nonlinearities with the quads are expected to be the same. However the resulting tunes or phase advances of the FODO cells are different in the two cases because of the extra focusing provided by bends. Comparison between the Fig. 5.13 and Fig. 5.15 shows little difference in the DA , suggesting

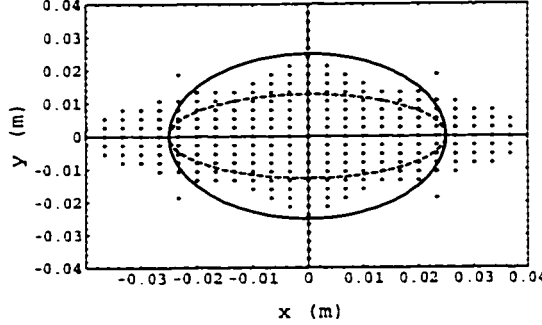


Figure 5.15: Modified E-Ring lattice (dipoles replaced by drifts). Dynamic aperture obtained by circulating through \mathcal{M}_I , \mathcal{M}_{II} with $\mathcal{M}_{FODO} = \mathcal{M}_I \circ \mathcal{M}_{II}$.

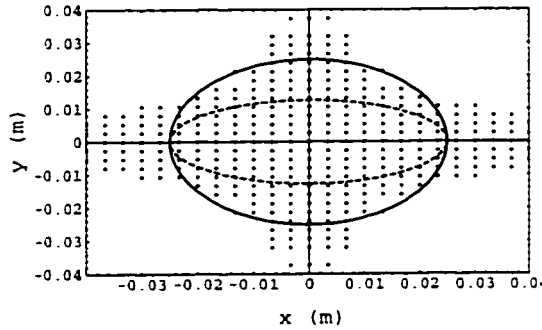


Figure 5.16: Modified E-Ring lattice. Dynamic aperture obtained by iterating \mathcal{M} .

that the dominant nonlinearities may be originating from quadrupole magnets. As we will show below in this chapter, this surmise is consistent with results from the normal form analysis. (see Sec. 5.8.1).

Since the modified E-Ring lattice (with the dipole magnets replaced by drifts) provides one with more flexibility in computation we have used it as a testbed for some additional checks. First of all we have compared the results of Fig. 5.15 with tracking done with a single FODO cell map. The result is shown in Fig. 5.16. One can observe a certain difference, particularly in the shape of the DA along the vertical axes. An additional test has also been made in which the map for the FODO cell was split into 4 pieces. The DA portrait in that case shows little

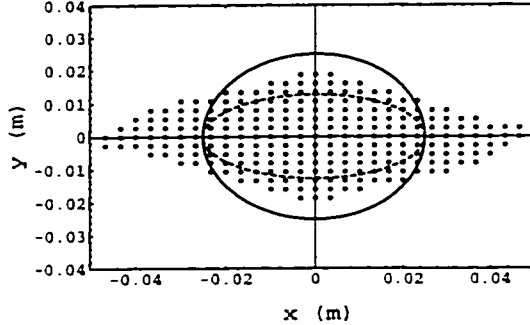


Figure 5.17: Modified E-Ring lattice. Dynamic aperture obtained by using the Cremona symplectified map \mathcal{M}_{FODO} .

difference from Fig. 5.15. This suggests that breaking the computation of the FODO map into two parts should be adequate. The DA computation carried out with the MARYLIE tracing routine has also been compared against calculations done with CTRACK [2]. The Cremona symplectification was determined starting from the Taylor map corresponding to the FODO cell map. The results shown in Fig. 5.17 from the the CTRACK calculation seem closer to those reported in Fig. 5.15 than to those shown in Fig. 5.16 . This finding corroborates the expectation that Cremona symplectification for a one-turn map can produce a DA which is closer to the DA for the ‘real’ map. Closer inspection shows that the DA from CTRACK is smaller by about 10%.

Additional computations not reported here on various modified lattices carrying additional nonlinearities in the form of kicks show that such a deviation of 10% between CTRACK and MARYLIE seems to be systematic.

As a further check we studied how the effect of the nonlinearities associated with fringes adds to the nonlinearities due to multipole errors. For this purpose we compared the modified E-Ring lattice with random multipole kicks added on top of the existing nonlinearities due to the fringes and systematic multipoles.

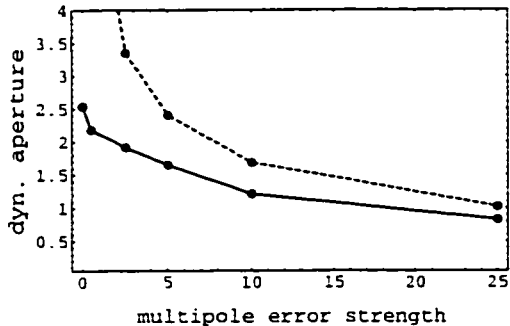


Figure 5.18: Dynamic aperture in the presence of random multipole errors on top of a linear lattice (dashed line) and the ideal lattice (solid line) with the nonlinear fringe effects included. Modified E-Ring model.

and a model lattice where the random multipoles were the same but the rest of the lattice was taken in the linear approximation. A comparison in terms of dynamic aperture for various values of the multipole strength is presented in Fig. 5.18. The difference between the two curves is entirely due the systematic nonlinearities present in the ideal (no errors) lattice. The dashed curve would be the result that one would obtain by applying to the study of the lattice the standard tools for simulations. Notice also that, as one could easily expect, the difference between the two curves becomes smaller as the strength of the error increases.

Finally we carried out a systematic study of the dependence of dynamic aperture on the tunes. Again for the modified E-Ring lattice with the dipoles replaced by drifts we varied the currents in the quadrupole magnets to adjust gradients. In this calculation, instead of computing the dynamic aperture as an area we found the projection of the Dynamic Aperture DA_x and DA_y along the x and y axis. The calculation was done by making a fine scanning of the initial conditions along the axes beginning from the origin. The first initial condition producing an unstable orbit determines the Dynamic aperture DA_i .

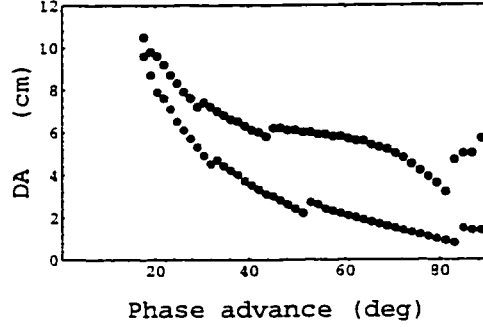


Figure 5.19: Dynamic aperture DA_x (gray points, bottom) and DA_y (black points, top) vs. phase advance per FODO Cell (which equals tune/36). Modified E-Ring model.

$i = x, y$. This methods may miss occasional isolated stable points beyond the first unstable orbit.

By looking at Fig. 5.19 one can notice that there is a distinctive trend of the dynamic aperture to increase as the phase advance decreases. Moreover one can also observe the presence of some discontinuities. For example, in proximity of the phase advance $\phi \simeq 80^\circ$ the dynamic aperture in both x and y has a sudden increase. The first pattern can be explained in terms of the strength of the nonlinearities associated with fringes and systematic multipoles. The phase advance per FODO cell increases with increasing quadrupole field strength. This implies that not only the magnetic field gradient, which controls the phase advance, but also the various nonlinearities associated with the gradient profile or the systematic duodecapoles become larger. This produces an erosion of the dynamic aperture.

On the other hand, the discontinuities one observe in the profiles of the Dynamic Aperture (like the one at $\phi \simeq 80^\circ$) are due to the emergence of nonlinear resonances. In particular the one responsible for the jump at $\phi \simeq 80^\circ$ is the 1:4 resonance (see [60]). What happens is that in the vicinity of those tunes the

DA is basically determined by the location of a chain of resonance islands in phase space. As the linear phase advance increases the resonance moves inward dragging along with it the border of the dynamic aperture. However, as soon the chain of resonance islands is close enough to the origin, it suddenly stops determining the dynamic aperture. The DA then experiences a jump upward.

Finally we mention a result concerning the dependence of DA on the physical aperture of the magnet. This was a practical problem at the initial stage of the E-Ring design when considered the alternative of an aperture of $R=2.2$ cm or $R=2.790$ cm for the magnets. The two values correspond to aspect ratios (the aspect ratio is the quantity radius/semilength) of 1 and .7935 . As a consequence of an increased aperture the extension of the fringes also increases. The question was: does the DA become worse if one chooses the larger aperture? There was the expectation that this could be the case based on some results from earlier studies [25]. This point will be specifically addressed in the next Chapter. From the simulations it turned out that the absolute size of the DA in going from an aperture of $R=2.2$ cm to an aperture of $R=2.790$ cm not only does not decrease, but seems to become slightly better.

5.8.1 Nonlinear (Nonresonant) Normal form Analysis

A normal form analysis provides some understanding of some of the results reported in the last Section. The idea of a normal form for a Lie map was introduced in Sec.1.5 from the viewpoint of map calculation. Given a map \mathcal{M} one introduces a transformation \mathcal{A} in such a way that the transformed map $\mathcal{N} = \mathcal{A}\mathcal{M}\mathcal{A}^{-1}$ is in some way simple. Let us restrict ourself to the 2D case (i.e ignore motion in the longitudinal direction). If all the eigenvalues of the linear

part of the map \mathcal{M} sit on the unit circle and their ratio is not a rational number (nonresonance condition) one can show using the results of Sec. 1.5 that the map \mathcal{N} can be written as

$$\mathcal{N} = \exp(- : \mathcal{H} :), \quad (5.38)$$

where \mathcal{H} is a pseudo-Hamiltonian of the form:

$$\begin{aligned} \mathcal{H}(I_x, I_y) &= \omega_{10}I_x + \omega_{01}I_y + \frac{1}{2}\omega_{20}I_x^2 + \frac{1}{2}\omega_{02}I_y^2 + \frac{1}{2}\omega_{11}I_xI_y \\ &+ \frac{1}{3}\omega_{30}I_x^3 + \frac{1}{3}\omega_{21}I_x^2I_y + \frac{1}{3}\omega_{12}I_xI_y^2 + \frac{1}{3}\omega_{03}I_y^3\dots \end{aligned} \quad (5.39)$$

Here I_x and I_y are the action-like variables:

$$I_x = \frac{1}{2}(x^2 + p_x^2). \quad (5.40)$$

$$I_y = \frac{1}{2}(y^2 + p_y^2). \quad (5.41)$$

The quantities $\nu_x = \omega_{10}/(2\pi)$ and $\nu_y = \omega_{01}/(2\pi)$ coincide with the horizontal and vertical *linear* tunes. The pseudo-Hamiltonian (5.39) provides a way to compute the nonlinear correction to the linear tune as a function of the amplitude of oscillation

$$2\pi\nu_x = \frac{\partial\mathcal{H}}{\partial I_x} = \omega_{10} + \omega_{01} + \omega_{20}I_x + \frac{\omega_{11}}{2}I_y + \omega_{30}I_x^2 + \frac{2\omega_{21}}{3}I_xI_y + \frac{\omega_{12}}{3}I_y^2 + \dots. \quad (5.42)$$

and similarly for ν_y .

These corrections are a measure of the nonlinearity of the system. For example, one can show that sextupole, octupole or pseudo-octupole components of the field contribute to the terms of first and higher order in I_x and I_y . On the other hand, decapoles and duodecapoles contribute to the terms of order three and higher in I_x and I_y . Comparison between the various coefficients may

Table 5.6: Pseudo Hamiltonian Coefficients (ideal E-Ring lattice)

ω_{20}	ω_{11}	ω_{02}	-
102.92	253.33	123.10	-
ω_{30}	ω_{21}	ω_{12}	ω_{03}
-2.295×10^4	-1.280×10^4	14.859×10^4	-9.343×10^4

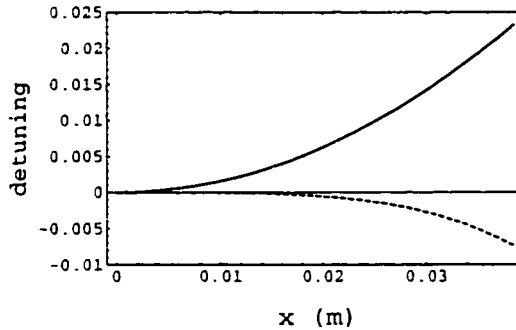


Figure 5.20: First order (solid line) and second order (dashed line) nonlinear detuning as a function of the physical amplitude of oscillations ($y = 0$).

give an idea of what terms are important. The table 5.6 reports the various coefficients for the ideal E-Ring model.

One can get a better understanding of the relative importance of the various coefficients by plotting the detuning as a function of amplitudes. Fig. 5.20 shows the functions $\omega_{20}I_x$ (solid line) and $\omega_{30}I_x^2$ (dashed line) as a function of x (having set $p_x = y = p_y = 0$). One can observe that the detuning due to the term linear in I_x (i.e. quadratic in x) is significantly larger than that due to the term quadratic in I_x (i.e. proportional to x^4). This is consistent with the fact that the DA is not very different if calculated using a third order or 5th order map.

Next, one would like to determine the source of the major contribution to the dominant nonlinearity. From the calculations shown in the previous section we already have some hints that point at the pseudo-octupoles associated with

Table 5.7: Pseudo Hamiltonian Coefficients

-	ω_{20}	ω_{11}	ω_{02}
Model A	102.92	253.33	123.10
Model B	102.38	245.00	102.378
Model C	11.87	17.39	13.10
Model D	146.40	314.88	142.24

the quadrupole fringes as the main source of nonlinearities. The normal form analysis confirms this suspicion.

Table 5.7 reports the coefficients ω for the ideal E-Ring lattice (Model A), against those of the modified E-Ring lattice with the dipoles replaced by drifts (Model B) and those obtained by a lattice built using MARYLIE standard elements with the hard edge treatment of the fields turned off (Model C) and on (Model D). In Model C the only nonlinearities come from the geometric terms of the Hamiltonian (i.e. the description of the fringe nonlinearities is not included).

Comparison between Model A and Model B shows that the source of the dominant nonlinearities is mostly localized in the quadrupoles. Comparison between Model A and Model C confirms that the pseudo-octupoles are the source of about 90% of the nonlinearity. Finally, comparison between Model A and Model D shows that in the hard edge limit one gets an overestimate of the nonlinearity.

5.9 Summary

In this Chapter we have used a detailed calculation of transfer maps for beamline elements, including fringe field effects, to determine the dynamic aperture of the

E-Ring under construction at the University of Maryland. We have shown that, although the effect of the nonlinearities associated with the fringes is significant, it is not sufficient to bring the dynamic aperture below the acceptance.

In the ideal lattice the major source of nonlinearities are the pseudo-octupoles associated with the z dependence of the gradient in the quadrupole magnets. These nonlinearities are significantly larger than the nonlinearities resulting from the systematic duodecapole components. The dynamic aperture depends substantially on the value of the gradient in the quadrupole magnets. A larger dynamic aperture can be obtained by reducing the phase advance for the FODO cells (i.e. by reducing the gradient in the quads).

Finally, random multipole errors added to the systematic multipoles already present in the ideal design and to nonlinearities due to fringes further decrease the dynamic aperture. The study set an upper limit to the tolerable strength of the integrated relative multipoles of the order of 5×10^{-4} .

Chapter 6

Dynamical Effects of Soft Fringes: an Analytical Model

The topic of the aberrations produced by fringe fields in magnets have been the subject of many studies and papers over the last three decades (see e.g. [29, 43, 35, 27, 71, 72]). A number of analytical results have been found: general formulas for the aberrations worked out perturbatively are now available as well exact formulas for aberrations in the hard edge limit. Moreover, many codes have been created that allow very accurate calculations of charged particle dynamics through fringes, upon specifications of the fringe distribution, and also incorporate the analytical formulas in the hard edge limit that can be used when detailed knowledge of the fields is missing.

However, in spite of the progress made in understanding fringe aberrations, there still seems to be some confusion about the scaling of the aberrations with the extension of fringes. A widespread belief rooted in the ‘common sense’ of the accelerator physics community is that the extension of fringes at the ends of magnets should be contained as much as possible. Although there may be some good reasons for that belief, limiting the strength of aberrations is not one of

them.

A source for this misconception may have been the fact that aberrations increase as the length of a magnet decreases. In other terms, given for instance two quadrupoles with the same focal length, the aberrations are larger for the magnet with shorter length. Because short magnets are usually associated with more extended fringe fields that fact may have generated the wrong perception that the more extended the fringes are the higher the aberrations.

Whatever the motivations may be, it is not unusual to find statements like the following, taken from an otherwise well written and interesting paper [25] p. 4 :

'As the aperture ratio [i.e. the ratio aperture/length] of a magnet quad increases [a larger aperture ratio means more extended fringes] a number of phenomena degrade the field quality. First, the $\cos 2\theta$ fringe field [i.e. the pseudo-octupoles] near the ends of the magnets begin to be *increasingly* important relative to the wanted z -independent component that dominate the center of the magnet. ... the pseudo-octupoles fields lead to net forces on the individual particles ... these forces are anharmonic and may lead to emittance growth.'

The statement above is at best ambiguous without specification of how a larger aperture ratio is obtained. It would be correct if the increase in the aperture ratio were achieved by varying the magnet length (and, correspondingly, the strength) and keeping the aperture fixed. On the contrary, if a larger aperture ratio is achieved by increasing the aperture and keeping the length of the magnet (and integrated strength) unvaried the opposite turns out to be true. Although it is a fact that for more extended fringes the z -dependent portion of the field becomes larger compared to the portion in the body of the magnet where the

field are basically z -independent, it does not follow that the nonlinearities of the particle dynamic becomes higher. In fact, the aberrations depend not only on the length of the fringe region but also on the derivatives of the fields with respect to z , and the value of the derivative will tend to decrease as the extension of the fringes increases. And in the balance between these two competing factors - a larger extension of the fringes and smaller values of the field derivatives - the latter will actually prevail.

To our knowledge there has not been any study done to explore even at the lowest order the scaling of the aberrations with respect to the extension of the fringe fields, with a realistic modeling of the fields. However, magnets with short length and relatively extended fringes are increasingly used in practical applications and an understanding of that scaling would be useful. The study presented here aims at clarifying this point. The motivation for this study came after some simulations done for the Maryland Electron Ring (see Chapter 5) at the early stage of the design process when it was necessary to see whether an enlargement of the pipe size from the value originally planned was consistent with an acceptable dynamic aperture.

The simulations showed that a further increase in the aperture ratio not only did not worsen the dynamic aperture, but seemed to improve it slightly (see Chapter 5). The study presented in this Chapter explains why. In the study we compute the transfer map for a charged particle passing through a printed circuit quadrupole of the type described in Sec. 5.3 , for which we have exact analytical formulas. The calculation of the map is repeated for various values of the aperture ratio and a constant magnet length in order to compare the pseudo-octupole aberrations in the various cases. In comparing the aberrations for the

various magnets with different aspect ratios, we make sure that the integrated quadrupole component of the field is kept constant. Physically this can be achieved by means of a suitable scaling of the current in the printed circuit. The calculation is done numerically and the results are then compared to analytical formulas.

6.1 The Quadrupole Magnet Model

The fields associated with a Lambertson printed circuit magnet are described in Chapter 5, where the lower terms in the multipole and Taylor expansion of the vector potential are reported. The analytical formulas involve summations over n loops of conductor. For simplicity in this Chapter we assume $n = 1$. In the gauge $A_\phi = 0$ the vector field Taylor expansion through the fourth order in the transverse variables reads:

$$\begin{aligned} A_z &= \frac{1}{2}\mathcal{G}(x^2 - y^2) - \frac{1}{12}\mathcal{G}''(x^4 - y^4), \\ A_x &= -\frac{1}{4}\mathcal{G}'(x^3 - xy^2), \\ A_y &= \frac{1}{4}\mathcal{G}'(y^3 - yx^2). \end{aligned} \quad (6.1)$$

where $\mathcal{G}(z) = 2C_2(z)$, is the on axis (magnetic field) gradient, with the function $C_2(z)$ defined in (5.11). Writing the vector potential in cylindrical variables will display the ‘cos 2 ϕ ’ azimuthal symmetry typical of a quadrupole

$$A_z = \frac{1}{2}\mathcal{G}\rho^2 \cos 2\phi - \frac{1}{12}\mathcal{G}''\rho^4 \cos 2\phi, \quad (6.2)$$

$$A_\rho = -\frac{1}{4}\mathcal{G}'\rho^3 \cos 2\phi, \quad A_\phi = 0. \quad (6.3)$$

The quadratic terms in (6.1) are associated with linear dynamics. The cubic and quartic terms are the source of the pseudo-octupole aberrations, as we will

see in more detail in the next section. In this study we neglect higher order aberrations.

Before ending this section it is useful to get an insight into the shape of the gradient function $\mathcal{G}(z)$ and its first derivative and how they vary as the aspect ratio of the magnet.

First of all it is useful to calculate the integrated gradient. Such a quantity is directly related to the focal length of the magnet. Typically, quadrupoles having the same integrated gradient will have very close focal lengths.

$$\int_{-\infty}^{\infty} \mathcal{G}(z) dz = 32 \frac{\mu_0}{4\pi} I \frac{\gamma^2}{l} \sum_{m=1}^n \lambda_m \cos(2\phi_m). \quad (6.4)$$

(For the meaning of the various parameters appearing in (6.4) see Sec. 5.3.) The formula for the integrated gradient tells us that for a fixed value of the magnet length the integrated gradient scales as the square of the aspect ratio (or with $1/R^2$). Therefore, if we want to compare quadrupoles with different aspect ratio and with the same integrated field gradient (that is with roughly the same focal length) we have to increase the current I accordingly. We can do that by defining the current as

$$I = \frac{I_1}{\gamma^2}. \quad (6.5)$$

where I_1 is a constant independent of the aspect ratio γ . With such a definition for the current the integrated gradient in (6.4) is independent of the aspect ratio.

Fig. 6.1 shows different profiles for the field gradient $\mathcal{G}(z)$ produced by a single quadruplet of loops $n = 1, \lambda_1 = 1, \phi_1 = .023$ with the current (6.5) and with $I_1 = 20A$. The different profiles correspond to different choices of the aspect ratio as indicated in the picture. We see that as the the aspect ratio becomes smaller (larger aperture of the magnet) the extension of the fringes becomes

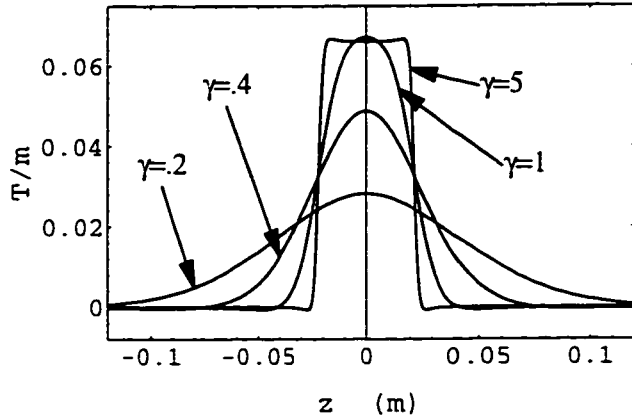


Figure 6.1: Gradient profiles for different values of the aspect ratio γ . The integral of the various curves are the same. (Quadrupole semilength $l = .022$ m. $I_1 = 20$ A).

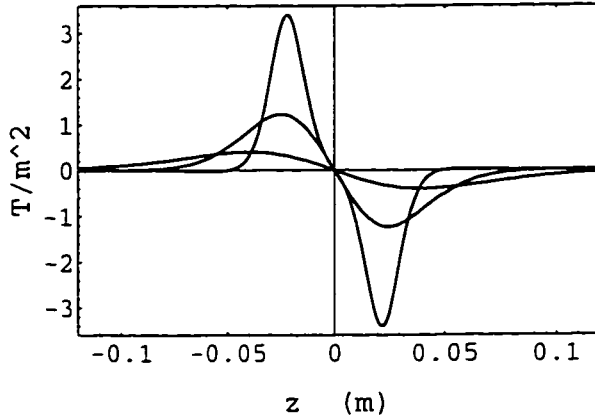


Figure 6.2: First derivative of the gradient profiles for $\gamma = 1, .4, .2$.

larger. Conversely, in the limit $\gamma \rightarrow \infty$ the field gradients approaches a box profile that can be expressed in terms of the Heaviside step function \mathbf{H} as

$$\lim_{\gamma \rightarrow \infty} \mathcal{G}(z) = \mathcal{G}_o [\mathbf{H}(z/l + 1) - \mathbf{H}(z/l - 1)] \quad (6.6)$$

with

$$\mathcal{G}_o = 16 \frac{I_1 \mu_o}{4\pi} \frac{\cos 2\phi_1}{l^2} \quad (6.7)$$

Fig. 6.2 displays the profile of the first derivative $\mathcal{G}'(z)$. As γ tends to ∞ .

$\mathcal{G}'(z)$ becomes singular at $z = \pm l$ approaching a delta function

$$\lim_{z \rightarrow \infty} \mathcal{G}'(z) = \frac{\mathcal{G}_o}{l} [\delta(z/l + 1) - \delta(z/l - 1)]. \quad (6.8)$$

6.2 Transfer Map Computation

The dynamics of a charged particle in the presence of the vector potential (6.1) is described through fourth order, by a Hamiltonian of the form

$$\begin{aligned} H = & \frac{1}{2}(p_x^2 + p_y^2) + \frac{1}{2}k(z)(x^2 - y^2) + \frac{1}{8}(p_x^2 + p_y^2)^2 + \frac{1}{12}\frac{q}{p_o}\mathcal{G}''(z)(x^4 - y^4) \\ & + \frac{1}{4}\frac{q}{p_o}\mathcal{G}'(z)(x^3p_x - y^3p_y) + \frac{1}{4}\frac{q}{p_o}\mathcal{G}'(z)(x^2yp_y - y^2xp_x), \end{aligned} \quad (6.9)$$

where the independent variable is the longitudinal position z . q is the charge of the particle, p_o its design mechanical momentum. The focusing function is $k(z) = (q/p_o)\mathcal{G}(z)$. In this model chromatic effects are neglected. One can write the Hamiltonian H as $H = H_2 + H_4$, the sum of a quadratic H_2 and a quartic H_4 term. The quadratic term governs linear dynamics while the quartic term is responsible for nonlinear aberrations. In the following \mathbf{z} will indicate the set of dynamical variables in 4D, $\mathbf{z} = (x, p_x, y, p_y)$.

One can use the Hamiltonian to write the canonical equation of motion or, alternatively but equivalently, to write the equation for the transfer map. Here we follow this second approach following the lines of map computation discussed in Chapter 1. We know already that a transfer map gives the point \mathbf{z}^f in phase space of a particle at $z = z_f$ as a function of the point \mathbf{z}^i at $z = z_i$:

$$\mathbf{z}^f = \mathcal{M}\mathbf{z}^i. \quad (6.10)$$

We recall the transfer map associated with the Hamiltonian (6.9) can be obtained

by solving the equation

$$\mathcal{M}' = \mathcal{M} : -H : , \quad (6.11)$$

where the transfer map \mathcal{M} , as a symplectic map, has the general representation

$$\mathcal{M} = \cdots \exp(: f_5 :) \exp(: f_4 :) \exp(: f_3 :) \mathcal{M}_2. \quad (6.12)$$

See Eqs. (1.38), (1.40). Here \mathcal{M}_2 describes the linear part of the map and is associated to the transfer matrix M by

$$z_a^f = \mathcal{M} z_a^i = \sum_{b=1}^4 M_{ab} z_b^i. \quad (6.13)$$

The f_n are homogeneous polynomials of order n in the dynamical variables. They contain all information about nonlinear aberrations. As pointed out in Chapter 1, writing the transfer map as in (6.12) is equivalent to but more convenient than using a Taylor map as it is done in the matrix formalism. Of course one can always recover the aberrations in the matrix formalism from the knowledge of the Lie generators f_n by applying the rules of the Lie calculus [19].

In the linear approximation equation (6.11) turns into a matrix equation for M , which can be written in either one of the following ways

$$\mathbf{M}' = \mathbf{JS}\mathbf{M}, \quad (6.14)$$

$$\mathcal{M}'_2 = \mathcal{M}_2 : -H_2 : , \quad (6.15)$$

with \mathbf{JS} being the Hamiltonian matrix associated with H_2 . If a solution of the linear equation (6.15) is known for any $z \in [z_i, z_f]$, which we write as $\mathcal{M}_2^{z_i \rightarrow z}$, one can immediately write an expression for the nonlinear generators of the map \mathcal{M} according to the theory outlined in [27]. The first nonvanishing Lie generator is

$$f_4 = - \int_{z_i}^{z_f} \mathcal{M}_2^{z_i \rightarrow z} H_4(\mathbf{z}, z) dz, \quad (6.16)$$

which describes third order aberrations.

For simplicity let us now limit ourselves to motion in the x plane; that is we let $y = p_y = 0$. The Hamiltonian then reads

$$H_x = \frac{1}{2}p_x^2 + \frac{1}{8}p_x^4 + \frac{1}{2}k(z)x^2 + \frac{1}{12}\frac{q}{p^o}\mathcal{G}''(z)x^4 + \frac{1}{4}\frac{q}{p^o}\mathcal{G}'(z)x^3p_x. \quad (6.17)$$

Suppose the linear matrix M is known and given at any location z as

$$M = \begin{bmatrix} m_{11}(z) & m_{12}(z) \\ m_{21}(z) & m_{22}(z) \end{bmatrix}. \quad (6.18)$$

Then we can write down the Lie generator for the third order aberrations in accordance with (6.16),

$$f_4 = -\frac{1}{8} \int_{z_i}^{z_f} \mathcal{M}_2 p_x^4 dz - \frac{1}{4} \frac{q}{p^o} \int_{z_i}^{z_f} \left[\frac{1}{3} \mathcal{G}''(z) \mathcal{M}_2 x^4 + \mathcal{G}'(z) \mathcal{M}_2 p_x x^3 \right] dz. \quad (6.19)$$

The first term in the right hand side is a purely kinematic term and is present even in the case $\mathcal{G}'(z)$ vanishes. In the following we will refer to the aberrations produced by this term as ‘kinematic’ third order aberrations. For the kinematic term, by using (6.13), we can immediately write:

$$f_4^{kin} = -\frac{1}{8} \int_{z_i}^{z_f} (m_{21}x + m_{22}p_x)^4 dz. \quad (6.20)$$

The second term depends on the derivative of $\mathcal{G}(z)$ and generates what we will call ‘dynamic’ aberrations. For the moment let us focus on the ‘dynamic’ term. The part of the dynamic term proportional to $\mathcal{G}''(z)$ can be integrated by part, so that the dynamic part of (6.19) can be written in the form,

$$f_4^{dyn} = -\frac{q}{p^o} \mathcal{G}'(z) \mathcal{M}_2 x^4 \Big|_{z_i}^{z_f} - \frac{1}{4} \frac{q}{p^o} \int_{z_i}^{z_f} [-\mathcal{G}'(z) \mathcal{M}_2' x^4 + \mathcal{G}'(z) \mathcal{M}_2 p_x x^3] dz. \quad (6.21)$$

If z_i and z_f are taken at a sufficient distance from the magnet so that the fields are in practice negligible the first term on the RHS may be made vanish. On

the other hand, by using (6.15):

$$\begin{aligned}
f_4^{dyn} &= -\frac{1}{12} \frac{q}{p^o} \int_{z_i}^{z_f} \mathcal{G}'(z) \mathcal{M}_2 : -H_2 : x^4 dz = -\frac{1}{4} \frac{q}{p^o} \int_{z_i}^{z_f} \mathcal{G}'(z) \mathcal{M}_2 p_x x^3 dz \\
&= \frac{1}{12} \frac{q}{p^o} \int_{z_i}^{z_f} \mathcal{G}'(z) \mathcal{M}_2 x^3 p_x dz \\
&= \frac{1}{12} \frac{q}{p^o} \int_{z_i}^{z_f} \mathcal{G}'(z) (m_{11}x + m_{12}p_x)^3 (m_{21}x + m_{22}p_x) dz. \tag{6.22}
\end{aligned}$$

In writing the second equality we have used the result

$$: H_2 : x^4 = [H_2, x^4] = [\frac{1}{2}p_x^2 + \frac{1}{2}k(z)x^2, x^4] = -4x^3p_x. \tag{6.23}$$

From (6.22) one can easily compute the map in the hard edge limit ($\gamma \rightarrow \infty$). For simplicity let us consider the transfer map only from $z = l - \epsilon$ to $z = l + \epsilon$ where ϵ is an infinitesimal quantity: $z = l$ is where one of the quadrupole edges is located. In this limit $\mathcal{G}(z)$ becomes the step function $\mathcal{G}_o \mathbf{H}(z - l)$ and $\mathcal{G}'(z)$ a Dirac δ function. Moreover as $\epsilon \rightarrow 0$ we have $\mathcal{M}_2^{(l-\epsilon)-(l+\epsilon)} \rightarrow \mathcal{I}$. Therefore $m_{11} = m_{22} \rightarrow 1$ and $m_{12} = m_{21} \rightarrow 0$. As a consequence in the hard edge limit we have from (6.20) $f_4^{kin} = 0$ and from (6.22) the result

$$f_4^{dyn} = \frac{1}{12} \mathcal{G}_o \frac{q}{p^o} x^3 p_x = \frac{k_o}{12} x^3 p_x. \tag{6.24}$$

Hence, the resulting map is

$$\mathcal{M}_2^{(l-\epsilon)-(l+\epsilon)} = \exp \left(\frac{k_o}{12} : x^3 p_x : \right). \tag{6.25}$$

The corresponding Taylor map can be readily be written as

$$\begin{aligned}
p_x^f &= \mathcal{M}_2^{(l-\epsilon)-(l+\epsilon)} p_x^i = p_x + \frac{k_o}{12} [x^3 p_x, p_x] = p_x + \frac{k_o}{4} x^2 p_x, \\
x^f &= \mathcal{M}_2^{(l-\epsilon)-(l+\epsilon)} x^i = x + \frac{k_o}{12} [x^3 p_x, x] = x - \frac{k_o}{12} x^3. \tag{6.26}
\end{aligned}$$

in agreement with the result obtained Lee-Whiting [43].

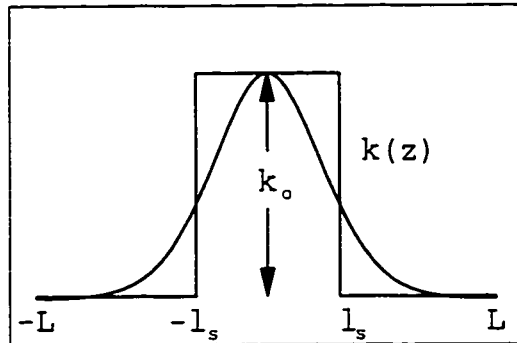


Figure 6.3: Approximation of the focusing function with a stepwise function.

6.3 Analytical Model

As one may have realized at this point, the main difficulty in dealing with z dependent Hamiltonians is not to determine the nonlinear generators as much as the linear part of the dynamics. In the general case one can neither integrate analytically equation (6.15), or reduce it to quadrature. Since the goal of this paper is to establish analytical formulas that give the scaling of aberrations and not to achieve exact results that can always be obtained numerically using the existing tools, it will be sufficient to find an approximated description for the linear part. The simplest method is to approximate the focusing function $k(z) = k_{step}(z)$ as a stepwise function, see Fig. 6.3. Two parameters need to be specified: the length l_s and the max value k_o of $k_{step}(z)$. One constraint we impose is that the integral of $k(z)$ equals that of $k_{step}(z)$. Therefore we need to specify either k_o or l_s , for any specified value of the aspect ratio. We can expect that as the aspect ratio decreases and the extension of the fringes increases, l_s should become larger and k_o smaller.

One possible choice is to use the standard definition of effective length and

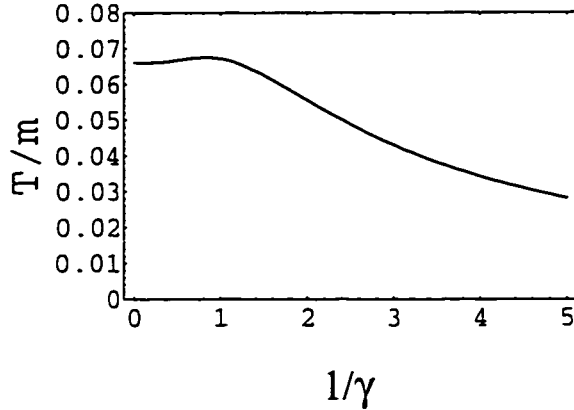


Figure 6.4: Gradient $\mathcal{G}(z = 0, \gamma)$ evaluated at $z = 0$ as a function of the aperture ratio (defined as $1/\gamma$, the inverse of the aspect ratio γ).

write:

$$k_o = \frac{q}{p^o} \mathcal{G}(z = 0, \gamma), \quad (6.27)$$

where we have explicitly highlighted the dependence on the aspect ratio γ . A plot for $\mathcal{G}(0, \gamma)$ as a function of the aperture ratio (the aperture ratio is defined as $1/\gamma$, the inverse of the aspect ratio γ) is shown in Fig. 6.4. Notice that $\mathcal{G}(0, \gamma)$ reaches a maximum and then decreases monotonically. At $\gamma = \gamma_1 \simeq 1/1.17$, $\mathcal{G}(z = 0, \gamma = \gamma_1)$ has the same value as at $1/\gamma = 0$. It turns out that if we modify the definition (6.27)

$$k_o(\gamma) = \frac{q}{p^o} \mathcal{G}(z = 0, \gamma/(1 + \gamma\gamma_1^{-1})) \quad (6.28)$$

we obtain a better approximation for the linear dynamics over a large range of values for the aspect ratio. The choice in (6.28) is equivalent to translating the graph of the curve in Fig. 6.4 on the left by the amount $1/\gamma_1$. For large values of the aperture ratio ($\gamma \rightarrow 0$) we have¹

$$l_s \rightarrow \frac{8}{9} \frac{l}{\gamma + \gamma_1^{-1}\gamma^2} \quad (6.29)$$

¹The constant \mathcal{G}_o was defined in (6.7).

$$k_o \rightarrow \frac{9}{8} \frac{q}{p_o} \mathcal{G}_o [\gamma(1 + \gamma_1^{-1} \gamma)]. \quad (6.30)$$

which is consistent with the observation that the extension of the fringes (roughly measured by l_s) is of the same order of the magnet aperture $R = l/\gamma$.

The transfer matrix M associated with the stepwise focusing function $k_{step}(z)$, between $z = z_i = -L$ and $z = z_f = L$ is the following. For $-L < z \leq -l_s$, M is a pure drift:

$$M = M_D(z + L) = \begin{bmatrix} 1 & z + L \\ 0 & 1 \end{bmatrix} \quad (6.31)$$

For $-l_s < z \leq l_s$, with $\omega = \sqrt{k_o}$

$$M = M_f(z) M_D(L - l_s) = \begin{bmatrix} \cos \omega(z + l_s) & \omega^{-1} \sin \omega(z + l_s) \\ -\omega \sin \omega(z + l_s) & \cos \omega(z + l_s) \end{bmatrix} M_D(L - l_s). \quad (6.32)$$

Finally, for $l_s < z \leq L$

$$M = M_D(z - l_s) M_f(2l_s) M_D(L - l_s). \quad (6.33)$$

The phase advance from $z = -l_s$ to $z = l_s$ is $\Phi = 2\omega l_s$. The phase advance Φ is defined in terms of the trace of the transfer matrix: $2 \cos \Phi = \text{tr}\{M\}$. For such a linear map the aberrations can be calculated explicitly. Consider the dynamic aberrations first. The Lie generator for the third order aberration for the motion in the x plane consists of 5 monomials:

$$f_4^{dyn} = x^4 f_{x^4}^{dyn} + x^3 p_x f_{x^3 p_x}^{dyn} + x^2 p_x^2 f_{x^2 p_x^2}^{dyn} + x p_x^3 f_{x p_x^3}^{dyn} + p_x^4 f_{p_x^4}^{dyn}. \quad (6.34)$$

Let us focus on $f_{x^4}^{dyn}$. We can decompose the integral defining the dynamic

aberrations into three parts [see Eq. (6.22)]:

$$f_{x^4} = -\frac{1}{12} \frac{q}{p^o} \int_{-L}^L \mathcal{G}' m_{11}^3 m_{21} dz = -\frac{1}{12} \frac{q}{p^o} \left\{ \int_{-L}^{-L+l_s} + \int_{-l_s}^{l_s} + \int_{L-l_s}^L \right\}. \quad (6.35)$$

The contribution from the first and the third integral on the RHS is negligible because \mathcal{G}' is almost zero for $|z| > l_s$. For the same reason we can approximate the second integral as

$$\int_{-l_s}^{l_s} \mathcal{G}' m_{11}^3 m_{21} dz \simeq \int_{-\infty}^{\infty} \mathcal{G}' m_{11}^3 m_{21} dz. \quad (6.36)$$

with $m_{11} = \cos \omega(z + l_s)$ and $m_{21} = -\omega \sin \omega(z + l_s)$. The integral on the RHS of (6.36) can be expressed in terms of the modified Bessel functions K_0 and K_1 (see Appendix B). Having introduced the definition

$$\begin{aligned} I(\Omega) &= \frac{q}{p^o} \int_{-\infty}^{\infty} \mathcal{G}' \sin(\Omega z) dz \\ &= \frac{1}{2} \frac{q}{p^o} \mathcal{G}_0 \sin(\Omega l) \frac{\Omega l}{\gamma} \left\{ \left[4 + \left(\frac{\Omega l}{\gamma} \right)^2 \right] K_1 \left(\frac{\Omega l}{\gamma} \right) + \frac{\Omega l}{\gamma} K_0 \left(\frac{\Omega l}{\gamma} \right) \right\} \end{aligned} \quad (6.37)$$

we find

$$f_{x^4}^{dyn} \simeq \frac{\omega}{48} [I(2\omega) \cos \Phi + I(4\omega) \cos 2\Phi]. \quad (6.38)$$

Similarly:

$$\begin{aligned} f_{x^3 p_x}^{dyn} &\simeq \frac{I(2\omega)}{24} [\sin \Phi + 2(L - l_s)\omega \cos \Phi] + \frac{I(4\omega)}{24} [\sin 2\Phi + (L - l_s)\omega \cos 2\Phi], \\ f_{x^2 p_x^2}^{dyn} &\simeq -\frac{L - l_s}{8} I(2\omega) [\sin \Phi + (L - l_s)\omega \cos \Phi] \\ &- \frac{L - l_s}{8} I(4\omega) \left[\sin 2\Phi + \frac{1 - \omega^2(L - l_s)^2}{2\omega(L - l_s)} \cos 2\Phi \right], \\ f_{x p_x^3}^{dyn} &\simeq -\frac{I(2\omega)}{8\omega^2} \left\{ [1 + \omega^2(L - l_s)^2] \sin \Phi + 2(L - l_s)^3 \omega^3 \cos \Phi \right\} \\ &+ \frac{I(4\omega)}{8\omega^2} [1 - \omega^2(L - l_s)^2] [\sin 2\Phi + (L - l_s)\omega \cos 4\Phi], \\ f_{p_x^4}^{dyn} &\simeq -\frac{I(2\omega)}{24\omega^3} \left[(L - l_s)\omega [1 + \omega^2(L - l_s)^2] \sin \Phi + \frac{1}{2} [1 - \omega^4(L - l_s)^4] \cos \Phi \right] \end{aligned}$$

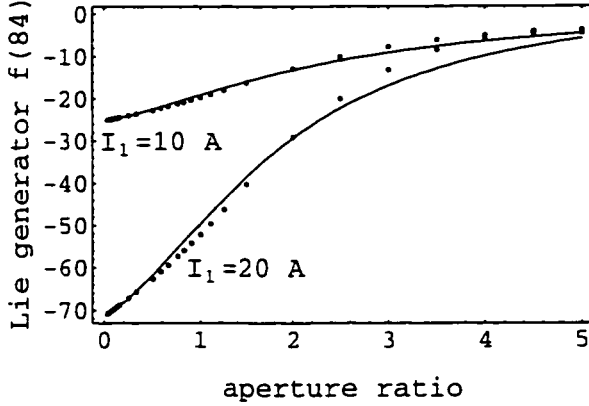


Figure 6.5: Lie generator $f_{x^4}^{dyn}$ as a function of the aperture ratio $1/\gamma$ for different values of I_1 . The hard edge limit is defined by $1/\gamma \rightarrow 0$. The solid lines correspond to the analytical calculation discussed in the paper, the dots to a numerical calculation using MARYLIE.

$$\begin{aligned}
& - \frac{I(4\omega)}{24\omega^3} \{ (L - l_s)\omega [1 + \omega^2(L - l_s)^2] \sin 2\Phi \\
& + \frac{1}{4} [1 - 6\omega^2(L - l_s)^2 + \omega^4(L - l_s)^4] \cos 2\Phi \}. \tag{6.39}
\end{aligned}$$

From the expression above one can recover the aberrations in the hard edge limit $\gamma \rightarrow \infty$ (with l kept fixed). We have

$$\lim_{\gamma \rightarrow \infty} I(\Omega) = -2 \frac{q}{p^o} G_o \sin(\Omega l) = -2\omega^2 \sin(\Omega l) \tag{6.40}$$

and

$$\begin{aligned}
f_{x^4}^{dyn} &= -\frac{\omega^3}{48} [\sin 2\Phi + \frac{1}{2} \sin 4\Phi], \\
f_{x^3 p_x}^{dyn} &= \frac{\omega^2}{12} \left[\sin^2 \Phi + \sin^2 2\Phi + \omega(L - l_s)(\sin 2\Phi + \frac{1}{2} \sin 4\Phi) \right]. \\
f_{x^2 p_x^2}^{dyn} &= \frac{\omega^2(L - l_s)}{4} \\
&\quad \times \left[\sin^2 \Phi + \sin^2 2\Phi + \frac{\omega(L - l_s)}{2} \sin 2\Phi - \frac{1 - \omega^2(L - l_s)^2}{4\omega(L - l_s)} \sin 4\Phi \right]. \\
f_{xp_x^3}^{dyn} &= \frac{3}{4} [1 + \omega^2(L - l_s)^2] \sin^2 \Phi + \frac{\omega^3(L - l_s)^3}{4} \sin 2\Phi \\
&\quad - \frac{1}{4} [1 - \omega^2(L - l_s)^2] \left(\sin^2 2\Phi + \frac{L - l_s}{2\omega^2} \sin 4\Phi \right),
\end{aligned}$$

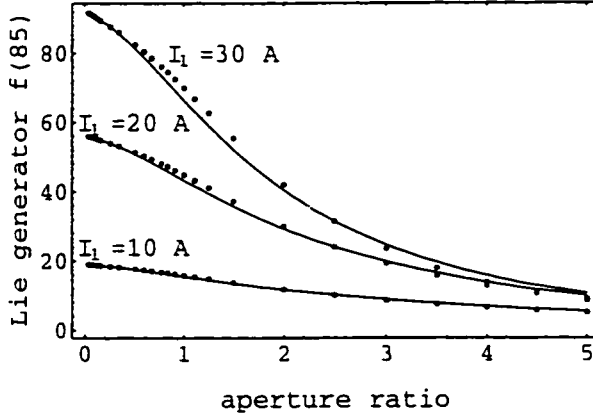


Figure 6.6: Lie generator $f_{x^3 p_x}^{dyn}$ as a function of the aperture ratio $1/\gamma$ for different values of I_1 . The hard edge limit corresponds to $1/\gamma \rightarrow 0$.

$$\begin{aligned} f_{p_x^4}^{dyn} &= \frac{L - l_s}{12} [1 + \omega^2(L - l_s)^2](\sin^2 \Phi + \sin^2 2\Phi) - \frac{1}{48\omega} [1 - \omega^4(L - l_s)^4] \sin 2\Phi \\ &\quad + \frac{1}{96\omega} [1 - 6\omega^2(L - l_s)^2 + \omega^4(L - l_s)^4] \sin 4\Phi. \end{aligned} \quad (6.41)$$

In the hard edge limit the quantities ω and Φ appearing in the expressions above are related by $2\omega l = \Phi$. We stress the fact that in the hard edge limit these expressions are exact.

The limiting form in the infinitely soft limit can also be written using

$$\lim_{\gamma \rightarrow \infty} I(\Omega) = -\frac{1}{2} \frac{q}{p^o p^o} G_o \sin(\Omega l) \sqrt{\frac{\pi}{2}} \left[4 \left(\frac{\Omega l}{\gamma} \right)^{\frac{1}{2}} + 2 \left(\frac{\Omega l}{\gamma} \right)^{\frac{3}{2}} + \left(\frac{\Omega l}{\gamma} \right)^{\frac{5}{2}} \right] \exp \left(-\frac{\Omega l}{\gamma} \right). \quad (6.42)$$

Notice that the aberrations are exponentially damped. For small values of γ , $\omega \propto \sqrt{\gamma}$ and the exponent in (6.42) goes like $\Omega l/\gamma \propto 1/\sqrt{\gamma}$. The limiting expression (6.42) deviates less than a few percent from (6.37) for $\Omega l/\gamma \geq 2$.

In the same way one can calculate the kinematic aberrations. Some of the formulas here are slightly involved and we only report the contribution of the kinematic aberrations to f_{x^4}

$$f_{x^4}^{kin} = \frac{\omega^3}{32} \left[3\Phi - \omega^3 \sin 2\Phi + \frac{1}{8} \sin 4\Phi + \omega(L - l_s) \sin^4 \Phi \right]. \quad (6.43)$$

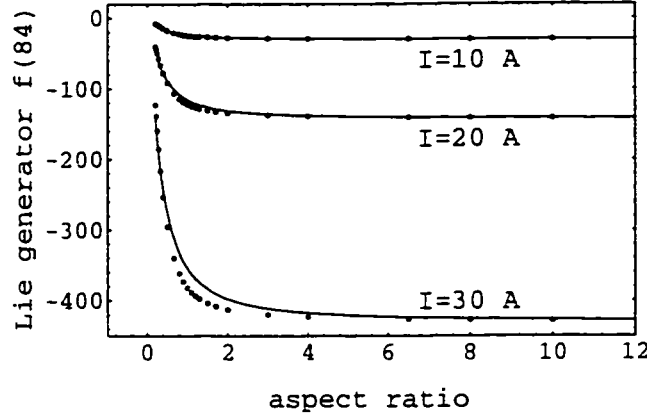


Figure 6.7: Lie generator f_{x^4} (including both the kinematic and dynamic term) as a function of the aspect ratio γ for different values of I_1 .

The analytical results obtained so far can be compared with a numerical evaluation of the Lie generators of the transfer map that can be calculated using the routine GENMAP in MARYLIE [22, 23]. Figures Fig. 6.5 and 6.6 report a comparison between the Lie generators $f_{x^4}^{dyn}$ and $f_{x^3 p_x}^{dyn}$ as calculated analytically with the approximated formulas presented in this paper (solid lines) and the numerical calculation made with MARYLIE (dots). As one can see the qualitative behavior of the aberrations as a function of the aperture ratio is well reproduced. And in the hard edge limit the analytical formulas reproduce the numerical result exactly.

In Fig. 6.7 and 6.8 we report the total Lie generators f_{x^4} and $f_{x^3 p_x}$, including both the kinematic and dynamic contributions, as a function of the aspect ratio. The phase advance Φ corresponding to $I_1 = 10, 20, 30$ A is respectively 14.3, 28.7, 43.1 deg. (Recall that Φ is the phase advance between $z = -l_s$ and $z = l_s$).

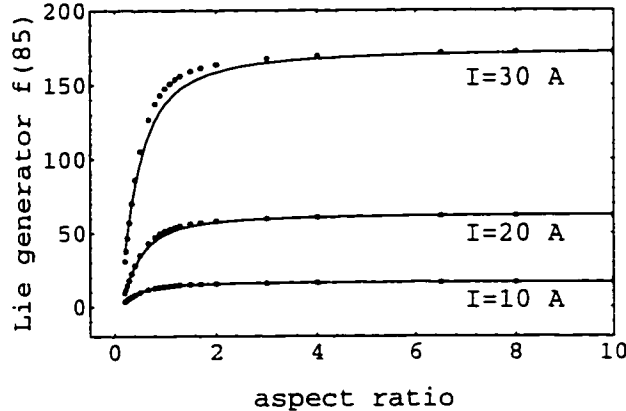


Figure 6.8: Lie generator $f_{r^3 p_x}$ (including both the kinematic and dynamic term) as a function of the aspect ratio γ for different values of I_1 .

6.4 Summary

The goal of this Chapter was to provide further evidence that extended fringe fields, *per se*, do not carry more aberrations than shorter fringes. Although it is true that for a fixed value of the focal length quadrupoles with shorter length have intrinsic larger nonlinearities, that is not related to the extension of the fringes. In fact, as the analytical model and the numerical computations show the aberrations are smaller if the fringes are more extended. This is related to the fact that the aberrations associated with the fringe fields depend on the derivatives of the on-axis gradient. As those derivatives are smaller if the magnet fringes are more extended.

Chapter 7

Magnetic Field Analysis for the LHC High Gradient Quadrupoles

7.1 Introduction

The Large Hadron Collider (LHC) which will be built at CERN within the next seven years will replace the Fermilab Tevatron as the largest existing hadron collider. As for the Tevatron, the LHC will rely on superconducting magnets to achieve the required field to contain the beam in a 27 km tunnel. The LHC poses a series of challenges both from the point of view of the construction of magnets with the required field strength and quality, and for modeling of the single particle dynamics.

In this Chapter we will apply the machinery of magnetic field reconstruction and map computation we have developed in the previous Chapters to a particular problem of beam dynamics for LHC. The problem is on the role of the so called ‘quadrupole triplets’ located next to the interaction points (IP). In the first stage of the machine operation there will be two high luminosity interaction points, where the collisions take place. In order to maximize the rate of collision

events per second (a quantity that in the accelerator physics language is called ‘luminosity’) one would like to compress the beam cross section at the interaction points as much as possible. Compressing the beam is the purpose of the triplets. In the LHC design each ‘triplet’ actually consists of four High Gradient (HG) quadrupoles with the same strength, and slightly different lengths in the combination DFFD or FDDF. In technical terms the action of the triplets is to reduce the size of the betatron functions at the interaction points [in linear approximation the beam size is proportional the square root of the betatron functions, see Eq. (5.35)].

The drawback is that to obtain a low value (0.5 meters) of the betatron functions at the interaction point one has to first allow the beam to expand considerably right before the IP. Before compression the betatron function can assume values as large as 4.700 m. These are the weakest points in the machine from the viewpoint of the particle dynamics. Because of the large beam size, the particles are more exposed to the presence of errors, imperfections, and nonlinearities in general that may undermine the dynamic aperture. Therefore particular care has to be placed in both the construction and field modeling of the triplet magnets.

There are two questions we want to address in this study. The first is the relevance of the intrinsic nonlinearities associated with the fringes (the so called pseudo-multipoles and in particular the pseudo-octupoles ¹). The second is the effect of the systematic additional multipoles (specifically the duodecapole multipoles) that are present because of mechanical constraints. The methods that we have developed in the previous Chapters give us the opportunity to compute

¹For this terminology see the comment on Eqs. (5.13) in Chapter 5.

the associated transfer maps with great accuracy and use them in conjunction with CTRACK to determine the dynamic aperture.

We should mention that in this study we do not consider the presence of possible errors located in the body of the magnets. Unlike the extra multipole components at the ends, the errors in the body are of random nature. Their strength will depend on magnet fabrication, mechanical tolerances etc.. and will be different for any particular realization of each physical magnet. The study of the effect of these errors is also important but it is not discussed here since it can be carried out with the existing standard computational tools.

7.2 Magnetic Field Analysis

The superconducting quadrupole fields result from a combination of superconducting coils and an iron joke. In the body of the quadrupole the coil design and location is determined by a 2D model, while the ends require a full 3D model. In the body of the magnet it is relatively easy to find current configurations that realize a pure quadrupole field. See for example the discussion presented in Chapter 4.

However, because of mechanical constraints, the two ends of the magnet coils will in general carry additional and undesired multipole terms in the field expansion. We point out that these components are ‘systematic’ since they are already in the magnet design. The process of the magnet coil design involves an optimization aiming at reducing as much as possible the strength of the undesired multipoles. The design is done independently for each of the two coil ends, the ‘Return end’ (RE) and ‘Lead end’ (LE). The Lead end differs from the Return

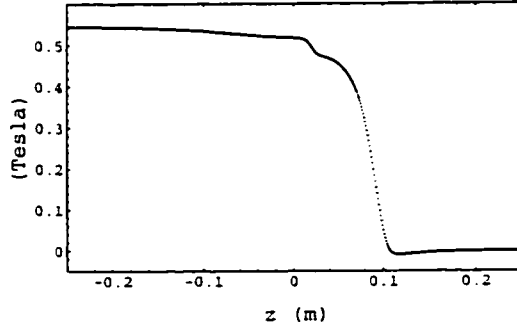


Figure 7.1: Harmonic $B_2(R, z)$ for the Return end; R=3 cm.

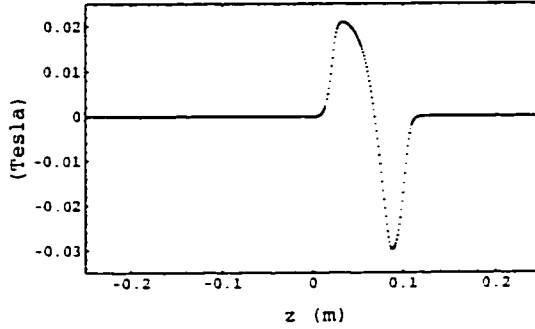


Figure 7.2: Harmonic $B_6(R, z)$ for the Return end; R=3 cm.

end in that it contains the connection of the coils with the power cable. Because of a more demanding mechanical constraint the field quality at the LE turns out to be somewhat worse than at the RE.

As part of the design optimization one has to carry out 3D computation of the magnetic fields. The idea is to use these already available data according to the prescription given in Chapter 3 to recover the expression for the generalized gradients. Eventually the generalized gradients can be used to compute transfer maps and to study the beam dynamics.

The calculation of the magnetic field data used in this study was carried out and provided to us by G.Sabbi [53, 54] using a code that integrates the Biot-Savart law and approximates the effect of the iron yoke in the limit of

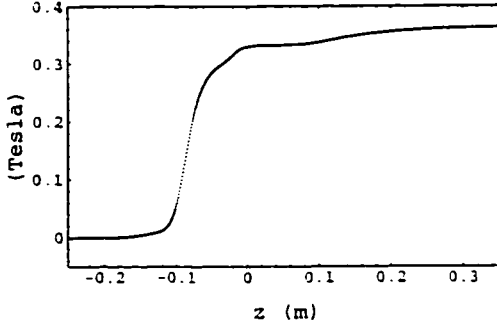


Figure 7.3: Harmonic $B_2(R, z)$ for the Lead end; $R=2$ cm.

infinite permeability. The three cartesian components of the magnetic field on the surface of a cylinder contained within the magnet quadrupoles have been provided us for both ends.

From the magnetic field data in cartesian coordinates we then computed the radial component and carried out the Fourier analysis to calculate the terms $B_m(R, z)$, $A_m(R, z)$ in the expansion (3.32). We carried out the computation for both ends, using the magnetic field data on the surface of the cylinder with the largest radius available. In particular $R=2$ cm for the Lead end and $R=3$ cm for the Return end. The design of the magnet end is the same for the quadrupoles of all the triplets.

In Figs. 7.1 through 7.4 we report the non vanishing normal harmonics for the radial component of the magnetic field on a cylindrical surface of radius R through 6th order. The harmonics are reported for both the Lead and Return end. The other harmonics are ruled out by the symmetry realized in the coil design.

Having calculated the field harmonics one can then apply the formulas discussed in Sec. 3.4.1 to recover the values of the on-axis generalized gradients that are needed for map computation. This calculation was done using the specifically

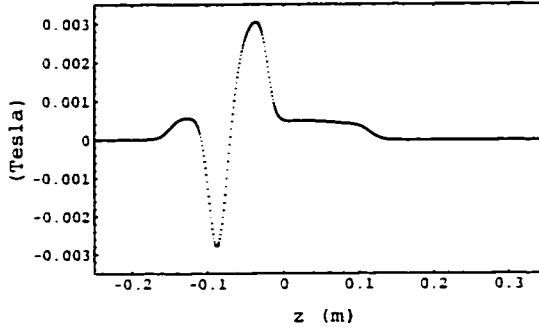


Figure 7.4: Harmonic $B_6(R, z)$ for the Lead end; $R=2$ cm.

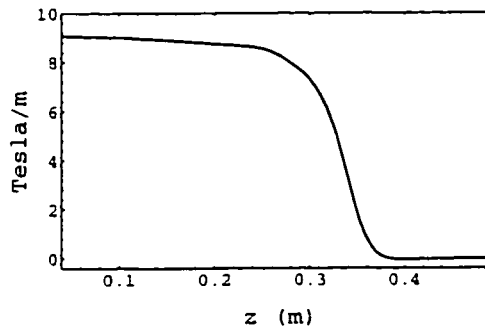


Figure 7.5: Generalized gradient $C_2(z)$ for the Return end.

written the user-defined MARYLIE routine that was discussed in Sec. 3.7.

The profiles for the generalized gradients $C_2(z)$, its derivatives $C_2^{[2]}(z)$, $C_2^{[4]}(z)$ and $C_6(z)$ for the Return end are shown in Figs. 7.5 through 7.8. Notice that in the pictures for the generalized gradient for convenience of computation the frame in z has been translated by 25 cm. That is, the origin in Fig. 7.1 and 7.2 corresponds to the point $z = 0.25$ m of Figs. 7.5 through 7.8.

We recall that the generalized gradients enter into the multipole expansion for the fields. For the two ends the multipole expansion for the magnetic field through 6th order in the radius is the same as for the PC quadrupoles discussed in Chapter 5. See Eq. (5.13).

The fields described here have been obtained from the magnet design opti-

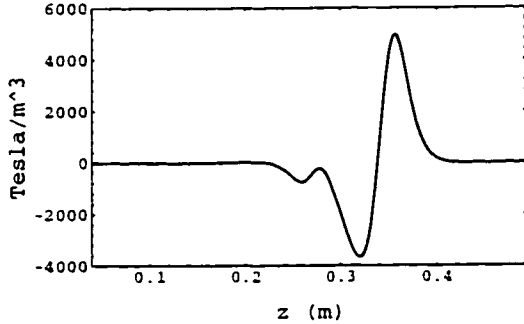


Figure 7.6: Second derivative of the generalized gradient $C_2^{[2]}(z)$ for the Return end.

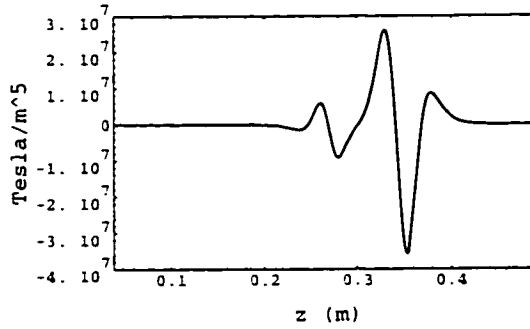


Figure 7.7: Fourth derivative for the generalized gradient $C_2^{[4]}(z)$ for the Return end.

mization carried between over the last year. The design has been implemented in the short model of HG quadrupole that has been recently built and tested at Fermilab [55]. Optimization of the quadrupole design, however, is still on-going and the final version is likely to display a significantly improved field quality.

7.3 Dynamical Effect of the HG Quad Triplets

Having determined the profile of the nonvanishing generalized gradient at the two ends one can then compute the corresponding transfer maps, concatenate them with the transfer map for the body of the magnet and finally compute the transfer map for the whole magnet.

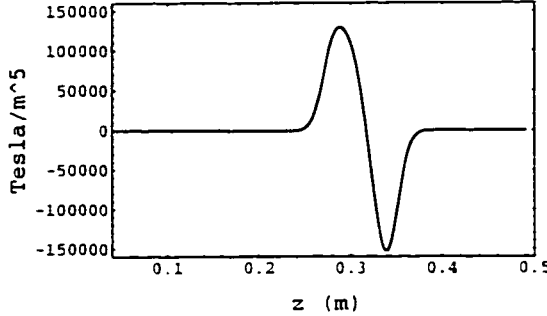


Figure 7.8: Generalized gradient $C_6(z)$ for the Return end.

In this calculation we assume the body of the magnet has only the design quadrupole component of the field. This corresponds to the ideal design with no errors coming from mechanical imperfections of various kinds.

As a result the transfer map for each quadrupole results from the following combination:

$$\mathcal{M}_Q = \mathcal{M}_{LE} \circ \mathcal{M}_{body} \circ \mathcal{M}_{RE}. \quad (7.1)$$

The quadrupoles in the triplet come with two different lengths. In both cases the Lead end and Return end span a length of respectively 56 cm and 46 cm, while the two body lengths are respectively 4.8526 m and 5.65258 m long. We should briefly comment on how these numbers are set. The model of reference is the standard LHC lattice [41] made of idealized hard edge model magnets. The quadrupoles in this model are characterized by a magnetic length and the on-axis gradient (which in the model is assumed to be constant all along the magnet). In this model the magnets appearing in the triplets all have all the same (in absolute value) gradient (200.415 T/m) and two different lengths of 5.5 m and 6.3 m. The lengths of the body in (7.1) are set in such a way that the integrated on-axis gradient is the same as in the hard edge model for the two kinds of magnets.

Incidentally, we mention that the magnetic field data provided by [53] as shown in the pictures do not correspond to the required values of the fields of the triplet quadrupoles in the collision regime. One needs to scale the field properly so that the overall on axis-gradient is continuous and the peak value is the same as in the hard edge model (200.415 T/m).

The next step is to build the transfer map for the triplet regions and concatenate them with the map describing the rest of the LHC lattice. Since this study is specifically aimed at investigating the effects of the fringe region in the triplet HG quadrupoles, for the rest of the machine (i.e. the maps \mathcal{M}_{c1} and \mathcal{M}_{c2} in the equation below) we adopted a linear approximation.

The one-turn map for the LHC (from IP to the same IP) can be written as:

$$\mathcal{M}_{LHC} = \mathcal{T}_+ \circ \mathcal{M}_{c1} \circ \mathcal{T}_- \circ \mathcal{T}_+ \circ \mathcal{M}_{c2} \circ \mathcal{T}_+. \quad (7.2)$$

The maps \mathcal{T}_\pm refers to half portions of the triplet. Each one is a combination of quadrupoles described in (7.1) and drifts. In particular:

$$\mathcal{T}_+ = \mathcal{D}_1 \circ \mathcal{M}_{QF} \circ \mathcal{D}_2 \circ \mathcal{M}_{qd} \circ \mathcal{D}_3 \circ \mathcal{M}_{qd} \circ \mathcal{D}_{4,5} \circ \mathcal{M}_{QF} \circ \mathcal{D}_6. \quad (7.3)$$

and

$$\mathcal{T}_- = \mathcal{D}_6 \circ \mathcal{M}_{QD} \circ \mathcal{D}_{4,5} \circ \mathcal{M}_{qf} \circ \mathcal{D}_3 \circ \mathcal{M}_{qf} \circ \mathcal{D}_2 \circ \mathcal{M}_{QD} \circ \mathcal{D}_1. \quad (7.4)$$

We used capitalized subscripts, as in \mathcal{M}_{QF} , to denote the transfer map for a focusing HG quadrupole with the longer magnetic length (6.3 m); and lower case subscript as in \mathcal{M}_{qf} to indicate the transfer map for a focusing HG quadrupole with the shorter magnetic length of 5.5 m. The maps \mathcal{D}_i represent drifts.

The maps for the individual elements are computed by MARYLIE including the nonlinear effects due to the fringes through 5th order. The maps for the

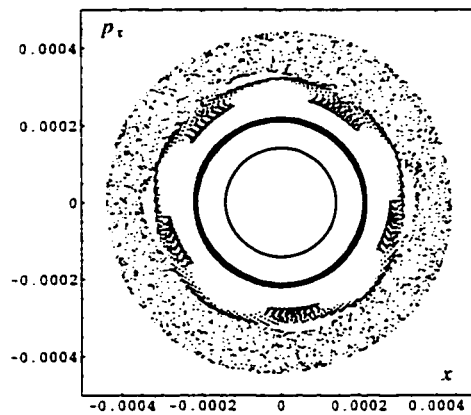


Figure 7.9: Projection of the Poincaré surface of section on the horizontal plane at the IP (normalized coordinates). Map calculated from the magnetic field data.

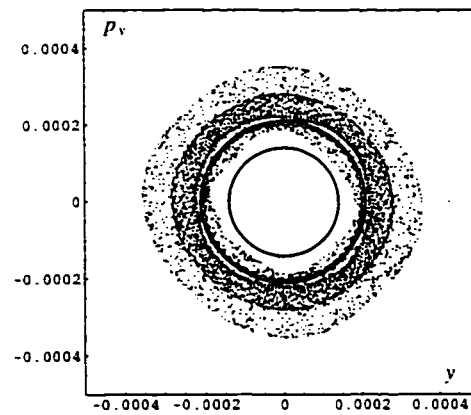


Figure 7.10: Projection of the Poincaré surface of section on the vertical plane at the IP (normalized coordinates). Map calculated from the magnetic field data.

triplets have also been computed using the MARYLIE concatenation routine, while the computation of the map for the remaining part of the machine was carried out using the MAD code [46]. Once the various pieces have been combined together into a 5th order one turn map \mathcal{M}_{LHC} , we applied CTRACK (see [1, 2] and also Chapter 5) to perform Cremona symplectification and the ray tracing study.

The projection of the Poincaré surface of section on the $x - p_x$ and $y - p_y$ planes (normalized variables) are shown in Fig. 7.9 and Fig. 7.10. ² In the normalized coordinates the orbits in the linear approximation would lie on circles. The normalization factors are given by the betatron function at the interaction point. For example, $x_{phys} = x_{norm} \sqrt{\beta_x}$, $(p_x)_{phys} = (p_x)_{norm} / \sqrt{\beta_x}$. Similarly for the motion in y . We recall that at the interaction point $\beta_x = \beta_y = 0.5$ m.

The initial conditions for the four orbits are such that $x = y$ and $p_x = p_y = 0$. The outmost orbit is the last surviving orbit at the edge of the dynamic aperture which is located at about $x_{phys} \simeq .28$ mm, which in turn is comparable to the acceptance corresponding to the magnet aperture.

In order to assess the importance of the various sources of nonlinearity we also studied the case in which we ignored the duodecapole components at the ends. In this case the main source of nonlinearities are the pseudo-octupoles associated with the z -dependence of the fringes. The result of this ray tracing is shown in Fig. 7.11.

As one can see the dynamic aperture increases by about a factor 5 as the duodecapoles terms are removed and lies well beyond the machine acceptance.

²In the pictures the one-turn map has been iterated 10^5 times and the points plotted every 50 iterations.

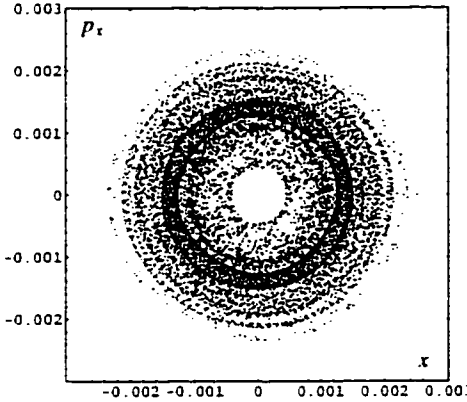


Figure 7.11: Projection of the Poincaré surface of section on the horizontal plane at the IP (normalized coordinates). Map calculated from the magnetic field data with the duodecapoles turned off.

This seems to suggest that for the model we are studying the effect of the nonlinearity due to the pseudo-octupoles is negligible. This is confirmed by normal form analysis. The detuning in the horizontal plane due to the nonlinearities associated to the duodecapoles (6^{th} order generators) at the dynamic aperture is about 0.01, while the detuning due to the pseudo-octupoles is about $\simeq 0.0001$. This is the opposite of what we observed in the case of the E-Ring quadrupoles discussed in Chapter 5.

As a further test we would like to check whether a cruder modeling of the fringes and the dupodecapoles at the ends would still be adequate. In particular, we want to check a model where the action of the duodecapole term is represented in terms of a kick of zero length and finite integrated strength. In terms of generalized gradients the kick at the location $z = z_o$ is represented by a Dirac δ function :

$$C_6^{kick}(z) = S_d \delta(z - z_o), \quad (7.5)$$

where S_d is the integrated duodecapole strength we want to model.

$$S_d = \int_{END} C_6(z) dz. \quad (7.6)$$

The action of the fringes (pseudo-octupoles) is modeled in the hard-edge limit using the Lee-Whiting formula (6.26) mentioned in Chapter 6 and implemented in MARYLIE. The linear part of the map for each quadrupole is also treated in the hard edge approximation. The integrated duodecapole for the LE and RE respectively are 8.148×10^4 T/m⁴ and 5.135×10^3 T/m⁴. The result of ray tracing in the $x - p_x$ plane is shown in Fig. 7.12 for the same initial conditions as in Fig. 7.9.

Comparison with Fig. 7.9 shows little difference in the shape of the orbits. The dynamic aperture in particular is unchanged. Comparison between the 6th order generators in the (nonresonant) normal form in the two cases shows a difference of only a few percent. This result confirms that the kick approximation for the duodecapole terms at the ends is adequate and no detailed knowledge of the generalized gradient C_6 seems to be necessary.

As a further check on the role of the pseudo-octupoles associated with the quadrupole magnets we carried out a calculation using the hard edge model described above without inclusion of the effects of the fringes. The result is shown in Fig. 7.13. Again there seems to be little difference from Fig. 7.12. This confirms that the nonlinearity associated with the pseudo-octupoles is negligible compared with the effect of the systematic duodecapoles at the ends.

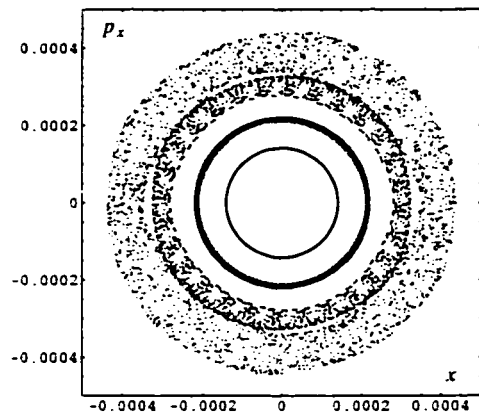


Figure 7.12: Hard edge model. The fringes are treated in the hard edge limit: the systematic duodecapoles in the kick approximation.

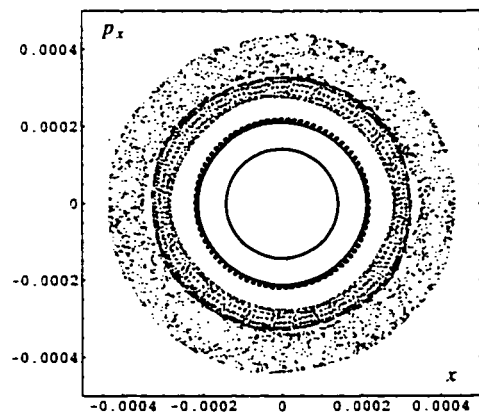


Figure 7.13: As in Fig. 7.12 but with the pseudo-octupoles turned off.

7.4 Summary

In this Chapter we applied the method for computing exact transfer maps from magnetic field data to study the dynamical implications of the end effects of the low-beta insertion quadrupoles in the LHC. The large value of the beam cross section at the point where the triplets are located makes the beam most vulnerable to the presence of undesired multipoles and the intrinsic nonlinearities associated with the fringes (pseudo-multipoles). The techniques described in Chapter 3 allowed us to study these effects without idealization of the field profiles. We found that in the model with a realistic description of fringes and magnet ends, the systematic duodecapole term dominate over the effect of pseudo-multipoles. Moreover, comparison with the hard-edge kick approximation has shown that a detailed local knowledge of the fields may not be necessary.

Chapter 8

Dispersion and Space Charge

8.1 Introduction

Very little can be found in the accelerator physics literature on the problem of the combined effect of space charge and dispersion [28, 7]. An obvious reason is that so far the beam intensity in circular accelerators has never been high enough to justify a treatment of dispersion different from the one usually done in a single particle perspective. Some advanced accelerator applications, however, require very high current beams for which the space charge effects are expected to play an important role. Examples include heavy ion fusion drives, high energy boosters, accumulator rings and spallation neutron sources. In these cases of highly space charge dominated beams an approach to calculate the dispersion function based on a single particle formalism would likely be inadequate. This is in particular to be expected for the small Electron Ring under construction at the University of Maryland where the goal is to produce, maintain and study a beam with a depressed-tune factor in the range between 0.2 and 0.4 (see Chapter 5 for details on the Project).

When a significant space charge force is present the dispersion function is no longer a lattice function but will depend in general on the beam density distribution. On the other hand the presence of dispersion itself has an effect in shaping the beam distribution and determining the resulting space charge forces. There are two ways in which this interplay may affect the performance of a circular machine. On the one hand, the presence of dispersion has the effect of changing the conditions for the beam equilibrium. In particular, the horizontal beam size becomes larger than expected in the absence of dispersion. And the effect is larger for higher space charge dominated beams. On the other hand the presence of space charge contributes to determining the analytic form of the dispersion function and consequently the matching conditions.

In this part of the Dissertation the goal is to set a framework to study both problems. We begin in this Chapter by first introducing the basic concepts regarding dispersion in the context of non-interacting particles and we will indicate the directions to go in order to extend the treatment to include space charge. Those directions are then explored in detail in the next two chapters. In Chapter 9 we specifically face the problem of characterizing equilibrium beam distributions. We will present a model that provides one possible natural generalization of a KV beam in a smooth dispersive channel. The study involves the derivation and the numerical solution of the proper Vlasov-Maxwell equations in a self-consistent treatment of the beam dynamics. The aim of the Chapter is to highlight the net contribution of dispersion in setting the shape and size of a space charge dominated beam in equilibrium. This approach is useful for it allows one to get an insight into the problem by studying the scaling of various quantities defining the beam (emittance, rms size etc.) as a function of the relevant

parameters (beam current, longitudinal momentum deviation etc.). However it does not provide us with the tools required to force a beam into a state close to equilibrium after injection. This is the so called 'matching problem'. For space charge dominated beams in straight transport lines the matching is usually done with the aid of the well known and widely used rms envelope equations. As we allow bends and a longitudinal momentum spread to come into the picture one would like to have a way to obtain a matching of both the envelopes and dispersion function as well. This problem is the topic of Chapter 10 where we present the derivation of a new set of equations that represents the natural generalization of the standard rms envelope equations to include dispersion. The new equations will allow one to obtain the desired rms matching of a continuous beam in the presence of bends and a longitudinal momentum spread. As one will see the key point in the derivation is the construction of a linear invariant that generalizes the rms emittance to the case where dispersion is present. The derivation is accompanied by two numerical tests aimed at checking the validity of the new equations. The first is against the self-consistent calculation presented in Chapter 9 in the smooth approximation. The second check is against some numerical calculations done using a PIC code for a FODO lattice. The interested Reader can find further reports in [61, 62, 63, 64].

8.2 Dispersion for Single Particles

In the accelerator physics language 'dispersion' has to do with the way the reference orbit depends on the longitudinal momentum. Circular machines are built in such a way that a particle with the design momentum follows a closed orbit

that is as close as possible to the geometric center of the vacuum pipe. However, a particle ‘off-momentum’, that has a longitudinal momentum slightly different from the design value will travel on a different closed orbit. The dispersion function describes the amount of the deviation at any point along the ring.

In first approximation dispersion manifests itself as a single inhomogeneous term in the equation of motion for the betatron oscillations (see e.g. [57, 66]):

$$x'' + k_x(z)x = \frac{\delta}{\rho(z)}, \quad (8.1)$$

where $\rho(z)$ is the local radius of curvature of the reference orbit having the design momentum p_0 , and $\delta = \frac{\Delta p}{p_0}$ describes the relative deviation from p_0 . In the common situation where the dipole field has only the y component, the motion in y is not affected by dispersion.

The general solution of (8.1) can be represented as the superposition of that particular solution and the general solution of its homogeneous part,

$$x(z) = x_b(z) + \delta D(z) \quad (8.2)$$

- i.e. $x_b(z)$ satisfies $x_b'' + k_x(z)x_b = 0$, while the dispersion function $D(z)$ obeys

$$D(z)'' + k_x(z)D(z) = \frac{1}{\rho(z)}. \quad (8.3)$$

The function $\delta D(z)$ describes the deviation from the designed orbit for a particle that undergoes zero-amplitude betatron oscillations. By inspecting (8.3) one realizes that the dispersion function in a single particle treatment is a lattice function, that is its value is entirely determined by the machine parameters. through that focusing function k_x and the local radius of curvature. We observe that equation (8.1) and the corresponding equation for the betatron oscillations

in the vertical plane can be derived from the Hamiltonian ($p_x = x'$, $p_y = y'$)

$$H = \frac{1}{2}(p_x^2 + p_y^2) + \frac{1}{2}(k_x(z)x^2 + k_y(z)y^2) - \frac{\delta}{\rho(z)}x. \quad (8.4)$$

For the particular case where the focusing and radius of curvature are constant (z -independent), the dispersion function is easily calculated to be $D = 1/\rho_0 k_x$. Because the focusing function depends on the horizontal tune ν_{ox} by $k_x = \nu_{ox}^2/\rho_0^2$, we can also write the dispersion function as $D = \rho_0/\nu_{ox}^2$.

8.3 A Multiparticle Perspective

In a multi-particle perspective we are interested in describing the particle distribution function and how it is affected by the presence of dispersion. In this section, however, we still assume the particles are not interacting with each other. For the sake of concreteness let us introduce a particular distribution in order to illustrate the various problems we are to face. An easy way to built a function f that at any location z gives the correct particle distribution in phase space in accordance to the dynamics of a Hamiltonian system, is to write f in terms of invariants, that is $f = f(I_1, I_2, \dots)$ where $\frac{dI_i}{dz} = 0$ for $i = 1, 2, \dots$. This choice, of course, automatically insures that $\frac{df}{dz} = 0$. For the case of the Hamiltonian (8.4), if we assume for simplicity that the external focusing functions k_x, k_y are z -independent, an invariant can be easily written as

$$I = \frac{1}{2}(p_x - \delta D(z))'{}^2 + \frac{1}{2}k_x(x - \delta D(z))^2 + \frac{1}{2}p_y^2 + \frac{1}{2}k_y y^2,$$

provided that the function $D(z)$ be identified with the dispersion function satisfying equation (8.3).

A straightforward but a little tedious way to show that $\frac{dI}{dz} = 0$ is to carry out the computation of the derivative by using the canonical equations of the motion. A different and more illuminating approach, makes use of the canonical transformation

$$\begin{aligned}\dot{x} &= x - \delta D(z), & \dot{y} &= y \\ \dot{p}_x &= p_x - \delta D(z)', & \dot{p}_y &= p_y\end{aligned}\tag{8.5}$$

induced by the generating function $G(x, \dot{p}_x, z) = \dot{p}_x[x - \delta D(z)] + x\delta D'(z) + \dot{p}_y y$. The canonical transformation brings the Hamiltonian (8.4) into a z -independent Hamiltonian $\tilde{H} = H + \frac{\partial G}{\partial z}$, that is

$$\tilde{H} = \frac{1}{2}(\dot{p}_x^2 + \dot{p}_y^2) + \frac{1}{2}(k_x(z)\dot{x}^2 + k_y(z)\dot{y}^2).\tag{8.6}$$

Because \tilde{H} is z -independent, an invariant for the system in the new variables can be immediately be written: the Hamiltonian \tilde{H} itself! We can then obtain an invariant for our original system by transforming \tilde{H} back into the original variables: $I(x, p_x, y, p_y) = \tilde{H}(\dot{x}(x, p_x), \dot{p}_x(x, p_x), y, p_y)$. Incidentally we anticipate that for different purposes we will make use of the transformation (8.5) again in Chapter 10.

Having succeeded in finding an invariant I for our system we can become more specific by choosing a distribution of the form:

$$f(x, p_x, y, p_y, \delta) = \frac{f_0 \sqrt{k_x k_y}}{2\delta_0 T \sqrt{\pi^5}} e^{-\frac{\delta^2}{\delta_0^2}} \exp(-\frac{I}{T}),\tag{8.7}$$

Such a distribution is the most obvious generalization to the case with dispersion of the Boltzmann-Maxwell distribution usually defined in beam physics textbooks (see e.g. [57]).¹ The parameter T , as the notation suggests, may be

¹The Boltzmann-Maxwell distribution is defined as the exponential of the Hamiltonian. One can argue that the same definition still holds in the case of (8.7), since I is related to the Hamiltonian in the transformed variables \tilde{x}, \tilde{p}_x .

interpreted as the transverse temperature.

Let us consider the example of a smooth ring where $D(z)$ is a certain periodic function solution of Eq. (8.3), having the same periodicity of the lattice. Then, the distribution function (8.7) represents a matched beam. That is, the distribution function itself has the periodicity of the lattice.

Given the distribution function f for the beam one can evaluate the second moments and find

$$\begin{aligned}\langle x^2 \rangle &= \langle x^2 \rangle_o + D(z)^2 \langle \delta^2 \rangle. \\ \langle p_x^2 \rangle &= \langle p_x^2 \rangle_o + D(z)^2 \langle \delta^2 \rangle. \\ \langle x\delta \rangle &= \langle \delta^2 \rangle D(z), \\ \langle p_x\delta \rangle &= \langle \delta^2 \rangle D'(z), \\ \langle \delta^2 \rangle &= \frac{\delta_o^2}{2}.\end{aligned}\tag{8.8}$$

Here we use the bracket notation $\langle \cdot \rangle$ to indicate the averaging with respect to all the dynamical variables of the system. Also, we wrote $\langle x^2 \rangle_o$ to indicate the second moment of the distribution when $\delta_o \rightarrow 0$. Observe that the dispersion function turns out to be a measure of the second moments of the distribution f . In particular, a non-vanishing dispersion will result in a net growth of the rms horizontal size of the beam as well as of all the other rms (horizontal) quantities. Incidentally notice that although Eqs. (8.8) have been derived for the particular case of a Boltzmann distribution, the result is more general and independent of a particular distribution. Also it does not depend on the smooth approximation.

See Appendix C.

The third equation in (8.8) suggests the possibility of defining the dispersion function directly in terms of cross second moment $\langle x\delta \rangle$. Indeed such a viewpoint

will turn out to be useful in identifying the dispersion function when one faces the problem of extending Eq. (8.3) to the case where space charge is included.

From the calculation of the second moments of the distribution we can then recover an expression for the rms emittance, which is usually taken as a measure of the beam quality.

$$\epsilon_x = (\langle x^2 \rangle \langle p_x^2 \rangle - \langle xp_x \rangle^2)^{1/2}.$$

We have

$$\epsilon_x^2 = \epsilon_{xo}^2 \left(1 + \frac{\delta_o^2 D(z)^2}{2\langle x^2 \rangle_o} \right) \left(1 + \frac{\delta_o^2 D(z)^{'2}}{2\langle p_x^2 \rangle_o} \right) \quad (8.9)$$

In a typical single particle situation, and in the presence of strong external focusing, the effect of a finite dispersion on the rms quantities shown above may be very small. For the Maryland Electron Ring, for example, in the smooth approximation the relative deviation of the horizontal rms size of the beam or the emittance between the case with and without dispersion would be of the order of 0.1%, if we assume a longitudinal momentum spread $\sigma_s = \sqrt{\langle \delta^2 \rangle} \simeq .007$. Inclusion of space charge, however, will make those deviation larger because of an increase in the value of the dispersion function.

8.3.1 The Matching Problem

Next, let us consider the problem of injecting the beam into a smooth ring characterized by the dispersion function $D(z)$ at the point $z = z_1$, using a certain injection line. The injection line is also characterized by a dispersion function: let us call it $D_{inj}(z)$. At the end of the injection line the dispersion function and its derivative will have the values $D_{inj}(z_1)$, $D_{inj}(z_1)'$. If we start at the beginning of the injection line, where we assume $D_{inj}(z) = 0$, $D_{inj}(z)' = 0$,

with a Boltzmann beam ²,

$$g(x, p_x, \delta, z) = \frac{g_o \sqrt{k_x}}{\delta_o \sqrt{2T\pi^3}} e^{-\frac{\delta^2}{\delta_o^2}} e^{-(\frac{1}{2}p_x^2 + \frac{1}{2}k_x x^2)/T}, \quad (8.10)$$

it is clear that the beam will match the distribution (8.7) in the ring only if

$$\begin{aligned} \Delta &= D(z_1) - D_{inj}(z_1) = 0, \\ \Delta' &= D(z_1) - D_{inj}(z_1)' = 0. \end{aligned} \quad (8.11)$$

What we want to do in this section is to evaluate the variation of the emittance and other rms quantities and their dependence on the dispersion mismatch parameters Δ, Δ' defined above.

At the end of the injection line $z = z_1$, the distribution function is

$$g_1(x, p_x, \delta, z) = \frac{g_{1o} \sqrt{k_x}}{\delta_o \sqrt{2T\pi^3}} e^{-\frac{\delta^2}{\delta_o^2}} e^{-(\frac{1}{2}(p_x - \delta D_{inj}(z_1)')^2 + \frac{1}{2}k_x(x - \delta D_{inj}(z_1))^2)/T}. \quad (8.12)$$

At subsequent z the distribution function can be recovered using the transfer map $M_{(z,z_1)}$, which gives the position of any point in the phase space at z as a function of the position in phase space at $z = z_1$, through the equation

$$f(\vec{\zeta}, z) = g_1(M_{(z,z_1)}^{-1}\vec{\zeta}), \quad (8.13)$$

where the symbol $\vec{\zeta}$ denotes the set of the dynamical variables. Under the assumption of the smooth approximation the transfer map is simply given by

$$\begin{pmatrix} x \\ p_x \end{pmatrix} = M_{(z,z_1)} \begin{pmatrix} x_1 - \delta D(z_1) \\ p_{x1} - \delta D(z_1)' \end{pmatrix} + \begin{pmatrix} \delta D(z_1) \\ \delta D(z_1)' \end{pmatrix}, \quad (8.14)$$

with ($\omega = \sqrt{k_x}$)

$$M_{(z,z_1)} = \begin{pmatrix} \cos \omega(z - z_1) & \frac{1}{\omega} \sin \omega(z - z_1) \\ -\omega \sin \omega(z - z_1) & \cos \omega(z - z_1) \end{pmatrix}. \quad (8.15)$$

²For the rest of the section we ignore the motion of the particle in the vertical plane, which is not relevant in this context.

After some algebra one finds that the distribution function has the form

$$f(x, p_x, \delta, z) = \frac{\sqrt{AB}}{\pi} \exp\left(-\frac{C^2}{4A} - \frac{F^2}{4B}\right) \exp[-(Ax^2 + Bp_x^2 + Cx\delta + Fp_x\delta)], \quad (8.16)$$

where

$$\begin{aligned} A &= \omega/(2T), & B &= 1/(2T), \\ C &= [-\omega D(z) + \Delta\omega^2 \cos \omega(z - z_1) + \Delta'\omega \sin \omega(z - z_1)]/T, \\ F &= [D(z)' + \Delta'\omega^2 \cos \omega(z - z_1) - \Delta'\omega \sin \omega(z - z_1)]/T. \end{aligned} \quad (8.17)$$

The rms quantities read

$$\langle x^2 \rangle = \frac{1}{2A} \left(1 + \frac{\langle \delta^2 \rangle C^2}{2A} \right). \quad (8.18)$$

$$\langle p_x^2 \rangle = \frac{1}{2B} \left(1 + \frac{\langle \delta^2 \rangle F^2}{2B} \right), \quad (8.19)$$

$$\langle xp_x \rangle = \frac{\langle \delta^2 \rangle CF}{2AB}, \quad (8.20)$$

and finally

$$\epsilon^2 = \frac{1}{2AB} \left(1 + \frac{\langle \delta^2 \rangle C^2}{2A} \right) \left(1 + \frac{\langle \delta^2 \rangle F^2}{2B} \right) - \langle \delta^2 \rangle^2 \frac{C^2 F^2}{4A^2 B^2}. \quad (8.21)$$

Suppose for simplicity that $\Delta' = 0$. We see that $\langle x^2 \rangle$ oscillates around the equilibrium value found in (8.8)

$$\langle x^2 \rangle = \langle x^2 \rangle_o + \langle \delta^2 \rangle [D(z)^2 + \Delta \cos \omega(z - z_1)]^2. \quad (8.22)$$

We observe that in presence of the mismatch the relative deviations from the equilibrium (matched) distributions can be 4 times as large as in the matched situation. The estimate follows from (8.22) by assuming a mismatch $\Delta = D$. The same is also true for the emittance as one can easily verify.

If the system was purely linear the emittance and envelope oscillations due to a dispersion mismatch would be completely reversible, and, if the extraction of the beam was done exactly at the point where the dispersion and its derivative vanish one would experience no emittance growth. But nonlinearities, however small, are unavoidable and they may trigger relaxation processes that could induce the beam distribution to fill all the volume available in the phase space. The result would be a net emittance growth. For this reason matching of dispersion is important in setting up a properly operating machine.

8.4 Inclusion of Space Charge

How does the scenario change if we include space charge into the picture? A consequence of the presence of space charge is to modify the strength of the effective focusing forces acting on the particles. In particular the self-force, which in a long beam is mostly directed outward, has the effect of shielding the external focusing forces. In the accelerator physics terminology one says that the tune, which is related to the frequency of the betatron motion is ‘depressed’ by space charge. The simplest model to account for the effect of space charge on the tune is the Kapchinsky Vladimirsy (KV) beam distribution [57]. A KV beam has an elliptic cross section of uniform density distribution. As a consequence the resulting forces due to space charge are linear. If a_x and a_y are the semiaxes of the elliptic cross section of the KV beam in the x and y direction the depressed tune in the horizontal plane in the smooth approximation has the form

$$\nu_x^2 = \nu_{ox}^2 - \frac{K}{a_x(a_x + a_y)} \rho_o^2, \quad (8.23)$$

where

$$K = \frac{I}{I_o} \frac{2}{\beta^3 \gamma^3} \quad (8.24)$$

is the generalized permeance [57] with I being the beam current, β, γ the relativistic factors and $I_o \simeq 17$ kA for electrons. If the beam has not a KV distribution one can introduce the definition of an rms tune by using the concept of the KV equivalent beam. Two beam distributions are said to be equivalent if the second moments of the two distribution in phase space are the same. For the general rms case the definition for the tune (8.23) becomes

$$\nu_x^2 = \nu_{ox}^2 - \frac{K}{2\sigma_x(\sigma_x + \sigma_y)} \rho_o^2, \quad (8.25)$$

where σ_x and σ_y are the horizontal and vertical rms size of the beam respectively. More about Eq. (8.25) can be found in Chapter 10.

In the smooth approximation and absence of space charge $D = \rho_o / \nu_{ox}^2$. Therefore, we can expect that D would be larger when space charge effects are taken into account. The extent of the growth, however, remains to be seen. One could question whether in the presence of space charge the expression for the second moments of the distribution can be recovered from (8.8) simply by the change $\nu_x \leftrightarrow \nu_{ox}$ in the expression for the dispersion. Incidentally, if this were the case, the effect on the beam parameters in the case of the Maryland Electron Ring would be quite dramatic, given the highly depressed tune. But it is clear that this may not be correct because the reshaping of the beam distribution due to the presence of dispersion also changes the value of the depressed tune ν_{ox} . The only way to answer quantitatively this question is to study the beam distribution self-consistently by solving at once the Vlasov and the Maxwell equations. This is what we will do in the next Chapter.

If the matching of dispersion were made by ignoring the space charge one would achieve very poor results since dispersion is affected by space charge. This is likely to be the case for the Maryland Electron Ring, for example if the thermal energy spread will turn out to be significant. Indeed a considerable emittance growth due to an energy spread has been observed in numerical simulations where bending magnets are present [7, 40]. Therefore, one would like to find the proper matching conditions.

The problem is that in order to do the matching one should have a proper way to compute the dispersion function when space charge is present. Finding the solution of this probelm is the content of Chaper 10 where we work out a generalization of the standard rms envelope equations to include both space charge and dispersion.

Chapter 9

Self-consistent Beam Distributions with Space Charge and Dispersion

In this chapter we investigate the combined effect of space charge and dispersion by looking at self-consistent solutions of the Vlasov-Poisson equation describing a beam of charged particles in a small recirculator. Self-consistency here means that in determining the beam distribution we take into account both the external focusing forces and the self-forces due to space charge, which depend on the beam distribution itself via the Maxwell equations.

We assume a smooth approximation: that is, the external focusing functions and radius of curvature are assumed to be independent of the longitudinal variable and we look for equilibrium distributions described by stationary solutions of the Vlasov-Poisson equation. Incidentally, because the solution representing the beam is stationary (i.e. time independent) the Poisson equation is the only relevant Maxwell equation.

In choosing stationary solutions of the Vlasov equation one has a certain freedom. Here we consider a particular kind of distribution that is the natural generalization of the KV beam to the case where one has dispersion. The choice

of such a distribution is mainly motivated by the importance of the usual KV beam in theoretical analysis. Other distributions can also be considered [65].

The goal is to understand how the beam is reshaped by the presence of dispersion and how the dispersion function itself is modified by the presence of space charge.

The structure of the Chapter is as follows. First we introduce the Hamiltonian for our model and the general form of the Vlasov-Poisson equation. Next, in Sec. 9.2 we write and solve the Poisson equation for the particular case of a KV beam where all the particles are equally off-momentum. In Sec. 9.3 we write the Poisson equation for the case where the beam has a generalized KV distribution in the transverse plane and a gaussian distribution for the longitudinal momentum spread. The following section contains a discussion of the numerical solution for the Poisson equation. Finally we treat the problem of the evolution of a beam through injection from a straight channel to a dispersive channel (Sec. 9.7).

9.1 The Vlasov-Poisson Equations

Our model is described by a Hamiltonian [57] $H = H_{\perp} + H_{\parallel}$, where $H_{\parallel} = \frac{m^2 c^4}{E_0^2} \delta^2$ is a purely longitudinal term and

$$H_{\perp} = \frac{1}{2}(p_x^2 + p_y^2) + \frac{k}{2}(x^2 + y^2) - \frac{x}{\rho_o} \delta + g_o \psi(x, y), \quad (9.1)$$

(with $g_o = q/mv_z^2 \gamma^3$).

The Hamiltonian refers to a beam of particles of charge q and mass m in a smooth circular channel where both the external focusing function k and the radius of curvature ρ_o are z-independent. Also, we assume that the external focusing is the same in the horizontal and vertical plane. The self-force is de-

scribed by the potential ψ . The design momentum, longitudinal velocity, and the corresponding relativistic factor are p_o , v_z , and γ .

In the model we neglect all the nonlinearities coming from the external focusing as well all the chromatic terms since they are of third order. We also ignore space charge effects due to the finite curvature of the beam.

Moreover, since the Hamiltonian is time independent (no beam acceleration) the momentum deviation δ is a constant of the motion. Clearly H_{\perp} is also an integral of the motion. By choosing a z -independent potential ψ describing the self-force we neglect the effects of the longitudinal space charge. By doing so the model is understood to describe the dynamics of continuous (unbunched) beams with a thermal energy spread. Clearly the effects of the energy spread induced by the bunch edge effects are not captured in our model - and would probably be rather challenging to incorporate them in a self-consistent treatment with dispersion. For a non self-consistent description of these effects for a single pass through bendings see [11].

We want to search for self-consistent solutions $f(x, p_x, y, p_y, \delta)$ of the Vlasov-Poisson equation associated with H

$$\frac{\partial f}{\partial z} + [f, H] = 0, \quad \nabla^2 \psi = -\frac{q}{\epsilon_0} n(x, y), \quad (9.2)$$

where $[\cdot, \cdot]$ are the Poisson brackets and $n(x, y)$ is the beam density

$$n(x, y) = \int \int \int f(x, p_x, y, p_y, \delta) d\delta dp_x dp_y. \quad (9.3)$$

In particular, we want to look for stationary solutions $\frac{\partial f}{\partial z} = 0$. We recall that any function of the integrals of motion of a Hamiltonian system is a stationary solution of the corresponding Vlasov equation. Therefore, a particular stationary

solution of the Vlasov equation associated with the Hamiltonian H is given by

$$f(x, p_x, y, p_y, \delta) = f_{\parallel}(\delta) f_{\perp}(H_{\perp}).$$

In this paper we consider a distribution in the transverse Hamiltonian $f_{\perp}(H_{\perp})$ in the form of a Dirac delta function. In the absence of dispersion such a choice leads to the usual KV-beam. For the distribution in the longitudinal momentum spread we discuss two cases: a monochromatic distribution and a gaussian distribution.

9.2 Monochromatic KV Beam

First of all, consider the particular choice

$$f_{\parallel}(\delta) = \hat{\delta}(\delta - \delta_o) \quad (9.4)$$

$$f_{H_{\perp}}(H_{\perp}) = f_o \hat{\delta}(H_{\perp} - H_o). \quad (9.5)$$

Here $\hat{\delta}$ is the Dirac delta function and f_o is a constant. Such a distribution describes a beam of particles that are off momentum by the same amount δ_o . Notice that for $\delta = \delta_o = 0$ we recover the usual KV beam.

The space density associated with the distribution function f is given by

$$\begin{aligned} n(x, y) &= f_o \int \int \int dp_x dp_y d\delta \hat{\delta}(\delta - \delta_o) \hat{\delta}(H_{\perp} - H_o) \\ &= 2\pi f_o \mathbf{H} \left(H_o - \frac{k}{2}(x^2 + y^2) + \frac{\delta_o}{\rho_o} x - g_o \psi \right). \end{aligned}$$

where \mathbf{H} is the Heaviside step function. The Poisson equation for the self-potential reads

$$\nabla^2 \psi = -\frac{q}{\epsilon_o} 2\pi f_o \mathbf{H} \left(H_o - \frac{k}{2}(x^2 + y^2) + \frac{\delta_o}{\rho_o} x - g_o \psi \right). \quad (9.6)$$

One can verify that a solution is given by

$$\psi(x, y) = -\frac{q\pi f_o}{2\epsilon_0} \left((x - \frac{\delta_o}{\rho_o k})^2 + y^2 \right). \quad (9.7)$$

for $[x - \delta_o/(\rho_o k_x)]^2 + y^2 \leq a^2$, and

$$\psi(x, y) = -\frac{q\pi f_o a^2}{\epsilon_0} \left\{ \ln \left[\frac{1}{a} \left((x - \frac{\delta_o}{\rho_o k})^2 + y^2 \right)^{\frac{1}{2}} \right] + \frac{1}{2} \right\}. \quad (9.8)$$

for $[x - \delta_o/(\rho_o k_x)]^2 + y^2 > a^2$, where

$$a^2 = \frac{1}{2} \left(k_x - g_o \frac{q\pi f_o}{\epsilon_0} \right)^{-1} \left(H_o + \frac{\delta_o^2}{2\rho_o^2 k_x} \right). \quad (9.9)$$

The calculation shows that in the presence of a momentum deviation represented by a delta function the beam density is that of an off-centered KV beam of radius a . The amount of the deviation from the axis is given by $\delta_o D$, with the dispersion function $D = 1/(\rho_o k_x)$ given in terms of the undepressed focusing function. In other words, particles of a monochromatic KV round beam, from the view point of dispersion behave like single particles.

9.3 Generalized KV Beam

Next, we look for solutions of the Vlasov-Poisson equations describing a beam with a gaussian-like distribution in the longitudinal momentum and a KV-beam like distribution in the transverse plane,

$$f_{||}(\delta) = \frac{1}{\delta_o \sqrt{\pi}} e^{-\frac{\delta^2}{\delta_o^2}} \quad (9.10)$$

$$f_{H_\perp}(H_\perp) = f_o \hat{\delta}(H_\perp - H_o). \quad (9.11)$$

We notice at this point that the resulting distribution will not have a perfect gaussian character in the longitudinal momentum spread, because the term

$f_{H_\perp}(H_\perp)$ also depends on δ . However, in the range of parameters considered in this paper the deviation from a pure gaussian distribution will be relatively small. In particular, the rms longitudinal momentum spread $\sigma_\delta = \sqrt{\langle \delta^2 \rangle}$ will differ from $\delta_o/\sqrt{2}$ by few percents.

Observe that in the limit $\delta_o \rightarrow 0$, we recover the usual KV distribution. In the following we will refer to the distribution described by equations (9.11) as a 'generalized KV beam'.

The corresponding space density is

$$n(x, y) = 2\pi f_o \frac{1}{\delta_o \sqrt{\pi}} \int_{-\infty}^{\infty} \mathbf{H} \left(\lambda(x, y) + \frac{\delta_o x}{\rho_o} t \right) e^{-t^2} dt. \quad (9.12)$$

where we have defined

$$\lambda(x, y) = H_o - \frac{k_x}{2}x^2 - \frac{k_y}{2}y^2 - g_o \psi(x, y). \quad (9.13)$$

The integral in (9.12) can be easily carried out and expressed in terms of the error function.

$$n(x, y) = \pi f_o \left[\operatorname{erf} \left(\frac{\lambda(x, y) \rho_o}{\delta_o |x|} \right) + 1 \right]. \quad (9.14)$$

with $\operatorname{erf}(\tau) = \frac{2}{\sqrt{\pi}} \int_0^\tau e^{-t^2} dt.$

The Poisson equation then reads

$$\nabla^2 \psi = -\frac{q}{\epsilon_o} \pi f_o \left[\operatorname{erf} \left(\frac{\rho_o}{\delta_o |x|} (H_o - \frac{k_x}{2}x^2 - \frac{k_y}{2}y^2 - g_o \psi) \right) + 1 \right]. \quad (9.15)$$

The two parameters f_o and H_o are related respectively to the density of the beam, and its size and emittance. They depend on each other through the normalization equation

$$\begin{aligned} N_L &= \iint n(x, y) dx dy \\ &= \pi f_o \iint \left[\operatorname{erf} \left(\frac{\lambda(x, y) \rho_o}{\delta_o |x|} \right) + 1 \right] dx dy, \end{aligned} \quad (9.16)$$

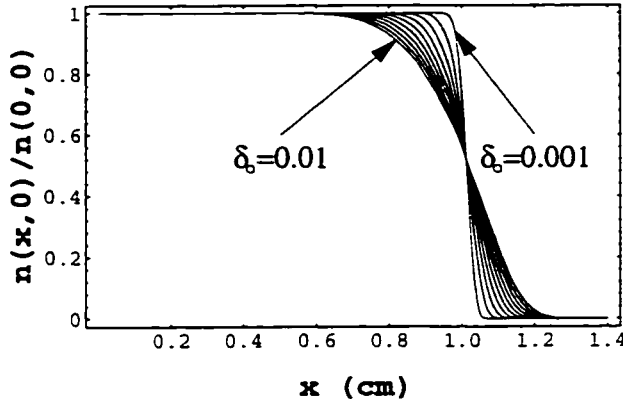


Figure 9.1: Scaled density profile $n(x,y)/n(0,0)$ for the generalized KV beam at $y = 0$. Ten density profiles are shown corresponding to values of δ_o ranging from .001 to .01, ($I = .105 \text{ A}$, $\nu/\nu_o = 0.317$).

where N_L is the linear (longitudinal) density of the beam: It depends on the current I by the relation $N_L = I/(qv_z)$. When we solve equation (9.15) for different values of the parameter δ_o we will be interested in comparing solutions corresponding to beams that carry the same current. After setting f_o to a fixed value, we shall use equation (9.16) to determine H_o .

Finally, notice that in the limit $\delta_o \rightarrow 0$ equation (9.15) turns into equation (9.6), as expected, since

$$\lim_{\delta_o \rightarrow 0} \left[\operatorname{erf} \left(\frac{\tau}{\delta_o} \right) + 1 \right] = 2H(\tau). \quad (9.17)$$

9.3.1 Emittance Calculation

The beam distribution can be characterized in terms of the emittance and related rms quantities. The rms emittance is defined by

$$\epsilon_x = (\langle x^2 \rangle \langle p_x^2 \rangle - \langle xp_x \rangle^2)^{1/2}.$$

(Analogous expression for ϵ_y).

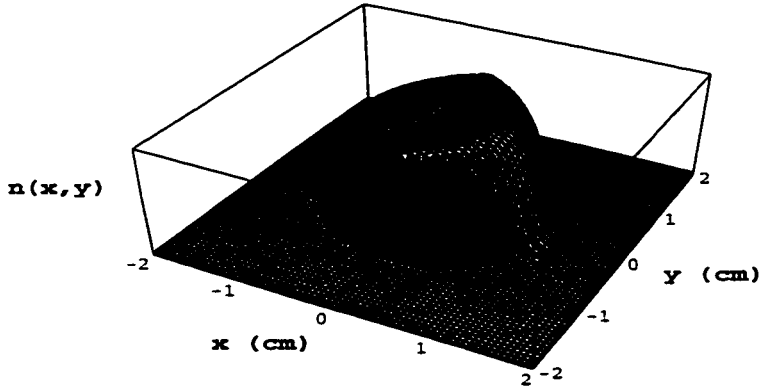


Figure 9.2: Density distribution $n(x, y)$ for $I = .105 \text{ A}$, $\nu/\nu_o = 0.317$, $\delta_o = .01$.

For a KV round beam of radius a without dispersion (see Eq. (9.5) with $\delta_o = 0$), it is easily found that

$$\langle x^2 \rangle_o = \frac{a^2}{4}, \quad \langle p_x^2 \rangle_o = \frac{H_o}{2}, \quad \langle x p_x \rangle_o = 0.$$

Therefore, the emittance reads

$$\epsilon_{ox} = \frac{a}{2} \sqrt{\frac{H_o}{2}}. \quad (9.18)$$

For the case with dispersion it is possible to reduce the expressions for the second moments to calculation of double integrals over x and y ¹.

$$\langle x^2 \rangle = \frac{f_o \pi}{N_L} \iint x^2 \left[\operatorname{erf} \left(\frac{\lambda(x, y) \rho_o}{\delta_o |x|} \right) + 1 \right] dx dy, \quad (9.19)$$

$$\begin{aligned} \langle p_x^2 \rangle &= \frac{f_o \pi}{N_L} \iint \lambda(x, y) \left[\operatorname{erf} \left(\frac{\lambda(x, y) \rho_o}{\delta_o |x|} \right) + 1 \right] dx dy \\ &\quad + \frac{f_o \sqrt{\pi}}{N_L} \iint \frac{\delta_o |x|}{\rho_o} e^{-\left(\frac{\lambda(x, y) \rho_o}{\delta_o |x|}\right)^2} dx dy, \end{aligned} \quad (9.20)$$

$$\langle x p_x \rangle = 0. \quad (9.21)$$

¹The function $\lambda(x, y)$ has been defined in (9.13).

By the same token we can evaluate the rms value of the longitudinal momentum spread as a function of the parameter δ_o ,

$$\langle \delta^2 \rangle = \frac{\delta_o^2}{2} - \frac{\delta_o^2}{2\sqrt{\pi}} \frac{f_o}{N_L} \iint dx dy \left(\frac{\lambda(x, y) \rho_o}{\delta_o |x|} \right) e^{-\left(\frac{\lambda(x, y) \rho_o}{\delta_o |x|}\right)^2}. \quad (9.22)$$

The normalization factor N_L is the same as in (9.16). In the limit of vanishing space charge $\psi \rightarrow 0$, the calculation of second moments can be carried out analytically. We found

$$\langle \delta^2 \rangle = \frac{\delta_o^2}{2} + \frac{1}{4} \frac{\delta_o^4}{k \rho_o^2 H_o}, \quad (9.23)$$

$$\langle x^2 \rangle = \frac{a^2}{4} + \frac{\langle \delta^2 \rangle}{k^2 \rho_o^2} + \frac{1}{16} \frac{\delta_o^4}{k^3 \rho_o^4 H_o}, \quad (9.24)$$

$$\langle p_x^2 \rangle = \frac{H_o}{2} + \frac{1}{16} \frac{\delta_o^4}{k^2 \rho_o^4 H_o}, \quad (9.25)$$

$$N_L = 2\pi^2 f_o \left(\frac{2H_o}{k} + \frac{\delta_o^2}{2k^2 \rho_o^2} \right).$$

Notice the expressions above are consistent with the equations (8.8) we derived for a general distribution (i.e. in the expression for $\langle x^2 \rangle$ the coefficient of $\langle \delta^2 \rangle$ is D^2 ; the first correction to $\langle p_x^2 \rangle$ is of order δ_o^4).

One of our goals will be to check the scaling of the rms quantities with respect to δ_o , when space charge effects are included.

9.4 The Algorithm

In solving numerically the nonlinear Poisson equation (9.15) we have used the Successive Overrelaxation Method (SOR) described in [50] and recommended in [58].

We implemented the SOR method without introducing a Newton step to treat the nonlinearity since it did not improve the convergence of the algorithm. The reason is probably that the derivative of the nonlinear term (RHS) of our equation vanishes on most of the area of integration.

We solved the equation over a squared grid of side $2b = .04$ m.

The dimension $n \times n$ of the grid ranged from $n = 195$ to $n = 265$, depending on the value of the parameter δ_o .

The SOR iterative algorithm was stopped when the norm of the residue turned out to be less than 10^{-5} times the norm of the RHS of the equation. The two norms are defined in the following way. The numerical solution $u_{j,l} = u(j, l)$ of the problem, with $1 \leq j, l \leq n$, satisfies the discretized equation.

$$\tilde{\nabla}^2 u(j, l) = f(j, l, u(j, l)), \quad (9.26)$$

where $\tilde{\nabla}^2$ is the discretized Laplacian

$$\begin{aligned} \tilde{\nabla}^2 u_{j,l} &= [u_{j-1} + u_{j+1,l} + u_{j,l-1} + u_{j,l+1} - 4u_{j,l}] \frac{1}{\Delta^2}, \\ f(j, l, u(j, l)) &= f_o \pi \left[\operatorname{erf} \left(\frac{\rho_o}{\delta_o |x_j|} (H_o - \frac{k_x}{2} x_j^2 - \frac{k_y}{2} y_l^2 - g_o u(j, l)) \right) + 1 \right]. \end{aligned}$$

with

$$x_j = -b + \Delta(j - 1),$$

$$y_l = -b + \Delta(l - 1).$$

and $\Delta = 2b/(n - 1)$.

The residue $res(j, l)$ is defined as the difference between the LHS and RHS of equation (9.26), and the norm of the residue is

$$normres = \sum_{j,l}^n |res(j, l)|.$$

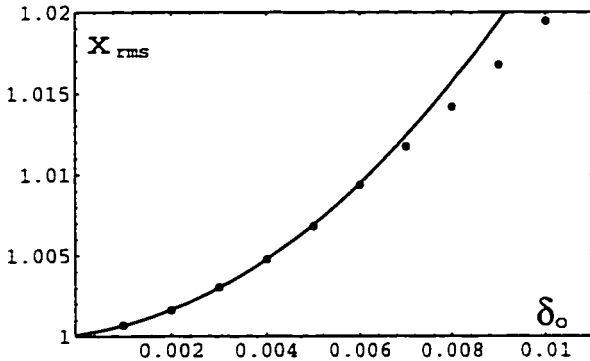


Figure 9.3: Scaled rms horizontal size of the beam, $x_{rms} = (\langle x^2 \rangle_{\delta_o} / \langle x^2 \rangle_o)^{\frac{1}{2}}$, as a function of δ_o , ($I = .105$ A, $\nu/\nu_o = 0.317$).

Our stopping criterion was

$$normres < 10^{-5} \sum_{j,l}^n |f(j,l, u(j,l))|.$$

With this choice $x |res(j,l)| / |f(j,l, u(j,l))|$ turned out to be less than 0.005 for all the points (j,l) such that $f(j,l, u(j,l))$ was larger than 0.005 times its peak value.

The number of iterations necessary to get the required accuracy ranged between 300 and 600, depending on the dimension of the grid.

9.5 The Numerical Solutions

The numerical solutions of the Poisson equation presented in this paper are based on a choice of parameters that mimic the design values of the Maryland Electron Ring [52] in the smooth approximation. See Table 9.1. In the calculations we consider the case of a beam passing through a pipe of square cross section with side of length 2 cm. The wall of the pipe is assumed to be an equipotential boundary for the potential ψ . In this paper we show two sets of solutions.

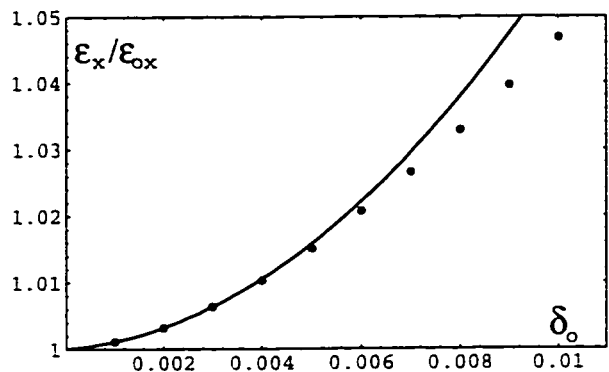


Figure 9.4: Scaled horizontal rms emittance ϵ_x/ϵ_{ox} , as a function of δ_o . ($I = .105$ A, $\nu/\nu_o = 0.317$).

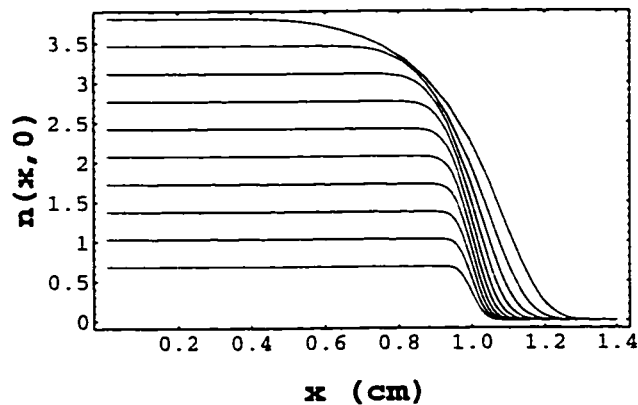


Figure 9.5: Section of the density distributions $n(x, y)$ at $y = 0$ for various beam currents (see Table 9.2). The densities are in units of 10^7 particles/cm 3 . $\delta_o = .01$.

Table 9.1: Parameters for the Maryland Electron Ring smooth model.

Beam energy E_o	10 keV
Tune ν_o	7.6
Focusing function k	17.437 m ⁻²
Radius of curvature ρ_o	1.82 m

The solutions of the first set have been obtained by varying the parameter δ_o , which is related to the rms value $\sigma_s \simeq \delta_o/\sqrt{2}$ of the longitudinal momentum distribution. In particular, δ_o ranges between 10^{-2} and 10^{-3} . The results, in terms of the horizontal profile ($y = 0$) of the beam density $n(x, y)$, see (9.14), are shown in Fig. 9.1.

The various solutions have been normalized in such a way that the corresponding beams carry the same current ($I = .105$ A). In other words, the normalization constant N_L , see (9.16), is the same in all the cases. Since N_L depends on δ_o , in order to achieve the desired normalization the parameter H_o has to be properly tuned. The dependence of H_o on δ_o , however, turns out to be quite weak. The other parameter of the problem, f_o , has been kept fixed: f_o governs the peak value of the beam density and should be independent of δ_o .

The current we have chosen corresponds to a tune depression $\nu/\nu_o = .317$. (The tune depression is evaluated for the KV-beam in the limit $\delta_o \rightarrow 0$). Fig. 9.2 shows the full density function in the (x, y) plane for $\delta_o = .01$.

The rms values $\langle x^2 \rangle_{\delta_o}$ of the horizontal size of the beams and the horizontal emittances have been calculated according to (9.21) and the results shown in Fig. 9.3 and Fig. 9.4. In both pictures we plot the scaled values $x_{rms} = (\langle x^2 \rangle_{\delta_o}/\langle x^2 \rangle_o)^{\frac{1}{2}}$ and ϵ_x/ϵ_{ox} , where $\langle x^2 \rangle_o$ and ϵ_{ox} are the values of the

corresponding quantities for $\delta_o = 0$ (standard KV beam). That is, the rms quantities are scaled with respect to the corresponding quantities of a KV beam in a straight channel under the same external focusing and with the same current.

The curves in the figures are the parabolic fitting obtained by retaining the first four points. As we can see, for small values of δ_o , $\delta_o < .005$, the rms quantities scale according to a quadratic power as in the limit of vanishing space charge (see 8.8).

In the second set of solutions the longitudinal momentum spread was kept fixed ($\delta_o = .01$), while varying the value of the beam currents. Again, for a given choice of the current (or N_L) the normalization equation (9.16) has to be solved for H_o (the other parameter f_o is kept constant). The dependence of H_o on the current is related to the fact that as the space charge increases the emittance of the beam has to be decreased in order for the beam to maintain the same size. Indeed, equation (9.18) shows that in the absence of dispersion the emittance is proportional to the square root of H_o .

Ten different currents have been considered, ranging from $I = .02$ to $I = .112$ A, and corresponding to a tune depression ranging between $\nu/\nu_o = .91$ and $\nu/\nu_o = .20$. The values of the parameters for the various beams are summarized in Table 9.2. The tune depression and emittance reported in the Table refer to the corresponding KV beams in straight channels. The density profiles are shown in Fig. 9.5.

The rms values of the horizontal size of the beam have also been calculated and are shown in Fig. 9.6 (again, what we actually plot is the scaled quantity $x_{rms} = (\langle x^2 \rangle_{\delta_o} / \langle x^2 \rangle_o)^{\frac{1}{2}}$). The data shown in the picture allow one to check the adequacy of the first of equations (8.8) to describe the horizontal rms size of the

beam after the substitution of the undepressed tune with the depressed tune in the expression for the dispersion.

The dashed curve in the picture is

$$x_{rms} = \left(1 + \frac{\delta_o^2 D^2}{2(x^2)_o} \right)^{\frac{1}{2}}. \quad (9.27)$$

with $D = \rho_o/\nu^2$, where ν is the depressed tune evaluated for the KV beam in the absence of dispersion. Although Eq. (9.27) gives a good approximation if the tune depression is sufficiently high, for a smaller tune depression it provides a very large upper bound.

Finally the scaled emittance has also been calculated and plotted in Fig. 9.7.

9.6 Discussion

The main purpose of this study was to evaluate the scaling of the parameters characterizing the beam (rms size, emittance) as a function of the longitudinal momentum deviations and space charge. The stationary solutions of the Vlasov-Poisson equation have been calculated in the form of generalized KV beam distributions, which turn into the standard KV distributions in the limit of vanishing longitudinal momentum spread. For a given current we see that the presence of a finite momentum spread smooths the space distribution in the horizontal plane. As a result a tail appears, which is responsible for the rms growth of the horizontal plane. The tail profile has a rough exponential behavior, which is a reflection of the particular distribution of the momentum spread we chose. For small values of the rms momentum spread $\sigma_\delta \simeq \delta_o/\sqrt{2}$ the rms horizontal scales quadratically with respect to δ_o as expected.

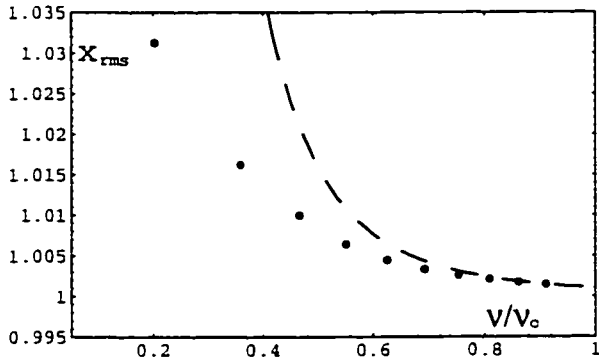


Figure 9.6: Scaled horizontal rms size $x_{rms} = (\langle x^2 \rangle_{\delta_0} / \langle x^2 \rangle_0)^{\frac{1}{2}}$ as a function of the tune depression ν/ν_0 . (dots). The dashed line represents Eq. (9.27).

The growth in the horizontal size of the beam, for a fixed momentum spread, is a function of the current. In particular, it increases with the current (i.e. it increases as the tune depression ν/ν_0 decreases). This effect is to be expected. For larger currents the effective focusing on the particles due to the space charge is smaller and therefore particles off momentum will tend to reach larger distances off axis on the horizontal plane. However as the beam spreads out transversely the charge density decreases and the net focusing gets less depressed. This mechanism explains the overestimate of the rms horizontal size growth, based on the simple replacement of the undepressed tune with the depressed tune in the expression for the dispersion function (Fig. 9.6, dashed line). For an attempt to give a more accurate analytical description of the rms quantities of the beam as a function of the tune depression we refer to the next Chapter.

Finally we want to remark that all the comparisons have been carried out between a solution of the full Vlasov-Poisson equation with the dispersive terms and a solution of the same equation without dispersive term (i.e. $1/\rho_0 = 0$) corresponding to a beam carrying the same current and exposed to the same external focusing. The last solution of course is just an ordinary KV beam.

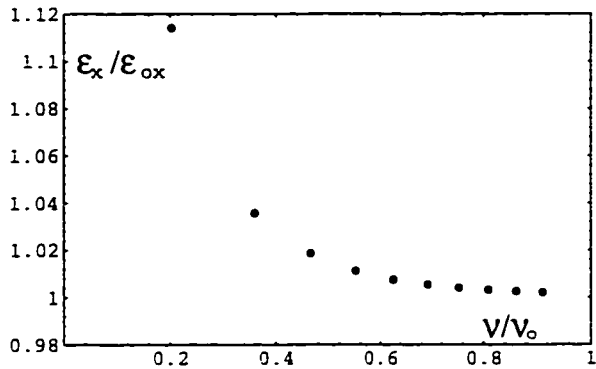


Figure 9.7: Scaled horizontal rms emittance ϵ_x/ϵ_{ox} , as a function of the tune depression ν/ν_o .

Both solutions are stationary solutions in smooth circular and straight channels respectively.

It is interesting to question whether the generalized KV beam is the result of the evolution of the corresponding KV beam after injection into a dispersive channel, or more generally what is the relationship between the two. It is our conjecture that at least for relatively small currents the generalized KV beam should provide a close approximation of the stationary solution of the Vlasov equation that is achieved after a matched injection of an ordinary KV beam with gaussian momentum spread into a circular channel. In the next section this issue is addressed by working out a simplified analytical model.

9.7 ‘Time’ Dependent Vlasov Equation

So far we have been dealing with the problem of studying the stationary solutions of the Vlasov equation. However, as pointed out in the last section, it would also be interesting to investigate the evolution of a (standard) KV beam after injection into a smooth dispersive channel. The exact treatment of this problem

Table 9.2: Current, perveance, tune depression and rms emittance for round KV beams of 10 keV electrons. Beam radius=1 cm.

I (A)	K	ν/ν_o	ϵ_{ox} (mm mrad)
0.0200	$0.2986 \cdot 10^{-3}$	0.910	95.03
0.0302	$0.4513 \cdot 10^{-3}$	0.861	89.88
0.0404	$0.6039 \cdot 10^{-3}$	0.809	84.40
0.0507	$0.7565 \cdot 10^{-3}$	0.752	78.54
0.0609	$0.9092 \cdot 10^{-3}$	0.692	72.22
0.0711	$1.0618 \cdot 10^{-3}$	0.625	65.28
0.0813	$1.2145 \cdot 10^{-3}$	0.551	57.51
0.0916	$1.3671 \cdot 10^{-3}$	0.465	48.52
0.1018	$1.5197 \cdot 10^{-3}$	0.358	37.41
0.1120	$1.6724 \cdot 10^{-3}$	0.202	21.12

would require the solution of the ‘time’-dependent Vlasov equation (9.2) and related Maxwell equations. The problem would probably be best and most efficiently solved by using a Particle In Cell (PIC) code instead of directly trying to solve the required PDE.

In this section we work out a simplified analytical model and explore the two cases of matched and mismatched injection. In the model we assume that the only and net effect of space charge is to depress the focusing function. Also, we neglect all the possible effects stemming from time-dependent fields.

First, let us introduce the symbol $\vec{\zeta}$ to denote the set of the dynamical variables. A certain distribution in the phase space at the initial location $z = z^o$, $g(\vec{\zeta}^o)$, evolves into a distribution $f(\vec{\zeta}^f, z^f)$ at $z = z^f$ given by

$$f(\vec{\zeta}^f, z^f) = g(\mathcal{M}_{(z^o, z^f)}^{-1} \vec{\zeta}^f), \quad (9.28)$$

where $\mathcal{M}_{(z^o, z^f)}$ is the transfer map that gives the position of any point in the phase space at $z = z^f$ as a function of the position in phase space at $z = z^o$

$$\tilde{\zeta}^f = \mathcal{M}_{(z^o, z^f)} \tilde{\zeta}^o.$$

For a continuous bend of radius ρ , in the linear approximation the transfer map reads

$$\begin{aligned} x^f &= x^o \cos \omega z^f + p_x^o \frac{1}{\omega} \sin \omega z^f + \frac{\delta}{\rho \omega^2} (1 - \cos \omega z^f), \\ p_x^f &= -x^o \omega \sin \omega z^f + p_x^o \cos \omega z^f + \frac{\delta}{\rho \omega} \sin \omega z^f, \\ y^f &= y^o \cos \omega z^f + p_y^o \frac{1}{\omega} \sin \omega z^f, \\ p_y^f &= -y^o \omega \sin \omega z^f + p_y^o \cos \omega z^f, \end{aligned} \quad (9.29)$$

where ω is the depressed betatron frequency.

We consider two cases: a mismatched injection given by an abrupt transition from a straight injection line to the smooth circular channel and a matched injection. The matched injection can be obtained by a continuous bend with radius of curvature $\rho_B = 2\rho_o$, the same focusing ω as in the circular machine and length $z_B = \pi/\omega = \lambda_b/2$. (λ_b is the betatron oscillation wavelength). In both cases we assume for the beam an initial KV distribution described by

$$g = \frac{f_o}{\delta_o \sqrt{\pi}} e^{-\frac{\delta^2}{\delta_o^2}} \hat{\delta} \left(\frac{1}{2}(p_x^2 + p_y^2) + \frac{\omega^2}{2}(x^2 + y^2) - H_o \right). \quad (9.30)$$

Next we want to calculate the evolution of the beam density after injection. Consider the matched case first. After evaluating the distribution function at $z = z^f < z_B$ using (9.28),(9.30) and the expression for the transfer map (9.29) we integrate over p_x, p_y, δ , to find the corresponding space density to be

$$n(x, y) = f_o \pi [erf(\tau_+(x, y, z)) - erf(\tau_-(x, y, z))]. \quad (9.31)$$

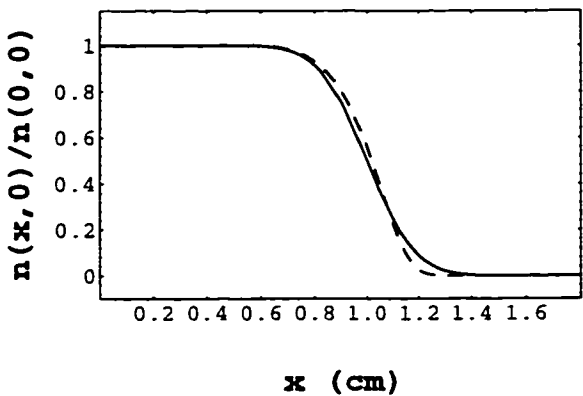


Figure 9.8: Scaled density profile $n(x,0)/n(0,0)$ of the KV beam (simplified analytical model) after a matched injection (solid line) and profile corresponding to the stationary solution of the Vlasov-Poisson equation evaluated numerically (dashed line).

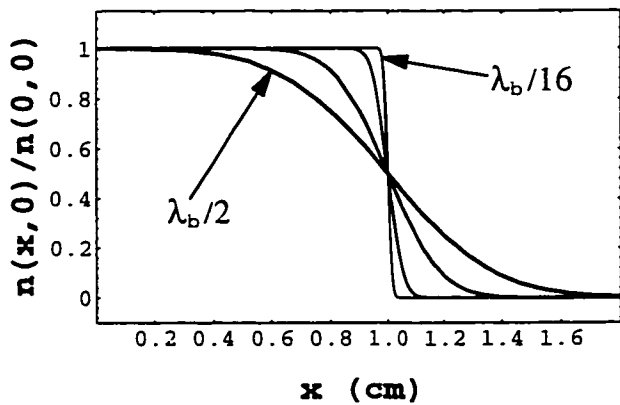


Figure 9.9: Evolution of a KV beam with gaussian longitudinal momentum spread injected into a smooth dispersive channel (simplified analytical model). Mismatched injection. The four beam density profiles correspond to $z = \lambda_b/16, \lambda_b/8, \lambda_b/4, \lambda_b/2$, where λ_b is the betatron oscillation wavelength.

Here τ_+ and τ_- are defined by

$$\tau_{\pm}(x, y, z) = \omega^2 \frac{\rho_B}{\delta_o} \frac{x \pm \sqrt{a^2 - y^2}}{(1 - \cos \omega z)}, \quad (9.32)$$

with a being the radius of the KV beam at injection. At $z = z_B$ we get a profile that matches the stationary beam density within the circular channel.

Comparison (Fig. 9.8) with the density profile obtained by numerical solution of the Vlasov-Poisson equation will allow us to determine $k_{eff} = \omega^2$, by numerical fitting. For the case $\delta_o = .01$ and $I = 1.05$ A, we find that we obtain relatively similar profiles if $k_{eff} = 2.63$ m⁻². If k_{eff} were calculated using an ideal KV beam model with radius a using Eq. (8.23) we would find the result $k_{eff} = 1.75$ m⁻². The deviation between the two values can be justified in terms of the enlargement of the horizontal cross section of the beam and consequent decrease of the space charge forces. In other terms, as we have already noticed, the effective tune, because of dispersion, is larger than before injection.

In the case of a mismatched injection the density is defined by (9.31) and (9.32) with ρ_o replacing ρ_B . The formula shows that the beam pulses around the equilibrium profile corresponding to the matched beam.

The profiles at four different values of z , ($\lambda_b/16, \lambda_b/8, \lambda_b/4, \lambda_b/2$), are shown in Fig. 9.9. At $z = \lambda_b/4$ the density profile is the same as in the case of a matched injection (solid line in Fig. 9.8; at $z = \lambda_b/2$ it reaches its maximum extension.

9.8 Summary

In this chapter we have shown and discussed stationary solutions of the Vlasov-Poisson equation describing beams of charged particles in the presence of dispersion. In particular, we have considered solutions that provide the general-

ization of the KV beam. The numerical solutions presented in the paper show, as expected, that dispersion reshapes and enlarges the beam distribution. The growth, however, evaluated with respect to ordinary KV beams obtained as solution of the same Vlasov equation with vanishing dispersive term, is modest. In a strong focusing lattice ($\nu_0 \gg 1$), for a tune depression (ν/ν_0) in the range $0.2 \div 0.4$ the growth for emittance and rms horizontal radius is of the order of or below 10%. One important lesson learnt from the study is that for highly space charge dominated beams, the dispersion function cannot be calculated simply by changing the undepressed tune with depressed tunes in the formulas. This result, obtained here in the smooth approximation, has motivated us to develop a method to calculate the dispersion function in the more general case with a z dependence, which is relevant for matching purposes [63].

Chapter 10

Envelope Equations in the Presence of Space Charge and Dispersion

10.1 Introduction.

A proper matching of the beam envelopes is usually necessary for a successful transport of space charge dominated beams. The matching forces the beam to undertake breathing modes consistent with the lattice periodicity and prevents the onset of fast growing instabilities. To this purpose the rms envelope equations are currently used. The rms envelope equations were first derived in [56] by writing the equations giving the evolution of the moments of the beam distribution in phase space. In the general case one finds an infinite hierarchy where equations for the lower moments involve moments of higher order. One can truncate the endless sequence and retain only the equations for the second moments if the rms emittance is known or it is an invariant. In a hydrodynamic approach this would be equivalent to assuming that the pressure or the temperature are known or constant [42]. For a generic Hamiltonian system the rms emittance is an exact invariant only in the linear approximation. However, it is

often the case that the rms emittance is roughly preserved even in the presence of nonlinear forces. Exceptions are those cases where a usually fast instability is driven by resonances between the envelope breathing and the motion of the individual particles. These instabilities occur at well defined values of phase advance and tune depression [37]. Incidentally, we recall that the rms emittance is exactly preserved for a KV beam distribution in an external linear focusing channel, because the resulting forces due to space charge are also exactly linear.

The approximate invariance of the rms emittance at least on a short run makes the rms envelope a useful and widely used tool for matching. Moreover, matching helps to limit the emittance growth by cutting on the process necessary to the beam to relax into a beam equilibrium distribution. Relaxation toward equilibrium usually results in a net emittance growth. It should be pointed out, however, that after the beam has reached a state close to equilibrium, either by proper matching or by natural relaxation, a number of phenomena can still cause emittance growth. Among these are the usually fast instabilities driven by possible resonances between the envelope breathing and the motion of the individual particles [37]; the formation of a halo [57, 14]; the equipartitioning between the longitudinal and transverse degrees of freedom [57].

One limitation of the usual rms envelope equations is that they apply only to straight transport lines or monochromatic beams. The problem is that the rms emittance is no longer a linear invariant in the presence of coupling between the longitudinal momentum and the betatron motion that occurs in the bending magnets.

In some cases the use of the standard rms equations may be adequate even if bending magnets are present provided that the beam current is not too high.

However, the growing interest for highly space charge dominated beams in small recirculators, mainly in connection with studies related to Inertial Fusion, is pushing toward achieving a tune depression in a range of values where proper matching can be obtained only with more accurate tools. This is the case, for example, for the Maryland Electron Ring [52] where a tune depression as small as 0.2 is planned.

In this Chapter we present a new set of rms envelope equations that can be applied in the general case where bending magnets and a longitudinal momentum spread are present. The new set of equations also includes the equation for the dispersion function, which is coupled to the equation for the horizontal beam envelope. The new equations apply to continuous beams and should provide the necessary framework to carry out simultaneous matching of the rms envelopes and the dispersion function.

We expect the new equations will have useful applications in very high current regime whenever proper envelopes and dispersion matching is needed or an accurate knowledge of dispersion is required for the purpose of chromaticity correction.

We first begin in Sec. 10.2 by revising the derivation of the standard rms-envelope equations. There we also set the directions for a possible generalization and point out the need to find an rms emittance-like invariant that generalizes the usual rms emittance to the more general case where bends and an energy spread are present. The construction of the new invariant is done in Sec. 3. Not surprisingly the new rms invariant turns out to depend on the dispersion function. The derivation of the new set of rms envelope and dispersion equation is presented in the following Section. The derivation follows [56] in assuming that

(i) the second moments of the beam distribution depend only on the linear part of the forces and (ii) the linear part of the self-force, defined by a least square method, depends only on the second moments (envelopes) of the distribution. These facts can actually be proved for the large class of beam density distribution that have an elliptic symmetry.

Earlier attempts to incorporate dispersion in the framework of the rms envelope equations [37, 28] are not satisfactory since they are based on the assumption of the linear invariance of the standard rms emittance. They hold only in the presence of a moderate dispersion and space charge.

In the final two sections of the chapter we report some tests of the solutions of the new rms envelope-dispersion equations against other independent calculations. In particular, in Sec. 10.5 we use the new equations to evaluate the transition of a continuous beam from a straight transport line into a small recirculator in the smooth approximation. The results are then compared to the calculations carried out in Chapter 9 where we looked for self-consistent equilibrium beam distributions in the form of generalized KV-beams by solving the Poisson-Vlasov equations. Finally in Sec. 10.6 we relax the smooth approximation assumption and test the solutions of the new equation against the simulations done by a PIC code (WARP, see [34]) for a hard edge model of the Maryland E-Ring.

10.2 Envelope Equations in the Absence of Dispersion

In this section we review the rms envelope equations for a straight beam line. For reference see [56], where these equations were first derived, and also [57, 13].

Our starting point is the 4D Hamiltonian

$$H = \frac{1}{2}(p_x^2 + p_y^2) + \frac{k_x(z)}{2}x^2 + \frac{k_y(z)}{2}y^2 + \frac{q}{mv_z^2\gamma^3}\psi. \quad (10.1)$$

The Hamiltonian describes a continuous beam of particles of charge q mass m travelling in a transport channel with longitudinal velocity v_z , relativistic factor γ . The potential ψ accounts for the self-force and includes the contribution from both the electric and magnetic forces. The external focusing is assumed to be purely linear. Chromatic terms are also neglected.

At any location z along the transport line the beam is characterized by the distribution function $f(x, p_x, y, p_y)$ in the 4D phase space, which obeys the Vlasov equation

$$\frac{\partial f}{\partial z} + \frac{\partial f}{\partial x}x' + \frac{\partial f}{\partial p_x}p'_x + \frac{\partial f}{\partial y}y' + \frac{\partial f}{\partial p_y}p'_y = 0. \quad (10.2)$$

The prime denotes a derivative with respect to z .

The Vlasov equation allows us to easily write the equations of motion for the second moments of the distribution,

$$\langle \xi_i \xi_j \rangle = \int \xi_i \xi_j f(x, p_x, y, p_y) d\mu,$$

(where ξ_i, ξ_j are any canonical variables). Here we used the notation $d\mu = dx dp_x dy dp_y$ to indicate the measure in the 4D phase space.

For example,

$$\frac{d}{dz} \langle x^2 \rangle = \frac{\partial}{\partial z} \int f x^2 d\mu = - \int x^2 p_x \frac{\partial f}{\partial x} d\mu = 2 \langle x p_x \rangle. \quad (10.3)$$

The second equality follows from straight use of the Vlasov equation and the canonical equation $x' = p_x$; the last term is obtained after integrating by parts,

having assumed that the distribution function f vanishes on the boundaries. In the same way ($g_o = q/mv_z^2\gamma^3$)

$$\frac{d}{dz}\langle p_x^2 \rangle = -2k_x(z)\langle xp_x \rangle - 2g_o\langle p_x \frac{\partial}{\partial x}\psi \rangle. \quad (10.4)$$

$$\frac{d}{dz}\langle xp_x \rangle = \langle p_x^2 \rangle - k_x(z)\langle x^2 \rangle - g_o\langle x \frac{\partial}{\partial x}\psi \rangle. \quad (10.5)$$

Analogous equations can be written for $\langle y^2 \rangle$, $\langle yp_y \rangle$ and $\langle p_y^2 \rangle$. Here we assumed, as Sacherer in [56], that the beam centroid remains on axis $\langle x \rangle = \langle y \rangle = 0$, and the transverse momenta also average to zero. However, this is not a serious restriction: one can relax this simplifying assumption by taking into account the equations for the first moments as well and consequently by redefining the second moments (e.g. $\langle (x - \langle x \rangle)^2 \rangle$ etc.).

The terms involving the self-potential in the RHS of equations (10.4) and (10.5) will depend in general on higher moments of the distribution (think about expanding ψ in Taylor series). Therefore, self-consistency would require that we should consider the equations for the higher order moments as well. However, under certain assumptions we can consistently limit ourselves to the equations for the second moments.

The first assumption is about the beam density. If the beam density has an elliptic symmetry one can prove [56] that the averages $\langle x \frac{\partial}{\partial x}\psi \rangle$ and $\langle y \frac{\partial}{\partial y}\psi \rangle$ depend only on the envelopes of the beams $\sigma_x = \sqrt{\langle x^2 \rangle}$, $\sigma_y = \sqrt{\langle y^2 \rangle}$ according to

$$\begin{aligned} g_o\langle \frac{\partial}{\partial x}\psi \rangle &= -\frac{K}{2\sigma_x(\sigma_x + \sigma_y)}x, \\ g_o\langle \frac{\partial}{\partial y}\psi \rangle &= -\frac{K}{2\sigma_y(\sigma_x + \sigma_y)}y. \end{aligned} \quad (10.6)$$

In the above equations we have used the generalized perveance K that was defined in (8.24). Before introducing the second assumption let combine Eq. (10.3) and Eq. (10.5) to get

$$\frac{1}{2} \frac{d^2}{dz^2} \langle x^2 \rangle = \langle p_x^2 \rangle - k_x(z) \langle x^2 \rangle - g_o \langle x \frac{\partial}{\partial x} \psi \rangle. \quad (10.7)$$

Because of (10.6) we can observe that if we could express $\langle p_x \rangle$ as a function of $\langle x^2 \rangle$ Eq. (10.7) would be self-contained. This is done by assuming that the rms emittance is known.

Clearly, the expression of the rms emittance.

$$\epsilon_x^2 = (\langle x^2 \rangle \langle p_x^2 \rangle - \langle xp_x \rangle^2), \quad (10.8)$$

allows us to eliminate the variable $\langle p_x^2 \rangle$ by expressing it in terms of ϵ_x , $\langle x^2 \rangle$ and the derivative of $\langle x^2 \rangle$ with respect to z , which by (10.3) is related to $\langle xp_x \rangle$. A similar argument can also be formulated for the moments involving the variables in the vertical plane.

The net result of the two assumptions is the following set of two second order equations for the transverse rms envelope

$$\frac{d^2}{dz^2} \sigma_x = \frac{\epsilon_x^2}{\sigma_x^3} - k_x(z) \sigma_x + \frac{K}{2(\sigma_x + \sigma_y)}, \quad (10.9)$$

$$\frac{d^2}{dz^2} \sigma_y = \frac{\epsilon_y^2}{\sigma_y^3} - k_y(z) \sigma_y + \frac{K}{2(\sigma_x + \sigma_y)}. \quad (10.10)$$

The assumption about the elliptic symmetry of the beam density leaves one with a large enough class of distributions to describe realistic beams.

On the other hand an a priori knowledge of the rms emittance is not in general accessible. In practical applications of the rms envelope equations one assumes

that the rms emittance does not vary significantly over the time scale necessary to achieve the matching. This is equivalent to assuming that the rms emittance which is an exact invariant in linear approximation is roughly preserved even in the presence of the nonlinearities due to the space charge.

How can the method outlined here be extended to include the possibility of a linear coupling between the horizontal motion and the longitudinal momentum that occurs in bends? The first problem to face is to find a rms emittance-like quantity that is linearly invariant in the more general case. In fact, the standard rms emittance ceases to be a linear invariant in the presence of coupling between x and the longitudinal momentum. The search for such an invariant is the topic of the next section.

10.3 Generalization of the rms Emittance

Consider the system

$$H = \frac{1}{2}p_x^2 + \frac{k_x(z)}{2}x^2 + \frac{1}{2m^*}\delta^2 - \frac{x}{\rho(z)}\delta. \quad (10.11)$$

(where $\delta = (p_z - p_o)/p_o$ is the relative deviation from the designed longitudinal momentum p_o and $m^* = E_o^2/(2m^2c^4)$. For simplicity, here we ignore the motion in the vertical plane which in our model is not affected by dispersion. Also, for the moment we ignore the presence of space charge). One can easily verify that the standard rms emittance

$$\epsilon_x^2 = (\langle x^2 \rangle \langle p_x^2 \rangle - \langle xp_x \rangle)^2,$$

is not an invariant for the system (10.11) because of the coupling term $\delta x/\rho$. Our problem is to find a new quantity similar to the rms emittance that is preserved in the presence of the coupling term. The strategy is to write a canonical

transformation that removes the coupling and casts the Hamiltonian in a form for which the invariant can be immediately written. The invariant in the original variables is then recovered by reversion of the canonical transformation.

Consider the canonical transformation

$$(x, p_x) \longrightarrow (\bar{x}, \bar{p}_x)$$

generated by the function

$$G(x, \bar{p}_x, z) = \bar{p}_x[x - \delta D(z)] + x\delta D'(z),$$

where $D(z)$ is a function that will eventually be identified with the dispersion function:

$$\begin{aligned} \bar{x} &= \frac{\partial}{\partial \bar{p}_x} G = x - \delta D(z), \\ p_x &= \frac{\partial}{\partial x} G = \bar{p}_x + \delta D'(z). \end{aligned} \quad (10.12)$$

Notice that our system, which is formally 4D¹, can be treated as a 2D system because δ is a constant of the motion. The transformed Hamiltonian reads

$$\bar{H}(\bar{x}, \bar{p}, \delta, z) = H(x(\bar{x}, \bar{p}_x), p_x(\bar{x}, \bar{p}_x), \delta, z) + \frac{\partial}{\partial z} G(x(\bar{x}, \bar{p}_x), \bar{p}_x, z).$$

We get

$$\bar{H} = \frac{1}{2}\bar{p}_x^2 + \frac{k_x}{2}\bar{x}^2 + \frac{1}{2m^*}\delta^2 + \delta\bar{x} \left(\frac{d^2}{dz^2}D + k_x(z)D - \frac{1}{\rho} \right) + \dots$$

The remaining terms (...) in the Hamiltonian contain a combination of δ and function of z . Since they only affect the evolution of the variable canonically conjugated to δ , which we are not interested in, they can be disregarded.

¹The canonical variables are x, p_x, δ and the variable canonically conjugated to δ , i.e. the RF phase.

Clearly, if the function D is chosen in such a way that

$$\frac{d^2}{dz^2}D + k_x(z)D - \frac{1}{\rho} = 0,$$

the coupling term between δ and \bar{x} vanishes and we can immediately conclude that the quantity

$$\bar{\epsilon}_x^2 = (\langle \bar{x}^2 \rangle \langle \bar{p}_x^2 \rangle - \langle \bar{x} \bar{p}_x \rangle)^2$$

is a linear invariant for the Hamiltonian \bar{H} . Then, if we express $\bar{\epsilon}_x$ in terms of the old variables we obtain a quantity invariant for our original system.

$$\begin{aligned} \langle \bar{x}^2 \rangle &= \int \bar{x}^2 f(\bar{x}, \bar{p}_x, \delta) d\bar{\mu} \\ &= \int (x - \delta D)^2 f(\bar{x}(x, p_x, \delta), \bar{p}_x(x, p_x, \delta), \delta) d\mu \\ &= \int x^2 \tilde{f}(x, p_x, \delta) d\mu - 2D \int x \delta \tilde{f}(x, p_x, \delta) d\mu + D^2 \int \delta^2 \tilde{f}(x, p_x, \delta) d\mu \\ &= \langle x^2 \rangle - 2D \langle x \delta \rangle + D^2 \langle \delta^2 \rangle. \end{aligned} \quad (10.13)$$

Here, $d\mu = dx dp_x d\delta$, $d\bar{\mu} = d\bar{x} d\bar{p}_x d\delta$, and $d\mu = d\bar{\mu}$ because the transformation is canonical. Notice that since $f(\bar{x}, \bar{p}_x, \delta)$ is a generic function, then $\tilde{f}(x, p_x, \delta) = f(\bar{x}(x, p_x, \delta), \bar{p}_x(x, p_x, \delta), \delta)$ is also a generic function. That is the equality (10.13) holds for any distribution function.

By the same token,

$$\langle \bar{p}_x^2 \rangle = \langle p_x^2 \rangle - 2D' \langle p_x \delta \rangle + D'^2, \quad (10.14)$$

$$\langle \bar{x} \bar{p}_x \rangle = \langle x p_x \rangle - D \langle p_x \delta \rangle - D' \langle x \delta \rangle + DD' \langle \delta^2 \rangle. \quad (10.15)$$

Therefore, our invariant reads

$$\begin{aligned}
\epsilon_{\bar{x}}^2 &= \epsilon_{dx}^2 = (\langle x^2 \rangle - 2D\langle x\delta \rangle + D^2\langle \delta^2 \rangle) \\
&\quad (\langle p_x^2 \rangle - 2D'\langle p_x\delta \rangle + D'^2\langle \delta^2 \rangle) \\
&\quad - (\langle xp_x \rangle - D\langle p_x\delta \rangle - D'\langle x\delta \rangle + DD'\langle \delta^2 \rangle)^2,
\end{aligned} \tag{10.16}$$

where we have introduced the notation ϵ_{dx} for the new invariant, to which in the following we will refer as 'generalized emittance'.

Notice that in a straight beam line, where no dispersion is present ($D = D' = 0$) or for a monochromatic beam with vanishing longitudinal momentum spread $\langle \delta^2 \rangle = 0$, the invariant ϵ_{dx} coincides with the usual rms emittance. It is possible to simplify the expression of the new invariant by making use of the result of Appendix C, i.e. the identification of the dispersion function and derivative in terms of the second moments of the distribution.

$$\begin{aligned}
\langle x\delta \rangle &= \langle \delta^2 \rangle D(z), \\
\langle p_x\delta \rangle &= \langle \delta^2 \rangle D'(z).
\end{aligned} \tag{10.17}$$

Use of (10.17) in (10.16) leads to

$$\epsilon_{dx}^2 = (\langle x^2 \rangle - D^2\langle \delta^2 \rangle)(\langle p_x^2 \rangle - D'^2\langle \delta^2 \rangle) - (\langle xp_x \rangle - DD'\langle \delta^2 \rangle)^2. \tag{10.18}$$

One can double-check the invariance of the new quantity by direct calculation with the aid of (C.2) and (C.3) and verify that $\frac{d}{dz}\epsilon_{dx}^2 = 0$.

Before ending this section it is instructive to comment on the nature of the invariant (10.16). The standard rms emittance is an example of a 'kinematic invariant'. In contrast to dynamic invariants, the form of which depends on the details of the system (e.g. the Courant-Snyder invariant), a kinematic invariant is preserved under any linear Hamiltonian system. The quantity (10.16) although

derived from a kinematic invariant has the nature of a 'dynamic invariant' since it depends on the particular system through the dispersion function $D(z)$. See [21] for this terminology.

It should be recalled that for a general linear system it is always possible (even in the presence of coupling between the various degrees of freedom) to write down a kinematic invariant (see [21]). However, that quantity is not useful for our purposes because it involves the statistics of the variable canonically conjugated to δ (i.e. the RF phase), which in our problem is left unspecified.

10.4 Envelope Equations in the Presence of Dispersion

Having succeeded in finding a linear invariant when the horizontal motion is coupled to the longitudinal momentum we are now able to write the rms envelope equations along the lines of Sec. 10.2.

The full Hamiltonian with space charge and dispersion reads

$$H = \frac{1}{2}(p_x^2 + p_y^2) + \frac{k_x}{2}x^2 + \frac{k_y}{2}y^2 + \frac{q}{mv_z^2\gamma^3}\psi - \frac{\delta}{\rho}x + \frac{1}{2m}\delta^2. \quad (10.19)$$

In writing (10.19) we neglect any possible effect coming from the transverse current in the bending as well as any chromatic terms.

From the Vlasov equations we get the following equations for the second moments.

$$\frac{d}{dz}\langle x^2 \rangle = 2\langle xp_x \rangle, \quad (10.20)$$

$$\frac{d}{dz}\langle p_x^2 \rangle = -2k_x(z)\langle xp_x \rangle - 2g_o\langle p_x \frac{\partial}{\partial x}\psi \rangle + \frac{2}{\rho}\langle p_x \delta \rangle, \quad (10.21)$$

$$\frac{d}{dz}\langle xp_x \rangle = \langle p_x^2 \rangle - k_x(z)\langle x^2 \rangle - g_o\langle x \frac{\partial}{\partial x} \psi \rangle + \frac{1}{\rho}\langle x\delta \rangle. \quad (10.22)$$

$$\frac{d}{dz}\langle x\delta \rangle = \langle p_x\delta \rangle. \quad (10.23)$$

$$\frac{d}{dz}\langle p_x\delta \rangle = -k_x(z)\langle x\delta \rangle - g_o\langle \delta \frac{\partial}{\partial x} \psi \rangle + \frac{1}{\rho}\langle \delta^2 \rangle. \quad (10.24)$$

$$\frac{d}{dz}\langle \delta^2 \rangle = 0. \quad (10.25)$$

The equations for $\langle y^2 \rangle$, $\langle p_y^2 \rangle$, $\langle yp_y \rangle$ are analogous to the equations for $\langle x^2 \rangle$, $\langle p_x^2 \rangle$, $\langle xp_x \rangle$ in the absence of dispersion

$$\frac{d}{dz}\langle y^2 \rangle = 2\langle yp_y \rangle, \quad (10.26)$$

$$\frac{d}{dz}\langle p_y^2 \rangle = -2k_y(z)\langle yp_y \rangle - 2g_o\langle p_y \frac{\partial}{\partial y} \psi \rangle. \quad (10.27)$$

$$\frac{d}{dz}\langle yp_y \rangle = \langle p_y^2 \rangle - k_y(z)\langle y^2 \rangle - g_o\langle y \frac{\partial}{\partial y} \psi \rangle, \quad (10.28)$$

The new system of equations for the second moments of the beam distribution differs from (10.4), (10.5), (10.7) in two regards. Three additional equations are present because of the extra degree of freedom δ and two extra terms involving second moments in δ are present in the remaining equations.

Again, following Sacherer [56] we assume that the beam density has an elliptic symmetry. This allows us to express the terms in eqs. (10.22) and (10.28) involving the self-potential ψ in terms of the envelopes only.

In order to resolve the term $\langle \delta \frac{\partial}{\partial x} \psi \rangle$ in Eq. (10.24) we follow a different reasoning that can also be traced back to Sacherer's paper [56]. He observed that again, under the assumptions of a beam with elliptic symmetry, if one defines the linear part of the force due to the self-potential by a least square method, one finds it depends only on the envelopes. That is, if we write the

linear part of the self-force in the horizontal plane as $xF(z)$ and define F as the function that minimizes the functional

$$I[F(z)] = \int dx dy \left[xF(z) - \frac{\partial}{\partial x} \psi \right]^2 n(x, y, z), \quad (10.29)$$

we find the result $F = K/[2\sigma_x(\sigma_x + \sigma_y)]$. The quantity $n(x, y, z)$ is the beam density. Therefore, in linear approximation

$$\langle \delta \frac{\partial}{\partial x} \psi \rangle \simeq \langle x \delta \rangle \frac{K}{2\sigma_x(\sigma_x + \sigma_y)}. \quad (10.30)$$

As a result the two equations in (10.23) and (10.24) can be combined into the single second order equation

$$\frac{d^2}{dz^2} \langle x \delta \rangle + \left[k_x - \frac{K}{2\sigma_x(\sigma_x + \sigma_y)} \right] \langle x \delta \rangle = \frac{1}{\rho} \langle \delta^2 \rangle. \quad (10.31)$$

As in the case of vanishing space-charge the form of Eq. (10.31) suggests the identification

$$\begin{aligned} \langle x \delta \rangle &= \langle \delta^2 \rangle D(z), \\ \langle p_x \delta \rangle &= \langle \delta^2 \rangle D'(z). \end{aligned} \quad (10.32)$$

Incidentally notice that the net result of our calculation so far is equivalent to having used an effective self-potential of the form

$$\psi(x, y) = -\frac{K}{4(\sigma_x + \sigma_y)} \left(\frac{x^2}{\sigma_x} + \frac{y^2}{\sigma_y} \right). \quad (10.33)$$

Therefore, for the dispersion function we have the equation

$$\frac{d^2}{dz^2} D + \left[k_x - \frac{K}{2\sigma_x(\sigma_x + \sigma_y)} \right] D = \frac{1}{\rho}. \quad (10.34)$$

Next we use the new linear invariant defined in the previous section, that is

$$\begin{aligned} \epsilon_{dx}^2 &= (\langle x^2 \rangle - D^2 \langle \delta^2 \rangle)(\langle p_x^2 \rangle - D'^2 \langle \delta^2 \rangle) \\ &\quad - (\langle x p_x \rangle - DD' \langle \delta^2 \rangle)^2. \end{aligned} \quad (10.35)$$

with the dispersion function D defined by (10.32) and obeying (10.34). As for the standard rms emittance in the derivation of the usual rms envelope equations we make the assumption that the new invariant is approximately preserved in the presence of space charge as well. Such an assumption allows us to express $\langle p_x^2 \rangle$ in terms of the x -envelope and its derivative.

$$\langle p_x^2 \rangle = \frac{\epsilon_{dx}^2 + (\langle xp_x \rangle - DD' \langle \delta^2 \rangle)^2}{\langle x^2 \rangle - D^2 \langle \delta^2 \rangle} + D'^2(z) \langle \delta^2 \rangle. \quad (10.36)$$

We recall that from Eq. (10.20) $2\langle xp_x \rangle = (\sigma^2)'$. After combining eqs. (10.20), (10.22), and (10.36) together we finally get

$$\begin{aligned} \frac{d^2}{dz^2} \sigma_x &= \frac{\epsilon_{dx}^2 + (\sigma_x \frac{d}{dz} \sigma_x - DD' \langle \delta^2 \rangle)^2}{\sigma_x(\sigma_x^2 - D^2 \langle \delta^2 \rangle)} - \frac{1}{\sigma_x} \left(\frac{d\sigma_x}{dz} \right)^2 \\ &\quad - k_x(z) \sigma_x + \frac{K}{2(\sigma_x + \sigma_y)} + \frac{\langle \delta^2 \rangle}{\sigma_x} \left(\frac{D}{\rho} + D'^2 \right). \end{aligned} \quad (10.37)$$

$$\frac{d^2}{dz^2} \sigma_y = \frac{\epsilon_y^2}{\sigma_y^3} - k_y(z) \sigma_y + \frac{K}{2(\sigma_x + \sigma_y)}. \quad (10.38)$$

The derivation of equation (10.38) is identical to the case without dispersion.

The three equations (10.34),(10.37),(10.38), in the variables D , σ_x , σ_y , provide a consistent description for the evolution of the rms envelopes of a beam in a dispersive channel. They can be used to achieve a simultaneous matching of the rms beam envelopes and dispersion function. Although more complicated, they are not conceptually different from the standard envelope equations. The techniques used to solve and optimize the solutions of the matching problem for the standard envelope equations should be applicable with few modifications to the new equations as well. We emphasize the fact that the invariant ϵ_{ds}^2 , appearing in Eq. (10.37) coincides with the rms emittance at those location where $D = 0$.

Finally notice that for $1/\rho(z) = 0$ or $\langle \delta \rangle = 0$, we recover the usual envelope

equations for straight transport lines.

10.5 Transition from a Straight Beam Line to a Dispersive Channel

As an application and first test of the theory outlined in the previous sections we want to estimate the variation of the beam parameters in the transition from a straight beam line to a dispersive channel. Eventually we want to compare the result with the calculations involving the solution of the Vlasov-Poisson equation in the form of a generalized KV distribution reported in Chapter 9.

We assume a smooth model where both the focusing functions and the radius of curvature are constant (z -independent). Furthermore, the external focusing is the same in the straight and in the dispersive channel.

We assume that the beam undergoes a transition between two stationary distributions before and after injection. For the purposes of this calculation how this matched injection is achieved does not need to be specified. In general the solution of the matching problem would require the solution of the rms envelope-dispersion differential equations (10.34),(10.37),(10.38) for specified initial and final beam conditons. Instead, the assumption that before and after injection the beam be stationary reduces the problem to solving a set of algebraic equations.

The two stationary solutions are described respectively by the standard envelope equations (10.9), (10.10) and the generalized rms envelope equations (10.34),(10.37),(10.38) by setting all the derivatives of the rms quantities to zero. By doing so we convert the original differential equations into two systems of algebraic equations involving the second moments of the distribution before

and after injection.

The connection between the two set of rms quantities (before and after injection) is provided by the assumption that the generalized emittance (10.16) in the horizontal plane is conserved through injection.

The rms envelope equations for the stationary distribution before injection read

$$\frac{(\epsilon_x^2)_s}{\sigma_{xs}^3} - k_x \sigma_{xs} + \frac{K}{2(\sigma_{xs} + \sigma_{ys})} = 0, \quad (10.39)$$

$$\frac{(\epsilon_y^2)_s}{\sigma_{ys}^3} - k_y \sigma_{ys} + \frac{K}{2(\sigma_{xs} + \sigma_{ys})} = 0. \quad (10.40)$$

The subscript s indicates that the various quantities refer to the beam in the straight channel before injection. For given values of the beam perveance K and emittances $(\epsilon_x^2)_s$, $(\epsilon_y^2)_s$ the two equations above can be solved for the rms size of the beam σ_{xs} , σ_{ys} .

After injection in the circular channel a stationary beam must satisfy

$$\left[k_x - \frac{K}{2\sigma_x(\sigma_x + \sigma_y)} \right] D = \frac{1}{\rho}. \quad (10.41)$$

$$\frac{\epsilon_{dx}^2}{\sigma_x(\sigma_x^2 - D^2(\delta)^2)} - k_x \sigma_x + \frac{K}{2(\sigma_x + \sigma_y)} + \frac{D^2(\delta)^2}{\rho \sigma_x} = 0. \quad (10.42)$$

$$\frac{\epsilon_y^2}{\sigma_y^3} - k_y \sigma_y + \frac{K}{2(\sigma_x + \sigma_y)} = 0, \quad (10.43)$$

The second equation (10.42) can be combined with (10.41) and replaced by

$$(\sigma_x^2 - D^2(\delta)^2)^2 = \rho D \epsilon_{dx}^2. \quad (10.44)$$

Because of its invariance the generalized emittance ϵ_{dx} appearing in the equations above is the same as the emittance at injection $(\epsilon_x)_s$. Of course it is also

$\epsilon_y = (\epsilon_y)_s$, because dispersion does not affect the rms emittance on the vertical plane.

A numerical solution for the system (10.43) will be given in Sec. 10.5.3 for various values of the perveance (or beam current). In the next two sections we work out an analytical first order approximation in $\langle \delta^2 \rangle$, for σ_x, σ_y, D .

From now on we will consider the case where the focusing functions are the same in the horizontal and vertical plane $k_x = k_y$, before and after injection. Also, we will assume that at injection the beam is round $\sigma_{xs} = \sigma_{ys}$, $((\epsilon_x)_s = (\epsilon_y)_s)$

10.5.1 Limit of vanishing space charge

Before tackling the full problem, it is useful to first consider the case where space charge is negligible. First we want to evaluate the variation of the rms horizontal size of the beam. Again, we shall use the subscript s to indicate quantities referring to the straight channel. The rms quantity σ_{xs} in the straight beam line obeys the rms envelope equation (see Eq. (10.9))

$$\frac{(\epsilon_x^2)_s}{\sigma_{xs}^3} - k_x \sigma_{xs} = 0,$$

that is

$$\sigma_{xs}^2 = (\epsilon_x^2)_s / \sqrt{k_x}. \quad (10.45)$$

On the other hand, in the circular channel we have the following set of equations

$$(\sigma_x^2 - D^2 \langle \delta^2 \rangle)^2 = \rho D \epsilon_{dx}, \quad (10.46)$$

$$\frac{\epsilon_y^2}{\sigma_y^3} - k_y \sigma_y = 0, \quad (10.47)$$

$$D = \frac{1}{\rho k_x}. \quad (10.48)$$

The equation for σ_y is the same as in the straight line. Equation (10.46) could be solved exactly in σ_x but we prefer to solve it perturbatively to illustrate the method we will follow in the next Section when space charge is taken into account.

We set

$$\sigma_x = \sigma_{xs} + \langle \delta^2 \rangle \eta_x + \mathcal{O}(\langle \delta^2 \rangle^2), \quad (10.49)$$

where σ_{xs} is a solution of the envelope equation when $\langle \delta^2 \rangle = 0$ and coincides with (10.45), and η_x is the first term of the perturbative series in $\langle \delta^2 \rangle$.

After substituting (10.49) in (10.46) and retaining only first order terms in $\langle \delta^2 \rangle$ or η_x we find

$$\eta_x = \frac{1}{2\rho^2 k_x^2 \sigma_{xs}} = \frac{D^2}{2\sigma_{xs}}, \quad (10.50)$$

or, after inserting (10.50) into (10.49),

$$\sigma_x^2 = \sigma_{xs}^2 + \langle \delta^2 \rangle D^2. \quad (10.51)$$

Although obtained perturbatively, one can verify that the result happens to coincide with the exact solution. The characteristic feature is that the horizontal rms size of the beam scales as the square of the dispersion function $D = 1/(\rho k_x)$.

Next let us focus on the emittance. As we already noticed, in the straight beam line the invariant ϵ_{dx} coincides with the usual rms emittance $(\epsilon_x^2)_s$. From Eq. (10.16)

$$\epsilon_{dx}^2 = (\epsilon_x^2)_s = (\langle x^2 \rangle - D^2 \langle \delta^2 \rangle) \langle p_x^2 \rangle - \langle xp_x \rangle^2 \quad (10.52)$$

$$= \epsilon_x^2 - D^2 \langle \delta^2 \rangle \langle p_x^2 \rangle, \quad (10.53)$$

where the first term on the RHS is the standard rms emittance after injection.

Notice that since the last term in the third equation of (10.53) is positive the standard rms emittance in the circular channel, ϵ_x , is larger than the standard rms emittance before injection $(\epsilon_x)_s = \epsilon_{dx}$. This is consistent with our intuition.

$$\epsilon_x^2 = (\epsilon_x^2)_s + D^2 \langle \delta^2 \rangle \langle p_x^2 \rangle. \quad (10.54)$$

Therefore, the relative growth of emittance through first order in the square of the rms momentum spread reads $\langle \delta^2 \rangle$ reads

$$\frac{\epsilon_x^2}{(\epsilon_x^2)_s} = 1 + D^2 \langle \delta^2 \rangle \frac{\langle p_x^2 \rangle}{\langle p_x^2 \rangle_s \langle x^2 \rangle_s}. \quad (10.55)$$

Here we have used the fact that in a stationary case

$$(\epsilon_x^2)_s = (\langle x^2 \rangle_s \langle p_x^2 \rangle_s)^{\frac{1}{2}}, \quad (10.56)$$

that is $\langle xp_x \rangle_s = 0$ as it can be seen from Eq. (10.3).

On the other hand from the rms equation (10.5) we have

$$\begin{aligned} \langle p_x^2 \rangle &= k_x \langle x^2 \rangle - \frac{D \langle \delta^2 \rangle}{\rho} \\ &= k_x (\langle x^2 \rangle - D^2 \langle \delta^2 \rangle) \\ &= k_x \langle x^2 \rangle_s = \langle p_x^2 \rangle_s, \end{aligned} \quad (10.57)$$

where the second equality follows from (10.48), the third from (10.51). Therefore,

$$\frac{\epsilon_x^2}{(\epsilon_x^2)_s} = 1 + D^2 \frac{\langle \delta^2 \rangle}{\langle x^2 \rangle_s}. \quad (10.58)$$

10.5.2 Space Charge Included

In the straight beam line before injection the rms $\sigma_{xs} = \sigma_{ys}$ envelopes are defined by the equation

$$\frac{(\epsilon_x^2)_s}{\sigma_{xs}^3} - k_x(z)\sigma_{xs} + \frac{K}{4\sigma_{xs}} = 0, \quad (10.59)$$

which has the solution

$$\sigma_{xs} = \sigma_{ys} = \left(\sqrt{\left(\frac{K}{8k_x} \right)^2 + \frac{(\epsilon_x^2)_s}{k_x}} + \frac{K}{8k_x} \right)^{\frac{1}{2}}. \quad (10.60)$$

After injection into the dispersive channel the beam size gets modified by dispersion. If we assume that $\langle \delta^2 \rangle$ is small we can represent the solutions σ_x , σ_y as

$$\sigma_x = \sigma_{xs} + \langle \delta^2 \rangle \eta_x + \mathcal{O}(\langle \delta^2 \rangle^2), \quad (10.61)$$

$$\sigma_y = \sigma_{ys} + \langle \delta^2 \rangle \eta_y + \mathcal{O}(\langle \delta^2 \rangle^2), \quad (10.62)$$

$$D = D_o + \langle \delta^2 \rangle D_1 + \mathcal{O}(\langle \delta^2 \rangle^2), \quad (10.63)$$

where η_x , η_y , D_1 are first order terms of a perturbative series.

First of all we can use equation (10.43) to express η_y in terms of η_x .

$$\eta_y = \eta_x \frac{K}{5K - 32k_x \sigma_{xs}^2}. \quad (10.64)$$

For future use we define

$$\eta_{xy} = \frac{K}{5K - 32k_x \sigma_{xs}^2}. \quad (10.65)$$

Next we use the equation (10.41) for dispersion to find

$$D_0 = \frac{1}{\rho} \left(k_x - \frac{K}{4\sigma_{xs}^2} \right)^{-1}, \quad (10.66)$$

and

$$D_1 = -\frac{\rho D_o K}{4\sigma_{xs}} \eta_x \frac{(3 + \eta_{xy})}{4\sigma_{xs}^2 k_x - K}. \quad (10.67)$$

From equation (10.44) we derive in first order

$$4\sigma_{xs}^3 \eta_x - 2\sigma_{xs}^2 D_o^2 = \rho D_1 \epsilon_{sx}^2. \quad (10.68)$$

Finally we insert (10.65), (10.67) into equation (10.68) to get

$$\eta_x = 4\sigma_{xs} D_o^2 \left(8\sigma_{xs}^2 + K \frac{\sigma_{xs}^2 (3 + \eta_{xy})}{4k_x \sigma_{xs}^2 - K} \right)^{-1}, \quad (10.69)$$

where η_{xy} indicates the ratio η_y/η_x (see Eq. (10.65)). In the limit of vanishing space charge, $K \rightarrow 0$, we have $D_o \rightarrow 1/(\rho k_x)$ and

$$\eta_x \longrightarrow \frac{1}{2\rho^2 k_x^2 \sigma_{xs}},$$

as expected from (10.50).

Next we can evaluate the emittance. As in the case of vanishing space charge the relative growth of the emittance due to the injection into the dispersive channel is given by

$$\epsilon_x^2 = (\epsilon_x^2)_s + D^2 \langle \delta^2 \rangle \langle p_x^2 \rangle. \quad (10.70)$$

Again, we can use the rms equations to evaluate the ratio $\langle p_x^2 \rangle / \langle p_x^2 \rangle_s$. In the straight channel before injection

$$\langle p_x^2 \rangle_s = \langle x^2 \rangle_s \left(k_x - \frac{K}{4\sigma_{xs}^2} \right). \quad (10.71)$$

After injection where the dispersive term is present we have

$$\langle p_x^2 \rangle = \langle x^2 \rangle \left(k_x - \frac{K}{2\sigma_x(\sigma_x + \sigma_y)} \right) - \frac{D}{\rho} \langle \delta^2 \rangle, \quad (10.72)$$

then,

$$\frac{\langle p_x^2 \rangle}{\langle p_x^2 \rangle_s} = \frac{4}{\rho D} \frac{\sigma_x^2 - D^2 \langle \delta^2 \rangle}{4\sigma_{xs}^2 k_x - K}, \quad (10.73)$$

and therefore

$$\frac{\epsilon_x^2}{(\epsilon_x^2)_s} = 1 + \frac{4D \langle \delta^2 \rangle (\sigma_x^2 - D^2 \langle \delta^2 \rangle)}{\rho \sigma_{xs}^2 (4\sigma_{xs}^2 k_x - K)}. \quad (10.74)$$

10.5.3 Numerical Solutions for the Stationary Case

So far we have written the algebraic rms-envelope dispersion equations that govern the transition of a beam from a straight to a dispersive channel and found a first order solution to those equations. As anticipated we would like to compare these results with the calculations presented in Chapter 9 where the same problem was faced by looking for self-consistent solutions of the Vlasov-Poisson equation. There we presented a study of the scaling of the rms horizontal size and emittance as a function of the current, or tune depression.

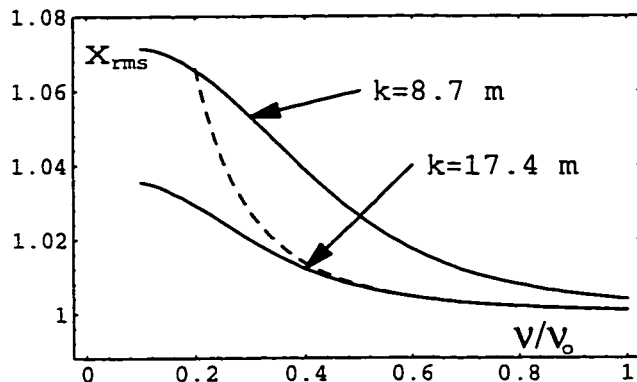


Figure 10.1: Scaled horizontal rms beam size $x_{rms} = \sigma_x / \sigma_{xs}$, after injection into a small recirculator as a function of the tune depression ν / ν_o (solid lines). See the text for further comments.

The beam size and emittance growth due to the injection were computed by comparing the self-consistent solutions of the Vlasov-Poisson equation in

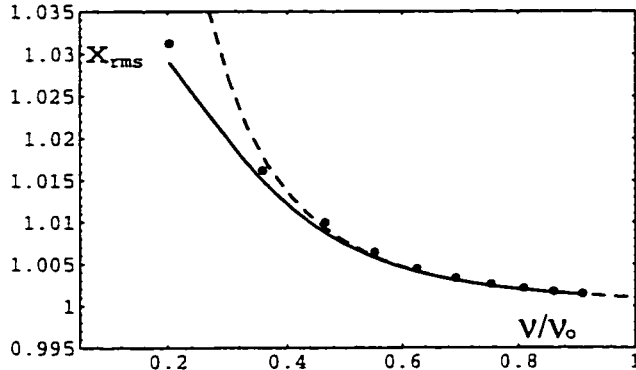


Figure 10.2: Scaled horizontal rms beam size $x_{rms} = \sigma_x/\sigma_{xs}$, after injection into a small recirculator as a function of the tune depression ν/ν_o (solid lines) compared with the results (dots) obtained in the previous Chapter by studying self-consistent beam distributions in the recirculator satisfying the Vlasov-Poisson equation.

the dispersive channel, in the form of generalized KV-distributions, with the corresponding distributions that were obtained by setting the rms longitudinal momentum spread to zero ($\langle \delta^2 \rangle = 0$) and leaving all the other beam parameters unaltered. The latter distributions corresponded to ordinary KV-beams. In Chapter 9 we made the conjecture that the generalized KV-beam in the dispersive channel is the result of a matched injection of an ordinary KV-beam having a gaussian distribution in the longitudinal momentum spread. Now we are in position to check on both the conjecture and the various assumptions that we have used in deriving the rms envelope-dispersion equations.

In solving equations (10.43) we are interested in comparing solutions for various values of the perveance K , corresponding to beams carrying different currents. By looking at equation (10.60) we realize there are two ways we can achieve our goal: either by modifying the strength of the external focusing or by modifying the rms emittance. Here we choose the second way in order to get results that will eventually be comparable to those reported in Chapter 9. To

this end we use the definition of the rms depressed tune ν introduced in (8.23)

$$\frac{\nu^2}{\rho^2} = \left(k_x - \frac{K}{4\sigma_{xs}^2} \right).$$

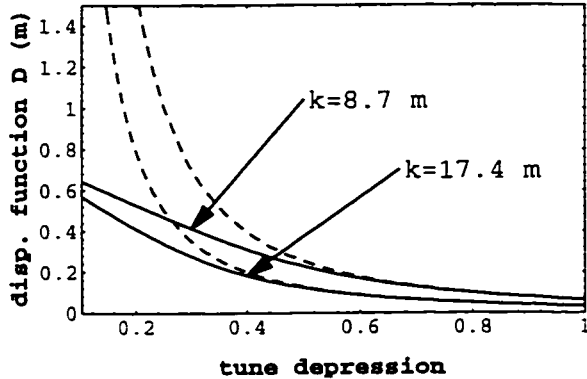


Figure 10.3: Dispersion function in the small recirculator as a function of the tune depression ν/ν_0 (solid lines). The dashed line is the value of the dispersion function as calculated without taking into account the enlargement of the horizontal beam size in the recirculator due to dispersion.

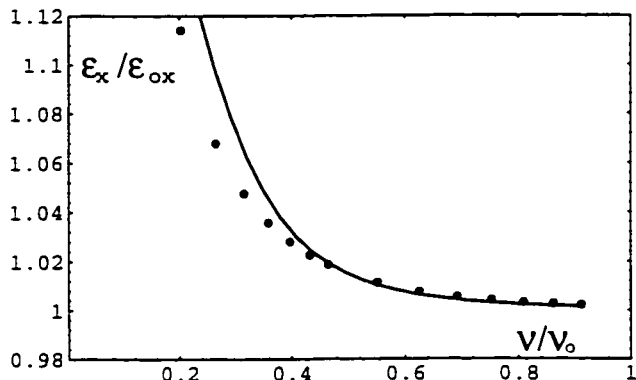


Figure 10.4: Scaled emittance as a function of the tune depression ν/ν_0 (solid line). The dots are from the self-consistent calculation of the previous chapter.

Then, after defining the tune depression $\xi = \nu/\nu_0$ (ν_0 indicates the undepressed tune) we rewrite Eq. (10.69) as

$$\eta_x = \left(\frac{1}{2\sigma_{xs}\rho^2 k_x^2} \right) \frac{1}{\xi^2} \left(\frac{5\xi^2 + 3}{3\xi^4 + 4\xi^2 + 1} \right). \quad (10.75)$$

It is also

$$K = 4\sigma_{xs}^2 k_x (1 - \xi^2), \quad (10.76)$$

$$\epsilon_x^2 = \sigma_{xs}^4 k_x \xi^2. \quad (10.77)$$

A first-order accurate solution for the dispersion function reads

$$D = \frac{1}{\rho} \left(k_x - \frac{K}{2(\sigma_{xs} + \eta_x)(2\sigma_{xs} + \eta_x + \eta_y)} \right)^{-1}. \quad (10.78)$$

where η_x were given in (10.75), and η_y depends on η_x through (10.64).

Equations (10.43) are solved numerically for various values of the tune depression and the solutions are shown in the pictures. In the calculation we set $\sqrt{\langle \delta \rangle^2} = .007$. The other parameters ν_o , ρ , k_x were set to mimic the parameters for the Maryland Electron Ring [52] in the smooth approximation, and are summarized in Table 9.1.

In Fig. 10.1 we plot the ratio x_{rms} between the rms horizontal size of the beam before and after injection. Two curves are plotted corresponding to two values of the external focusing functions as indicated in the picture. For the case $k = 17.4$ m (corresponding to the smooth modeling of the Maryland E-Ring) we report (dashed line) the result from the first order calculation [Eq. 10.61 and (10.75)]. One can observe that the first order analytical curve gives a good approximation for $\nu/\nu_o > 0.4$. In Fig. 10.2 the curve for the case $k = 17.4$ is compared against the results (dots) obtained in Chapter 9 from the self-consistent solutions of the Vlasov-Poisson equation in the form of generalized KV-beams (the dots in Fig. 10.2 are the same as those shown in Fig. 9.6). For comparison the curve from the first order analytical calculation is also reported (dashed line). We can see that the agreement is very good. This result makes us confident that both the conjecture made at the end of the previous Chapter (an ordinary KV

beam injected into a smooth recirculator evolves into a generalized KV beam if proper matching is achieved) and the various assumptions made in this Chapter in deriving the rms envelope equations have some ground.

Fig. 10.3 shows the dispersion functions D corresponding to the two cases presented in Fig. 10.1. The dashed lines represents the dispersion $D = 1/(\xi^2 \rho k_x)$ as calculated by replacing the (rms) undepressed tune with the (rms) depressed tune; that is, without taking into account the enlargement of the horizontal size of the beam induced by dispersion.

Finally in Fig. 10.4 we show the relative emittance growth for the case $k = 17.4$. The emittance is calculated using the expression (10.74). Again the result is compared with the outcome from the self-consistent calculation presented in Chapter 9 (Fig. 9.7).

10.6 Numerical Tests over a FODO Lattice

In this section we test the rms envelope-dispersion equations against some results obtained by using the PIC code WARP [34] in the modeling of the Maryland Electron Ring [52].

In the study reported here we adopted a hard-edge model of the E-Ring design. The E-Ring model consists of 36 equal FODO cells. Each FODO cell is 32 cm long and includes a 10° bending dipole. In this calculation the bends are assumed to be sector bends. See Chapter 5 and references there mentioned for a detailed description of the E-Ring lattice, magnet and beam parameters.

Let us first consider the evolution of the rms emittances after injection of a continuous beam with a longitudinal momentum spread into the E-Ring as

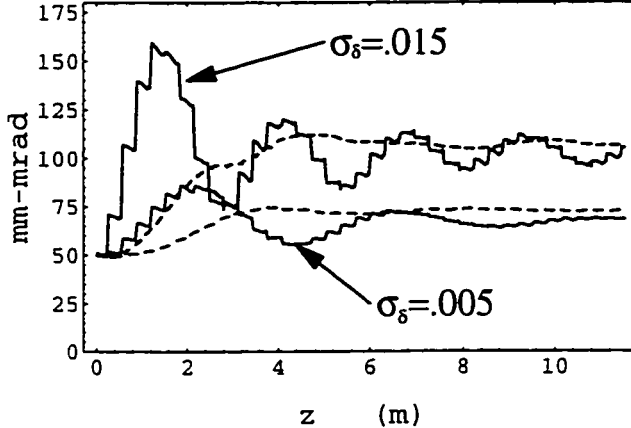


Figure 10.5: Effective emittances $4\epsilon_x$ (solid lines), $4\epsilon_y$ (dashed lines) as calculated by WARP as a function of z for two beams with different rms relative longitudinal momentum spreads σ_δ .

calculated by the PIC code. Fig. 10.5 shows the results of the simulations after injecting two beams with an initially uniform distribution in space and gaussian distribution in the transverse momenta. The rms relative longitudinal momentum spread $\sigma_\delta = \sqrt{\langle \delta^2 \rangle}$ for the two beams is indicated in the figure. The beams are initially matched with regard to the envelopes only and the matching is done using the standard rms envelope equations. The initial effective emittance in both planes is $4\epsilon_x = 4\epsilon_y = 50$ mm-mrad; the beam energy 10 keV and current $I=100$ mA.

The picture shows large emittance oscillations that eventually die off leaving a net emittance growth. Those oscillations can have a qualitative explanation in terms of a dispersion mismatch. Let us rewrite equation (10.35) in the form

$$\epsilon_x^2 = \epsilon_{dx}^2 + \langle \delta^2 \rangle \langle [p_x D(z) - x D'(z)]^2 \rangle. \quad (10.79)$$

The expression above shows that if ϵ_{dx} , the new invariant we have defined, is preserved the standard rms emittance undergoes oscillations that are proportional to the dispersion function. The large oscillations we see in the picure are due to

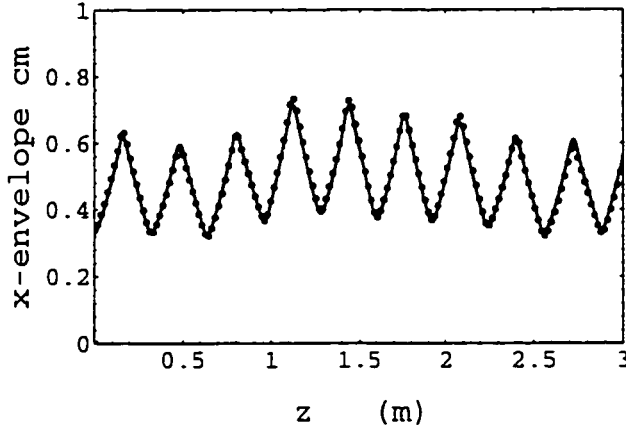


Figure 10.6: Beam envelope σ_x as calculated by WARP (solid line) and from the rms envelope-dispersion equations ($\sigma_s = .015$).

the large oscillations experienced by the unmatched dispersion function.

It is easy to write in the smooth approximation a solution of Eq. (10.34) with the initial conditions $D = D' = 0$. From this approximated solution one can observe the dispersion function undergoes sinusoidal oscillations around what, in the smooth approximation, would be its matched value. The frequency of oscillation is the same as the incoherent depressed tune. On the other hand the depressed tune is sensitive to the beam envelopes which in turn depend on the longitudinal momentum spread. For a large longitudinal momentum spread we expect larger envelopes and, therefore, a less depressed tune. This is consistent with the scaling of the period of oscillation we observe in Fig. 10.5.

There are, however, two patterns that an interpretation based on Eq. (10.79) cannot evidently explain, i.e. the damping and the increase in the vertical emittance. Eq. (10.79) as well as the rms envelope-dispersion equations presented in this paper do not account for the thermalization process we see acting here between the two degrees of freedom. This effect, triggered by the nonlinear coupling between x and y due to space charge is responsible for both the damping

and the increase in the vertical rms emittance. We believe that the thermalization process is considerably enhanced by a mismatch of the beam. A properly matched injection is likely to reduce both the excursion in the emittances oscillation and the final net emittance growth.

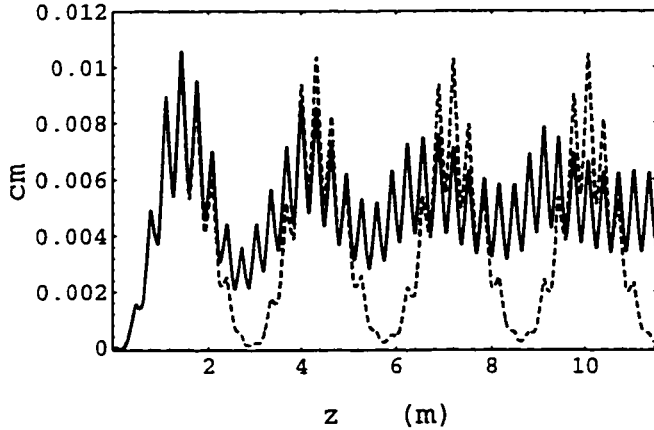


Figure 10.7: The second moment $\langle x\delta \rangle$ as calculated by WARP (solid line) and $\langle \delta^2 \rangle D(z)$ as calculated from the rms envelope-dispersion equations ($\sigma_\delta = .015$).

The remaining figures show a comparison between the beam envelopes and dispersion function as calculated from the rms envelope-dispersion equations and by the PIC code, for the same case of an initially dispersion-mismatched beam. Having in mind the discussion above we should expect that an agreement, if any, between the two calculations, should take place only over a time scale shorter than the thermalization time. Indeed this is the case. We observe a very good agreement between theory and simulation over the first half period of the (depressed) betatron oscillation period. This defines the length scale over which a matching of the dispersion function has to be accomplished.

In particular, Fig. 10.6 shows the horizontal envelope σ_x as calculated using equations (dots) and WARP (solid line) over the first betatron oscillation period. The envelope profile as calculated by WARP is well reproduced by the solutions

of the rms envelope-dispersion equation. In Fig. 10.7 and Fig. 10.8 we show the second moment $\langle x\delta \rangle$ as calculated by WARP and the scaled dispersion function $\langle \delta^2 \rangle D(z)$. The two quantities, as indicated in the previous Section, are expected to be equal. The two figures refer to two different values of the longitudinal momentum spread as indicated in the captions.

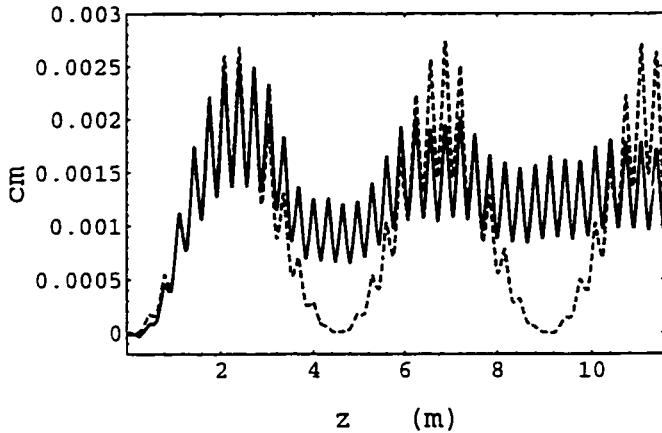


Figure 10.8: As in Fig. 10.7 but with a smaller rms longitudinal momentum spread $\sigma_\delta = .005$.

Again, thermalization can be seen in action in the way the two curves (dashed curve from the theory, solid line from the simulation) separate after the first period of oscillation. However, notice how the agreement is very good up to separation, and how the scaling of the period of the oscillation is faithfully reproduced by the solutions of the rms envelope-dispersion equations. Also notice that the oscillation periods are consistent with those displayed by the horizontal rms emittances in Fig. 10.5 for the corresponding cases of equal longitudinal momentum spread.

10.7 Summary

In this chapter we have presented the derivation of a new set of equations that generalize the standard rms envelope equations to the case where dispersion is present. The new set is made of three equations as opposed to the two equations for the vertical and horizontal rms size of the beam in the usual approach. The extra equation is needed to accommodate the additional variable of the problem i.e. the dispersion function. The derivation relies on the existence of a linear invariant that generalizes the usual rms emittance to the case where there is dispersion. We made the assumption that the invariance is approximately maintained in the presence of the nonlinearities due to the space charge. Such an ansatz is not different from a similar assumption that is made for the standard rms emittance in the derivation of the usual rms envelope equations. Strictly speaking assuming that the rms emittance or the generalized rms emittance are preserved is not necessary in order to derive the standard rms envelope equations or the rms envelope-dispersion equations. One can simply assume that those quantities are known. In practice, however, the only case where one may have a knowledge of the rms emittance or generalized emittance is when they are invariant or almost invariant. Only in this case the envelope equations are useful.

The new equations have been used to estimate the rms emittance and beam size growth in the transition from a smooth straight transport line to a dispersive channel. The results have been compared to those obtained from a previous study based on the numerical solutions of the Vlasov-Poisson equation and show a reasonable agreement. Moreover, we have applied the rms envelope-dispersion equations to the description of a beam with a longitudinal momentum spread

in a periodic lattice in the case of a dispersion-mismatch. The solutions of the equations have been compared to the results obtained using a PIC code. A good agreement is found between theory and simulations over a time shorter than the time scale over which thermalization takes place. The study suggests that the new equations should be adequate to find the matching conditions for the injection of a space charge dominated beam, provided that matching is done within the first half of the period of the betatron oscillation . The new rms envelope-dispersion equations are planned to be used to check possible matching schemes for the E-Ring at Maryland.

Appendix A

Multipole expansion for the Vector Potential in the Coulomb Gauge

In the Coulomb gauge ($\nabla \cdot \mathbf{A} = 0$) and absence of currents the vector potential \mathbf{A} obeys the vectorial Laplace equation,

$$\nabla^2 \mathbf{A} = 0.$$

The three components of the LHS of the Laplace equation in cylindrical variables (r, ϕ, z) are [48]

$$\begin{aligned} (\nabla^2 \mathbf{A})_\rho &= \nabla^2 A_\rho - \frac{1}{\rho^2} A_\rho - \frac{2}{\rho^2} \frac{\partial}{\partial \phi} A_\phi, \\ (\nabla^2 \mathbf{A})_\phi &= \nabla^2 A_\phi - \frac{1}{\rho^2} A_\phi + \frac{2}{\rho^2} \frac{\partial}{\partial \phi} A_\rho, \\ (\nabla^2 \mathbf{A})_z &= \nabla^2 A_z; \end{aligned} \quad (\text{A.1})$$

where the Laplacian is given by

$$\nabla^2 = \frac{1}{\rho} \frac{\partial}{\partial \rho} \rho \frac{\partial}{\partial \rho} + \frac{1}{\rho^2} \frac{\partial^2}{\partial \phi^2} + \frac{\partial^2}{\partial z^2}.$$

The third equation in (A.1) is the same as the scalar Laplace equation (3.1). Therefore we can immediately write the multipole expansion for $A_z(\rho, \phi, z)$ using the results of Section 3.2

$$A_z(\rho, \phi, z) = \sum_m A_{z,c}^{(m)}(\rho, z) \cos m\phi + A_{z,s}^{(m)}(\rho, z) \sin m\phi \quad (\text{A.2})$$

where

$$A_{z,\alpha}^{(m)}(\rho, z) = \sum_{l=0}^m (-1)^l \frac{m!}{2^{2l} l!(l+m)!} \Gamma_{m,\alpha}^{[2l]}(z) \rho^{2l+m} \quad (\text{A.3})$$

and $\Gamma_{m,\alpha}^{[2l]}(z) = \frac{d^{2l}}{dz^{2l}} \Gamma_{m,\alpha}(z)$. The subscript α refers to the cosine (c) or sine (s) part of the solution.

Our goal is to obtain for A_ϕ and A_ρ a multipole expansion similar to (A.2)

$$\begin{aligned} A_\phi(\rho, \phi, z) &= \sum_m A_{\phi,c}^{(m)}(\rho, z) \cos m\phi + A_{\phi,s}^{(m)}(\rho, z) \sin m\phi, \\ A_\rho(\rho, \phi, z) &= \sum_m A_{\rho,c}^{(m)}(\rho, z) \cos m\phi + A_{\rho,s}^{(m)}(\rho, z) \sin m\phi, \end{aligned} \quad (\text{A.4})$$

where $A_{\phi,\alpha}^{(m)}(\rho, z)$ and $A_{\rho,\alpha}^{(m)}(\rho, z)$ are to be determined. In the following we will assume

$$\lim_{z \rightarrow \pm\infty} A_{\phi,\alpha}^{(m)} = \lim_{z \rightarrow \pm\infty} A_{\rho,\alpha}^{(m)} = 0. \quad (\text{A.5})$$

First of all let us insert (A.4) and (A.2) into the gauge equation.

$$\nabla \cdot \mathbf{A} = \frac{1}{\rho} \frac{\partial}{\partial \rho} \rho A_\rho + \frac{1}{\rho} \frac{\partial}{\partial \phi} A_\phi + \frac{\partial}{\partial z} A_z = 0, \quad (\text{A.6})$$

to get the following conditions:

$$\begin{aligned} \frac{1}{\rho} A_{\rho,c}^{(m)} + \frac{\partial}{\partial \rho} A_{\rho,c}^{(m)} + \frac{m}{\rho} A_{\phi,s}^{(m)} + \frac{\partial}{\partial z} A_{z,c}^{(m)} &= 0, \\ \frac{1}{\rho} A_{\rho,s}^{(m)} + \frac{\partial}{\partial \rho} A_{\rho,s}^{(m)} - \frac{m}{\rho} A_{\phi,c}^{(m)} + \frac{\partial}{\partial z} A_{z,s}^{(m)} &= 0. \end{aligned} \quad (\text{A.7})$$

Notice the ‘cos-like’ terms in the multipole expansions for A_z and A_ρ are conjugated to ‘sin-like’ terms of the expansion for A_ϕ (and viceversa). The two solutions correspond to the ‘normal’ and ‘skew’ multipoles respectively.

For simplicity of notation let us consider only a single ‘normal’ multipole

$$\begin{aligned} A_z &= A_{z,c}^{(m)} \cos m\phi, \\ A_\phi &= A_{\phi,s}^{(m)} \sin m\phi, \\ A_\rho &= A_{\rho,c}^{(m)} \cos m\phi. \end{aligned} \quad (\text{A.8})$$

Next, assume the following power series expansions:

$$\begin{aligned} A_{z,c}^{(m)} &= \sum_{n=0} \Gamma_n(z) \rho^n, \\ A_{\phi,s}^{(m)} &= \sum_{n=0} \Delta_n(z) \rho^n, \\ A_{\rho,c}^{(m)} &= \sum_{n=0} E_n(z) \rho^n. \end{aligned} \quad (\text{A.9})$$

The $\Gamma_n(z)$ are already known [see (A.3)]. We want to calculate the functions $\Delta_n(z)$ and $E_n(z)$. The gauge relations (A.7) provide a first relation between those functions:

$$(1+n)E_n + m\Delta_n + \Gamma'_{n-1} = 0. \quad (\text{A.10})$$

(The prime indicates a derivative with respect to z). A second set of relations is obtained by inserting (A.9) and (A.8) into the Laplace equation (A.1). Those relations are better written after introducing the quantity $\mathcal{A}_{m,n}$ defined by the equation

$$\mathcal{A}_{m,n} = [(n+2)^2 - m^2 - 1].$$

We find the relations:

$$\begin{aligned} \mathcal{A}_{m,n} E_{n+2} - 2m\Delta_{n+2} &= -E''_n, \\ -2mE_{n+2} + \mathcal{A}_{m,n}\Delta_{n+2} &= -\Delta''_n, \end{aligned} \quad (\text{A.11})$$

$$\begin{aligned} mE_1 + 2\Delta_1 &= 0 \\ (m^2 + 1)\Delta_0 + 2mE_0 &= 0 \end{aligned} \quad (\text{A.12})$$

Equations (A.11) define some recursive relations for E_{n+2}, Δ_{n+2} in terms of E_n, Δ_n . Suppose E_{k+2}, Δ_{k+2} are the first nonvanishing terms in the series (A.9); that is $E_n = \Delta_n = 0$ for $n \leq k+1$. Consistency with equation (A.11) requires the conditions

$$\begin{aligned} \mathcal{A}_{m,k} E_{k+2} - 2m\Delta_{k+2} &= 0, \\ -2mE_{k+2} + \mathcal{A}_{m,k}\Delta_{k+2} &= 0. \end{aligned} \quad (\text{A.13})$$

The two equations above imply that the determinant $(\mathcal{A}_{m,k}^2 - 4m^2)$ must vanish. Since

$$\mathcal{A}_{m,k}^2 - 4m^2 = [(k+2)^2 - (m+1)^2][(k+2)^2 - (m-1)^2]. \quad (\text{A.14})$$

the determinant vanishes for $k = m-1$ or $k = m-3$. Let us consider separately the two cases. For $k = m-1$, we have $\mathcal{A}_{m,k} = 2m$ and the relations (A.11) become

$$\begin{aligned} E''_{m-1} &= -2mE_{m+1} + 2m\Delta_{m+1}, \\ \Delta''_{m-1} &= 2mE_{m+1} - 2m\Delta_{m+1}, \end{aligned} \quad (\text{A.15})$$

which imply that

$$E''_{m-1} = -\Delta''_{m-1}. \quad (\text{A.16})$$

Notice that because of the condition (A.5), equation (A.16) implies

$$E_{m-1} = -\Delta_{m-1}. \quad (\text{A.17})$$

On the other hand, for $k = m-3$ we have $\mathcal{A}_{m,k} = -2m$ and from the relations (A.11) we get

$$\begin{aligned} E''_{m-3} &= 2m\Delta_{m-1} + 2mE_{m-1} = 0, \\ \Delta''_{m-3} &= 2m\Delta_{m-1} + 2mE_{m-1} = 0, \end{aligned} \quad (\text{A.18})$$

where the last equalities in the two equations follow from (A.17). Therefore, we conclude that the first nonvanishing terms in the powers series in ρ for a multipole of order m are Δ_{m-1} and E_{m-1} .

Our next goal is to find a compact formula to express Δ_n and E_n in terms of Δ_{m-1} and E_{m-1} for an arbitrary value of $n > m-1$. First, let rewrite the recursive formula (A.11) in the following form:

$$\begin{pmatrix} E_{m+2l+1} \\ \Delta_{m+2l+1} \end{pmatrix} = R_l \begin{pmatrix} E''_{m+2l-1} \\ \Delta''_{m+2l-1} \end{pmatrix}. \quad (\text{A.19})$$

Here R_l is the matrix

$$R_l = \frac{-1}{\mathcal{A}_{m,m+2l-1}^2 - 4m^2} \begin{pmatrix} \mathcal{A}_{m,m+2l-1} & 2m \\ 2m & \mathcal{A}_{m,m+2l-1} \end{pmatrix}. \quad (\text{A.20})$$

Clearly

$$\begin{pmatrix} E_{m+2l+1} \\ \Delta_{m+2l+1} \end{pmatrix} = R_l R_{l-1} \dots R_2 R_1 \begin{pmatrix} E_{m+1}^{[2l]} \\ \Delta_{m+1}^{[2l]} \end{pmatrix}. \quad (\text{A.21})$$

Notice that in writing (A.21) we stopped at R_1 because R_0 is not defined (since for $l = 0$, $\mathcal{A}_{m,m-1}^2 - 4m^2 = 0$). The connection between the coefficients at the $m+1$ step to those at the $m-1$ step can be obtained by combining the first Eq. in (A.15) and the equation expressing the gauge (A.10):

$$E_{m+1} = \frac{-1}{4(m+1)} (E''_{m-1} + 2\Gamma'_m), \quad (\text{A.22})$$

$$\Delta_{m+1} = \frac{1}{4(m+1)} [(m+2)E''_{m-1} - 2m\Gamma'_m]. \quad (\text{A.23})$$

What is left to do is to evaluate the product $R_l R_{l-1} \dots R_1$. That is easily done because each R_s , with $s = 1, 2, \dots, l$ can be diagonalized by using the same similarity transformation:

$$S^{-1} R_s S = \frac{-1}{\mathcal{A}_{m,m+2s-1}^2 - 4m^2} \begin{pmatrix} \mathcal{A}_{m,m+2s-1} + 2m & 0 \\ 0 & \mathcal{A}_{m,m+2s-1} - 2m \end{pmatrix}. \quad (\text{A.24})$$

with

$$S = \frac{1}{\sqrt{2}} \begin{pmatrix} 1 & -1 \\ 1 & 1 \end{pmatrix}.$$

The final result reads

$$E_{m+2l+1} = \frac{(-1)^{l+1} m!}{2^{2l+1} (l+m+1)! (l+1)!} \left[\frac{1}{2} E_{m-1}^{[2l+2]} + (l+1) \Gamma_m^{[2l+1]} \right], \quad (\text{A.25})$$

$$\Delta_{m+2l+1} = \frac{(-1)^l m!}{2^{2l+1} (l+m+1)! (l+1)!} \left[\frac{(m+2+2l)}{2m} E_{m-1}^{[2l+2]} - (l+1) \Gamma_m^{[2l+1]} \right]. \quad (\text{A.26})$$

Notice that the expressions above are correct also for $l=0$ and $l=-1$.

Finally we can write $A_{\phi,s}^{(m)}$ and $A_{\rho,c}^{(m)}$, ($l=\ell-1$):

$$\begin{aligned} A_{\rho,c}^{(m)}(\rho, z) &= \sum_{\ell=0}^{\infty} \frac{(-1)^\ell m!}{2^{2\ell} (\ell+m)! \ell!} [E_{m-1,c}^{[2\ell]}(z) + 2\ell \Gamma_{m,c}^{[2\ell-1]}(z)] \rho^{m+2\ell-1}, \\ A_{\phi,s}^{(m)}(\rho, z) &= \sum_{\ell=0}^{\infty} \frac{(-1)^\ell m!}{2^{2\ell} (\ell+m)! \ell!} \left[-\frac{(m+2\ell)}{m} E_{m-1,c}^{[2\ell]}(z) + 2\ell \Gamma_{m,c}^{[2\ell-1]}(z) \right] \rho^{m+2\ell-1}, \\ A_{z,c}^{(m)}(\rho, z) &= \sum_{l=0}^{\infty} (-1)^l \frac{m!}{2^{2l} l! (l+m)!} \Gamma_{m,c}^{[2l]}(z) \rho^{2l+m}. \end{aligned} \quad (\text{A.27})$$

(In the notation of the expressions above we have reintroduced the subscript $\alpha=c, s$). Notice we have recovered the expansion (3.27).

For the case of 'skew' multipoles, if we write them as (notice the minus sign in the expression for A_ϕ)

$$\begin{aligned} A_z &= A_{z,s}^{(m)} \sin m\phi, \\ A_\phi &= -A_{\phi,c}^{(m)} \cos m\phi, \\ A_\rho &= A_{\rho,s}^{(m)} \sin m\phi, \end{aligned} \quad (\text{A.28})$$

we find that $A_{\rho,s}^{(m)}(\rho, z)$ and $A_{\phi,c}^{(m)}(\rho, z)$ have the same expression as $A_{\rho,c}^{(m)}(\rho, z)$ and $A_{\phi,s}^{(m)}(\rho, z)$ respectively, after the substitution of the subscripts s an c .

Appendix B

Miscellanea of Mathematical Formulae

The following are useful formulae that have been used throughout this paper.

- From Jackson [38] p. 118,

$$\frac{1}{|\mathbf{x} - \mathbf{x}'|} = \frac{4}{\pi} \int_0^\infty dk \cos[k(z - z')] \\ \times \left\{ \frac{1}{2} I_o(k\rho_<) K_o(k\rho_>) + \sum_{n=1}^{\infty} \cos[m(\phi - \phi')] I_n(\rho_<) K_n(\rho_>) \right\}, \quad (\text{B.1})$$

where $\rho_<$ is the smaller between ρ' and ρ , and $\rho_>$ the larger.

- From Erdelyi [24] p. 105 (with $\operatorname{Re} \mu > -3/2$, Γ is the Euler Gamma function),

$$\int_0^\infty x^{\mu+1} K_\mu(ax) \sin(xy) dx = \sqrt{\pi}(2a)^\mu \Gamma\left(\mu + \frac{3}{2}\right) \frac{y}{(y^2 + a^2)^{\mu+3/2}}. \quad (\text{B.2})$$

- From Erdelyi [24] p. 49 (with $\operatorname{Re} \mu > -1/2$) :

$$\int_0^\infty x^\mu K_\mu(ax) \cos(xy) dx = \frac{\sqrt{\pi}}{2} (2a)^\mu \Gamma\left(\mu + \frac{1}{2}\right) \frac{1}{(y^2 + a^2)^{\mu+1/2}}. \quad (\text{B.3})$$

For an integer $\mu = m$, we have $\Gamma(\mu + 1/2) = \sqrt{\pi}(2m - 1)!!/2^m$.

- From [30]:

$$\int \frac{dt}{(t^2 + 1)^{\frac{2m+1}{2}}} = \frac{1}{(2m - 1)} \\ \times \left\{ \frac{t}{(t^2 + 1)^{\frac{2m-1}{2}}} \left[1 + \sum_{k=1}^{m-1} \frac{2^k(m-1)(m-2)\dots(m-k)(t^2 + 1)^k}{(2m-3)(2m-5)\dots(2m-2k-1)} \right] \right\}. \quad (\text{B.4})$$

- An integral representation of the modified Bessel function K_0 is given by [5],

$$K_0(x) = \int_1^\infty \frac{e^{-xt}}{\sqrt{t^2 - 1}} dt.$$

By choosing an appropriate integration contour in the complex plane, and by using the relation $\frac{d}{dx} K_0(x) = -K_1(x)$, we can derive the relations:

$$\int_{-\infty}^\infty \frac{te^{ixt}}{[\sqrt{t^2 + 1}]^3} dt = 2ixK_0(x),$$

$$\int_{-\infty}^\infty \frac{e^{ixt}}{\sqrt{t^2 + 1}} dt = 2K_0(x),$$

$$\int_{-\infty}^\infty \frac{e^{ixt}}{[\sqrt{t^2 + 1}]^3} dt = 2xK_1(x).$$

The two Bessel functions $K_0(x)$, $K_1(x)$ have the following limiting behavior.

For $x \gg 1$

$$K_0(x) \simeq K_1(x) \simeq \sqrt{\frac{\pi}{2x}} e^{-x}. \quad (\text{B.5})$$

For $x \rightarrow 0$

$$K_0(x) \simeq -[\ln\left(\frac{x}{2}\right) + .5772...], \quad (\text{B.6})$$

$$K_1(x) \simeq \frac{1}{x}. \quad (\text{B.7})$$

$$(\text{B.8})$$

- Solutions of a general algebraic cubic equation.

After defining

$$q = \frac{1}{3}a_1 - \frac{1}{9}a_2, \quad (\text{B.9})$$

$$r = \frac{1}{6}(a_1a_2 - 3a_0) - \frac{1}{27}a_2^3, \quad (\text{B.10})$$

$$(\text{B.11})$$

and

$$s_1 = [r + \sqrt{q^3 + r^2}]^{\frac{1}{3}}, \quad (\text{B.12})$$

$$s_2 = [r - \sqrt{q^3 + r^2}]^{\frac{1}{3}}, \quad (\text{B.13})$$

$$(\text{B.14})$$

the roots of the equation

$$z^3 + a_2 z^2 + a_1 z + a_0 = 0,$$

are [5]:

$$z_1 = (s_1 + s_2) - \frac{a_2}{3}, \quad (\text{B.15})$$

$$z_{2,3} = -\frac{1}{2}(s_1 + s_2) - \frac{a_2}{a_3} \pm \frac{i\sqrt{3}}{2}(s_1 - s_2). \quad (\text{B.16})$$

Appendix C

Dispersion and Second Moments of a Beam Distribution

In this appendix we prove Eqs. (8.8) for a larger class of distribution functions in phase space in the limit of vanishing space charge.

From the Hamiltonian

$$H = \frac{1}{2}(p_x^2 + p_y^2) + \frac{1}{2}(k_x(z)x^2 + k_y(z)y^2) - \frac{\delta}{\rho(z)}x \quad (\text{C.1})$$

and the associated Vlasov equation we can easily derive the differential equations for the second moments of the distribution:

$$\begin{aligned} \frac{d}{dz}\langle x^2 \rangle - 2\langle xp_x \rangle &= 0, \\ \frac{d}{dz}\langle p_x^2 \rangle + 2k_x(z)\langle xp_x \rangle &= \frac{2}{\rho}\langle p_x \delta \rangle, \\ \frac{d}{dz}\langle xp_x \rangle - \langle p_x^2 \rangle + k_x(z)\langle x^2 \rangle &= \frac{1}{\rho}\langle x \delta \rangle, \end{aligned} \quad (\text{C.2})$$

$$\begin{aligned} \frac{d}{dz}\langle x \delta \rangle &= \langle p_x \delta \rangle, \\ \frac{d}{dz}\langle p_x \delta \rangle &= -k_x(z)\langle x \delta \rangle + \frac{1}{\rho}\langle \delta^2 \rangle. \end{aligned} \quad (\text{C.3})$$

The brackets $\langle \cdot \rangle$ denote, as usual, the averaging over the phase space variables

according to

$$\langle \xi_i \xi_j \rangle = \int \xi_i \xi_j f(x, p_x, y, p_y) d\mu,$$

where ξ_i, ξ_j are any canonical variables, and $d\mu = dx dp_x dy dp_y d\delta$. Here we have assume for simplicity that $\langle x \rangle = \langle y \rangle = \langle p_x \rangle = \langle p_y \rangle = 0$. The last two equations (10.25) can be combined into a single differential equation

$$\frac{d^2}{dz^2} \langle x \delta \rangle + k_x \langle x \delta \rangle = \frac{1}{\rho} \langle \delta^2 \rangle. \quad (\text{C.4})$$

From comparison between eq. (8.3) and (C.4) we conclude:

$$\begin{aligned} \langle x \delta \rangle &= \langle \delta^2 \rangle D(z), \\ \langle p_x \delta \rangle &= \langle \delta^2 \rangle D(z)'. \end{aligned} \quad (\text{C.5})$$

Equations (C.5) hold for any z provided they are satisfied at one point (it follows from the uniqueness of the solution of linear differential equations). This is the case if we assume for example that the beam distribution is such that it is $\langle x \delta \rangle = \langle p_x \delta \rangle = 0$ when $D = D' = 0$. This is not too a restrictive assumption. Physically it implies that at injection the variables x, δ , and p_x, δ are not correlated. i.e. $\langle x \delta \rangle = \langle x \rangle \langle \delta \rangle = 0, \langle p_x \delta \rangle = \langle p_x \rangle \langle \delta \rangle = 0$.

After substituting equations (C.5) into (C.2) we see that (C.2) turns into an inhomogeneous linear system a particular solution of which, as it can be easily verified by direct substitution, is given by $\langle x^2 \rangle = \langle \delta^2 \rangle D(z)^2, \langle p_x^2 \rangle = \langle \delta^2 \rangle D(z)^2, \langle x p_x \rangle = \langle \delta^2 \rangle D(z)D(z)'$. Therefore, we can write the general solution as a superposition of that particular solution and the general solution of the homogeneous part of the differential system, which we indicate with the subscript ' $_o$ ':

$$\begin{aligned} \langle x^2 \rangle &= \langle x^2 \rangle_o + \langle \delta^2 \rangle D(z)^2, \\ \langle p_x^2 \rangle &= \langle p_x^2 \rangle_o + \langle \delta^2 \rangle D(z)^{\prime 2}, \\ \langle x p_x \rangle &= \langle x p_x \rangle_o + \langle \delta^2 \rangle D(z)D(z)'. \end{aligned} \quad (\text{C.6})$$

In the general case the solution of the homogeneous part of eq. (10.22) will also depend on $\langle \delta^2 \rangle$. In those cases where the dependence is of an order higher than $\langle \delta^2 \rangle$, we see from Eq. (8.8) that the dispersion function weights the dependence of the moments on $\langle \delta^2 \rangle$. Moreover, the $\langle \delta^2 \rangle$ -independent part of the solution of the homogeneous part of Eq. (10.22) can be interpreted physically as describing the moments of the distribution either in the limit of vanishing momentum spread ($\langle \delta^2 \rangle = 0$), or at those locations in z where the dispersion function vanishes. For the case of a Boltzmann distribution the solution of the homogeneous part of Eq. (10.22) does not depend on δ_o .

Appendix D

Mathematica Notebook

This Mathematica notebook contains a program to compute the Taylor splitting formula (2.15). The program also writes the differential equations obeyed by the nonlinear beam generators. See Sec. 1.4.

The user has to specify at the beginning the order of the largest polynomial (*maximor*) and the maximum order of the Taylor expansion (*nmaxt*).

- Set the max order of the polynomials *maximor* and the max order of expansion in t

```
maximor=8;  
nmaxt=4;
```

- Rules and formats

```
ScalarQ[a_]:=  
Head[a] == Scalar || Head[a] == Integer || Head[a] == Real  
|| Head[a] == Power || Head[a] == Rational  
Rule1 = Pb[f_, a_*g_] :> a*Pb[f, g]/; ScalarQ[a];
```

```

Rul2 = Pb[a_*f_,g_] :> a*Pb[f,g]/; ScalarQ[a];
Rul3 = Pb[a_,g_] :> 0 /; ScalarQ[a];
Rul4 = Pb[g_,a_] :> 0 /; ScalarQ[a];
Rul4ter = Pb[g_,g_] :> 0 ;
roulette1 = Pb[f_,g_] :> -Pb[g,f] /; Head[g] == Pb;
roulette2 = Pb[f_,g_] :> -Pb[g,f] /; Head[f] == Pb;

Rul5= Pb[f_,g_ + h_] :> Pb[f,g] + Pb[f,h];
Rul5bis= Pb[g_ + h_,f_] :> Pb[g,f] + Pb[h,f] ;
Rul6= Pb[f_,g_ - h_] :> Pb[f,g] - Pb[f,h] ;
Rul6bis= Pb[g_ - h_,f_] :> Pb[g,f] - Pb[h,f] ;
rulesdis:={Rul5,Rul5bis,Rul6,Rul6bis}

Regola=Pb[PowerPb2[f_,m_,g_],PowerPb2[f_,n_,g_]]:>
If[m<n,-Pb[PowerPb2[f,n,g]],PowerPb2[f,m,g]] ,
Pb[PowerPb2[f,m,g],PowerPb2[f,n,g]]]

Regola2= Pb[Pb[f_,g_],h_] :> -Pb[h,Pb[f,g]]

Regolatot={Regola,Rul1,Rul2,Regola2,Rul1,Rul2};

PowerPb[a_,n_,f_]:=If[n==1,Pb[a,f],
If[n==0,f,Lieopa[x_]=Pb[a,x];Nest[Lieopa,f,n]]]

Format[Pb[f_,g_]] := SequenceForm["[",f,".",",",g,"]"]
Format[Poly[g_,m_]] := SequenceForm[g,m]
Format[gdot[g_,m_]]:=SequenceForm[g,m,"'"]

```

```

Format[hint[m_]]:= SequenceForm[H,m]
Format[Scalar[w_]]:=w

Unprotect[Times]
Format[Times[Rational[f_,g_],h_]] :=
SequenceForm[f/g,h];

Format[PowerPb2[f_,n_,g_]] =If[n==0,
SequenceForm[g],
SequenceForm[":",f,":"^n,"" g]];

```

□ Truncate a polynomial to order n

```

trunc[w_,f_,n_]:=Table[Scalar[w]^i,{i,0,n}].
Table[Coefficient[f,Scalar[w],i],{i,0,n}]

```

□ Expansion of $\exp(- : g_m :) f$ and $i \exp(- : g_m :) f$ through order n

```

listg[m_,n_,f_]:=Table[(Scalar[w]^(m-2))^i*PowerPb[-Poly[g,m],i,f],
{i,0,Floor[n/(m-2)]}];

expg[m_,n_,f_]:=Table[1/i!,{i,0,Floor[n/(m-2)]}].listg[m,n,f];
trexpg[f_,m_]:=trunc[w,Expand[expg[m,maximor,f] //. rul],maximor]

iexpg[m_,n_,f_]:=
```

```
Table[1/(i+1)!,{i,0,Floor[n/(m-2)]}].listg[m,n,f]
```

□ Equations of motion for the generators g_n . $gdl[i]$ contains the expression of g'_i .

```
termmm[i_,nmax_]:=  
If[i==2,Expand[iexpg[i+1,nmax-i-1,gdot[g,i+1]*Scalar[w]^(i+1)]],  
Fold[trexpq,iexpg[i+1,nmax-i-1,  
gdot[g,i+1]*Scalar[w]^(i+1)] //. rul,Table[i-j,{j,0,i-3}]]]  
  
knownterm[nmax_]:=Table[Scalar[w]^(i+2),{i,1,nmax-2}].  
Table[hint[i+2],{i,1,nmax-2}]  
  
eq[m_,nmax_]:=  
Sum[Expand[termmm[j,nmax]] //.rul,{j,2,m}]+knownterm[nmax]  
  
listcoeff[m_,nmax_]:=  
CoefficientList[eq[m,nmax] //. rulesdis,Scalar[w]]  
  
Do[equation[i]=listcoeff[maximor,maximor][[i+1]],{i,3,maximor}]  
  
Do[gdl[i]=Expand[-(equation[i]-gdot[g,i]) //. rul] ;  
gdot[g,i]=gdl[i],  
{i,3,maximor}]
```

```
Table[gdl[i],{i,3,maximor}];
```

-H3

[g3,H3]

-H4 - -----

2

[g3,[g3,H3]]

-H5 - [g3,H4] - -----

3

(...)

□ Transformation into the interaction picture.

```
lsh[n_,f_] :=
```

```
Table[(-Scalar[t])^i*PowerPb2[Poly[h,2],i,f],{i,0,n}];
```

```
exph2[n_,f_] := Table[1/i!,{i,0,n}].lsh[n,f]
```

```
Do[hint[i]=
```

```
exph2[nmaxt,Poly[h,i]] //. rul,
```

```
{i,3,maximor}]
```

\$\\$bl\\$ Final results (\$finalg[i]\$ contain the Taylor eexpansion of the

polynomial \$g_i\$ throu the desired order

```
Do[finalg[i]=Integrate[trunc[t,gdl[i] //. rul,nmaxt],  
Scalar[t]];Poly[g,i]=finalg[i],{i,3,maximor}]
```

□ Feed-up terms only

```
Do[hintintegrated[i]=Integrate[hint[i],Scalar[t]],  
{i,3,maximor}]
```

```
Do[  
feedup[i]=Collect[Expand[finalg[i] //Regolatot ] +  
hintintegrated[i],  
Scalar[t]],  
{i,4,maximor}]
```

fu	1	3	1	2	4
g	= $\frac{1}{4}$	$-\frac{1}{12}$	$\frac{1}{24}$		
	1	2	1	3	5
	(---)	$+\frac{1}{120}$	$-\frac{1}{80}$		
	:h2:	:h3,	:h2:	:h3,	:h2:

$$\begin{aligned}
 g = & -[h_3, h_4] t + (-(-)[h_3, :h_2: h_4] - -[:h_2: h_3, h_4]) \\
 & 5 \quad 2 \qquad \qquad \qquad 3 \qquad \qquad \qquad 6 \\
 \\
 & 3 \quad 1 \qquad \qquad \qquad 1 \quad 2 \\
 t = & + (-(--)[h_3, [:h_2: h_3, h_3]] + -[h_3, :h_2: h_4] + \\
 & 24 \qquad \qquad \qquad 8 \\
 \\
 & 1 \qquad \qquad \qquad 1 \quad 2 \qquad \qquad \qquad 4 \\
 - & [:h_2: h_3, :h_2: h_4] + --[:h_2: h_3, h_4]) t + \\
 & 8 \qquad \qquad \qquad 24 \\
 \\
 & 1 \quad 2 \qquad \qquad \qquad 1 \quad 3 \\
 (- & --[h_3, [:h_2: h_3, h_3]] - --[h_3, :h_2: h_4] + \\
 & 45 \qquad \qquad \qquad 30 \\
 \\
 & 1 \qquad \qquad \qquad 1 \quad 2 \\
 -- & [:h_2: h_3, [:h_2: h_3, h_3]] - --[:h_2: h_3, :h_2: h_4] - \\
 & 60 \qquad \qquad \qquad 20 \\
 \\
 & 1 \quad 2 \qquad \qquad \qquad 1 \quad 3 \qquad \qquad \qquad 5 \\
 -- & [:h_2: h_3, :h_2: h_4] - ---[:h_2: h_3, h_4]) t \\
 & 30 \qquad \qquad \qquad 120 \\
 \\
 (\dots)
 \end{aligned}$$

Bibliography

- [1] D. Abell, *Analytic Properties and Cremona Approximation of Transfer Maps for Hamiltonian Systems*, Ph. D. Dissertation, University of Maryland, College Park MD, 1995. Unpublished.
- [2] D. Abell, Private Communication.
- [3] V. Arnold, *Geometric Methods in the Theory of Ordinary Differential Equations*, Springer-Verlag, New York, (1983).
- [4] V. Arnold, S. Novikov, *Dynamical Systems IV*. Springer-Verlag, New York. (1980).
- [5] M. Abramowitz, V. Stegun, *Handbook of Mathematical Functions*. Dover Publications INC New York, (1972).
- [6] R.T. Avery, G.R. Lambertson, C.D. Pike, *Printed Circuit Steering Coils*. 1971 PAC Conference Proceedings.
- [7] J.J. Barnard et al. *Emittance growth in Heavy ion Recirculators*. 1992 Linear Accelerator Conference Proc. AECL-10728, Vol. 1, p.229
- [8] M. Bassetti, C. Biscari, *Analytical Formulae for Magnetic Multipoles, Particle Accelerators*, 1996, Vol. 52, p.221.

- [9] M. Berz, *Differential Algebraic Description of Beam Dynamics to very High Orders*. Part. Accel. 24, 2 (1989) 109-124.
- [10] T.J.Bridges, R.H.Cushman, *Unipotent Normal Forms for Symplectic Maps*. Physica D 65 (1993) 211-241.
- [11] B.E. Carlsten, T.O.Raubenheimer, *Emissance Growth of Bunched Beams in Bends*. Phys. Rev. E. Vol. 51, 2, p.1453 (1995).
- [12] S.Caspi, M.Helm, L.J.Laslett, *The Use of Harmonics in 3-D Magnetic Fields*, IEEE Trans. on Magnetics, vol.30, no. 4, 1994.
- [13] A. Chao, *Physics of Collective Beam Instabilities in High Energy Accelerators*, Wiley & Son (1993).
- [14] C.Chen,Q. Qian,C.Davidson, *Chaotic Behavior and Halo Development in the Transverse Dynamics of Heavy-ion Beams*. Fusion Engineering and Design 32-33 (1996) 159-167: R. Gluckstern. Phys. Rev. Lett.. 73 (1994) 1247.
- [15] S.N. Chow, C. Li, D.Wang, *Normal Forms and Bifurcation of Planar Vector Fields*. Cambridge University Press. (1994).
- [16] E.D. Courant, H.S. Snyder, *Theory of the Alternating-Gradient Synchrotron*, Annals of Phys. 3, 1-18 (1958).
- [17] R.Cushman, J.A.Sanders. *Splitting Alghorithm for Nilpotent Normal Forms*. Dynamics and Stability of Systems Vol.2 No. 4 1988.

- [18] W.G. Davies. *The Theory of the Measurement of Magnetic Multipole Fields with Rotating Coil Magnetometers*, Nuclear Intr. and Methods in Physics Research A311 (1992) 399-436.
- [19] A. Dragt, *Lectures on Nonlinear Dynamics and Lie Methods with Applications to Accelerator Physics*, University of Maryland, College Park (1998).
- [20] A. Dragt, *Computation of Maps for Particle and Light optics by Scaling. Splitting and Squaring*, Phys. Rev. Lett. Vol. 75, 10 (1995) 1946.
- [21] A. Dragt, R. Gluckstern, F. Neri, and G. Rangarajan, *Theory of Emittance Invariants. in Frontiers of Beam Physics, Diagnostic Observation*, p. 94. M. Month, S Turner Eds, Lecture Notes in Physics 343, Springer Verlag, New York (1988).
- [22] A. Dragt, F. Neri, G. Rangarajan, D. Douglas, L. Healy and R. Ryne. *Lie Algebraic Treatment of Linear and Nonlinear Beam Dynamics*. Ann. Rev. Nucl. Part. Sci. 38 (1988) pp. 455-96.
- [23] A. Dragt, D. Douglas, J. van Zeijts, F. Neri, C.T. Mottershead, R. Ryne, E. Forest, L. Healy, and P. Schutt. *MARYLIE 3.0. User's Manual: A program for Charged Particle Beam Transport Based on Lie Algebraic Methods*, University of Maryland, Physics Department Report, (1994).
- [24] A. Erdelyi, *Table of Integral Transforms*, Vol.I, McGraw-Hill Book Company, 1954.
- [25] W.M. Fawley, *Space-Charge Dominated Beam Transport in Magnetic Quadrupoles with Large Aperture Ratios*, Lawrence Berkeley Laboratory, Internal Report LBL-33608.

- [26] E. Forest, *A New Attitude and Framework for Beam Dynamics*, Harwood Academic Publishers, Amsterdam (1998).
- [27] E. Forest and J. Milutinovic, Nucl. Instr. and Meth., A269:474, 1988.
- [28] A. Garren. *Studies of a Beam Line for Transport to a Target*. Proc. Heavy Ion Fusion Workshop, 1979 Reports LBL-10301/SLAC-PUB 2575. UC-28, p.397.
- [29] Gluckstern, Proc. Linear Accelerator Conf, p. 250, Los Alamos, 1996.
- [30] I.S. Gradshteyn, I.M. Ryzhik, *Table of Integrals, Series, and Products*, Academic Press, New York, 1980.
- [31] T. Godlove, M. Venturini. *Design of the Panofsky Quads for the Maryland Electron Ring*. Technical Report, work in progress.
- [32] T. Godlove. *Design of the PC Quadrupoles for the Maryland Electron Ring*. Technical Report.
- [33] T. Godlove. *Design of the PC Dipoles for the Maryland Electron Ring*. Technical Report.
- [34] D.P. Grote et al., Fus. Eng. and Design 32-33, (1996) 193-200.
- [35] K. Halbach, Nucl. Instr. and Meth., A187:109, 1981.
- [36] P.W. Hawkes, E. Kasper, *Principles of Electron Optics*, Academic Press, 1989.
- [37] I. Hofmann, *Transport of High-Intensity Beams, in Applied Charged Particles Optics*. Part C, p. 49, A. Septier Ed., Academic Press (1983).

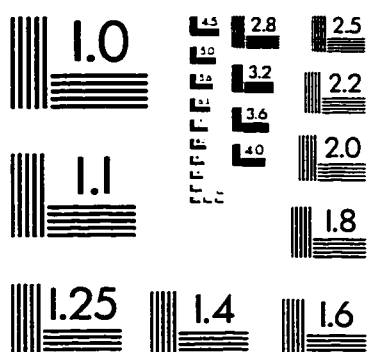
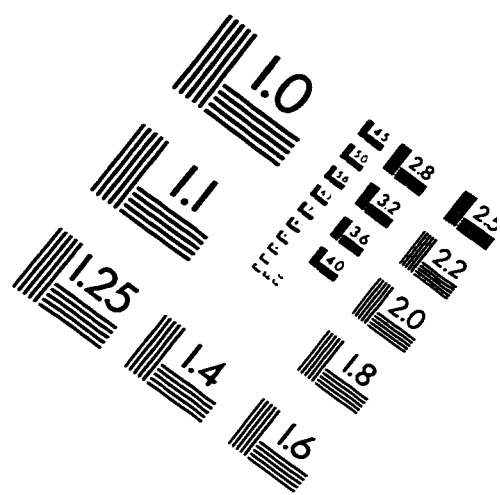
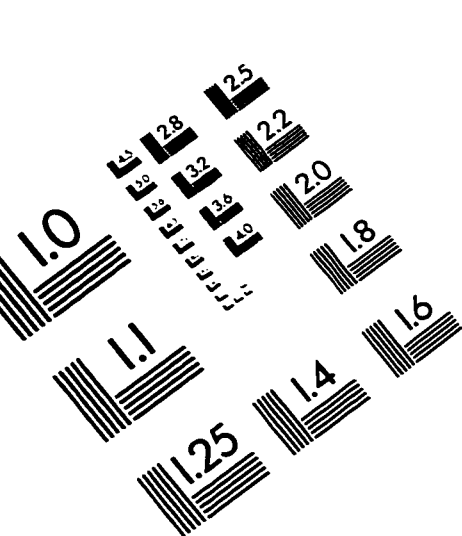
- [38] Jackson, *Classical Electrodynamics*. Wiley, 1975.
- [39] R.A. Kishek, S.Bernal, M.Reiser, M.Venturini, J.G. Wang, I.Haber, T.F. Godlove, *Beam Dynamics Simulations of the University of Maryland Electron-Ring Project*, (to be published in NIM-A).
- [40] R.A. Kishek, M. Venturini, M.Reiser, I. Haber, *PIC Code Simulations of Space-Charge Dominated Beams in the University of Maryland Electron Ring*, AIP Proceedings of the Workshop on Space Charge, Shelter Island 1998. A. Luccio W.T. Weng Eds, to be published.
- [41] The LHC lattice files are posted on the Web at '<http://www-ap.fnal.gov/lhc/database/lattices>' .
- [42] J.D. Lawson, *Plasma Physics*, 117, 567 (1975).
- [43] G.E. Lee-Whiting, *Third-order Aberrations of a Magnetic Quadrupole Lens*, Nuclear Instr. and Methods 83 (1970) p.232.
- [44] G.E. Lee-Whiting, *Measurement of Quadrupole Lens Parameters*. Nuclear Instr. and Methods 82 (1970) 157-161.
- [45] R.R London, H.P. Rogosinski *Decomposition Theory in the Teaching of Elementary Linear Algebra*. American Mathematical Monthly (1990). 478-485.
- [46] H.Grote, F.C. Iselin, *The mad Program Version 8.11. User Reference Manual*. Internal Report CERN, Geneva, CERN/SL/90-13 (AP).
- [47] S. Wolfram *Mathematica. A System for Doing Mathematics by Computers*. Addison-Wesley, 1991.

- [48] Morse P.M. and H. Feshbach. *Methods of Theoretical Physics*. McGraw-Hill, New York, 1953.
- [49] C.Moler, C. Van Loan, *Nineteen Dubious Ways to Compute the Exponential of a Matrix*. SIAM Review, Vol 20,4, (1978), p.801.
- [50] W.H Press et al. *Numerical Recipes in Fortran*, Cambridge University Press, 1992.
- [51] Reiser M. *Theory and Design of Charged Particle Beams*. Wiley, New York. 1994.
- [52] M. Reiser, S. Bernal, A. Dragt, M. Venturini, J.G. Wang, H. Onishi, and T.F. Godlove, *Design Features of a Small Electron Ring for Study of Recirculating Space-Charge Dominated Beams*, 'Fusion Engineering and Design', 32-33, 293-298 (1996); J.G. Wang et al, *Design and Developement of an Electron Recirculator for Study of High-Current Beam Dynamics*. PAC97 Proceedings.
- [53] G. Sabbi, Private Communication.
- [54] G. Sabbi, *Magnetic Field Analysis of HGQ Coil Ends*, TD-97-040 (1997). Fermilab Report.
- [55] G. Sabbi, *Comparison of calculated vs. measured harmonics in HGQS01 Lead End*, Fermilab Report TD-98-036 (1998).
- [56] F.J.Sacherer, *RMS Envelope Equations with Space Charge*, IEEE Transactions on Nuclear Science NS-18,1105 (1971).
- [57] M. Reiser, *Theory and Design of Charged Beams*, Wiley & Son (1994).

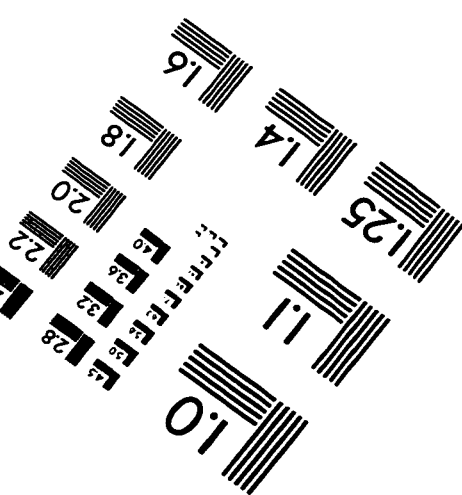
- [58] R.L. Spencer, S.N.Rasband, R.R. Vanfleet, *Numerical Calculation of Axisymmetric Non-neutral Plasma Equilibria*, Phys. Fluids B 5 (12), 1993.
- [59] M. Venturini, A.Dragt, *Accurate Computation of Transfer Maps from Magnetic Field Data*, to be published in NIM-A.
- [60] M.Venturini, S.Bernal, A. Dragt, M.Reiser, J.G.Wang, T.F. Godlove, *Single Particle Dynamics Study for a University of Maryland Electron Ring*, 'Fusion Engineering and Design', 32-33 p. 283-291 (1996).
- [61] M. Venturini, M.Reiser, *Generalized KV Beam in a Dispersive Channel*, PAC97 Proceedings.
- [62] M. Venturini, M.Reiser, *Self-Consistent Beam Distributions with Space Charge and Dispersion*, Phys. Rev. E, 57, 4 (1998) 4725.
- [63] M. Venturini, M. Reiser, *RMS Envelope Equations in the Presence of Space Charge and Dispersion*, Phys. Rev. Letter 81, 1 (1998) 96.
- [64] M. Venturini, R.A. Kisheck, and M. Reiser, *Dispersion and Space Charge*,AIP Proceedings of the Workshop on Space Charge, Shelter Island 1998. A. Luccio W.T. Weng Eds, to be published.
- [65] M. Venturini, *Generalized Gaussian beam in a Dispersive Channel*, University of Maryland, Technical Report (1997).
- [66] H. Wiedemann, Particle Accelerator Physics, Springer-Verlag 1993.
- [67] P. Walstrom, *Private Communication*.

- [68] P. Walstrom, F. Neri, T. Mottershead. *High-Order Optics of Multipole Magnets*. Proceedings of the 1990 Linac Conference, Los Alamos. Internal Report LA-UR-90-2888 (1990).
- [69] P. Walstrom, *Dipoles-Sheet Multipole Magnets for Accelerators*. 13th Conference on Magnet Technology. Los Alamos. Internal Report. LA-UR-93-3321 (1993).
- [70] J.Williamson, *On an Algebraic Problem Concerning the Normal Forms of Linear Dynamics Systems*. Amer. J. of Math. 58 n.1. 1936, 141-163.
- [71] H.Matsuda, H.Wollnik, *Third order Transfer Matrices for the Fringing Field of Magnetic and Electrostatic Lenses*. Nuclear Instr. and Methods 103 (1972) p.117.
- [72] B. Pfreundtner, B.Hartmann, H.Wollik, *Fifth-order Aberrations Due to the 12-pole Component of the Fringing Field in Magnetic Lenses*. Optik 97 N0.3 (1994) 91-93.

IMAGE EVALUATION TEST TARGET (QA-3)



150mm 6"



APPLIED IMAGE, Inc.
1653 East Main Street
Rochester, NY 14609 USA
Phone: 716/482-0300
Fax: 716/288-5989

© 1993, Applied Image, Inc., All Rights Reserved

